Evaluation of Tsunami Levels Along the British Columbia Coast

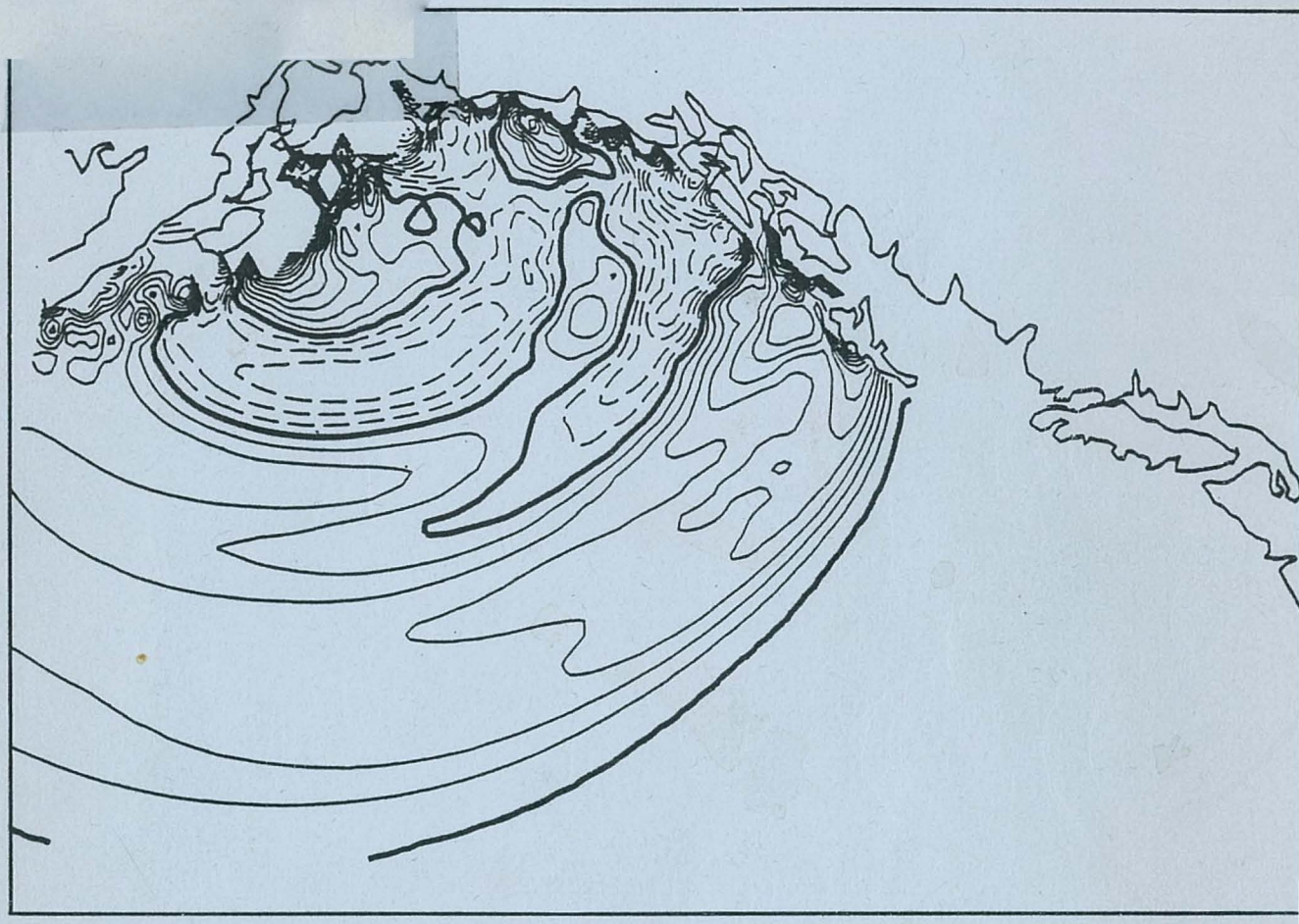

Prepared By

Seaconsult Marine Research Ltd.

March 1988

Final Report

EVALUATION OF TSUNAMI LEVELS ALONG THE BRITISH COLUMBIA COAST

Prepared for

Department of Fisheries and Oceans
Institute of Ocean Sciences
9860 West Saanich Road
Sidney, British Columbia

Dr. T. Murty
Scientific Authority
SSC Contract No. 01SB.FP941-5-1641

By

Donald S. Dunbar, Ph.D.
Paul H. LeBlond, Ph.D.
Donald O. Hodgins, Ph.D.

Seaconsult Marine Research Ltd.
820-1200 West 73rd Avenue
Vancouver, British Columbia

March 1988

SUMMARY

Maximum tsunami water levels and currents along the British Columbia outer coast have been computed for waves originating from Alaska, Chile, the Aleutian Islands (Shumagin Gap) and Kamchatka. Three computer models have been developed to generate and propagate a tsunami from each of these source regions in the Pacific Ocean to the continental shelf off Canada's west coast, and into twenty separate inlet systems. The model predictions have been verified against water level measurements made at tide gauges after the March 28, 1964 Alaska earthquake.

Simulated seabed motions giving rise to the Alaskan and Chilean tsunamis have been based on surveys of vertical displacements made after the great earthquakes of 1964 (Alaska) and 1960 (Chile). Hypothetical bottom motions have been used for the Shumagin Gap and Kamchatka simulations. These simulations represent the largest tsunamigenic events to be expected from these areas.

Maximum wave and current amplitudes have been tabulated for each simulated tsunami at 185 key locations along the British Columbia coast. On the north coast of British Columbia, the Alaska tsunami generated the largest amplitudes. In all other regions of the west coast, the largest amplitudes were generated by the Shumagin Gap simulation. Wave amplitudes in excess of 9 m were predicted at several locations along the coast, and current speeds of 3 to 4 m/s were produced. The most vulnerable regions are the outer coast of Vancouver Island, the west coast of Graham Island, and the central coast of the mainland. Some areas, such as the north central coast, are sheltered enough to limit expected maximum water levels to less than 3 m.

TABLE OF CONTENTS

TABLE OF CONTENTS
(Continued)

LIST OF TABLES

LIST OF FIGURES

LIST OF FIGURES
(Continued)

LIST OF FIGURES
(Continued)

LIST OF FIGURES
(Continued)

1.0 INTRODUCTION

1.1 The Tsunami Hazard in British Columbia

The west coast of Canada is vulnerable to the effects of seismic sea waves, or tsunamis, generated at numerous locations along the active subduction zones of the Pacific Rim. These events are infrequent and often cause little or no damage. Occasionally, however, a great earthquake generates a large tsunami that may cause extensive loss of life and property damage. This was demonstrated on March 28, 1964 when a magnitude 8.4 earthquake in Prince William Sound, Alaska, generated the most damaging tsunami to date on Canada's west coast. Fortunately, no loss of life occurred in British Columbia, but property damage in Port Alberni was estimated to be several million dollars (Spaeth and Berkman, 1967).

Forecasting future earthquakes is not possible at present, and hence the time of arrival of the next large tsunami is unknown. It is certain, however, that these events will continue to occur and that the risk to lives and property is very real, and should not be ignored. To implement effective planning of land use and disaster relief it is necessary to have an estimate of the largest waves that can be expected to arrive along the British Columbia coastline.

Through the use of digital computers it is now possible to simulate tsunami generation and propagation by numerically solving the appropriate mathematical equations. This approach allows complete flexibility in specifying tsunami source regions and generation mechanisms, as well as treating the complex topography and bathymetry of the coastal waterways.

This report contains the results of a study that has determined representative tsunami wave heights and current velocities along the British Columbia coastline that are likely to result from great earthquakes around the Pacific Rim. The methods used to accomplish this rely on advanced numerical modelling techniques for simulating tsunami generation and propagation using a digital computer. The numerical models solve complex mathematical equations over a large portion of the Pacific Ocean, the continental shelf off Canada's west coast, and the major inlet systems of British Columbia.

This is the first time that numerical modelling methods have been applied to such an extensive and complex system of waterways in order to estimate tsunami wave heights. Previously, estimates have been based solely on experience and intuition, or on statistical methods applied to historical tsunami records (e.g. Marshall, Macklin Monahan, 1986). This study provides a major improvement in accuracy of estimated tsunami waves over a large portion of British Columbia's coastline.

1.2 Study Objectives

The focus in the present study has been to develop new tools for estimating tsunami wave heights over the entire coastline of British Columbia. The objectives of this study are to:

- derive a set of numerical models for tsunami generation and propagation from their point of origin to the heads of inlets along the British Columbia coast;

- examine the sensitivity of tsunami water levels in inlets to different source locations (directional effect on water levels), and to source strength by varying the magnitude of bottom motions;

- identify the source region that is most likely to produce the largest tsunamis along the British Columbia coast from epicentres located in Alaska, Chile, the Aleutian Islands (Shumagin Gap), and Kamchatka;

- determine the maximum expected water levels at selected locations along the British Columbia coast for earthquakes at the above sources, and identify critical inlets where tsunamis are magnified by topography;

- identify areas in the modelled inlets where large current speeds will result from the passage of a tsunami wave; and

- provide recommendations on improved estimates of most probable maximum tsunami levels.

Output from the numerical models consists of wave heights and current velocities at discrete locations and times. The time interval between values is typically a few minutes, and the spatial separation between output points ranges from 2 to 5 km along the coast. This information has been used to prepare maps and tables showing the largest wave heights and currents from each source area at many locations along the British Columbia coastline. These locations were selected primarily on the basis of local human activity, including townsites, Indian villages, log booming grounds, recreational areas, and industrial development.

We note that the effects of dry land flooding have not been included owing to the large amount of additional topographic data that is required and the special demands created for high-resolution, local-area models in many locations. This does not pose serious problems in most areas; however, near the heads of inlets--where there is often an extensive area of flatlands associated with a river mouth--modelled wave heights may be appreciably overestimated.

The four source areas shown in Fig. 1.1 have been identified as likely sites for generation of tsunamis that could threaten Canada's coastline. This is based on the occurence of previous tsunamigenic earthquakes and on estimates of the likelihood of future great earthquakes in each area.

1.3 Report Organization

Chapter 2 presents a description of the study region along the British Columbia coast and gives an overview of the methods used to simulate the tsunamis. Data resources used in the modelling are outlined in Chapter 3.

The governing mathematical equations are given in Chapter 4 for each model type, followed in Chapter 5 by the numerical procedures used to construct each model.

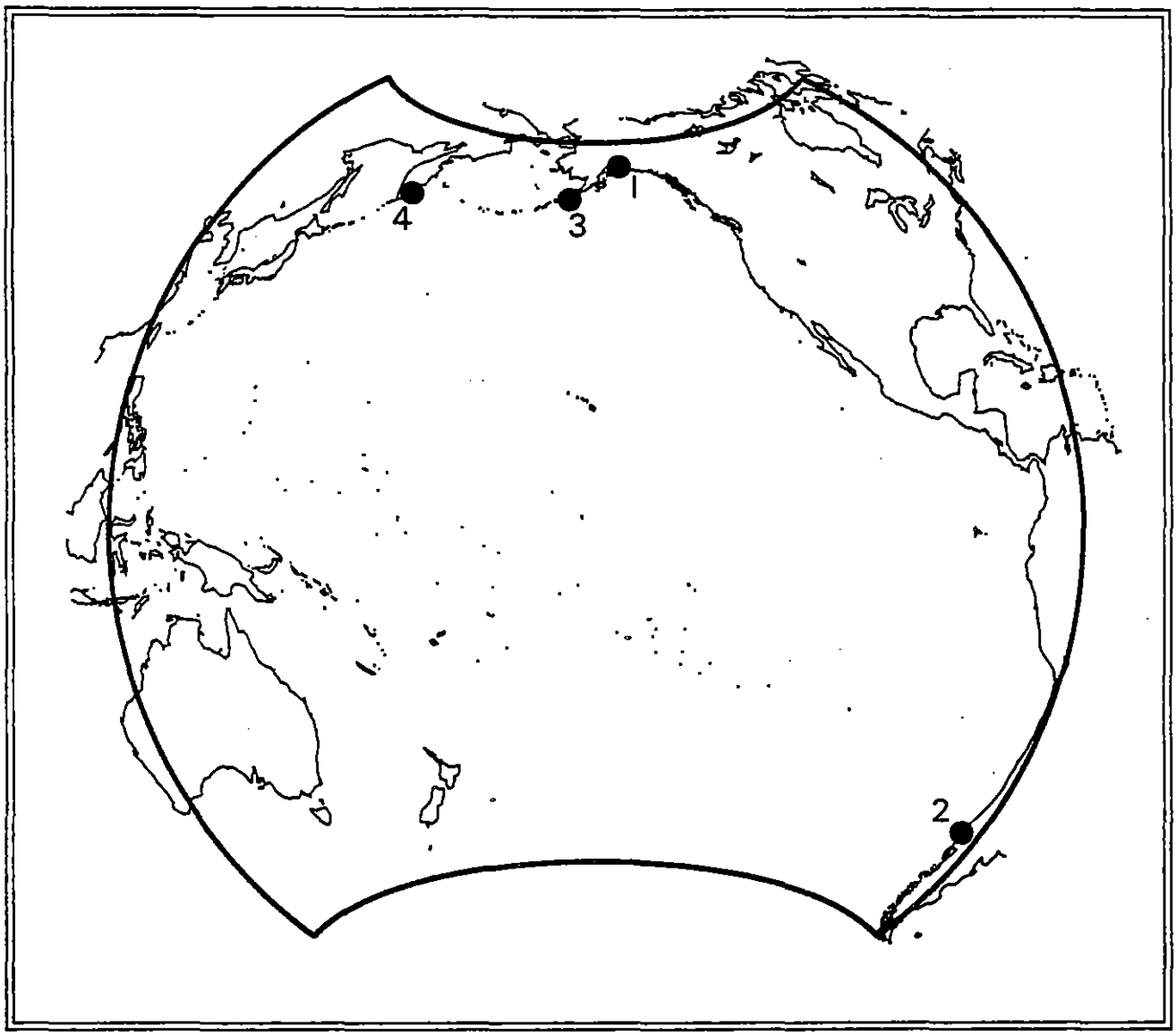

Fig. 1.1 Epicentres of earthquakes used in tsumani simulations. The bold line is the boundary of the deep ocean model (DOM).

(1: Alaska, 2: Chile, 3: Shumagin Gap, 4: Kamchatka)

Model verification is described in Chapter 6. The results are presented and discussed in Chapter 7 for the four source regions. Our conclusions and recommendations are presented in Chapter 8.

2.0 METHODOLOGY

2.1 The Study Region

British Columbia's outer coast is characterized by the presence of numerous deep and sinuous inlets that were formed thousands of years ago by the movement of glacial ice sheets. These inlets are often interconnected in complex ways, and are usually freely connected to the adjacent continental shelf. British Columbia's inlets are frequently the sites of commercial and recreational activity, and harbour numerous settlements along their shores.

A typical inlet has steeply sloping sides that extend downward several hundred metres, and upward from the water's surface to adjacent mountain peaks. They are usually of roughly uniform width and have lengths that greatly exceed their lateral dimensions.

Tsunamis arriving at British Columbia's outer coast propagate into all exposed inlet systems. Twenty of the more exposed systems (Table 2.1; Fig. 2.1 and 2.2) have been identified and incorporated into this study. Each has a corresponding numerical model that uses time-varying water elevations at one or more connections to the continental shelf to calculate the water surface response within the system. Construction of each model required detailed extraction of bathymetry and dimensional data (cross-sectional and surface areas) and calibration.

2.2 Tsunami Sources

Seismic activity in the Pacific Ocean is confined primarily to zones adjacent to the continental margins, where subduction of the oceanic plates under the continental land masses episodically releases bursts of energy in the form of an earthquake. Other areas, such as the Hawaiian Islands, are also sites of large earthquakes, but pose only a local threat of producing a destructive tsunami.

The likelihood of an earthquake resulting in a major tsunami is partly dependent on the energetics of the resulting ground motion, or the earthquake's magnitude. Magnitude is measured in several ways. The most familiar measure is probably the Richter scale. This value is not always a good indicator of tsunamigenic potential, however, as it reflects the energy of the earthquake at its epicentre, which may be tens of kilometres below the surface. A more appropriate measure is the surface magnitude, Ms--an indicator of the earthquake energy that is radiated in the surface of the earth's crust. This is more relevant to tsunami gneration than the Richter scale since it is surface crustal motions that generate tsunamis.

If an earthquake results in vertical (dip-slip) motion of the oceanic crust then it is tsunamigenic; that is, it will result in the deformation of the water surface, and subsequent propagation of the disturbance outward from the source as a seismic sea wave (tsunami). Tsunamis from even moderately small earthquakes may result in significant damage within a short distance of the source. If the earthquake is sufficiently large (Ms > 7.5 to 8.0), however, then a large tsunami may be generated, and damage will result at great distances from the source. This latter situation is most relevant to the west coast of Canada.

Table 2.1

British Columbia Inlet Systems Included in Tsunami Simulations

System	Areas Included	System	Areas Included
A	Portland Canal	J	Smith Inlet
	Observatory Inlet-Hastings Arm		
	Alice Arm	K	Mereworth Sound
	Khutzeymateen Inlet		Belize Inlet
	Work Channel		Nugent Sound
			Seymour Inlet
B	Prince Rupert Inlet		
		L	Holberg-Rupert Inlet
C	Rennell Sound		Quatsino Sount-Neroutsos Inlet
			Forward Inlet
D	Tasu Sound		
		M	Klaskino Inlet
E	Douglas Channel		
	Kildala Arm	N	Quoukinsh Inlet
	Gardner Canal		
	Sheep Passage-Mussel Inlet	O	Nuchalitz Inlet
F	Spiller Channel	P	Port Eliza
	Roscoe Inlet		Espinosa Inlet
	Cousins Inlet		Tahsis Inlet
	Cascade Inlet		Cook Channel-Tlupana Inlet
	Dean Channel		Zuciarte Channel-Muchalat Inlet
	Kwatna Inlet		
	South Bentinck Arm	Q	Sydney Inlet
			Shelter Inlet
G	Laredo Inlet		Herbert Inlet
H	Surf Inlet	R	Pipestem Inlet
I	Rivers Inlet	S	Effingham Inlet
	Moses Inlet		
		T	Alberni Inlet

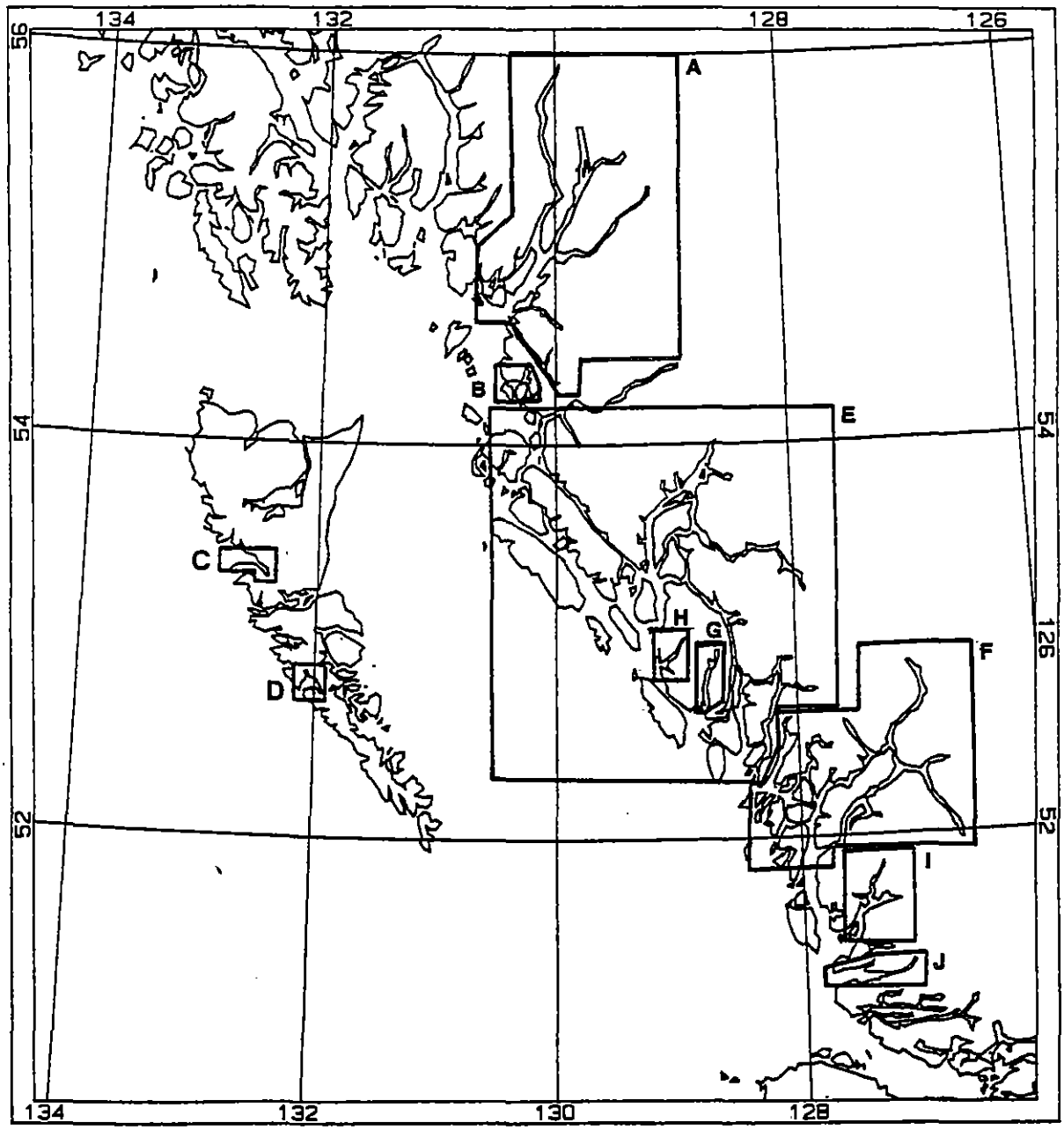

Fig. 2.1 Inlet systems for the north coast of British Columbia.

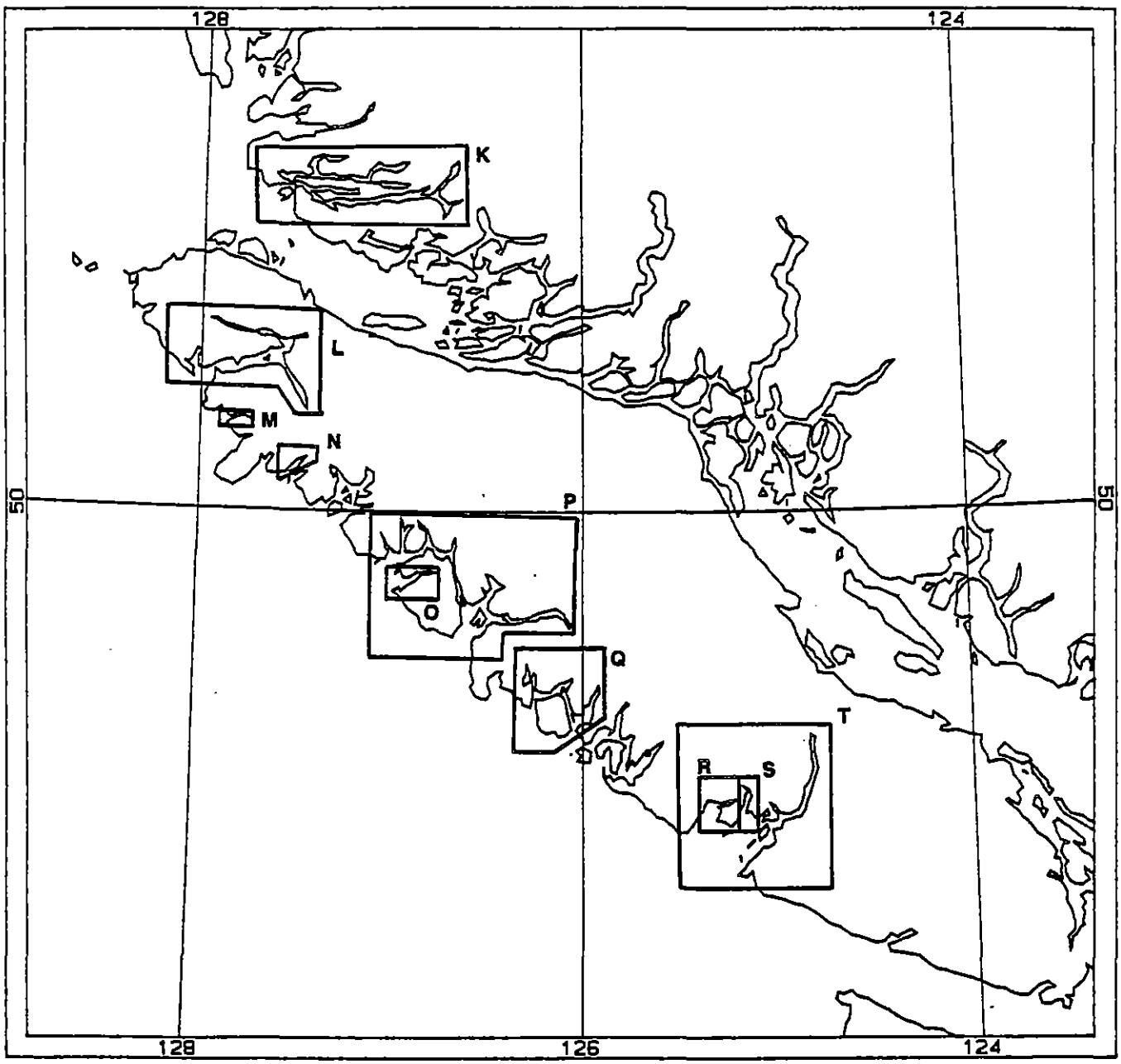

Fig. 2.2 Inlet systems for the south coast of British Columbia.

Wigen (1981) summarizes the tsunamis that have been recorded by the Tofino tide gauge between 1906 and 1980. The three largest tsunamis during this period arrived from the Gulf of Alaska (1964), Chile (1960), and Kamchatka (1952). Although no one knows for certain where the next major tsunami will originate from, recent discussions (Davies et al., 1981) have identified the Shumagin Gap (Fig. 1.1) as a likely location for a great earthquake within the next few decades. Because of its location in an area that has produced previous large tsunamis, we have selected the Shumagin Gap, together with the three regions mentioned above, for simulations of tsunami generation and propagation.

The epicentre locations for each of the three historical tsunamigenic earthquakes mentioned above have been used for the simulations. In the case of the Shumagin Gap, the position of a hypothetical epicentre has been selected based on past seismic activity in the region.

2.3 Tsunami Generation

Tsunamis result from the dip-slip motion of the ocean floor after an earthquake has transmitted energy from its epicentre by means of seismic waves in the earth's crust. Vertical displacements may be as large as 10 m and may occur over several seconds. In addition, the lateral dimensions of the motion may extend over several hundred kilometres (Plafker, 1969; Plafker and Savage, 1970).

Seismic waves travel at speeds of 3 to 4 km/s through the earth's crust, and hence motion does not take place simultaneously at every point. Thus, the total length of time over which the tsunami is generated (the generation phase) may last several minutes.

The mechanism for tsunami gneration in the numerical simulations assumes that seismic waves produced by an earthquake radiate from the epicentre at constant speed of 3.5 km/s through a displacement zone that encompasses all points where vertical motions take place. Because the horizontal dimensions of this region may be as great as a few hundred kilometres, the time taken for the disturbance to propagate across the displacement zone can be of the order of one to two minutes. At any fixed point in this zone, however, vertical motions are expected to take place over about 10 seconds (Hwang and Divoky, 1970).

For each simulated tsunamigenic earthquake, the final vertical bottom dispalcements were prescribed at each point in the model grid that fell within the displacement zone for that event. Water surface displacements were produced by having the bottom move vertically over a prescribed time interval (fixed for all points) to their final displacement values. The start of the vertical motion at each point was delayed an interval of time that was proportional to the distance of the point from the epicentre. This simulated the finite speed of propagation of the disturbance. During the generation phase of the simulation the model time step was limited to 2 seconds to give good resolution of the evolving sea bed shape. Upon cessation of bottom movement after a prescribed time, the time step was increased to 45 seconds and the deep water propagation phase was begun.

2.4 Tsunami Propagation

(a) Effect of the Generation Zone

The initial displacement of the ocean's surface resulting from the vertical motion of the underlying crust may be a depression or a mound of water. In either case, the surface slope results in a pressure gradient that ultimately leads to outward propagation of the disturbance as a series, or train, of individual waves. This effect is not unlike the pattern of ripples that results from tossing a stone into a pond.

It was noted in the last section that the horizontal scale of a large disturbance is typically several hundred kilometres. The interval of time between the resulting tsunami waves depends on the area of the disturbance and is generally 20 minutes or more. The tsunami waves, like other long period waves such as the tides, have wavelengths that are very much greater than the maximum depth of the ocean. In addition, tsunami amplitudes tend to be very small in comparison to both the ocean depth and the distance between waves, generally being less than 1 m at points far from the tsunami source. Tsunamis are thus classified as small amplitude, shallow water waves.

(b) Depth Effects

Linear long-wave theory approximates the behaviour of tsunamis and predicts that they will propagate at a speed that is proportional to the square root of the local water depth. This is independent of the wave length (provided it is sufficiently long). This result is only an approximation, however, and wave components with different periods actually travel at slightly different speeds. Over long periods of time this small effect will result in a distortion of the wave form that is not predicted by long-wave theory. Another small adjustment may be necessary due to the slightly greater water depth under the wave crests that results in crests travelling slightly faster than the troughs. If these small effects become important, then an alternate theory is appropriate. The Boussinesq equations derived in Chapter 4 are suitable for the case when these two effects, phase and amplitude dispersion, are small and of approximately the same size.

Since tsunami wave speed is dependent on depth, refraction of individual waves will occur where the depth changes along a wave crest. This necessitates the inclusion of water depths (bathymetry) in the numerical models. Figure 2.3 shows contours of depth (at 1000 m intervals) used in the deep ocean propagation model.

(c) Boundary Effects

When any surface gravity wave encounters a solid, nearly vertical barrier, such as a coastline or rapid change in water depth it undergoes severe modification. At one extreme, the wave energy will be completely reflected and propagation will continue in a direction different to the one from which the wave arrived. At the other extreme, wave energy will be completely dissipated. Intermediate between these extremes is partial reflection and absorption. Waves will be reflected (wholly or in part) by any barrier whose slope extends over a length that is much smaller than the length

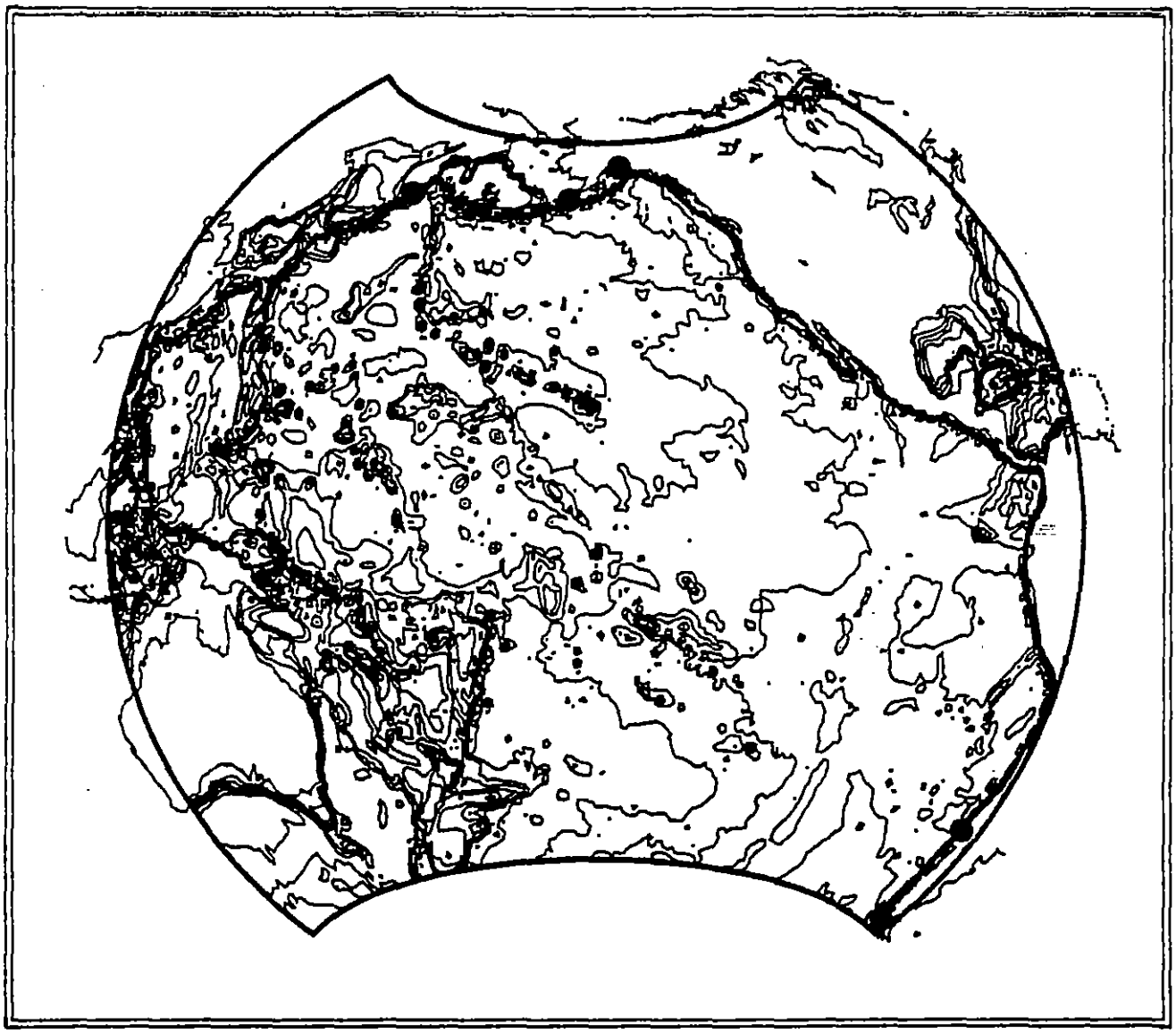

Fig. 2.3 Contoured bathymetry used in the deep ocean model. Contour interval is 1000 m.

between wave crests. In the case of tsunamis, this means that the continental shelf break off the coast of British Columbia acts to partially reflect wave energy. Further reflection occurs at the coastline, with energy being dissipated in proportion to the work that the wave does on the shoreline and in breaking.

2.5 The Numerical Models

Three distinct numerical models were used to simulate tsunami generation and propagation to the inlets of British Columbia taking the above generation and propagation factors into account. All share certain features in common. They all solve coupled systems of partial differential equations using finite difference techniques over regularly spaced grids. A fixed time step is used in each to provide a time dependent solution at each calculation point. Temporal and spatial resolution varies in the models, increasing toward the coast so as to provide greater accuracy in the solutions.

A deep ocean model (DOM) has been used to simulate the bottom motions that give rise to tsunamis, and to propagate the resulting waves to the continental shelf off Canada's west coast. The DOM uses a semi-implicit finite difference scheme in spherical polar coordinates to solve for wave heights and current velocities over the solution domain. A regular rectangular grid with columns and rows aligned with meridians and parallels is used. Resolution is 30 minutes angular distance along both axes. Waves result from prescribed bottom motions which take the form of vertical displacements at two second intervals. Wave propagation is realized by numerically solving the mathematical equations governing long wave propagation.

Ocean bathymetry has been included in the DOM by prescribing the water depth at each elevation calculation point. Thus, refraction and reflection by changes in depth are explicitly included in the model. At coastal boundaries a reflection condition is imposed.

Wave propagation near the coast of British Columbia is carried out using a high resolution hybrid model of the shelf and adjoining inlet systems. The shelf model (Hodgins, 1977) uses an implicit finite difference scheme with a resolution of 5 km between elevation (velocity) calculation points. Wave heights and resulting currents are calculated in the two horizontal dimensions every 90 seconds. At the entrance to each inlet system, elevations are passed to connecting one-dimensional inlet models having a spatial resolution of 2 km.

The DOM and shelf-inlet models are run separately. Surface elevations from the DOM run at grid points near the coast of British Columbia are saved and linearly interpolated onto the boundary of the two-dimensional shelf-inlet model. Subsequently, these are read from a file and used to force the model solution over the coastal areas of British Columbia.

2.6 Simulations

After confirming the correctness of all model components using tide and historical tsunami data, the two model systems were run for a set of simulated tsunamigenic earthquakes. These included simulations for measured

bottom displacements at the source regions of the 1960 Chilean and 1964 Alaskan tsunamigenic earthquakes, and hypothetical earthquakes at the Shumagin Gap and Kamchatka Peninsula sites. In addition, the Alaskan simulation was repeated for a case where bottom motions were amplified by 25%. The simulations provided the wave amplitudes and currents discussed in Chapter 7.

3.0 DATA RESOURCES

3.1 Bathymetry

Both the deep ocean model (DOM) and shelf-inlet model require water depths specified at each calculation point. These depths were derived from the U.S. National Geophysical Data Center (NGDC) world bathymetry and topography database, and from Canadian Hydrographic Service (CHS) navigation charts. Software, developed by Seaconsult, was used to extract the original 5-minute latitude-longitude gridded data from the NGDC database and to interpolate or subsample these data onto the appropriate two-dimensional calculation grids of the DOM and shelf models. Depths in the fjord models were extracted from standard navigation charts prepared by CHS. No spatial filtering of the data was performed and two-dimensional, bilinear interpolation was performed as required to calculate depths at grid vertices.

3.2 Bottom Displacement

No clear relationship exists between earthquake location and magnitude, and the final pattern of bottom displacements that will result. It is known (Hammack, 1973) that the time history of the crustal motion is unimportant in establishing the final tsunami wave form provided that the motion occurs over an interval of time that is much shorter than the period of the waves. Since the wave period tends to be greater than 20 minutes while bottom motions occur over a few seconds (Hwang and Divoky, 1970), this criterion is always satisfied.

Final bottom displacements are known for very few earthquakes. Plafker (1969), and Plafker and Savage (1970) have mapped bottom motions for the 1964 Alaskan and 1960 Chilean earthquakes respectively. Contoured displacements obtained from these sources were electronically digitized and interpolated to vertices of the corresponding DOM calculation grid. The final displacement map for the 1964 Alaskan earthquake, used to generate the tsunami, is shown in Fig. 3.1.

The displacements for the Shumagin Gap and Kamchatka simulations have been specified over prescribed elliptically shaped regions whose major axes are approximately aligned with the prevailing fault zone. Across ellipse variability was modelled on a section presented in Plafker (1969) which cut across the displacement region of the 1964 Alaska earthquake (see Table 7.2). The general features of this cross-section are a downthrust on the landward side of the displacement zone and a maximum upthrust of 10 m on the seaward side of the zone.

3.3 Tide Gauge Records

Twelve tide gauge records for the 1964 Alaska tsunami were digitized for comparison with model calculations (Table 3.1; Fig. 3.2). The tidal record for Port Alberni was estimated from measurements made 5.5 km up the Somass River. The heights of the first three wave crests at this location are given in Table 3.2 (Wigen and White, 1964). Water levels are measured relative to the normal river level in the absence of a tsunami. The time and height intervals from Table 3.2 were assumed to be the same as those at Port Alberni. It has only been possible to estimate the first three peak

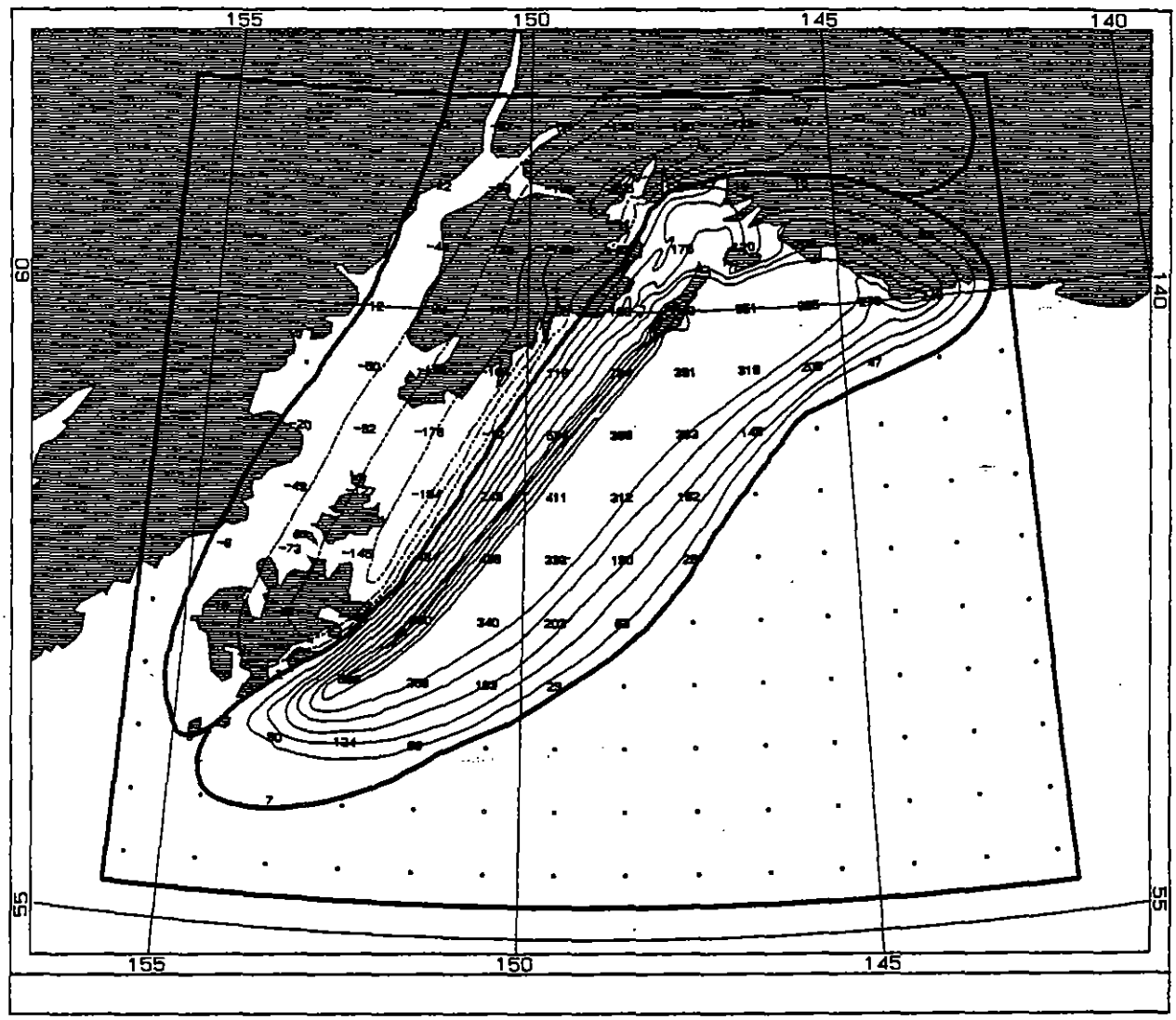

Fig. 3.1 Seabed displacements used to generate the 1964 Alaska tsunami.

Table 3.1

Tide Gauge Records for the 1964 Alaskan Tsunami Used to Calibrate and Verify the Numerical Models

No.	Location	Longitude deg min	Latitude deg min	Model
1	Sweeper Cove, Alaska	176 39	51 51	DOM
2	Unalaska, Alaska	166 32	53 53	DOM
3	Yakutat, Alaska	139 44	59 33	DOM
4	Sitka, Alaska	135 20	57 03	DOM
5	Ketchikan, Alaska	131 39	55 21	Shelf
6	Prince Rupert	130 20	54 19	Fjord
7	Tasu Sound	132 01	52 45	Shelf
8	Bella Bella	128 08	52 10	Fjord
9	Ocean Falls	127 41	52 51	Fjord
10	Alert Bay	126 56	50 35	Shelf
11	Tofino	125 55	49 09	Shelf
12	Port Alberni	124 49	49 14	Fjord

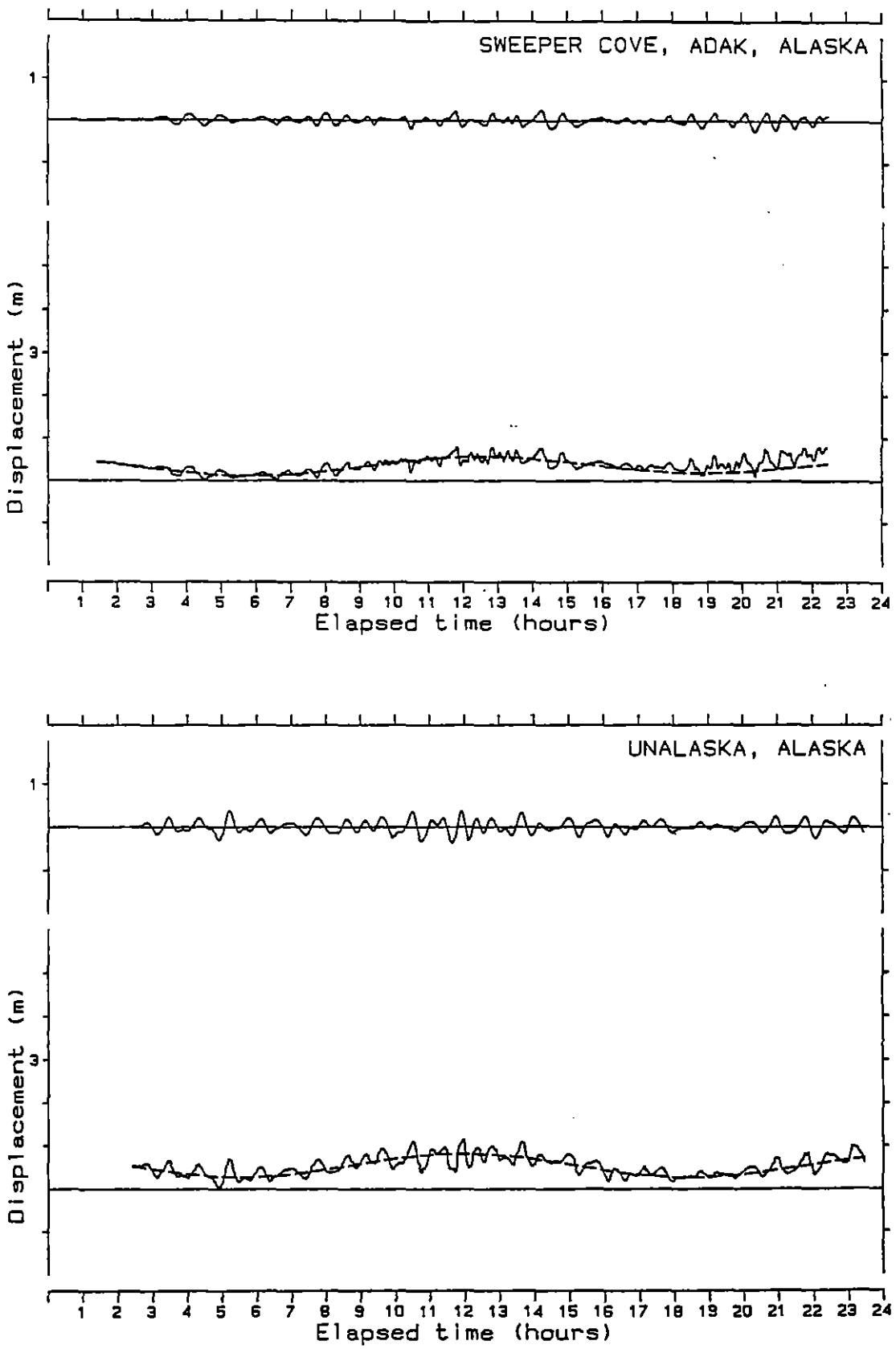

Fig. 3.2 Tide gauge records (bottom panels, solid line); calculated tidal elevations (bottom panels, dashed line); and derived tsunami wave heights (top panels) for the 24-hour period commencing at 03:36 GMT, the time of the 1964 Alaskan earthquake.

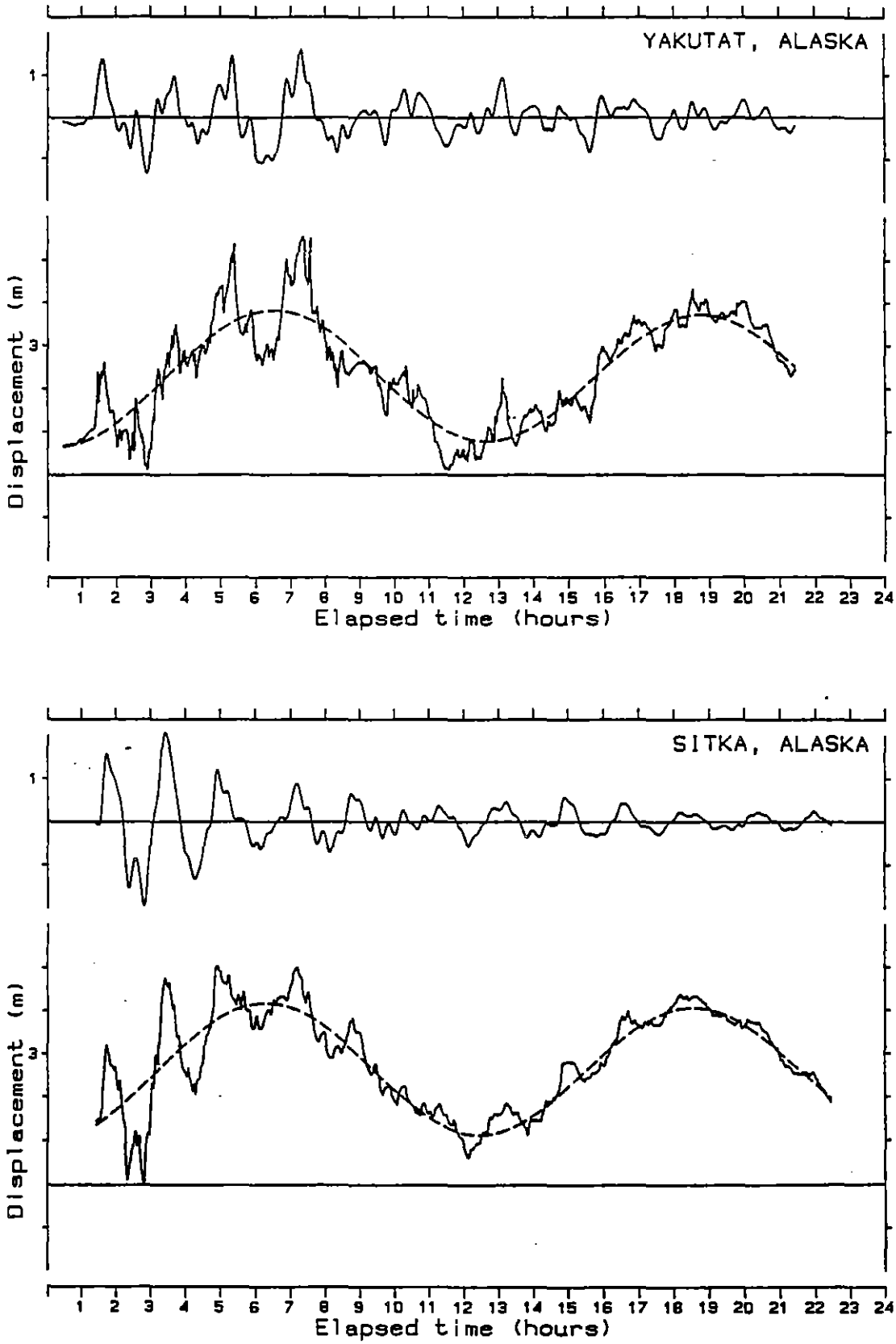

Fig. 3.2 Continued.

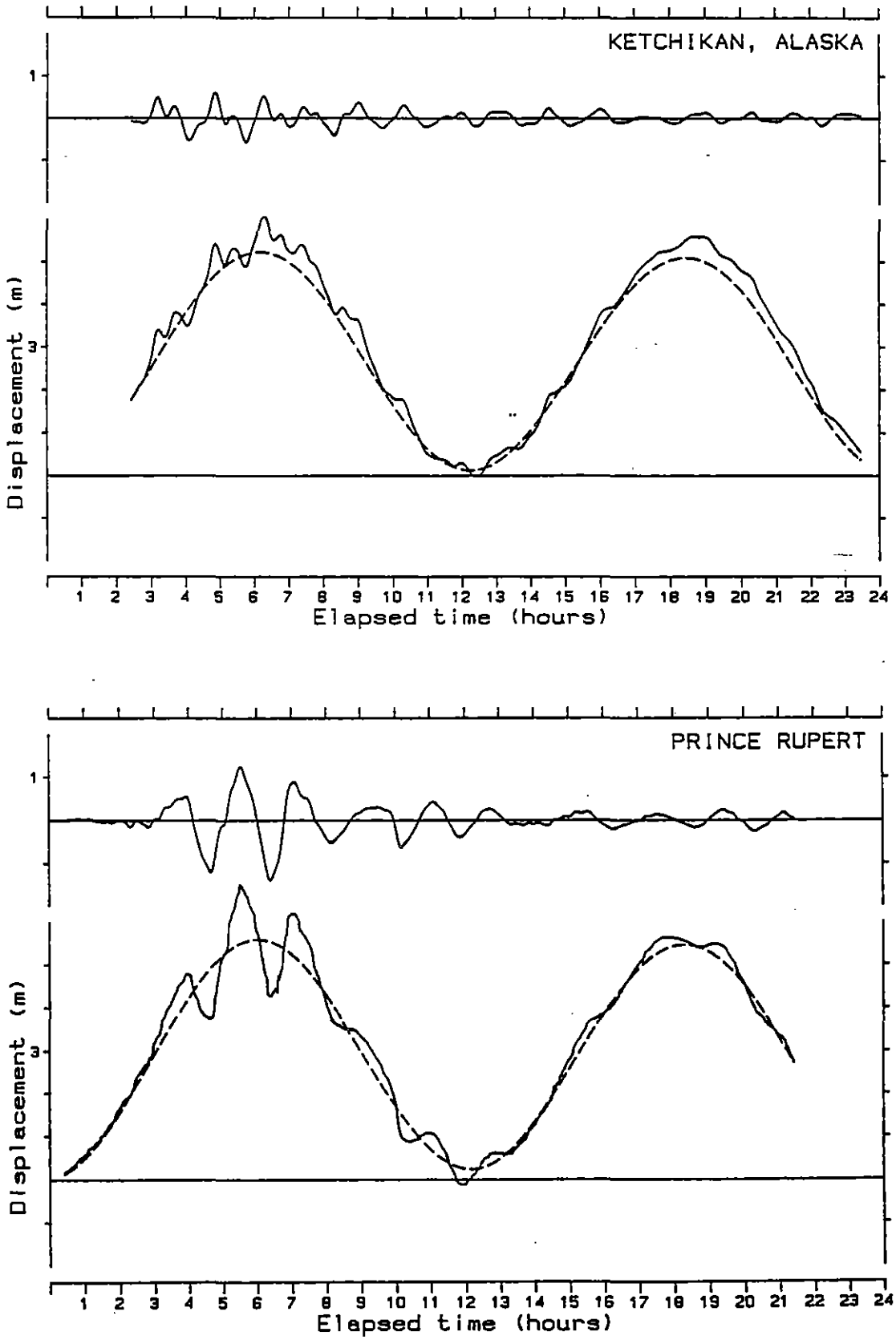

Fig. 3.2 Continued.

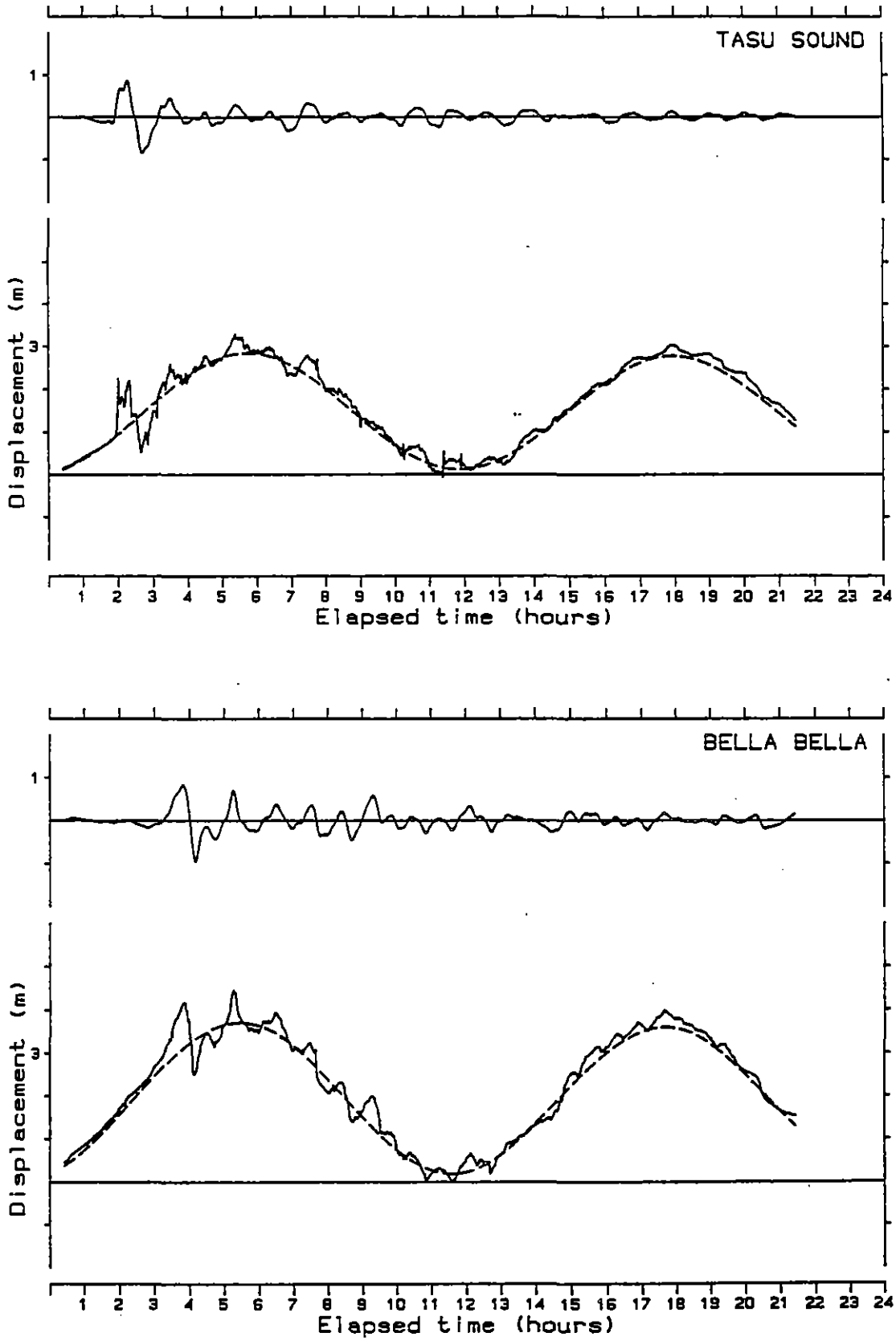

Fig. 3.2 Continued.

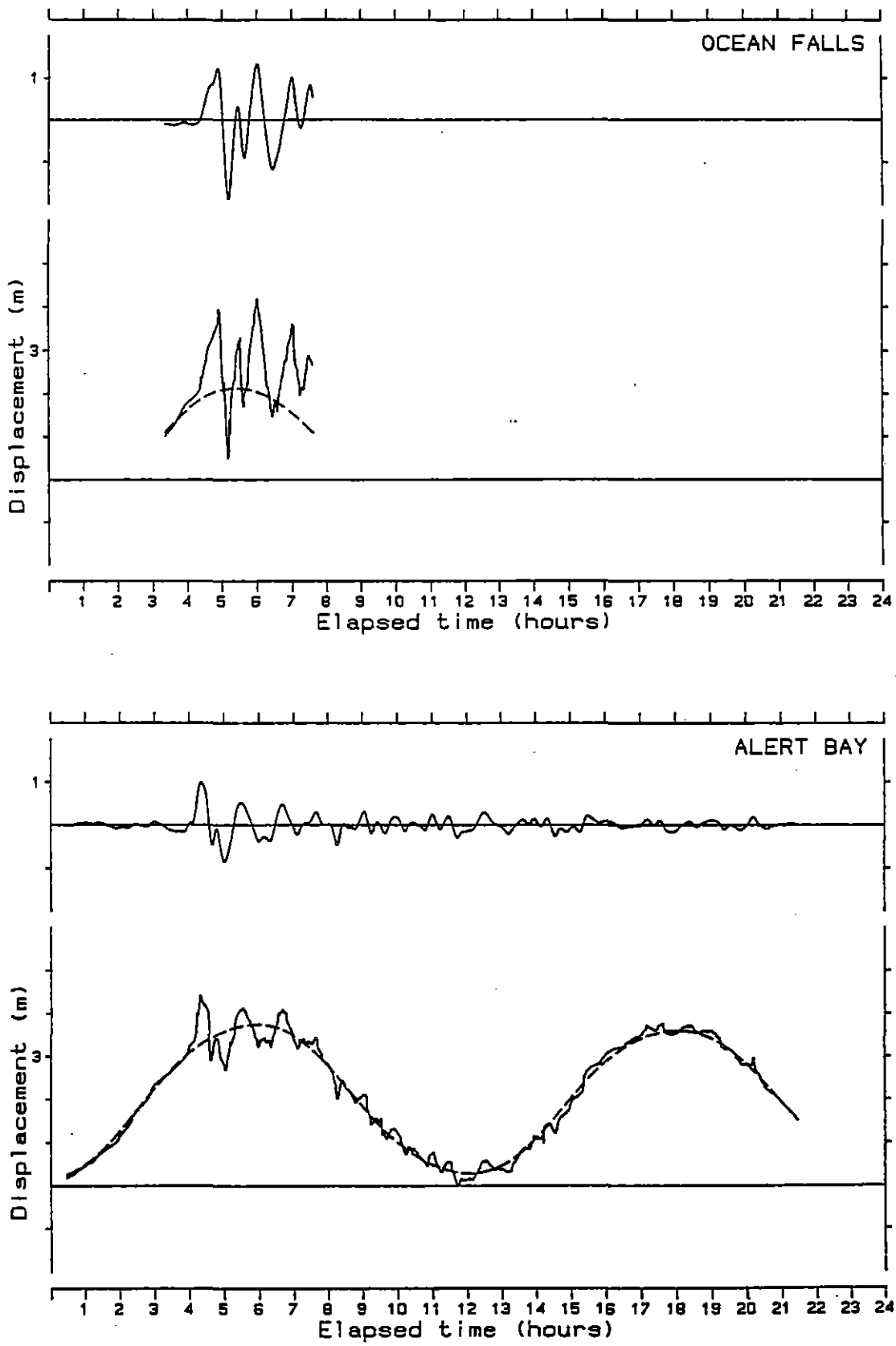

Fig. 3.2 Continued.

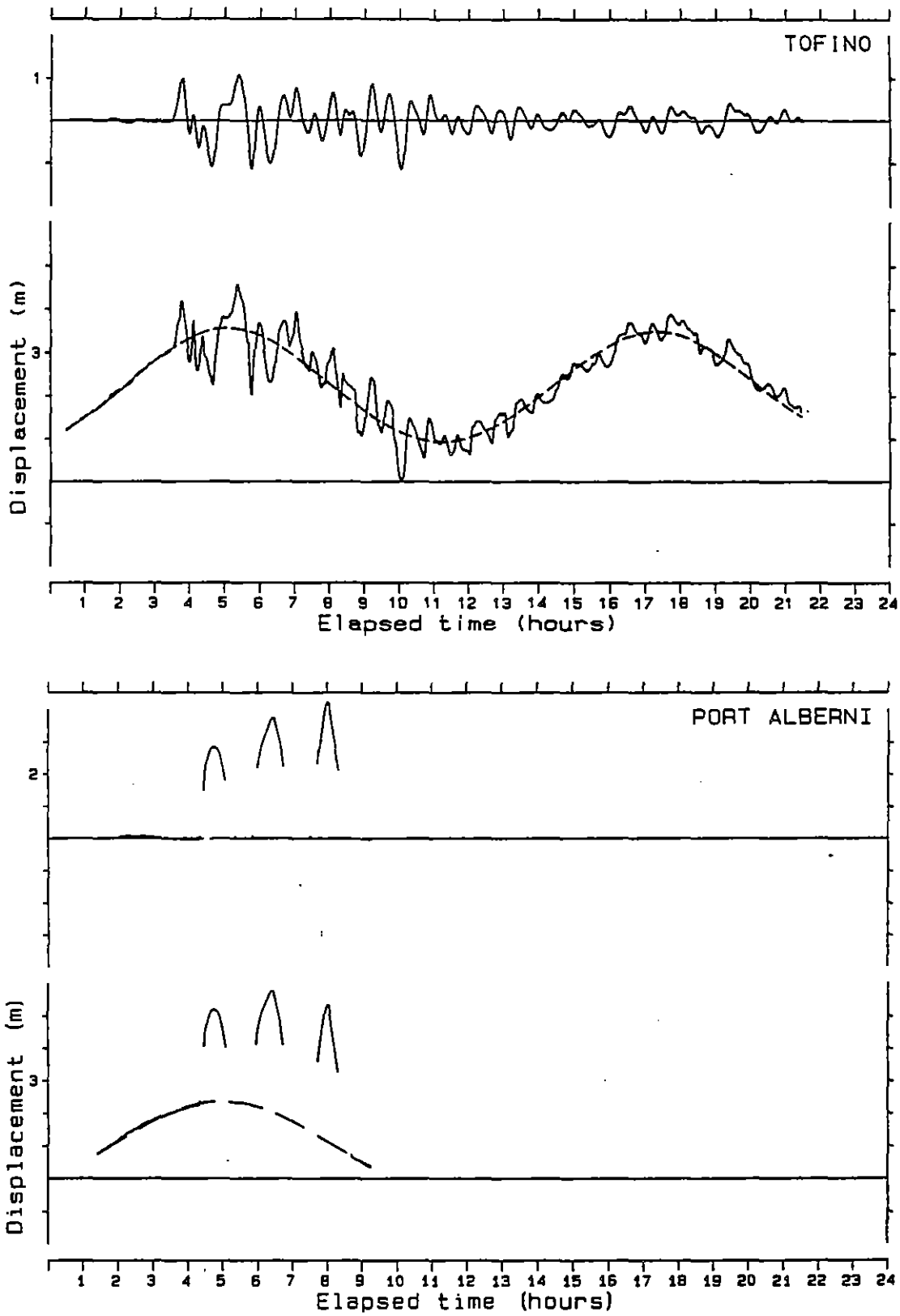

Fig. 3.2 Continued.

Table 3.2

Tsunami Crest Heights Measured 5.5 km Up the Somass River

Date	Time GMT	Tsunami (ft)	Crest Height (m)
March 28, 1964	1016	0.8	0.24
March 28, 1964	1153	2.6	0.79
March 28, 1964	1330	1.0	0.30

Note: the crest height is specified here as the peak water level measured above the mean water level

Source: Wigen and White, 1964.

wave heights for the tsunami at Port Alberni. Other details of the wave form such as trough depth, or secondary oscillations between peaks are completely unknown because the tide gauge failed at the time the first wave arrived.

Each tide station has a corresponding calculation point in one of the three numerical models. In each case the calculation point nearest the tide gauge location was selected. The entries under "Model" in Table 3.1 indicate the highest resolution model which includes that tide gauge.

The tide gauge records for stations listed in Table 3.1 are presented in Fig. 3.2. Each record is reproduced in the bottom panel as the solid line. The tide level for the same period was calculated from harmonic constants and vertically offset to match the gauge level prior to arrival of the tsunami; this level is shown in each bottom panel as a dashed line. The tidal signal was subtracted from the record and a Butterworth digital filter was used to remove energy from periods below 14 minutes and above 4 hours. The resulting tsunami record is presented in the top panels. Elapsed time is measured from the time of the earthquake which occurred at 03:36:14 GMT, March 28, 1964.

4.0 MODEL THEORY

4.1 The Deep Ocean Model

The model of tsunami propagation which forms the corner stone of this study consists of an adaptation of the Boussinesq equations (Peregrine, 1967) to a spherical surface. As has been demonstrated by Hammack (1973) and more recently by Seabra Santos (1985), dispersive and nonlinear effects which may appear locally negligible in the propagation of long gravity waves are nevertheless important for long travel distances; their cumulative influence is dominant in determining the form of the leading edge of the wavefront, where much of the energy is concentrated. An approximate form of the long wave equations which keeps both nonlinear and dispersive terms to leading order as well as depth variations was derived by Peregrine (1967). Special applications to nearly cylindrical wavefronts such as by Chwang and Wu (1976), Chwang and Power (1983) and Power and Chwang (1984) cannot be carried over to the study of tsunami propagation in the ocean because they are restricted to unidirectional propagation, as is also the familiar Korteweg-de Vries equation, a special case of the Boussinesq equations (see Miles, 1981 for a historical summary). It is thus necessary to extend Peregrine's form of the Boussinesq equations to a thin spherical shell of variable depth.

Our derivation follows the general lines of that of Peregrine (1967), with particular emphasis on the differences introduced by the spherical geometry and on the approximations made. The problem is formulated first in the spherical polar coordinate system of Fig. 4.1, with velocity components u, v, w corresponding to the directions of increasing ϕ, θ and r.

The momentum and volume continuity equations for an inviscid, incompressible fluid then read

$$\frac{Du}{Dt} + \frac{uw}{r} - \frac{uv}{r}\tan\theta - fv + \frac{1}{\rho r\cos\theta}\frac{\partial p}{\partial \phi} = 0 \qquad (4.1)$$

$$\frac{Dv}{Dt} + \frac{vw}{r} + \frac{u^2}{r}\tan\theta + fu + \frac{1}{\rho r}\frac{\partial p}{\partial \theta} = 0 \qquad (4.2)$$

$$\frac{Dw}{Dt} - \frac{(u^2+v^2)}{r} + \frac{1}{\rho}\frac{\partial p}{\partial r} + g = 0 \qquad (4.3)$$

$$\frac{\partial w}{\partial r} + \frac{1}{r\cos\theta}\frac{\partial}{\partial \theta}(v\cos\theta) + \frac{1}{r}\frac{\partial u}{\partial \phi} \qquad (4.4)$$

where

$$\frac{D}{Dt} = \frac{\partial}{\partial t} + w\frac{\partial}{\partial r} + \frac{v}{r}\frac{\partial}{\partial \theta} + \frac{u}{r\cos\theta}\frac{\partial}{\partial \phi} \qquad (4.5)$$

and only the locally vertical component of the earth's rotation component has been retained, in anticipation of the usual situation where the ocean is

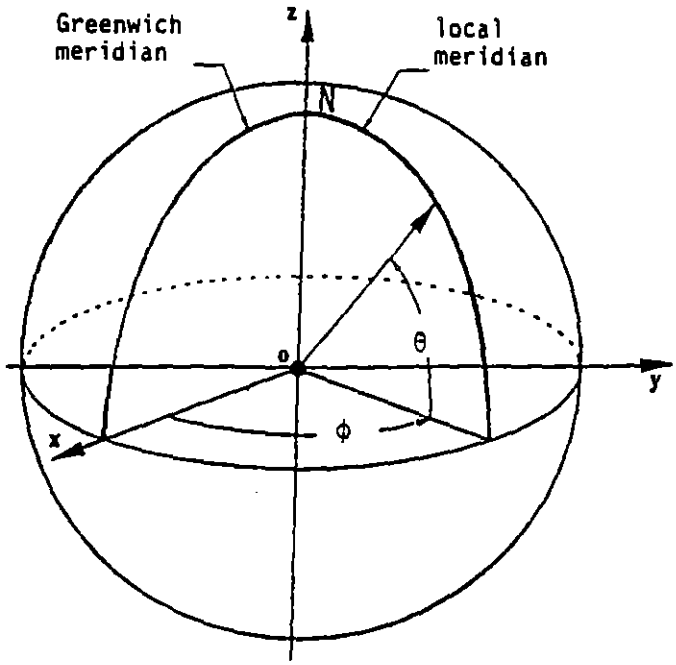

Fig. 4.1 The spherical polar coordinate system. = latitude, = longitude, and r = radius of sphere.

thin relative to the earth's radius. Thus,

$$f = 2\Omega \sin\theta \tag{4.6}$$

with $2\Omega = 4\pi/24 = 1.458 \times 10^{-4}\ s^{-1}$

The ocean is contained in the range $R+\eta \leq r \leq R-H$, where $\eta(\theta,\phi)$ and $H(\theta,\phi)$ are the upper, free surface and the unperturbed oceanic depth respectively. At the bottom, the normal velocity component vanishes:

$$w(-H) + \frac{v}{r}\frac{\partial H}{\partial\theta} + \frac{u}{r\cos\theta}\frac{\partial H}{\partial\phi} = 0 \tag{4.7}$$

At the top, the pressure is constant (taken as zero)

$$p(\eta) = 0 \tag{4.8}$$

and the kinematic boundary condition gives

$$w(\eta) = \frac{\partial\eta}{\partial t} + \frac{v}{r}\frac{\partial\eta}{\partial\theta} + \frac{u}{r\cos\theta}\frac{\partial\eta}{\partial\phi} \tag{4.9}$$

Integrating (4.4) in the r-direction and using (4.7) and (4.9) yields the integrated continuity equation:

$$\frac{\partial\eta}{\partial t} + \nabla_h \cdot \underset{\sim}{Q} = 0 \tag{4.10}$$

where the horizontal mass flux vector Q has components

$$\underset{\sim}{Q} = \frac{1}{(R+\eta)}\left[\int_{R-H}^{R+\eta} rv\,dr,\quad \int_{R-H}^{R+\eta} ru\,dr\right] \tag{4.11}$$

and

$$\nabla_h = \frac{1}{(R+\eta)\cos\theta}\left[\frac{\partial}{\partial\theta}(\cos\theta),\ \frac{\partial}{\partial\phi}\right] \tag{4.12}$$

It is extremely convenient to express the problem in coordinates which are more closely tied to the earth's surface. We now shift from the (r,θ,ϕ) system to a "surface" coordinate system (x,y,z) related to the previous as follows,

$$z = r-R \tag{4.13a}$$

$$x = R\cos\theta\cdot\phi \tag{4.13b}$$

$$y = R\theta \tag{4.13c}$$

We also introduce scaled, non-dimensional variables and coordinates, denoted by primes, as follows:

$$(x',y',z') = (x,y,z)/H_o \tag{4.14a}$$

$$t' = t(g/H_o)^{1/2} \tag{4.14b}$$

$$(u',v',w') = (u,v,w)/(gH_o)^{1/2} \tag{4.14c}$$

$$p' = p/(\rho g H_o) \tag{4.14d}$$

$$(\eta',H') = (\eta,H)/H_o \tag{4.14e}$$

The reference depth H_o is small with respect to the radius of the earth R; we write

$$\frac{H_o}{R} = \delta << 1 \tag{4.15}$$

The momentum and integrated continuity equations are now written in the new variables as

$$\frac{Du'}{Dt'} + \frac{\delta}{(1+\delta z')}[u'w' - u'v'\tan\theta] - f'v' + \frac{1}{(1+\delta z')}\frac{\partial p'}{\partial x'} = 0 \tag{4.16}$$

$$\frac{Dv'}{Dt'} + \frac{\delta}{(1+\delta z')}[v'w' + u'^2\tan\theta] + f'u' + \frac{1}{(1+\delta z')}\frac{\partial p'}{\partial y'} = 0 \tag{4.17}$$

$$\frac{Dw'}{Dt'} - \frac{\delta}{(1+\delta z')}[u'^2 + v'^2] + \frac{\partial p'}{\partial z'} + 1 = 0 \tag{4.18}$$

$$\frac{\partial \eta'}{\partial t'} + \nabla_h' \cdot \underset{\sim}{Q}' = 0 \tag{4.19}$$

where

$$\frac{D}{Dt'} = \frac{\partial}{\partial t'} + w'\frac{\partial}{\partial z'} + \frac{1}{(1+\delta z')}\left[u'\frac{\partial}{\partial x'} + v'\frac{\partial}{\partial y'}\right] \tag{4.20}$$

$$f' = f(H_o/g)^{1/2} \tag{4.21}$$

$$\underset{\sim}{Q}' = \frac{1}{(1+\delta\eta')}\int_{-H'}^{\eta'}(1+\delta z')\,u'dz', \int_{-H'}^{\eta'}(1+\delta z')\,v'dz' \tag{4.22}$$

$$\nabla_h' = \left\{\frac{1}{(1+\delta\eta')}\frac{\partial}{\partial y'}(\cos\theta\ ),\ \frac{\partial}{\partial x'}\right\} \tag{4.23}$$

The boundary conditions (4.7) to (4.9) become

$$w'(-H') + \frac{1}{(1+\delta H')}\left[v'\frac{\partial H'}{\partial y'} + u'\frac{\partial H'}{\partial x'}\right] = 0 \tag{4.24}$$

$$p'(\eta') = 0 \tag{4.25}$$

$$w'(\eta') = \frac{\partial \eta'}{\partial t'} + \frac{1}{(1+\delta\eta')} \left[v' \frac{\partial \eta'}{\partial y'} + u' \frac{\partial \eta'}{\partial x'} \right] \tag{4.26}$$

We identify four small parameters relevant to this problem. As in the classical case, $\varepsilon = |\eta|/H_o$, the ratio of wave amplitude to water depth and $\sigma = H_o/\lambda$, the ratio of water depth to wave length represent the effects of non-linearity and phase dispersion respectively. Ursell (1953) has discussed the importance of the ratio $\varepsilon / \sigma^2 = Ur$ (the Ursell number). When $Ur = O(1)$, solitary and cnoidal waves occur; nonlinear and dispersive effects balance. Seabra Santos (1985) has shown that whether one starts with initial conditions of $Ur>>1$ or $Ur<<1$ the cumulative influence of small ε and σ terms is to make the long wave propagation evolve towards $Ur=O(1)$. Here, following Peregrine and all previous authors, we assume $\varepsilon << 1$, $\sigma^2 << 1$, $Ur = O(1)$.

The additional parameters appearing in our problem are $\delta = H_o/R$, the relative measure of the ocean's depth in units of the earth's radius ($\delta \cong 10^{-3}$) and $f = f\sqrt{H_o/g}$, the ratio of Coriolis to local accelerations. This latter parameter is also of $O(10^{-3})$ for a 5000 m deep ocean. Since we cannot *a priori* dismiss the effect of any one of these small parameters, we shall retain them all and pose

$$\varepsilon \cong \sigma^2 \cong \delta << 1 \tag{4.27a}$$

$$f' \cong \sigma\varepsilon << 1 \tag{4.27b}$$

Because the Coriolis force has been taken to act only in the local horizontal plane, as in usual oceanographic models, we may still assume that the components of the vorticity in the horizontal plane remain zero, as in the full irrotational case. The only vorticity remains in the z'-direction. Applying the same coordinate and variable changes to the spherical coordinate form of the rotational, we have the conditions

$$\frac{\partial}{\partial z'} \left[(1+\delta z') \, u' \right] - \frac{\partial w'}{\partial x'} = 0 \tag{4.28a}$$

$$\frac{\partial}{\partial z'} \left[(1+\delta z') \, v' \right] - \frac{\partial w'}{\partial y'} = 0 \tag{4.28b}$$

Let us then expand η', p', u', v', $\underset{\sim}{Q}'$ in the form

$$X = X_o + \varepsilon X_1 + \varepsilon^2 X_2 \ldots \tag{4.29}$$

as well as

$$w' = \sigma(w_o + \varepsilon w_1 + \ldots) \tag{4.30}$$

Together with the horizontal to vertical distortion scaling

$$\frac{\partial}{\partial x'} = \sigma \frac{\partial}{\partial x^*} \; ; \; \frac{\partial}{\partial y'} = \sigma \frac{\partial}{\partial y^*} \; ; \; \frac{\partial}{\partial t'} = \sigma \frac{\partial}{\partial t^*} \; . \tag{4.31}$$

The zeroth order solution is still water: $p'_o = -z'$, from (4.18); all other zeroth order variables are zero.

To first order, (4.28) gives

$$\frac{\partial u'_1}{\partial z'} = 0 \ , \quad \frac{\partial v'_1}{\partial z'} = 0 \ : \tag{4.32}$$

to a first approximation, the horizontal velocity components are depth independent: the usual representation. Hence, from (4.22),

$$\underset{\sim}{Q}_1 = (Hu'_1, Hv'_1) \tag{4.33}$$

From (4.18), $\partial p'_1 / \partial z' = 0$. Since the boundary condition (4.28) requires $p'_o + \varepsilon p'_1 = 0$ at $z' = \varepsilon\eta'$, we find $p'_1 = \eta'_1$. Hence (4.16) and (4.17) give the long wave equations to $O(\varepsilon)$:

$$\frac{\partial u'_1}{\partial t^*} + \frac{\partial \eta'_1}{\partial x^*} = 0 \tag{4.34}$$

$$\frac{\partial v'_1}{\partial t^*} + \frac{\partial \eta'_1}{\partial y^*} = 0 \tag{4.35}$$

$$\frac{\partial \eta'_1}{\partial t^*} + \frac{\partial}{\partial x^*} Hu'_1 + \frac{\partial}{\partial y^*} \cos\theta \ Hv'_1 = 0 \tag{4.36}$$

The influence of the spherical coordinate geometry is present in the definition of the x and y variables from (4.13b), (4.13c) and in the last term of the continuity equation.

The first order vertical velocity is obtained by integrating (4.4), which reads, in the scaled variables

$$\frac{\partial}{\partial z'} (1 + \varepsilon z')^2 \, w' + (1 + \varepsilon z')^2 \left[\frac{\partial}{\partial y'} \cos\theta \ v' + \frac{\partial u'}{\partial x'}\right] = 0 \tag{4.37}$$

Hence, to $O(\varepsilon)$,

$$\frac{\partial}{\partial z'} w'_1 + \frac{\partial}{\partial y^*} \cos\theta \ v'_1 + \frac{\partial}{\partial x^*} u'_1 = 0 \quad ,$$

so that integrating from -H to z',

$$w'_1(z') - w'_1(-H) + (z'+H) \left[\frac{\partial}{\partial y^*} v'_1 \cos\theta + \frac{\partial u'_1}{\partial x^*}\right] = 0$$

and with the help of the boundary condition (4.24),

$$w_1' = -z' \left[\frac{\partial}{\partial y^*} v_1' \cos\theta + \frac{\partial u_1'}{\partial x^*}\right] - \tag{4.38}$$

$$\frac{\partial}{\partial x^*} u_1' H' - v_1' \frac{\partial H'}{\partial y^*} - H' \frac{\partial}{\partial y^*} v_1' \cos\theta = 0$$

an expression which is less compact than that found by Peregrine due to the presence of the $\cos\theta$ term associated with the spherical geometry.

At the next order, the irrotationality condition (4.28) yields

$$\frac{\partial u_2'}{\partial z'} = -\frac{\delta}{\varepsilon} u_1' + \frac{\partial}{\partial x^*} w_1' \quad , \tag{4.39a}$$

$$\frac{\partial v_2'}{\partial z'} = -\frac{\delta}{\varepsilon} v_1' + \frac{\partial}{\partial y^*} w_1' \quad , \tag{4.39b}$$

from which we obtain u_2' and v_2' as

$$u_2' = U_2(\underset{\sim}{x^*}, t^*) - \frac{\delta}{\varepsilon} z' u_1' - \frac{z'^2}{2} \frac{\partial}{\partial x^*} \left[\frac{\partial}{\partial y^*} v_1' \cos\theta + \frac{\partial u_1'}{\partial x^*}\right] \tag{4.40a}$$

$$- z' \frac{\partial}{\partial x^*} \left[\frac{\partial}{\partial x^*} u_1' H' + v_1' \frac{\partial H'}{\partial y^*} + H' \frac{\partial}{\partial y^*} v_1' \cos\theta\right]$$

$$v_2' = V_2(\underset{\sim}{x^*}, t^*) - \frac{\delta}{\varepsilon} z' v_1' - \frac{z'^2}{2} \frac{\partial}{\partial y^*} \left(\frac{\partial}{\partial y^*} v_1' \cos\theta + \frac{\partial u_1'}{\partial x^*}\right) \tag{4.40b}$$

$$- z' \frac{\partial}{\partial y^*} \left[\frac{\partial}{\partial x^*} u_1' H' + v_1' \frac{\partial H'}{\partial y^*} + H' \frac{\partial}{\partial y^*} v_1' \cos\theta\right]$$

where u_2 and v_2 are arbitrary functions of integration. The vertical momentum equation now includes vertical acceleration, i.e. a slight non-hydrostatic correction:

$$\frac{\partial w_1'}{\partial t^*} + \frac{\partial p_2'}{\partial z'} = 0 \tag{4.41}$$

Other nonlinear terms contribute to $O(\sigma)$ and to $O(\delta)$ lower. We then integrate (4.41) to find

$$p_2' = \eta_2'(x^*, t^*) + z' \frac{\partial}{\partial t^*} \left[\frac{\partial}{\partial x^*} u_1' H' + v_1' \frac{\partial H'}{\partial y^*} + H \frac{\partial}{\partial y^*} v' \cos\theta\right] \tag{4.42}$$

$$+ \frac{z'^2}{2} \frac{\partial}{\partial t^*} \left[\frac{\partial}{\partial y^*} v_1' \cos\theta + \frac{\partial u_1'}{\partial x^*}\right]$$

The second order momentum equations are now

$$\frac{\partial u_2'}{\partial t^*} + [u_1'\frac{\partial u_1'}{\partial x^*} + v_1'\frac{\partial u_1'}{\partial y^*}] - \frac{f'}{\sigma\varepsilon} v_1' + \frac{\partial p_2'}{\partial x^*} - \frac{\delta}{\varepsilon} z' \frac{\partial p_1'}{\partial x^*} = 0 \qquad (4.43a)$$

$$\frac{\partial v_2'}{\partial t^*} + [u_1'\frac{\partial v_1'}{\partial x^*} + v_1'\frac{\partial v_1'}{\partial y^*}] + \frac{f'}{\sigma\varepsilon} u_1' + \frac{\partial p_2'}{\partial y^*} - \frac{\delta}{\varepsilon} z' \frac{\partial p_1'}{\partial y^*} = 0 \qquad (4.43b)$$

The curvature terms in (4.16) and (4.17) contribute to order (δ/σ) lower. The finite depth of the ocean brings in the last geometrical term in $\delta/\varepsilon \sim 0(1)$ Substituting for u_2', v_2' and p_2', p_1', we get

$$\frac{\partial U_2}{\partial t^*} - \frac{\delta}{\varepsilon} z' \frac{\partial u_1'}{\partial t^*} - \frac{z'^2}{2} \frac{\partial}{\partial t^*}\frac{\partial}{\partial x^*}(\frac{\partial}{\partial y^*} v_1' \cos\theta + \frac{\partial u_1'}{\partial x^*})$$

$$- z' \frac{\partial}{\partial t^*}\frac{\partial}{\partial x^*}[\frac{\partial u_1'H'}{\partial x^*} + v_1'\frac{\partial H'}{\partial y^*} + H'\frac{\partial}{\partial y^*} v' \cos\theta] + (u_1'\frac{\partial u_1'}{\partial x^*} + v_1'\frac{\partial u_1'}{\partial y^*})$$

$$- \frac{f'}{\sigma\varepsilon} v_1' + \frac{\eta_2'}{\partial x^*} + z' \frac{\partial}{\partial x^*}\frac{\partial}{\partial t^*}[\frac{\partial}{\partial x^*} u_1'H' + v_1'\frac{\partial H'}{\partial y^*} + H'\frac{\partial}{\partial y^*} v' \cos\theta]$$

$$+ \frac{z'^2}{2} \frac{\partial}{\partial x^*}\frac{\partial}{\partial t^*}[\frac{\partial}{\partial y^*} v_1' \cos\theta + \frac{\partial u_1'}{\partial x^*}] - \frac{\delta}{\varepsilon} z' \frac{\partial \eta_1'}{\partial x^*} = 0$$

All terms in z'^2 and z' cancel out, either directly, or from the first order momentum equation (4.34). A similar result holds for the y-component.

Hence, as in Peregrine, except for the Coriolis force correction

$$\frac{\partial}{\partial t^*} U_2 + (u_1'\frac{\partial u_1'}{\partial x^*} + v_1'\frac{\partial u_1'}{\partial y^*}) - \frac{f'}{\sigma\varepsilon} v_1' + \frac{\partial \eta_2'}{\partial x^*} = 0 \qquad (4.44a)$$

$$\frac{\partial}{\partial t^*} V_2 + (u_1'\frac{\partial v_1'}{\partial x^*} + v_1'\frac{\partial v_1'}{\partial y^*}) + \frac{f'}{\sigma\varepsilon} u_1' + \frac{\partial \eta_2'}{\partial y^*} = 0 \qquad (4.44b)$$

Going back to the Q expansion from (4.22):

$$\underset{\sim}{Q}' = (1 - \delta\varepsilon\eta_1' + \ldots)\int_{-H'}^{\varepsilon\eta_1'+\ldots} (1 + \delta z')\,(\varepsilon\underset{\sim}{u}_1' + \varepsilon^2\underset{\sim}{u}_2' + \ldots)\,dz'$$

$$= \varepsilon H'\underset{\sim}{u}_1' + \varepsilon^2\left\{\int_{-H'}^{0}\underset{\sim}{u}_2'\,dz' + \frac{\delta}{\varepsilon}\int_{-H'}^{0} z'\underset{\sim}{u}_1'dz' + \frac{1}{\varepsilon}\int_{0}^{\varepsilon\eta_1'} u_1'dz'\right\}$$

hence

$$\underset{\sim}{Q}_2' = \int_{-H}^{0} \underset{\sim}{u}_2' dz' - \frac{\delta}{\epsilon} \underset{\sim}{u}_1' \frac{H'^2}{2} + \underset{\sim}{u}_1' \eta_1' \tag{4.45}$$

Substituting for u_2' from (4.40a), v_2' from (4.40b):

$$\underset{\sim}{Q}_2' = \Bigg\{ u_1' \eta_1' + U_2 H' + \frac{H'^2}{2} \frac{\partial}{\partial x^*} \left[\frac{\partial}{\partial x^*} u_1' H' + v_1' \frac{\partial H'}{\partial y^*} + H' \frac{\partial}{\partial y^*} v_1' \cos\theta\right]$$

$$- \frac{H'^3}{6} \frac{\partial}{\partial x^*} \left[\frac{\partial}{\partial y^*} v_1' \cos\theta + \frac{\partial u_1'}{\partial x^*}\right] ,$$

$$v_1' \eta_1' + V_2 H' + \frac{H'^2}{2} \frac{\partial}{\partial y^*} \left[\frac{\partial}{\partial x^*} u_1' H' + v_1' \frac{\partial H'}{\partial y^*} + H' \frac{\partial}{\partial y^*} v_1' \cos\theta\right]$$

$$- \frac{H'^3}{6} \frac{\partial}{\partial y^*} \left[\frac{\partial}{\partial y^*} v_1' \cos\theta + \frac{\partial u_1'}{\partial x^*}\right] \Bigg\} \tag{4.46}$$

The second order continuity equation is thus

$$\frac{\partial \eta_2'}{\partial t^*} + \nabla_h^* \cdot \underset{\sim}{Q}_2' = 0 \tag{4.47}$$

with $\nabla_h^* = \left\{ \frac{\partial}{\partial x^*} , \frac{\partial \cos\theta()}{\partial y^*} \right\}$ and Q_2' as in (4.46).

These results are thus far very close to those of Peregrine for propagation on a plane, the only differences being the appearance of the Coriolis term and the presence of the geometrical corrections factor $\cos\theta$ within the divergence term.

We now define, as does Peregrine, a surface displacement variable

$$\eta = \epsilon \eta_1' + \epsilon^2 \eta_2'$$

and a mean velocity $\bar{u}$ as

$$\underset{\sim}{\bar{u}} = \underset{\sim}{Q}'/(H' + \eta).$$

Substituting for Q_1' and Q_2' from (4.33) and (4.46) we obtain

$$\bar{\underset{\sim}{u}} = \varepsilon \underset{\sim}{u}_1' + \varepsilon^2 \left[\underset{\sim}{U}_2 + \frac{H'}{2} \frac{\partial}{\partial \underset{\sim}{x}^*} \left(\frac{\partial}{\partial x^*} u_1' H' + v_1' \frac{\partial H'}{\partial y^*} + \frac{\partial}{\partial y^*} v_1' \cos\theta H' \right) \right.$$

$$\left. - \frac{H'^2}{6} \frac{\partial}{\partial \underset{\sim}{x}^*} \left(\frac{\partial u_1'}{\partial x^*} + \frac{\partial}{\partial y^*} v_1' \cos\theta \right) \right] \qquad (4.48)$$

Now add, as Peregrine does, the $O(\varepsilon)$ and $O(\varepsilon^2)$ equations, i.e.

$$\begin{bmatrix} (4.34) \\ (4.35) \end{bmatrix} + \varepsilon \begin{bmatrix} (4.44a) \\ (4.44b) \end{bmatrix} \qquad \text{and} \quad (4.36) + \varepsilon\ (4.47)$$

Thus, (4.36) + ε(4.47) gives

$$\varepsilon \left[\frac{\partial \eta_1'}{\partial t^*} + \frac{\partial}{\partial x^*} H' u_1' + \frac{\partial}{\partial y^*} \cos\theta\ H v_1' \right]$$

$$+ \varepsilon^2 \left[\frac{\partial \eta_2'}{\partial t^*} + \nabla_h^* \cdot \left(\underset{\sim}{u}_1' \eta_1' + \underset{\sim}{U}_2 H' + \frac{H'^2}{2} \frac{\partial}{\partial \underset{\sim}{x}^*} \left[\frac{\partial}{\partial x^*} u_1' H' + v_1' \frac{\partial H'}{\partial y^*} + H' \frac{\partial}{\partial y^*} v_1' \cos\theta \right] \right.\right.$$

$$\left.\left. - \frac{H'^3}{6} \frac{\partial}{\partial \underset{\sim}{x}^*} \left[\frac{\partial}{\partial y^*} v_1' \cos\theta + \frac{\partial u_1'}{\partial x^*} \right] \right) \right] = 0$$

Substituting for η and $\bar{u}$ from their definitions above, this becomes

$$\frac{\partial \eta}{\partial t^*} + \frac{\partial}{\partial x^*} (H + \eta)\ \bar{u} + \frac{\partial}{\partial y^*} [\cos\theta\ (H + \eta)\ \bar{v}] = 0 \qquad (4.49)$$

The only visible difference due to the spherical coordinates is the $\cos\theta$ factor; one must not forget however that $dx = R \cos\theta\ d\phi$ and $dy = Rd\theta$.

The momentum equation $\varepsilon(4.34) + \varepsilon^2(4.44a)$ gives

$$\varepsilon \left[\frac{u_1'}{\partial t^*} + \frac{\partial \eta_1'}{\partial x^*} \right] + \varepsilon^2 \left[\frac{\partial}{\partial t^*} U_2 + u_1' \frac{u_1'}{\partial x^*} + v_1' \frac{u_1'}{\partial y^*} - \frac{f'}{\sigma\varepsilon} v_1' + \frac{\partial \eta_2'}{\partial x^*} \right] = 0 \qquad (4.50)$$

From the definition of $\bar{u}$ in (4.49), and to $O(\varepsilon^2)$, we then find

$$\frac{\partial \bar{u}}{\partial t^*} - \frac{f'}{\sigma} \bar{v} + \left(\bar{u} \frac{\partial \bar{u}}{\partial x^*} + \bar{v} \frac{\partial \bar{u}}{\partial y^*} \right) + \frac{\partial \eta}{\partial x^*} =$$

$$\frac{\partial}{\partial t^*} \left\{ \frac{H'}{2} \frac{\partial}{\partial x^*} \left(\frac{\partial}{\partial x^*} \bar{u} H' + \bar{v} \frac{\partial H'}{\partial y^*} + H' \frac{\partial}{\partial y^*} \bar{v} \cos\theta \right) - \frac{H'^2}{6} \frac{\partial}{\partial x^*} \left(\frac{\partial u}{\partial x^*} + \frac{\partial}{\partial y^*} \bar{v} \cos\theta \right) \right\}$$

We may now return to primed (rather than starred) coordinates and rearrange the inhomogeneous term slightly to obtain the momentum equations for long wave propogation on a spherical shell of varying thickness. Recalling that

η and $\bar{u}$ are the surface displacement and the horizontal velocity respectively with H_o, the reference depth and $\sqrt{gH_o}$, the reference speed, and $H' = H/H_o$, the relevant equations are

$$\frac{\partial \eta}{\partial t'} + \nabla'.(H' + \eta)\,\underset{\sim}{\bar{u}} = 0 \tag{4.51}$$

$$\frac{\partial \underset{\sim}{\bar{u}}}{\partial t'} + f'(\underset{\sim}{k} \times \underset{\sim}{\bar{u}}) + \underset{\sim}{\bar{u}}.\nabla'\underset{\sim}{\bar{u}} + \nabla'\eta = \frac{\partial}{\partial t'}\left[\frac{H'}{2}\nabla'(\underset{\sim}{\bar{u}}.\nabla'H') + \frac{H'^2}{3}\nabla'(\nabla'.\underset{\sim}{\bar{u}})\right] \tag{4.52}$$

where

$$\nabla' = \text{grad} = \left\{\frac{\partial}{\partial x'}\ ,\ \frac{\partial}{\partial y'}\right\}$$

$$\nabla'.\underset{\sim}{A} = \text{div} = \frac{\partial}{\partial x'} A_1 + \frac{\partial}{\partial y'} A_2 \cos\theta$$

and

$$(x',y') = (x,y)/H_o$$

$$t' = t(g/H_o)^{1/2}$$

$$f' = f(H_o/g)^{1/2}$$

$$y = R\theta;\ x = R\cos\theta\phi$$

with θ the latitude and ϕ the longitude.

Comparison with Hammack's (1973) Equations

Hammack treats the one-dimensional non-rotating case with the equations

$$u_t + (1 + \frac{3}{2}u)\,u_x - \frac{1}{6}u_{xxt} = 0 \tag{4.53a}$$

$$\eta = u + \frac{1}{4}u^2 - \frac{1}{6}u_{xx} \tag{4.53b}$$

These are readily derived as a special case of ours, which, under the same conditions, read for a uniform depth $H' = 1$

$$\bar{u}_t + \bar{u}\bar{u}_x + \eta_x - \frac{1}{3}\bar{u}_{xxt} = 0 \tag{4.54a}$$

$$\eta_t + \bar{u}_x + (\eta u)_x = 0 \tag{4.54b}$$

For uni-directional waves travelling towards $x>0$, $u = \eta + O(\varepsilon)$, $\partial t = -\partial x + O(\varepsilon)$. Hence $(\partial_x + \partial_t)(u-\eta) = O(\varepsilon^2)$, and we may add this term to the

sum of (4.54a) and (4.54b) to obtain

$$2(\bar{u}_t + \bar{u}_x) + \bar{u}\,\bar{u}_x - \frac{1}{3}\,\bar{u}_{xxt} + (\eta u)_x = 0 \qquad (4.55)$$

which reduces to (4.53a) if we replace η by u in the last term, which is still correct to the order required for unidirectional propagation. From (4.54a) [we drop the bar over the u] we have

$$\eta_x = -u_t - uu_x + \frac{1}{3}\,u_{xxt}$$

substituting for u_t from (4.53a),

$$\eta_x = (1+\frac{3}{2}\,u)\,u_x - \frac{1}{6}\,u_{xxt} - uu_x + \frac{1}{3}\,u_{xxt}$$

which readily reduces to (4.53b) by integration with respect to x if u_{xxt} is replaced by $-u_{xxx}$. Thus, Hammack's equations are seen to be a special case of ours.

4.2 The Shelf Model

The ocean currents model (C2D) employed in this application is a two-dimensional, depth-averaged implicit finite difference approximation of the differential equations for conservation of mass and momentum

$$\frac{\partial \eta}{\partial t} + \frac{\partial (ud)}{\partial x} + \frac{\partial (vd)}{\partial y} = 0 \qquad (4.56)$$

$$\frac{\partial u}{\partial t} + u\,\frac{\partial u}{\partial x} + v\,\frac{\partial u}{\partial y} - fv = -g\,\frac{\partial \eta}{\partial x} - \frac{k_f u|u|}{d} \qquad (4.57)$$

$$\frac{\partial v}{\partial t} + u\,\frac{\partial v}{\partial x} + v\,\frac{\partial v}{\partial y} + fu = -g\,\frac{\partial \eta}{\partial y} - \frac{k_f v|v|}{d} \qquad (4.58)$$

where

η = elevation relative to mean water level (m)
u = the east-west velocity component (m/s)
v = the north-south velocity component (m/s)
d = the total water depth (m)
t = time (s)
x = distance in the east-west direction (m)
y = distance in the north-south direction (m)
f = the Coriolis parameter: $2\Omega \sin\theta = 1.46 \times 10^{-4} \sin\theta$ (Hz)
θ = the latitude (rad)
g = the gravitational acceleration (9.81 m/s^2)
k_f = the friction coefficient: g/C_h^2
C_h = the Chezy coefficient

Equations similar to (4.56) to (4.58) have been used in many previous simulations of long wave propagation such as tides (Flather and Heaps, 1975; Crean, 1976), and tsunamis (Hwang and Divoky, 1970).

4.3 The Inlet Models

The fjord model (FJORD1D) utilized in this application is a one-dimensional, depth-averaged explicit finite difference model of the differential equations for conservation of mass and momentum

$$\frac{\partial \eta}{\partial t} + \frac{\partial q}{\partial x} = 0 \qquad (4.59)$$

$$\frac{\partial u}{\partial t} + g \frac{\partial \eta}{\partial x} + \frac{\tau_H}{\rho d} = 0 \qquad (4.60)$$

where

η = the elevation relative to mean water level (m)
q = the flow rate per unit width of the fjord (m^2/s)
u = the water velocity up the fjord (m/s)
d = the total water depth (m)
t = time (s)
x = distance along the water centre line of the fjord (m)
g = the gravitational acceleration (9.81 m/s^2)
ρ = the density of water (10^3 kg/m^3)
τ_H = the frictional shear stress (N/m^2)

These equations are suitable for simulating long-wave propagation in narrow bodies of water such as inlets and straits (Dronkers, 1964). They have been used in the past for other studies of tsunami propagation in inlets (e.g. Henry and Murty, 1973).

5.0 NUMERICAL METHODS

5.1 The Deep Ocean Model

We recall, for convenience, the equations derived in Section 4.1 which govern the surface elevation and two components of velocity:

$$\frac{\partial \eta}{\partial t} + \frac{\partial}{\partial x}\left[(H+\eta)u\right] + \frac{\partial}{\partial y}\left[(H+\eta)v\right] = 0 \tag{5.1}$$

$$\frac{\partial u}{\partial t} - fv + u\frac{\partial u}{\partial x} + v\frac{\partial u}{\partial y} + \frac{\partial \eta}{\partial x} + SINK(u) =$$

$$\frac{\partial}{\partial t}\left\{\frac{H}{2}\left[\frac{\partial}{\partial x}\left\{u\frac{\partial H}{\partial x}\right\} + \frac{\partial}{\partial x}\left\{v\frac{\partial H}{\partial y}\right\} + \frac{H^2}{3}\left[\frac{\partial^2 u}{\partial x^2} + \frac{\partial^2}{\partial x \partial y}(v\cos\phi)\right]\right]\right\} \tag{5.2}$$

$$\frac{\partial v}{\partial t} + fu + u\frac{\partial v}{\partial x} + v\frac{\partial v}{\partial y} + \frac{\partial \eta}{\partial y} + SINK(v) =$$

$$\frac{\partial}{\partial t}\left\{\frac{H}{2}\left[\frac{\partial}{\partial y}\left\{u\frac{\partial H}{\partial x}\right\} + \frac{\partial}{\partial y}\left\{v\frac{\partial H}{\partial y}\right\} + \frac{H^2}{3}\left[\frac{\partial^2 u}{\partial x \partial y} + \frac{\partial^2}{\partial y^2}(v\cos\phi)\right]\right]\right\} \tag{5.3}$$

where all quantities are nondimensional, and SINK contains all dissipative terms. This set of equations is known as the Boussinesq equations.

(a) The Solution Grid

Equations (5.1) to (5.3) are solved using finite differences on a spatially staggered grid (Fig. 5.1). Elevations (η) are located at grid centres, while velocity components (u,v) are located at the centres of the edges of each grid cell. Expressed in terms of (x,y) coordinates, is located at ($i\Delta x, j\Delta y$), u at (($i \pm 1/2$) $\Delta x, j\Delta y$), and v at ($i\Delta x, (j \pm 1/2)\Delta y$) for each grid cell. The grid spacings Δx and Δy were both set equal to 0.5 degrees.

(b) Interpolation Formulae

To evaluate the difference forms of (5.1) to (5.3), values of η, u, and v are required at locations other than on the grid points in Fig. 5.1. Fourth-order accurate interpolation formulae are then used to define values at these locations. One of two different formulae (Fig. 5.2) is selected depending on the location of the interpolation point relative to known values.

Formula (A) is used to obtain values of u_{ij}, v_{ij}, $\eta_{i+1/2,j}$, and $\eta_{i,j+1/2}$. Formula (B) is used to obtain values of $v_{i+1/2,j}$ or $u_{i,j+1/2}$.

(c) Difference Formulae

Equations (5.1)-(5.3) contain first and second order spatial derivatives and first order time derivates. In the corresponding finite difference equations these derivatives are replaced by second-order accurate (for time derivatives) and fourth-order accurate (for space derivatives) difference formulae. First and second order spatial derivatives are also required near boundaries. The formulae used are conveniently expressed in terms of

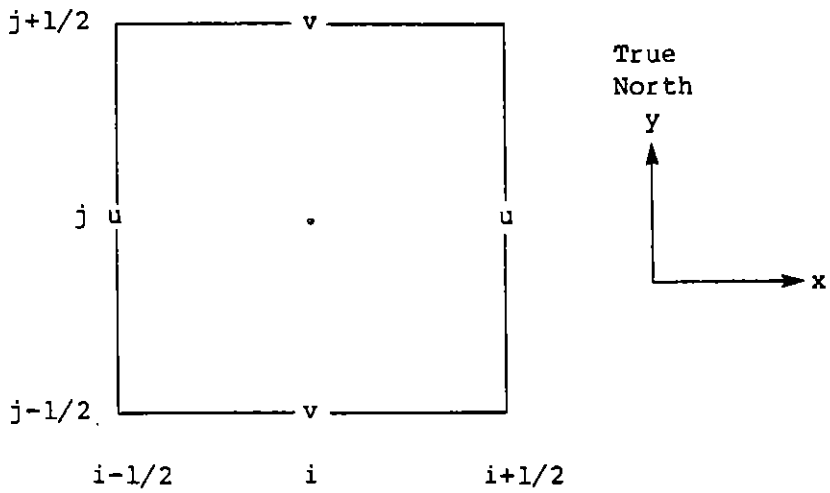

Fig. 5.1 An (i,j) element of the space-staggered solution grid for the DOM.

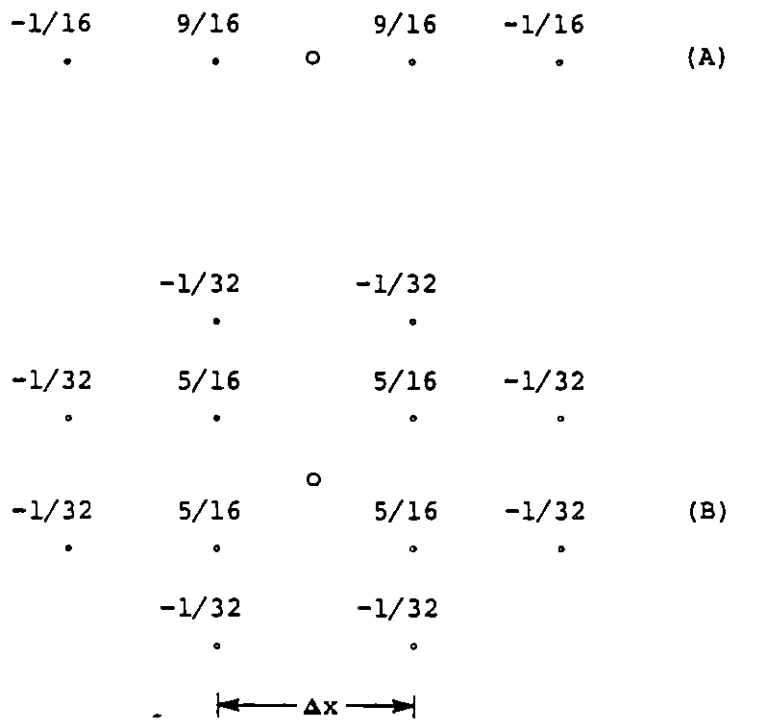

Fig. 5.2 Fourth-order accurate interpolation formulae expressed as weights applied to locations neighbouring the interpolation point (o).

weights applied to neighbouring points (Fig. 5.3).

(d) The Solution Domain

The complete domain of the deep ocean model encompasses most of the Pacific Ocean (Fig. 5.4). The total number of points in the grid is 99813, with 78430 of these corresponding to water. For each simulation it was necessary to restrict the calculations to a subset of these points in order to have the model execute in a reasonable length of time. This was accomplished in several different ways.

An artificial fixed boundary was imposed for each simulation by requiring that the sum of the distances along great circles from each DOM calculation point to the earthquake epicentre and to the reference coordinate (126°W, 49°N) be less than a prescribed value. Thus, each boundary defined in this way falls on the perimeter of an ellipse whose focii are the epicentre and reference point. The prescribed value for the total distance was defined as a certain number of deep water wavelengths added to the distance between focii. The restricted solution domains for the four epicentres used in the simulations are shown in Fig. 5.5.

The initial number of calculation points was restricted to the generation zone. Additional points were added to the solution domain at subsequent time steps in the model as the wave group travelled outward from the source. This was accomplished by monitoring the position of the leading edge of the wave group and adding adjacent grid elements as required to solve the finite difference equations.

The extent of the solution domain was also limited by deleting calculation points from the trailing edge of the wave group. A count was maintained at each elevation point of the number of zero crossings made by the free surface. When this number reached a prescribed value, the elevation was attenuated exponentially over the next 25 model iterations to a value of zero.

(e) Boundary Conditions

At solid horizontal boundaries the order of all spatial derivatives was maintained at fourth order by assuming that energy is completely reflected. In optics, this is equivalent to assuming the presence of a perfectly reflecting mirror at all boundaries. All interpolation and finite difference formulae that are evaluated near solid boundaries use, as required, "mirrored" variable values.

(f) Initial Conditions

To initialize all deep ocean model calculations the elevation and velocity fields were set to zero. The bottom bathymetry was set to values derived from the various data sources as described in Section 3. The number of calculation points was set to zero.

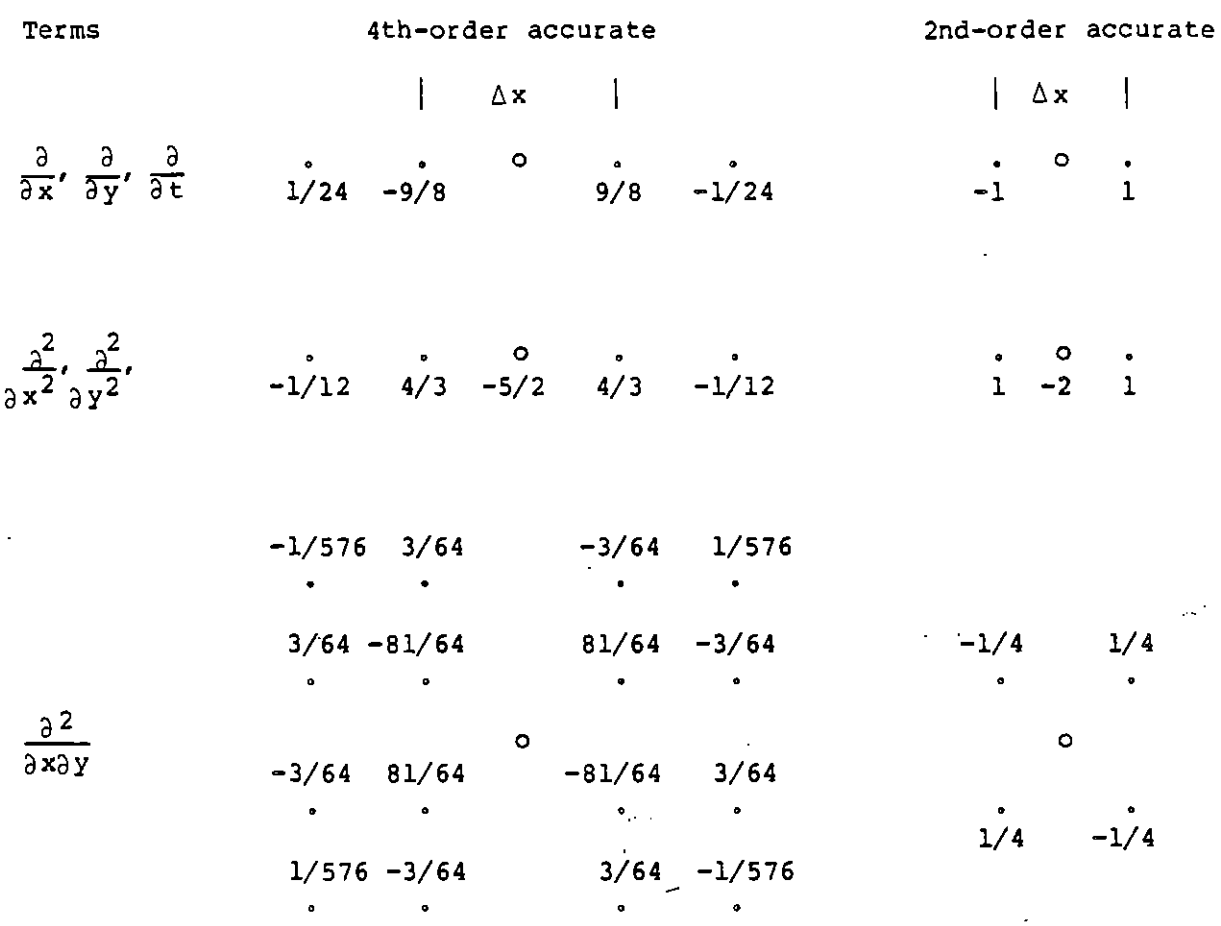

Fig. 5.3 Difference formulae expressed as weights to be applied to locations neighbouring the calculation point (o).

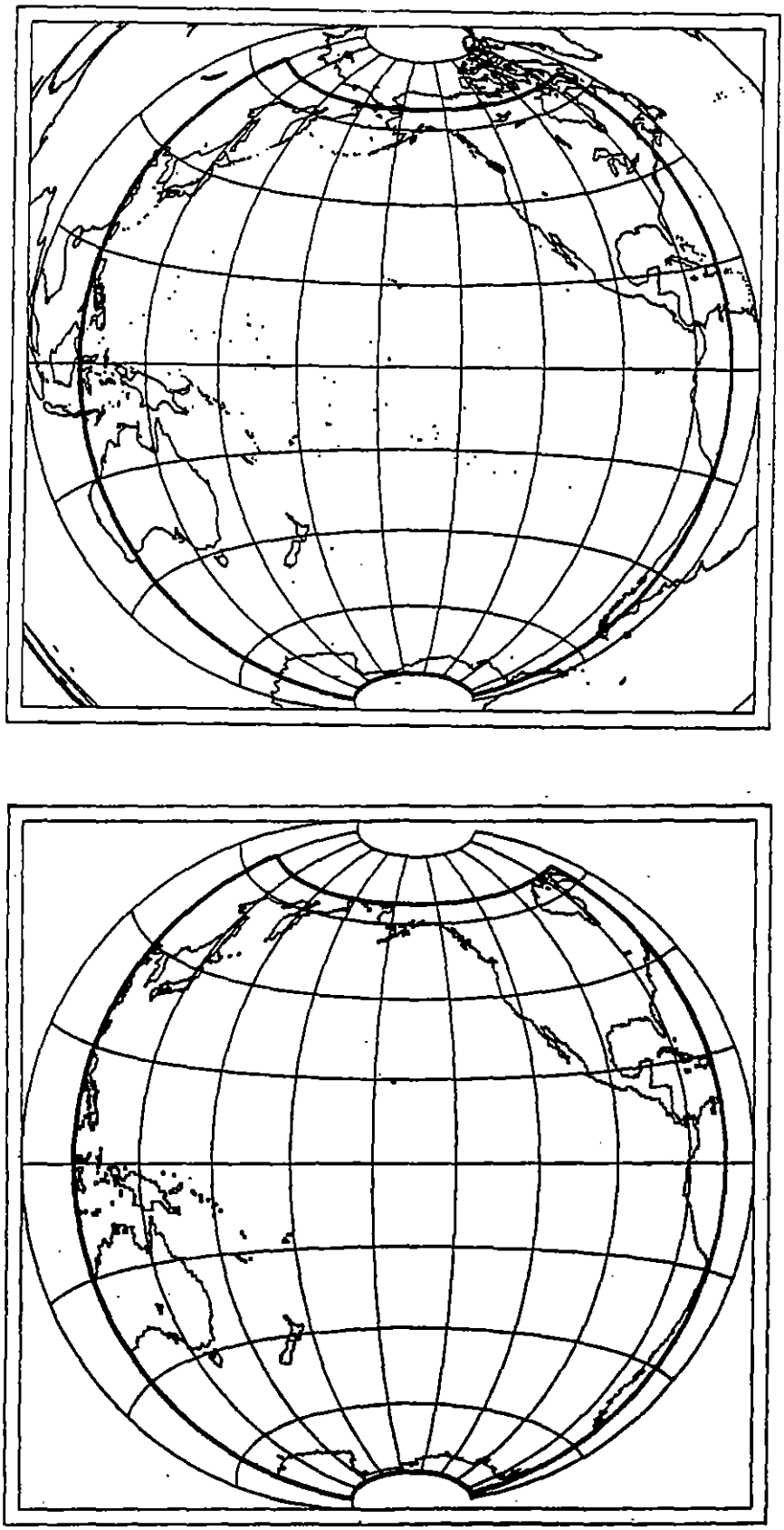

Fig. 5.4 Deep ocean model grid boundary (bold line) with (a) the actual coastline, and (b) the coastline approximated by the 0.5-degree grid spacing.

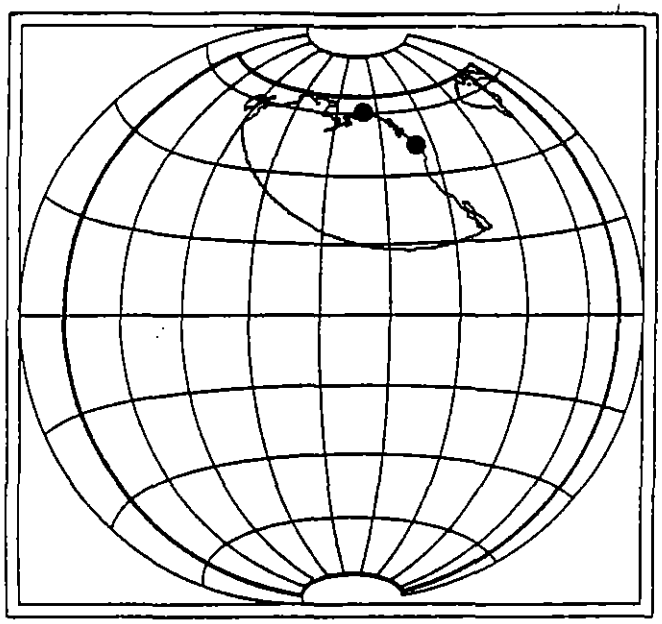

Alaska (1964)

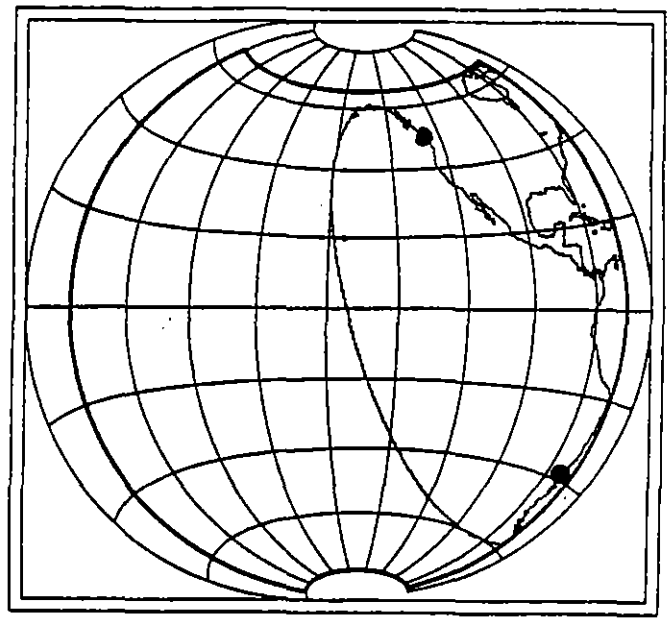

Chile (1960)

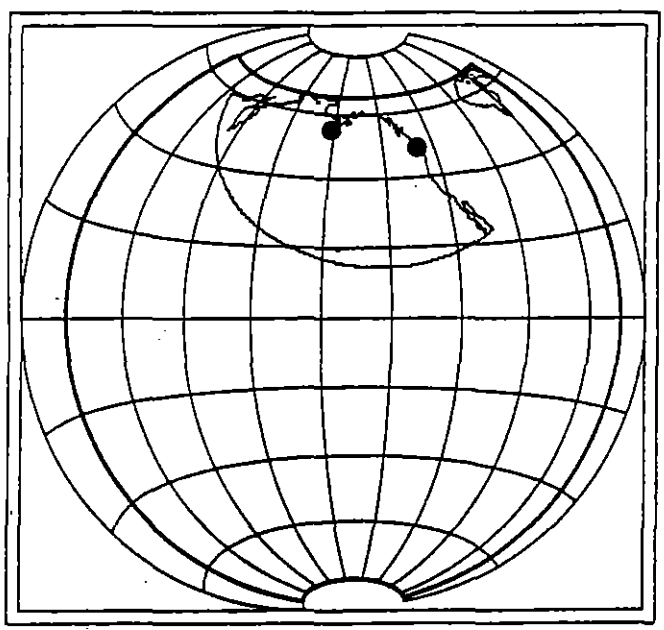

Shumagin Gap

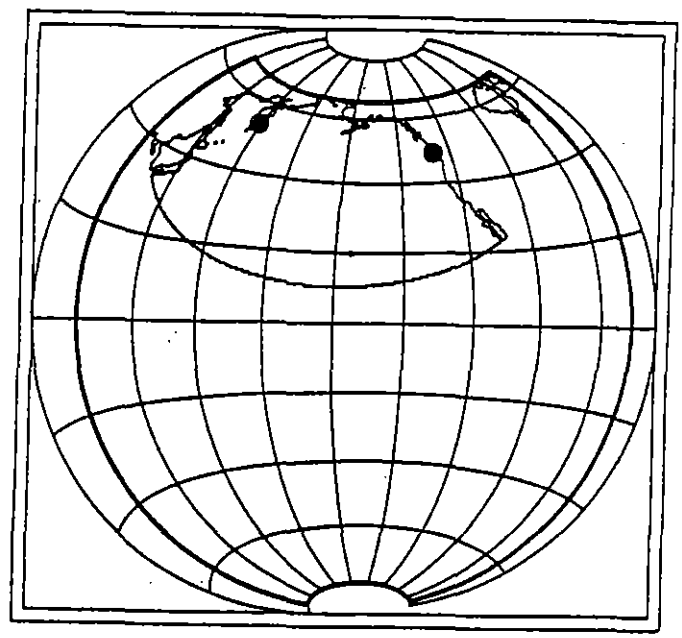

Kamchatka

Fig. 5.5 Ellipse focii and perimeter used to restrict the solution domains for each deep ocean model simulation.

(g) Dissipation Terms

The sink terms SINK(u) and SINK(v) appearing in (5.2) and (5.3) allow for real and artificial dissipation of energy. Real dissipation occurs in the form of bottom drag, while artificial dissipation is required due to the limited resolution of the model. If the grid spacing is Δx then the smallest waves that can be resolved have spatial frequency $1/(2\Delta x)$. As a consequence of the nonlinear terms in the governing equations there will be a cascade of energy toward higher spatial frequencies. In nature, the energy associated with these waves is dissipated by turbulent viscosity at scales that may be quite small (less than 1 metre). The model does not resolve scales this fine, hence a mechanism for removing this energy must be introduced to avoid aliasing, and possible nonlinear instabilities. A turbulent viscosity term of the form $K(\partial^2 u/\partial x^2+\partial^2 u/\partial y^2)$ has been used to filter out energy at high spatial frequencies. A value of 100 m^2/s was found to provide a suitable degree of smoothing.

The bottom drag term was set to zero for all simulations because water depths are great enough that frictional dissipation is negligible compared to the other terms in (5.2) and (5.3).

(h) The Storage Reduction Scheme

An indexing scheme has been implemented to accomplish two objectives: (1) to decrease computer memory requirements, and (2) to decrease execution time over coding of the Boussinesq model using standard, fully two-dimensional arrays. This is accomplished by limiting storage and calculations to grid points "near" the propagating wave group. The increase in efficiency is accomplished at the expense of increased complexity of the program code, a slight decrease in accuracy due to truncation of the solution domain, and increased computational overhead.

The method works by providing pools of storage for the dynamic variables u, v, and η (eastward speed, northward speed, and surface elevation). Each of these variables is associated with a set of active points (i,j) of the computational grid, and is stored at three time levels. Thus, at a point (i,j) there is a requirement for 3x3 = 9 values to be stored. Rather than provide storage for every point in the grid, the pool supplies a much smaller area to store only those points actively involved in the computations.

Locations in the storage pool are associated with unique locations (i,j coordinates) in the grid. This correspondence is maintained by index arrays that map each grid coordinate onto a pool location and vice versa.

(i) Solution Method

The finite difference equations representing (5.1) to (5.3) are solved over the calculation domain in two phases. In the generation phase, all dynamic variables are initialized to zero prior to commencement of bottom motion. Ocean bottom displacements and their grid locations are then inputed at each time step and (5.1)-(5.3) are solved subject to the restriction that the right hand sides of (5.2), (5.3) are set to zero. This greatly reduces execution time and is completely valid over the relatively short generation

phase. A small time step (2 s) is used here in order to properly resolve the bottom motions. When bottom motion ceases, the generation phase ends and the propagation phase begins. The integration continues at the propagation time step (45 s), but with the right-hand side dispersive terms now included. This requires that an iterative solution technique be used from this point onward due to the now implicit nature of the equations. Accordingly, the execution time required per time step increases markedly.

The finite difference equations are formulated as a mixed explicit-implicit scheme (purely explicit when the right hand dispersive terms are omitted) and hence the maximum allowable time step is governed by the relationship

$$C = \frac{\Delta t}{\Delta x}\sqrt{gH} < 1 \tag{5.4}$$

where C is the Courant number, H is the maximum water depth, and Δx the smallest grid spacing in the model. Δx is constant along grid columns, but varies as $\cos\theta$ for latitude θ. Thus, the restriction on the time step is affected by the maximum northward or southward calculation point. The maximum value for H is about 9600 m, and the maximum value for $|\theta|$ is about 70°, hence for Δt=45 s we have C = 0.7 for a 0.5 degree grid spacing.

5.2 The Shelf Model

(a) Difference Equations

The differential equations (4.56) to (4.58) are solved using finite differences on the 5-km shelf grid. The differencing scheme is described in Hodgins (1977) and is based on the time- and space-centred approach described by Leendertse (1967). It is a fully implicit scheme which uses an Alternating Direction Implicit (ADI) method, and thus is not restricted to Courant numbers less than or equal to unity. The only limitation on Δt, Δx and Δy is that the modelled waveform must be well-resolved in time and space. The model, denoted by C2D, was shown (Hodgins, 1977) to be unconditionally consistent with the differential equations and to be second order accurate (i.e., to have truncation errors of $O(\Delta t^2, \Delta x^2, \Delta y^2)$). The one-dimensional non-linear equations without frictional dissipation are analytically unconditionally stable.

The finite difference equation corresponding to the differential equation for the conservation of mass is

$$\frac{\eta_{j,k}^{n+1/2} - \eta_{j,k}^{n}}{\Delta t/2} + \frac{d_{j+1,k}^{n+1/2}\, u_{j+1,k}^{n+1/2} - d_{j-1,k}^{n+1/2}\, u_{j-1,k}^{n+1/2}}{2\Delta x} + \frac{d_{j,k+1}^{n}\, v_{j,k+1}^{n} - d_{j,k-1}^{n}\, v_{j,k-1}^{n}}{2\Delta y} = 0 \tag{5.5}$$

The corresponding difference equations for the conservation of momentum are (for time step $n\Delta t$ to $(n+1/2)\Delta t$:

$$\frac{u^{n+1/2}_{j,k} - u^{n}_{j,k}}{\Delta t/2} + u^{n+1/2}_{j,k}\left\{\frac{u^{n+1/2}_{j+2,k} - u^{n+1/2}_{j-2,k}}{4\Delta x}\right\} + v^{n}_{j,k}\left\{\frac{u^{n}_{j,k+2} - u^{n}_{j,k-2}}{4\Delta y}\right\}$$

$$+ g\left\{\frac{\eta^{n+1/2}_{j+1,k} - \eta^{n+1/2}_{j-1,k}}{2\Delta x}\right\} + \frac{k_f\, u^{n}_{j,k}\left[\left[u^{n}_{j,k}\right]^2 + \left[v^{n}_{j,k}\right]^2\right]^{1/2}}{d^{n}_{j,k}} = 0 \qquad (5.6)$$

$$\frac{v^{n+1/2}_{j,k} - v^{n}_{j,k}}{\Delta t/2} + u^{n+1/2}_{j,k}\left\{\frac{v^{n+1/2}_{j+2,k} - v^{n+1/2}_{j-2,k}}{4\Delta x}\right\} + v^{n}_{j,k}\left\{\frac{v^{n}_{j,k+2} - v^{n}_{j,k-2}}{4\Delta y}\right\}$$

$$+ g\left\{\frac{\eta^{n}_{j,k+1} - \eta^{n}_{j,k-1}}{2\Delta y}\right\} + \frac{k_f\, v^{n+1/2}_{j,k}\left[\left[u^{n+1/2}_{j,k}\right]^2 + \left[v^{n}_{j,k}\right]^2\right]^{1/2}}{d^{n+1/2}_{j,k}} = 0 \qquad (5.7)$$

For the one-half time step from n+1/2 to n+1, the differential equation for continuity becomes:

$$\frac{\eta^{n+1}_{j,k} - \eta^{n+1/2}_{j,k}}{\Delta t/2} + \frac{u^{n+1/2}_{j+1,k}\, d^{n+1/2}_{j+1,k} - d^{n+1/2}_{j-1,k}\, u^{n+1/2}_{j-1,k}}{2\Delta x}$$

$$+ \frac{d^{n+1}_{j,k+1}\, v^{n+1}_{j,k+1} - d^{n+1}_{j,k-1}\, v^{n+1}_{j,k-1}}{2\Delta y} = 0 \qquad (5.8)$$

During the same interval, the corresponding equations for momentum become:

$$\frac{u^{n+1}_{j,k} - u^{n+1/2}_{j,k}}{\Delta t/2} + u^{n+1/2}_{j,k}\left\{\frac{u^{n+1/2}_{j+2,k} - u^{n+1/2}_{j-2,k}}{4\Delta x}\right\} + v^{n+1}_{j,k}\left\{\frac{u^{n+1}_{j,k+2} - u^{n+1}_{j,k-2}}{4\Delta y}\right\}$$

$$+ g\left\{\frac{\eta^{n+1/2}_{j+1,k} - \eta^{n+1/2}_{j-1,k}}{2\Delta x}\right\} + \frac{k_f\, u^{n+1}_{j,k}\left[\left[u^{n+1/2}_{j,k}\right]^2 + \left[v^{n+1}_{j,k}\right]^2\right]^{1/2}}{d^{n+1}_{j,k}} = 0 \qquad (5.9)$$

$$\frac{v^{n+1}_{j,k} - v^{n+1/2}_{j,k}}{\Delta t/2} + u^{n+1/2}_{jk}\left\{\frac{v^{n+1/2}_{j+2,k} - v^{n+1/2}_{j-2,k}}{4\Delta x}\right\} + v^{n+1}_{j,k}\left\{\frac{v^{n+1}_{j,k+2} - v^{n+1}_{j,k-2}}{4\Delta y}\right\}$$

$$+ g\left\{\frac{\eta^{n+1}_{j,k+1} - \eta^{n+1}_{j,k-1}}{2\Delta y}\right\} + \frac{k_f\, v^{n+1/2}_{j,k}\left[\left[u^{n+1/2}_{j,k}\right]^2 + \left[v^{n+1/2}_{j,k}\right]^2\right]^{1/2}}{d^{n+1/2}_{j,k}} = 0 \qquad (5.10)$$

(b) Solution Grid

The dependent variables of the shelf model were solved on a spatially staggered grid (Fig. 5.6) with 70 columns and 220 rows. The grid is oriented at an angle of 30 degrees counter-clockwise from East, and is centred at the point (129.5°W, 51.5°N). The separation between rows and columns is 5 km. Fig. 5.7(a) shows the coastline and boundary of the shelf model grid. Fig. 5.7(b) and 5.7(c) show the same grid border together with the coastline as appproximated in the shelf and deep ocean models respectively.

(c) Boundary Conditions

Elevations derived from a run of the deep-ocean model were precribed at the seaward open boundaries of the shelf model at 90 s intervals. Forty coastal open boundary points were defined at the entrances to inlet systems modelled by the one-dimensional inlet models. Elevations at these junctions were calculated by coupling the shelf and inlet models and running them simultaneously. The method of characteristics was used to estimate the elevation at each common boundary point (x_o). The procedure evaluates the elevations at the next C2D model time step ($t_o+\Delta T$) given values of all dependant variables at the present time step (t_o). If we denote ΔT=90 s and Δt=15 s as the time steps in the C2D and fjord models respectively ($\Delta t=\Delta T/6$), then the following steps were used, refering to Fig. 5.8:

1. The normal velocity component (u) and total water depth (h) were evaluated at (x_o,t_o).

   i. $u(x_o,t_o)$ was evaluated by linear spatial interpolation of u values from either side of x_o (one each from C2D and the fjord model).

   ii. $h(x_o,t_o)$ was set to: $h(x_o,t_o) = \eta(x_o,t_o)+d(x_o)$, where η is the free surface displacement, and d is the mean water level.

2. The characteristic lines c_+ and c_- were evaluated using these values for u and h according to

   i. $c_+ = u + \sqrt{gh}$

   ii. $c_- = u - \sqrt{gh}$

3. c_+ and c_- were assumed constant during the interval $[t_o-\Delta t,\ t_o+\Delta T]$ and used to extrapolate backward in time from the point $(x_o,t_o+\Delta T)$ to evaluate $u_1(x_o-\Delta T.c_+,t_o)$, $h_1(x_o-\Delta T.c_+,t_o)$, $h_2(x_o+\Delta T.c_-,t_o)$, and $u_2(x_o+(\Delta T+\Delta t).c_-,t_o-\Delta t)$ using linear spatial interpolation.

4. The Riemann invariants along each characteristic (Abbott, 1975) provide two equations for (u_3, h_3):

   i. $u_1 + 2\sqrt{gh_1} = u_3 + 2\sqrt{gh_3}$

   ii. $u_2 - 2\sqrt{gh_2} = u_3 - 2\sqrt{gh_3}$

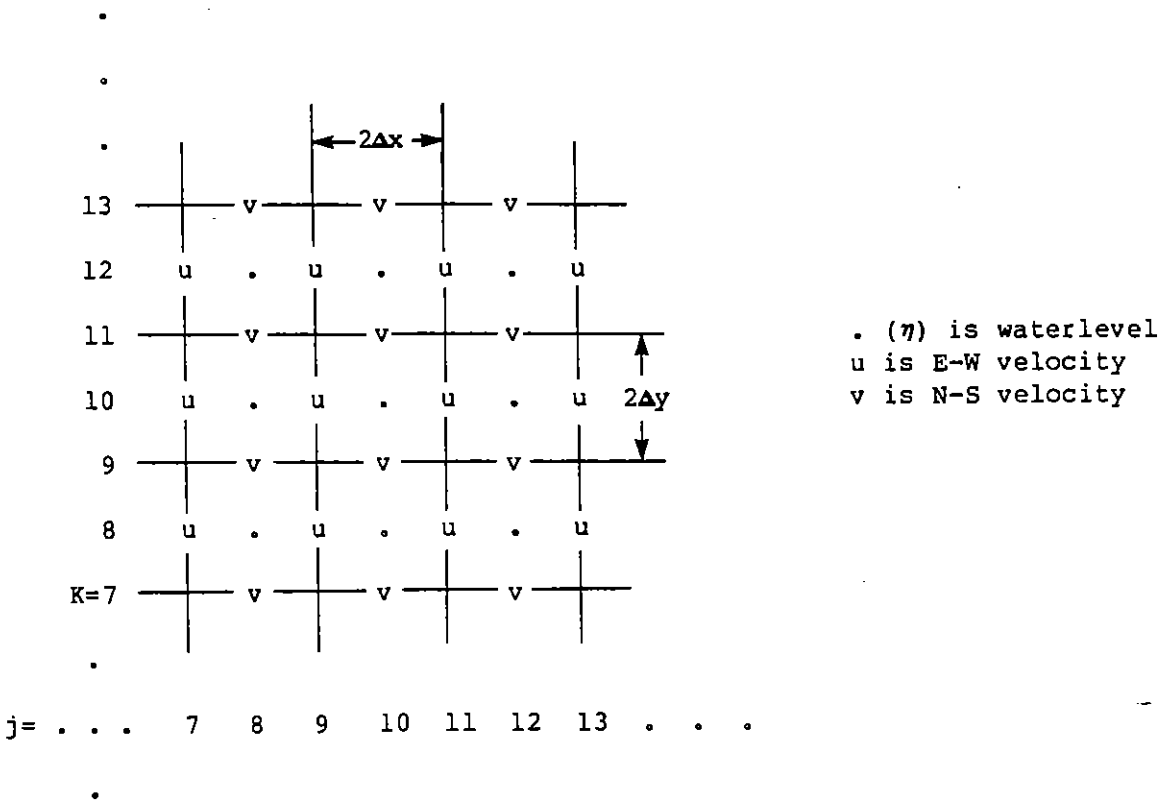

Fig. 5.6 Dependent variable grid for the C2D model.

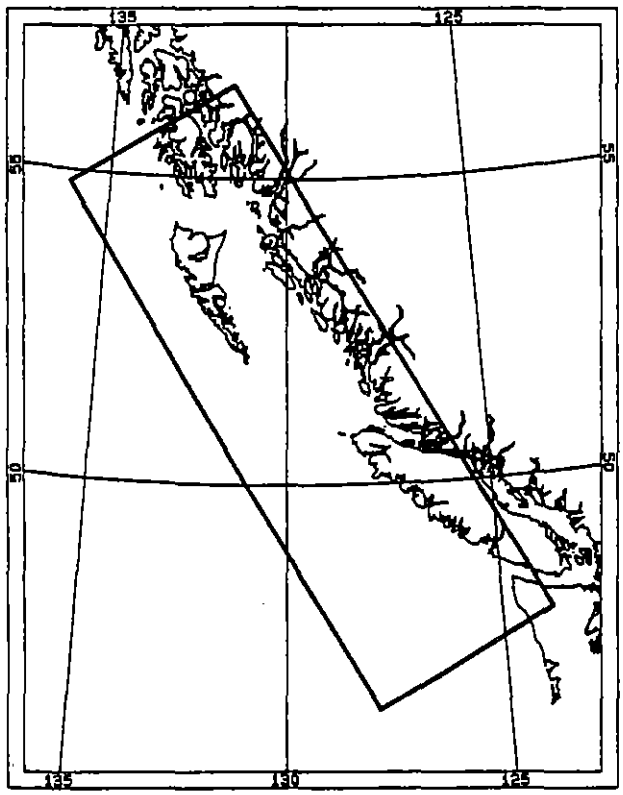

(a)

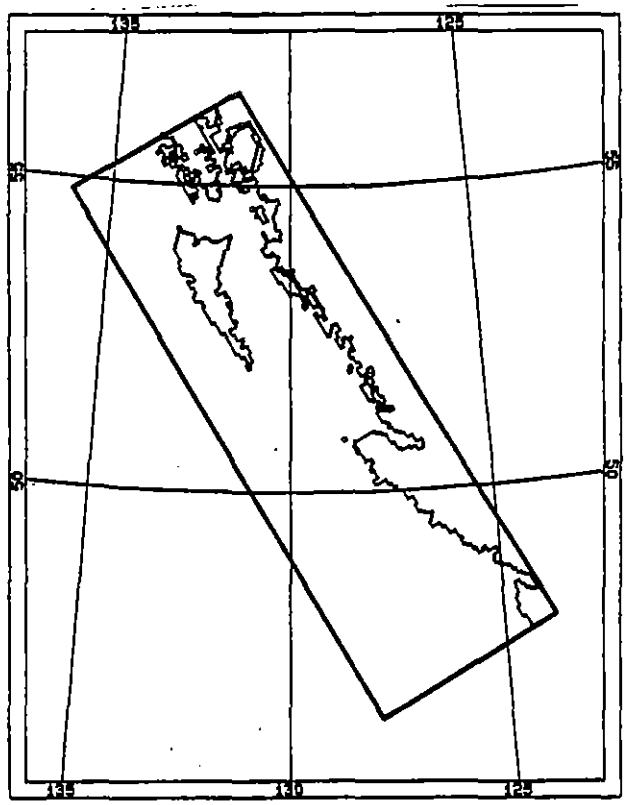

(b)

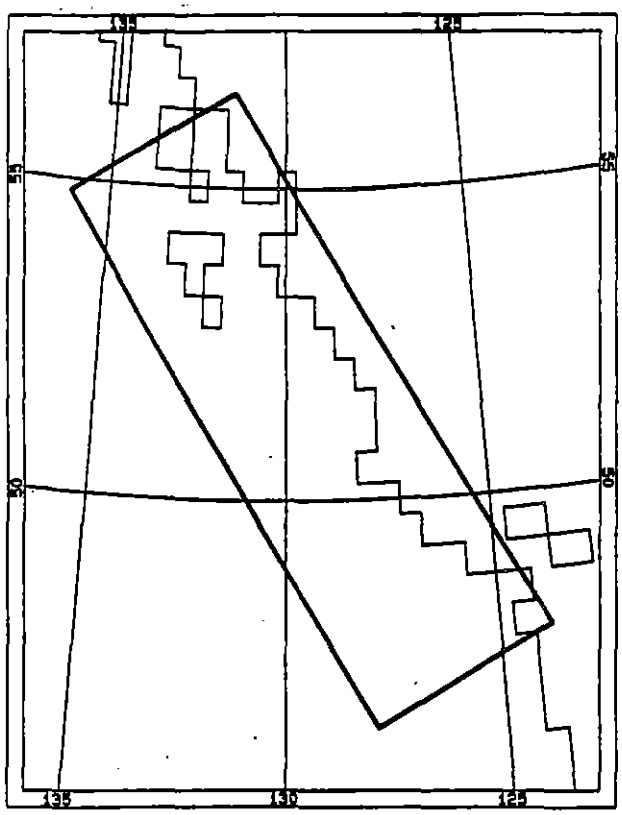

(c)

Fig. 5.7

Shelf model boundary (bold line) and (a) the actual coastline; (b) the coastline as approximated by 5-km grid spacing in shelf model; (c) the coastline as approximated by 0.5 degree grid spacing in deep ocean model.

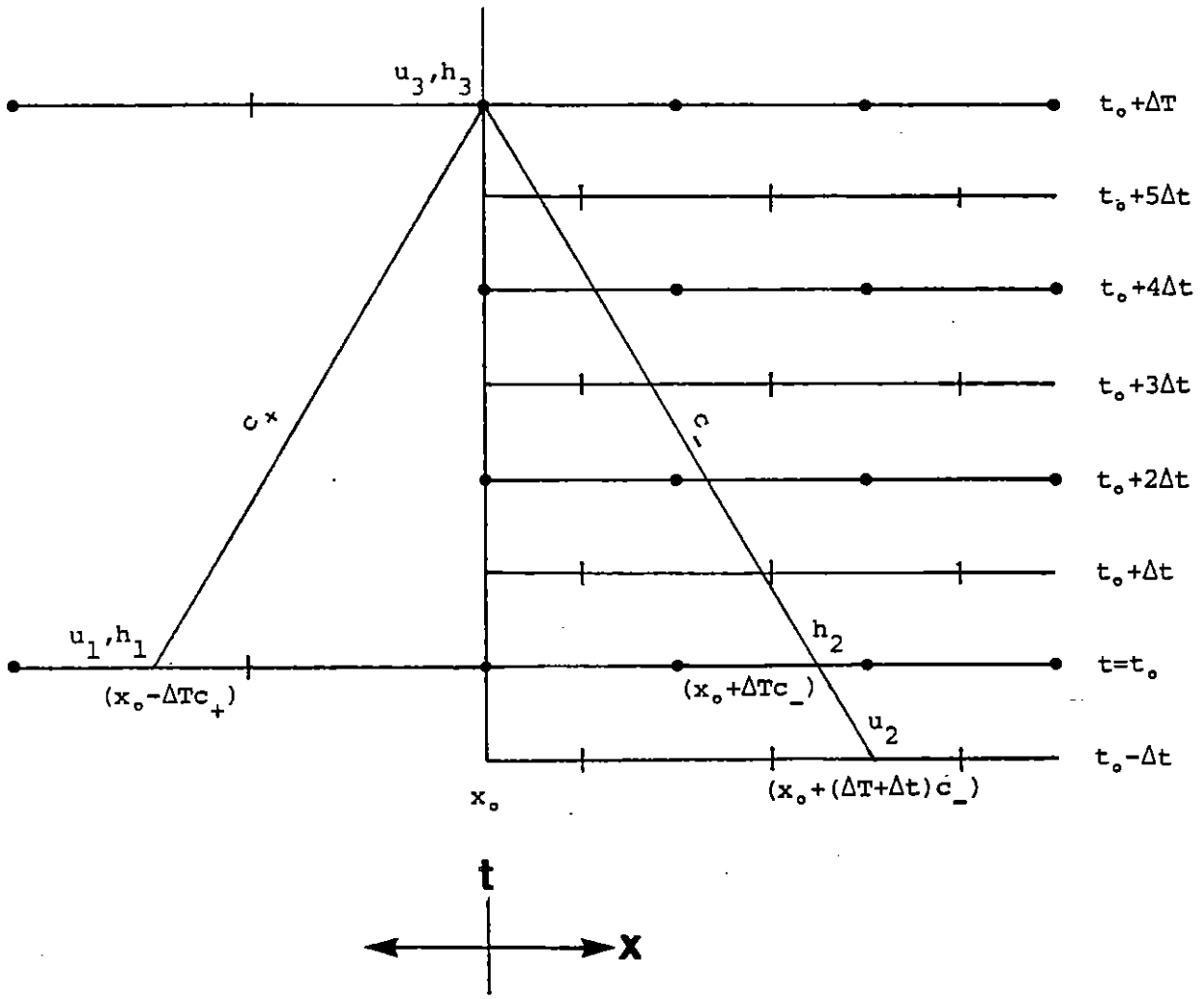

Fig. 5.8 Schematic diagram showing details of the method of characteristics used to evaluate surface elevations at junction points between the shelf model (C2D) and the inlet models (FJORD1D).

5. The equations were solved for h_3; the total depth at $(x_o, t_o + T)$:

$$h_3 = \frac{1}{16g}[(u_1 - u_2) + 2\sqrt{g}(\sqrt{h_1} + \sqrt{h_2})]^2$$

(d) Initial Conditions

The initial elevation and current fields were set to zero at the beginning of each simulation.

5.3 The Inlet Models

The numerical solution of equations (4.59) and (4.60) was obtained with a finite difference scheme centred in both space and time. The model (FJORD1D) is fully explicit and is therefore restricted to a Courant number (see equation 5.4) of less than unity. A fixed time step of 15 s was selected to ensure that the Courant number remained within this bound for all inlet systems. The wave height and velocity are staggered in time and space (Fig. 5.9). Δx is defined as the distance between wave height and velocity points while Δt is defined as the time between calculations of these quantities.

The inlet models consist of a set of nodes interconnected by branches that correspond to sections of the inlets. Each branch was subdivided into segments that are $2\Delta x$ long. Velocities were calculated at the ends of segments while elevations are calculated at the centres. Only elevations were calculated at the nodes. Fig. 5.10 shows the coastline for each inlet model (labelled by letters A-T). For all but the simplest systems a network schematic has been drawn that represents the nodes and branches of the corresponding numerical model. For clarity, nodes in each representation of the inlet are connected by straight lines.

The momentum and mass balance equations (4.59) and (4.60) are solved to calculate wave height (η) and transport (Q) at each branch. The finite difference equation corresponding to (4.59) is:

$$\frac{\eta_i^{n+1} - \eta_i^{n-1}}{2\Delta t} + \frac{Q_{i+1}^n - Q_{i-1}^n}{S_i} = 0 \qquad (5.11)$$

where S_i is the surface area over a segment of length $2\Delta x$.

The difference equation corresponding to (4.60) is:

$$\frac{Q_i^{n+1} - Q_i^{n-1}}{[A_i + W_i(\eta_i^n + \eta_{i+1}^n)/2]2\Delta t} + \frac{(\eta_{i+1}^n - \eta_{i-1}^n)g}{2\Delta x} + \frac{\tau_H}{d_i} = 0 \qquad (5.12)$$

where A and W denote cross-sectional area and surface width of the inlet respectively, and where friction (τ_H) was calculated from:

$$\tau_H = |u_i^{n-1}| u_i^{n+1} \, g/C_i^2 \qquad (5.13)$$

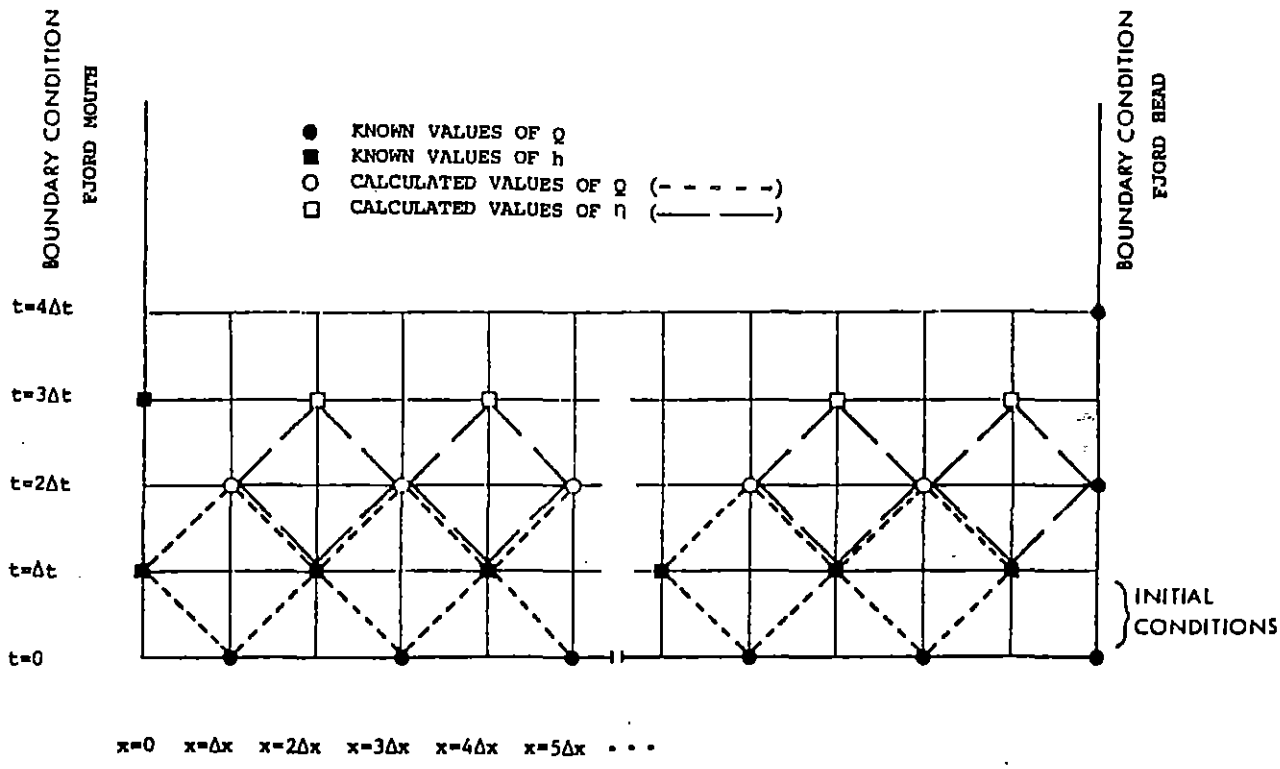

Fig. 5.8 Finite difference scheme used in FJORD1D.
9

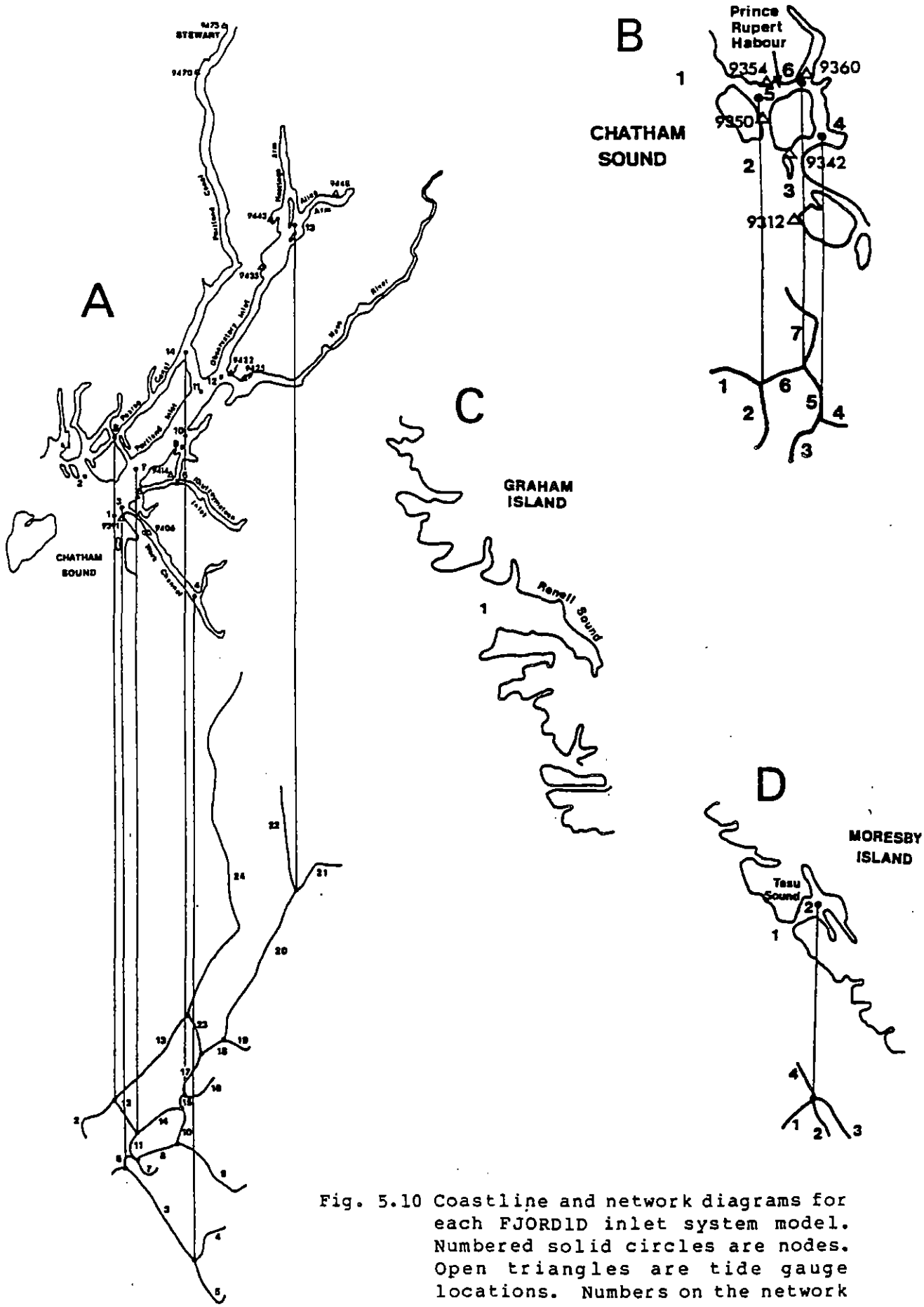

Fig. 5.10 Coastline and network diagrams for each FJORD1D inlet system model. Numbered solid circles are nodes. Open triangles are tide gauge locations. Numbers on the network denote branches.

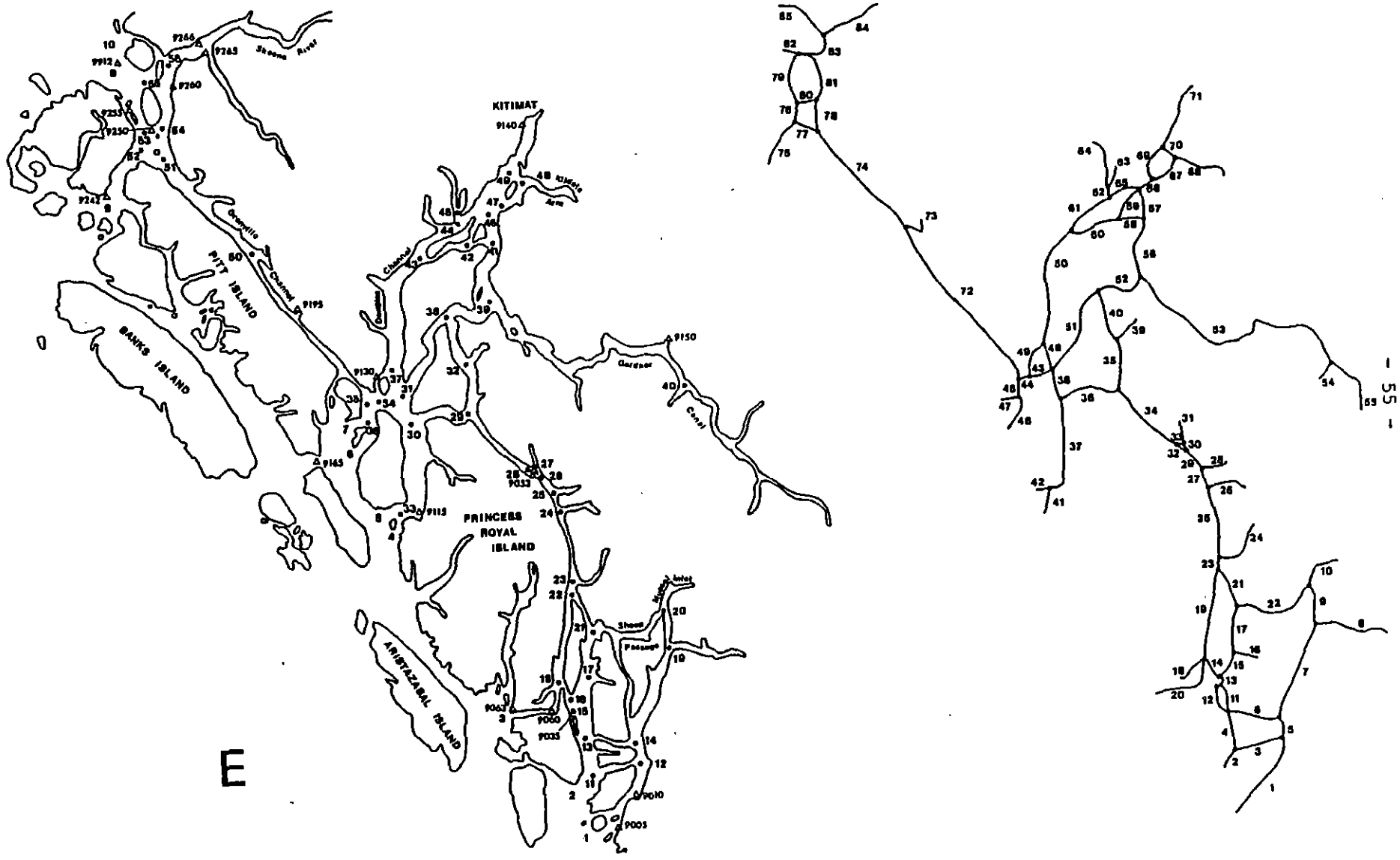

Fig. 5.10 Continued

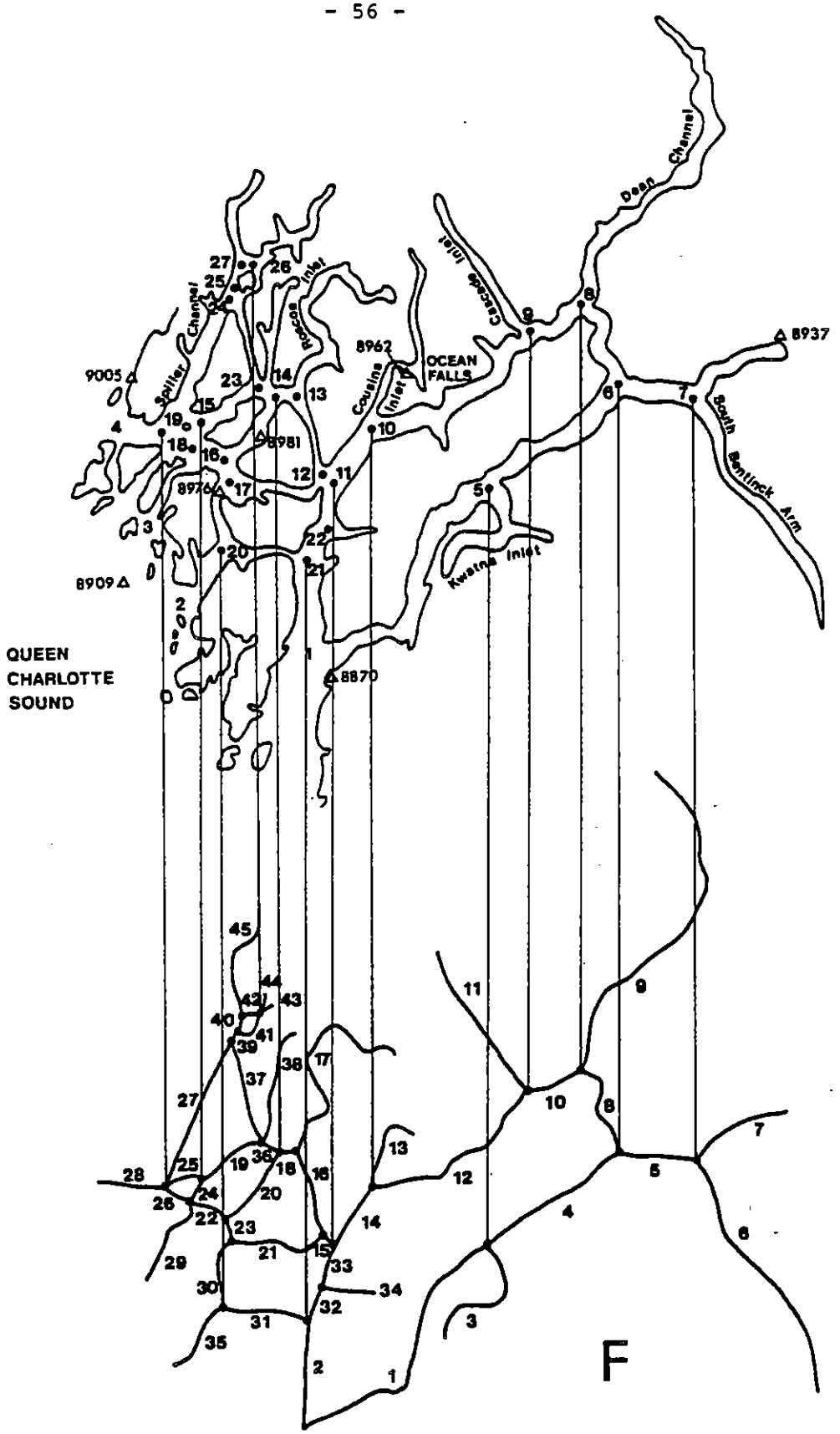

Fig. 5.10 Continued

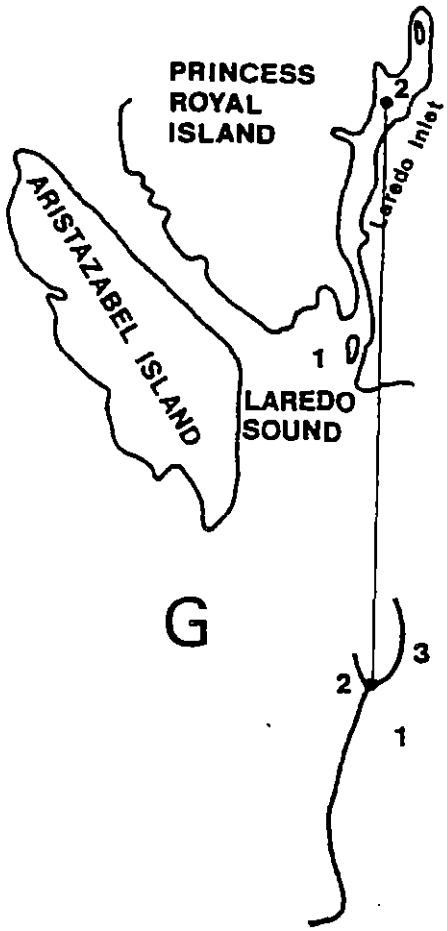

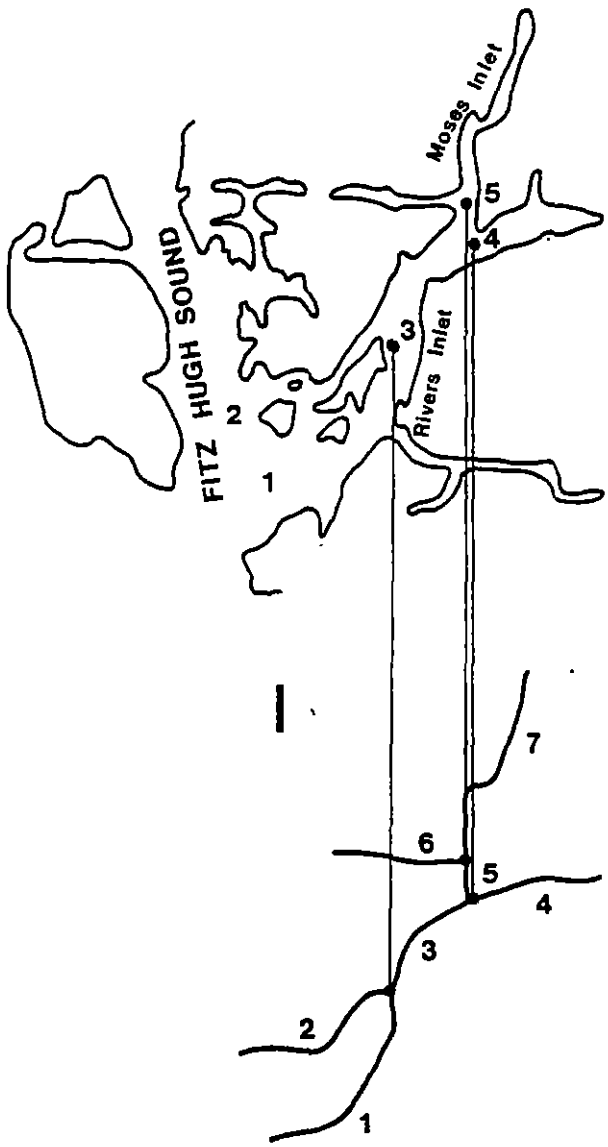

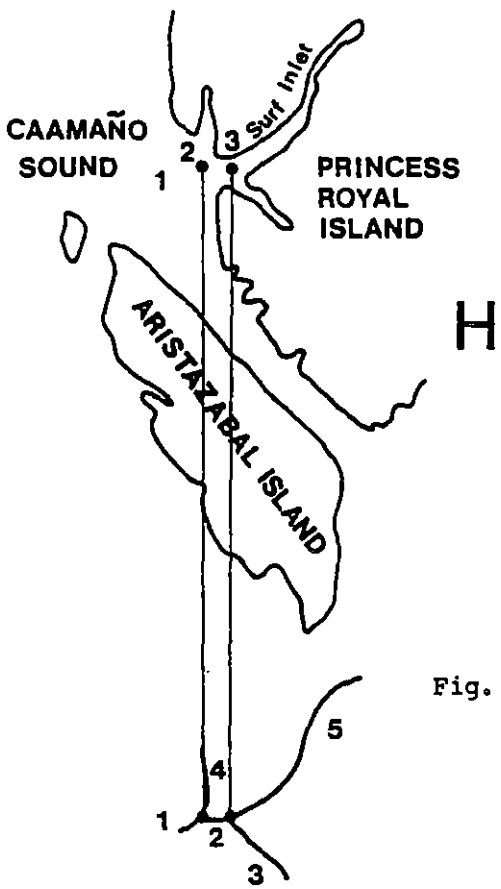

Fig. 5.10 Continued

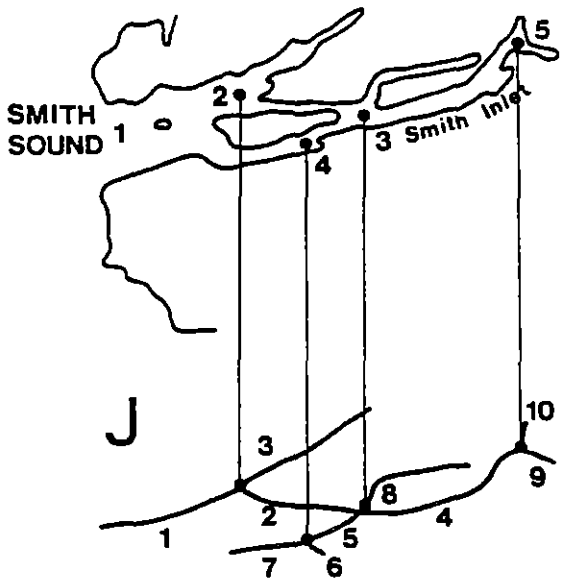

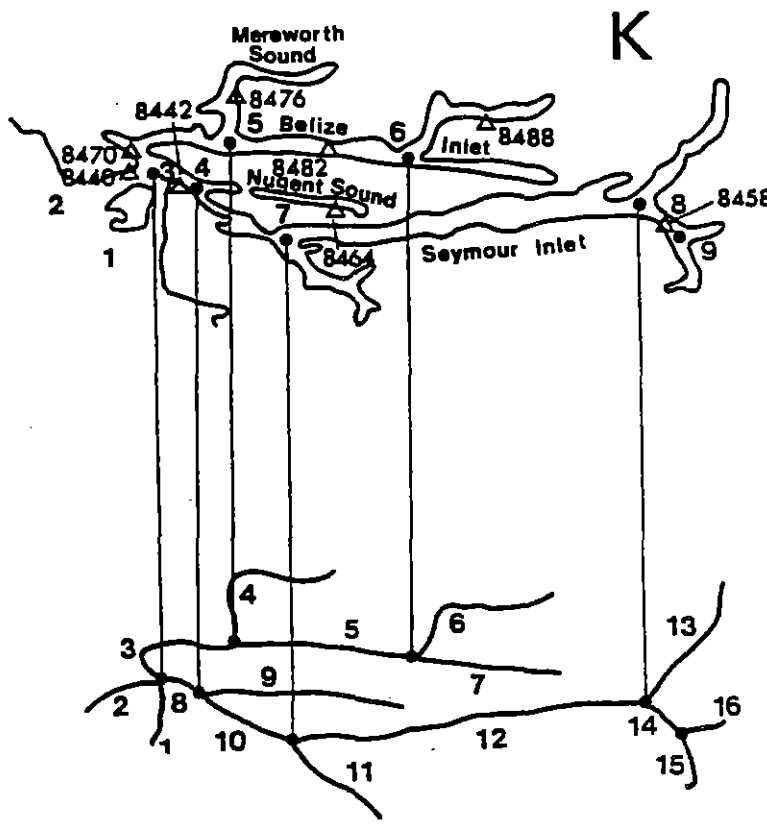

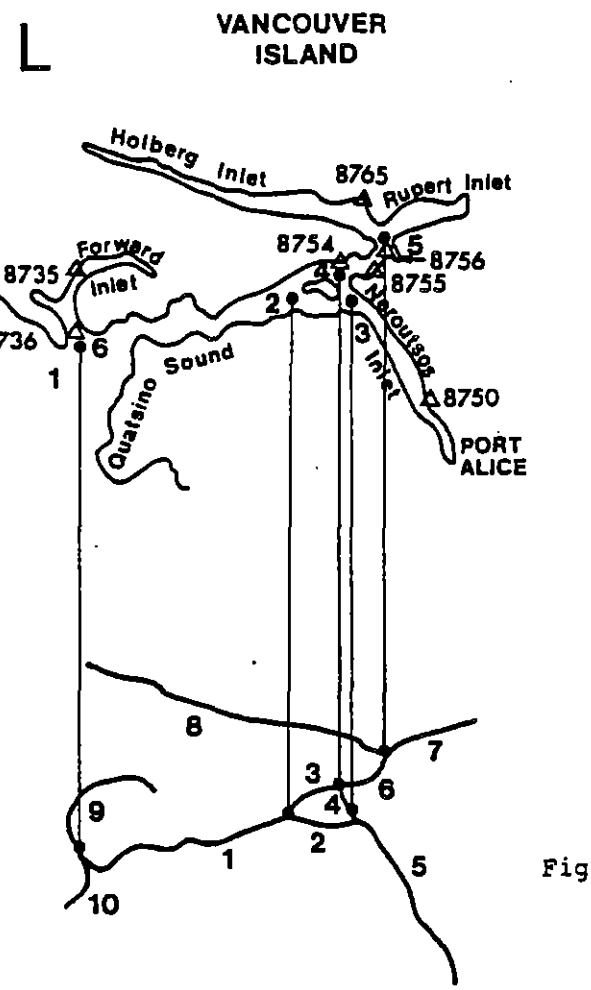

Fig. 5.10 Continued

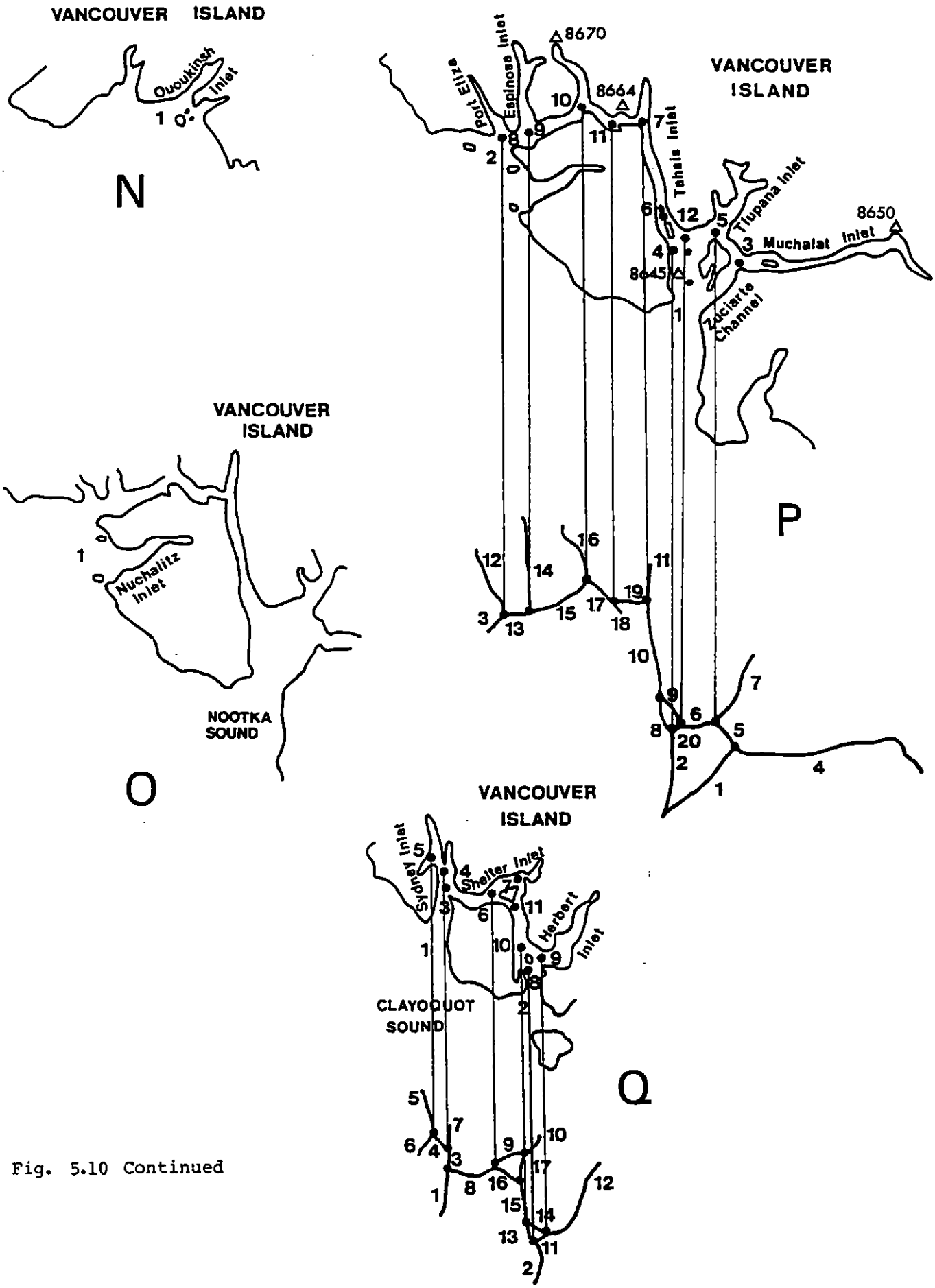

Fig. 5.10 Continued

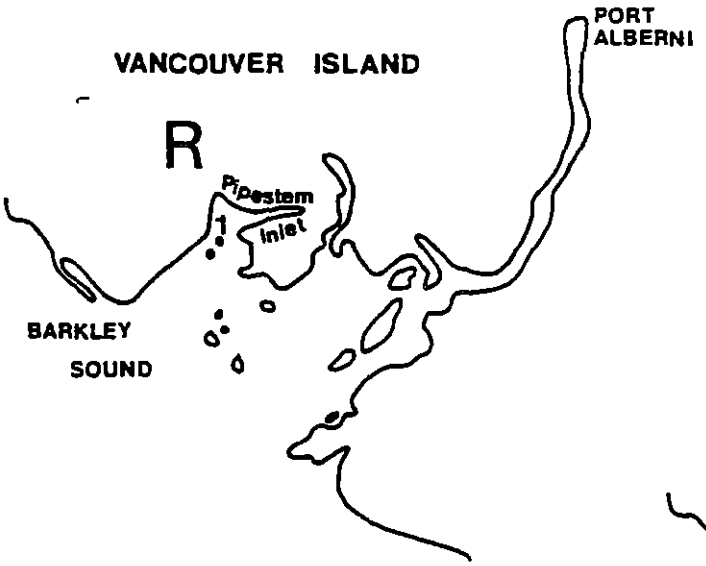

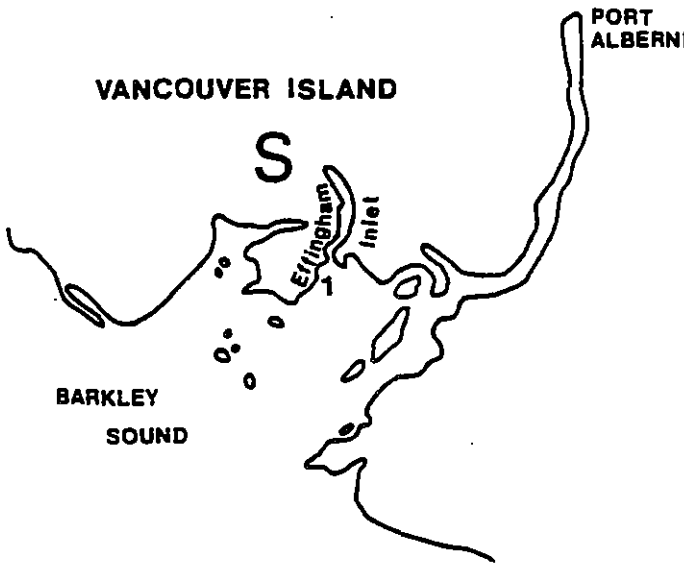

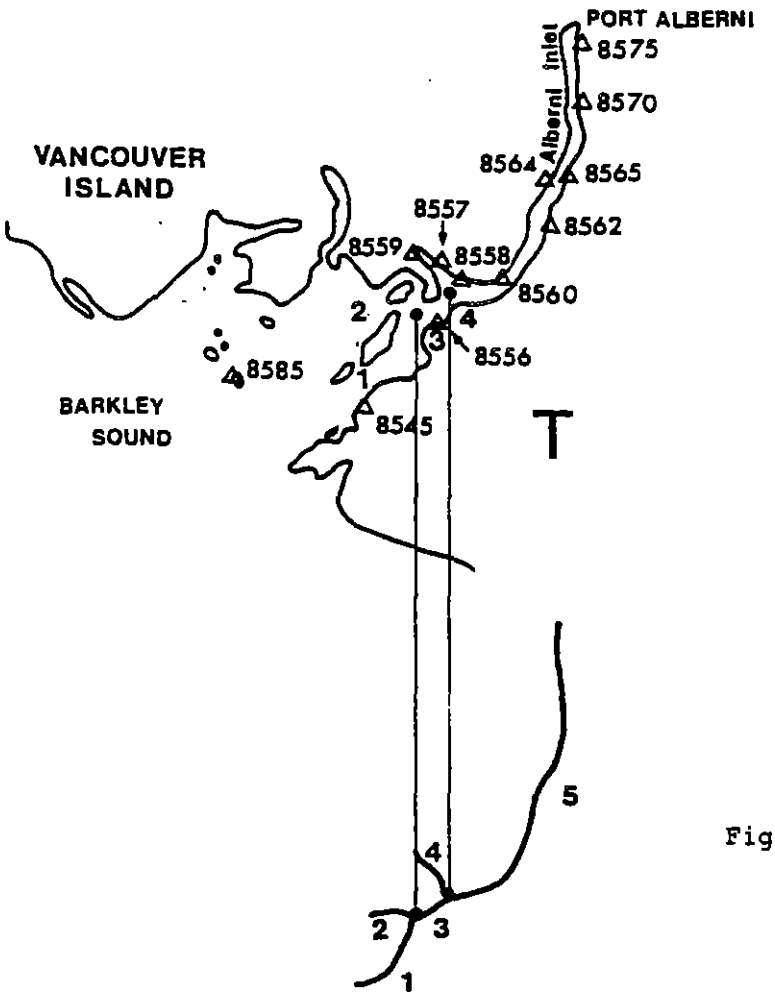

Fig. 5.10 Continued

where u_i^{n-1} is the water velocity from the previous time step (m/s)

u_i^{n+1} is the water velocity at the present time step (m/s)

C_i is the Chezy coefficient of friction ($m^{1/2}/s$)

Rearranging (5.11) and (5.12) with (5.13) yields explicit equations for Q and η:

$$Q_i^{n+1} = \frac{Q_i^{n-1}/(gA_i) - \frac{\Delta t}{\Delta x}(\eta_{i+1}^n - \eta_i^n)}{1/(gA_i) + 2\Delta t|Q_i^{n-1}|/(C_i^2 A_i^2 D_i)}$$

and

$$\eta_i^{n+1} = \eta_i^{n-1} - \frac{2\Delta t(Q_{i+1}^n - Q_{i-1}^n)}{S_i} \qquad (5.14)$$

where η is the surface elevation above mean sea level

Q is the flow rate (m^3/s)

A_i^n is the cross sectional area (m^2) at a Q point [$A_i^{n+1} = A_i^0 + W_i(\eta_{i-1}^n + \eta_{i+1}^n)/2$]

d^n is the depth (m) at a Q point [$d_i^n = d_i^0 + (\eta_{i-1}^n + \eta_{i+1}^n)/2$]

C_i is the Chezy friction coefficient at a Q point

S_i is the surface area (m^2) of a segment of the fjord branch between adjacent Q points ($2\Delta x$ in length).

At a node the mass balance equation yields the following finite difference expression for the surface elevation:

$$\eta_i^{n+1} = \eta_i^{n-1} - \frac{\Delta t}{S_i}\sum_{j=1}^{N_i} Q_{ij} \qquad (5.15)$$

where the subscript i refers to the ith node; N_i is the number of branches that terminate at that node; Q_{ij} is the transport at the node of the jth branch and S_i is the surface area of the node.

(a) Boundary Conditions

The open boundary conditions in the FJORD1D model consist of prescribed surface elevations at terminal nodes. In the tsunami simulations these were provided directly by the shelf model (C2D) as described in Section 5.2(c). In total, there were forty terminal nodes in the complete set of FJORD1D models.

All closed boundaries in FJORD1D are located at inlet heads. A condition of zero velocity is imposed at these points, and no mass loss is permitted. This results in complete reflection of the tsunami waves at the head.

Water depths were extracted from Canadian Hydrographic Charts and represent levels at lowest low water. Provision for adding a fixed offset to these values was included in FJORD1D so that the effect of higher tidal levels could be included. In each simulation an offset of 2.5 m was added to the base levels.

(b) Initial Conditions

All transports and elevations were set to zero to initialize the simulations, thus matching initial conditions in C2D over the shelf. Friction coefficients, input for each segment, were held at fixed values for the duration of the run.

6.0 MODEL VERIFICATION

Verification of computed elevations and velocities from the three numerical models consisted of three phases:

1. Preliminary testing - Basic tests were performed to prove the correctness of the finite difference schemes and boundary data for each model. Highly specific initial and boundary conditions were used to compare model output with known solutions.

2. Tidal Calibrations - These calibration runs were applied primarily to the inlet models, where relatively shallow depths result in water level predictions that are sensitive to the values assigned to the friction coefficients. Similar tests with the shelf model verified the overall correctness of the model geometry and bathymetry.

3. 1964 Alaskan Tsunami - Tide gauge data were compared with calculated wave heights in the simulation of the March 28, 1964 tsunami generated by an earthquake in Prince William Sound, Alaska.

6.1 Preliminary Testing

(a) The Deep Ocean Model

Tests were performed using radially symmetric bathymetry (Fig. 6.1) to verify that the solution of the Boussinesq equations in the absence of rotation is also radially symmetric. Failure of this condition to hold exactly could indicate errors in programming the finite difference equations. The results of the tests with the full Boussinesq equations confirmed that symmetry is preserved to the level of machine accuracy.

One-dimensional tests were performed to compare the solution of the Boussinesq equations with measurements made by Hammack (1973) of wave amplitude in a long narrow channel. Fig. 6.2 compares Hammack's measurements with results from the deep ocean model solved for an initial waveform in a long, narrow channel of uniform width and depth. Results are also presented (Fig. 6.3) for the case where the right-hand terms in the governing equations are omitted. In these two figures the horizontal axis is nondimensional time, while the vertical scale refers to the percentage change in either volume (marked V) or total energy (marked E) in the closed system. These figures show that volume is conserved while there is some energy dissipation.

The results of the simulation show good agreement with Hammack's measurements of wave amplitude made in a wave tank. Small time shifts have been introduced to align the measured and calculated wave peaks. This is made necessary by the presence of friction in the wave tank which tends to add a small phase shift (time delay). In all cases this shift represents less than 3% of the total elapsed time.

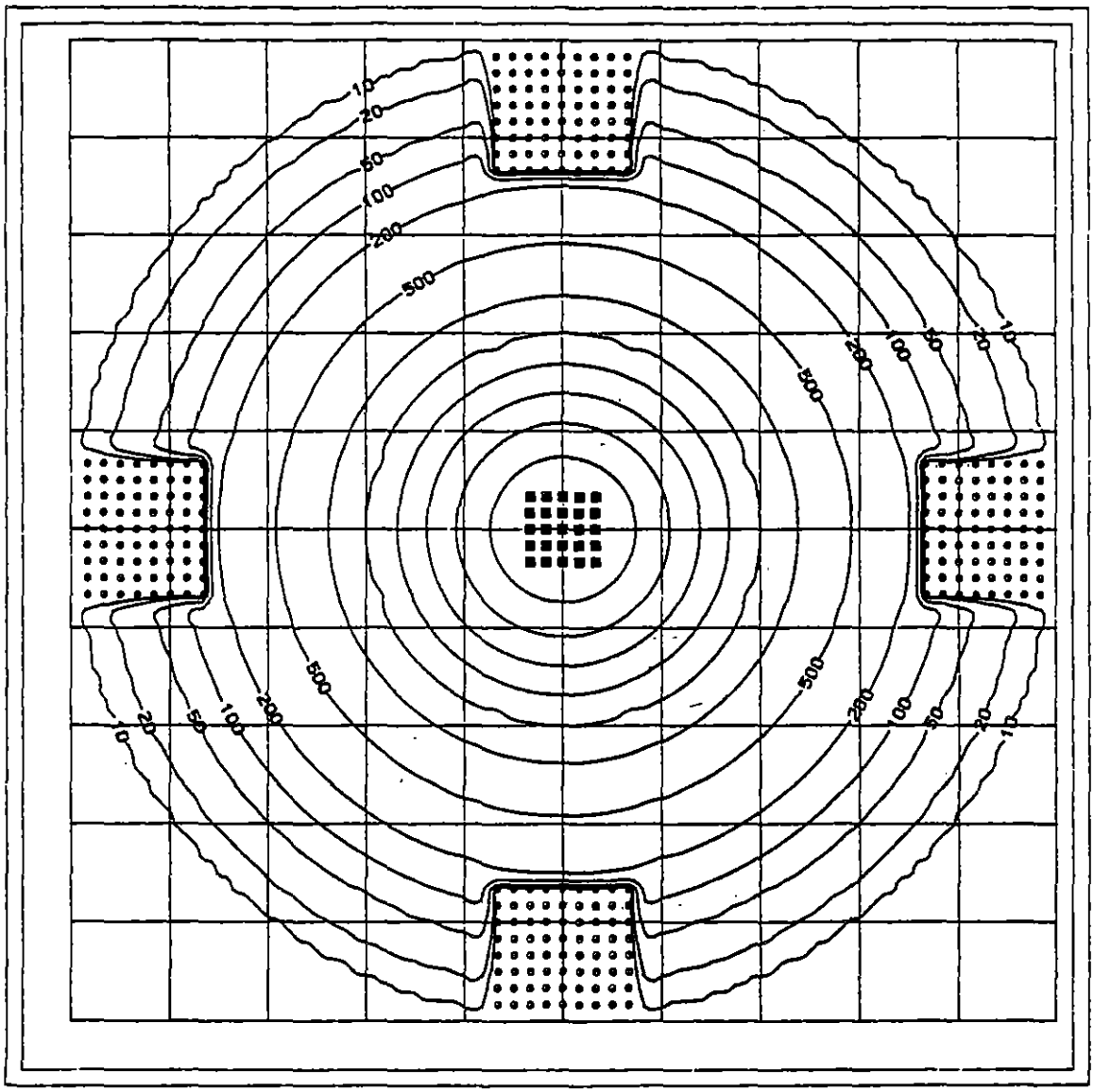

Fig 6.1 DOM model grid and bathymetry used to test preservation of symmetry and general correctness of coded finite difference schemes. Unlabelled contours are 500 m apart. Dots correspond to land, and indicate grid spacing used.

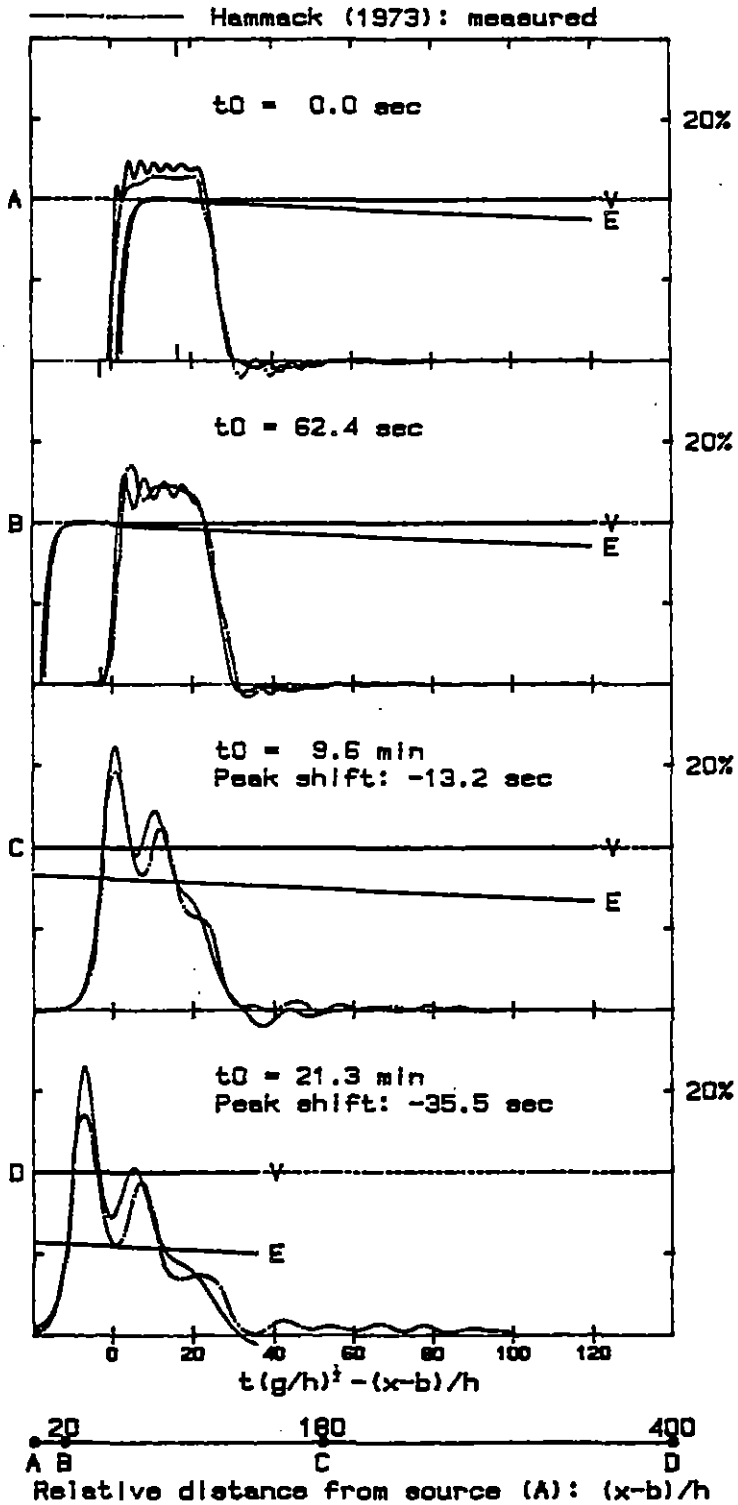

Fig. 6.2 A comparison between measured (dashed line) and deep-ocean model (solid line) elevations for the case of a channel of constant width and depth. The nonlinear dispersive terms have been retained in the DOM. The vertical axis gives the percentage change in the total volume (V) and energy (E) in the system.

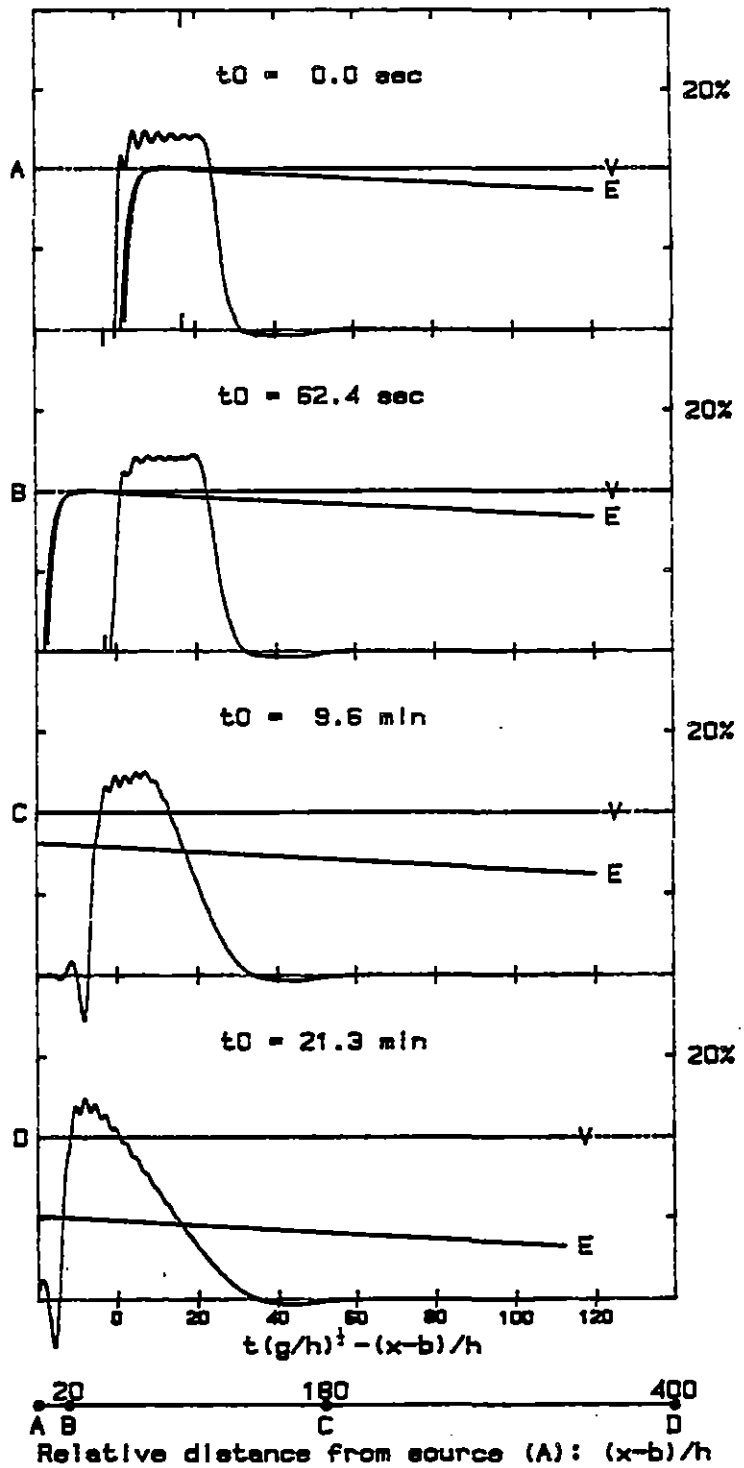

Fig. 6.3 A comparison between measured (dashed line) and deep-ocean model (solid line) elevations for the case of a channel of constant width and depth. The nonlinear dispersive terms have been omitted in the DOM. The vertical axis gives the percentage change in the total volume (V) and energy (E) in the system.

(b) The Shelf Model (C2D)

The shelf model did not undergo the same level of initial testing in this study as was done for the other two models. Basic code integrity for C2D and numerical characteristics of the scheme have been fully established in previous studies (Hodgins, 1977; Hodgins and Hodgins, 1986). The code has been shown to be accurate and reliable for tidal frequency waves and storm surges.

(c) The Inlet Model (FJORD1D)

Linear bottom friction was substituted for the quadratic friction term in (4.60) in order to compare FJORD1D calculated wave heights with a known analytical solution.

Assuming τ_H, the bottom stress per unit mass, to have the linear form

$$\tau_H = Hk_H u, \tag{6.1}$$

a solution to (4.59) and (4.60) using (6.1) with periodic forcing at the mouth of amplitude H and angular frequency is given by Ippen (1966) as

$$\eta(x,t) = \delta H e^{-\mu x} \cos(\omega t - kx), \tag{6.2}$$

$$u(x,t) = C_o e^{-\mu x} \frac{k_o}{\sqrt{\mu^2+k^2}} \cos(\omega t - kx + \alpha), \tag{6.3}$$

where definitions, and values of parameters used in (6.2) and (6.3) are listed separately in Table 6.1.

Equations (6.2) and (6.3) represent a damped, purely progressive wave. To simulate this solution with a model having a reflecting boundary condition it is necessary to have sufficient damping so that the wave amplitude at the closed boundary is negligible. The parameter values in Table 6.1 provide for an e-folding length of 382 km, and a total damping factor over the length of the modelled channel.

Fig. 6.4 compares the exact solution (dotted line) with the FJORD1D calculated solution for the case of linear friction and two formulations of the quadratic friction term, designated Type A and Type B. These correspond to equation (6.4) with k=0 for type A and k=1 for type B

$$\tau_H = |u_i^n| u_i^{n+k} \rho g / C_i^2 \tag{6.4}$$

Type A friction coresponds to the formulation used in subsequent model runs. The results show that the FJORD1D model accurately reproduces the analytical solution know for the case of linear bottom friction. They also indicate that the quadratic formulation of the bottom friction term results in more gradual damping of the wave form, and that there is little difference between the solutions produced by the two quadratic friction formulations.

Table 6.1

Parameter Definition and Values Used in Comparing the FJORD1D Numerical Solution to Equations (4.59) and (4.60) with the Exact Solution (6.2) and (6.3)

parameter	definition	value
ω	$2\pi/T$	1.45×10^{-4} s^{-1}
T	wave period	12 hours
C_o	$\sqrt{gH}$	9.40 m/s
k_o	ω/C_o	1.47×10^{-7} cm^{-1}
k	$k_o(1-\beta^2)^{-\frac{1}{2}}$	1.57×10^{-7} cm^{-1}
μ	$k\beta$	2.62×10^{-8} cm^{-1}
β	$(-w+\sqrt{\omega^2+k_H^2})/k_H$	0.168
α	$\tan^{-1}(\mu/k)$	9.49°
δ		10^{-4}
k_H	friction coefficient	4×10^{-5}
C_i	Chezy coefficient	3.4

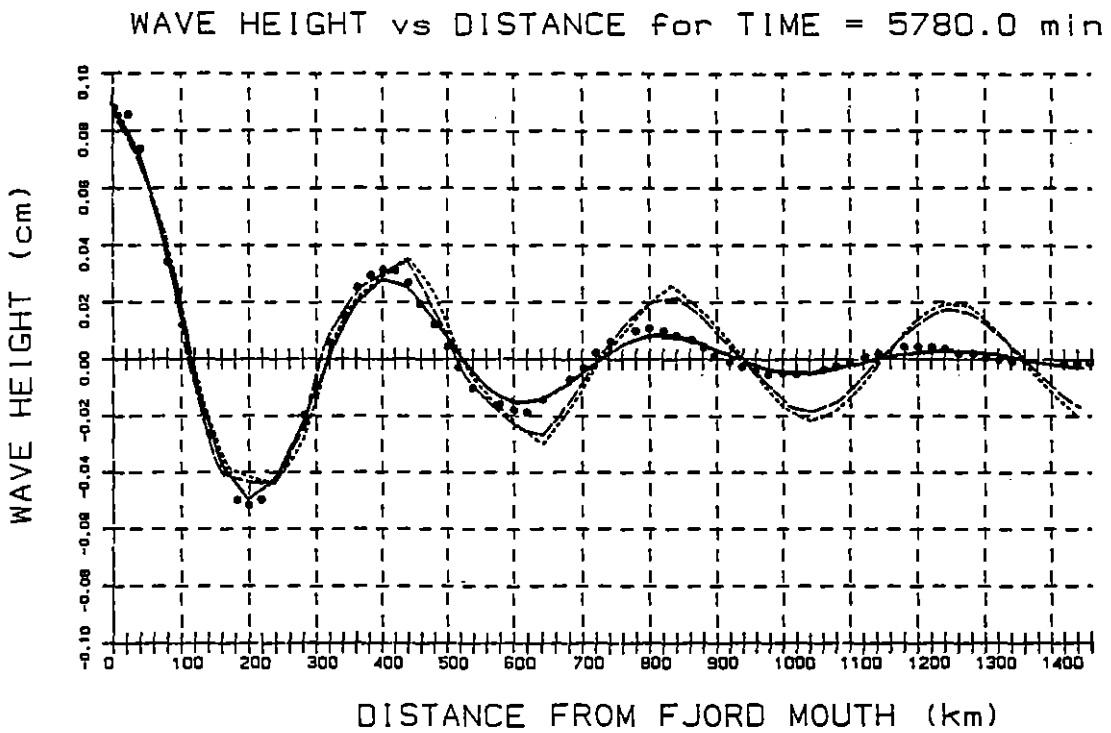

LEGEND

• • • • • Analytical Solution
——— Linear Friction
..... Quadratic Friction Type A (C = 3.4)
_ _ _ _ _ Quadratic Friction Type B (C = 3.4)

Fig. 6.4 A comparison between an analytical solution for strongly damped wave propagation in a flat-bottomed, rectangular channel with linear friction, and numerical model results using linear friction and two types of quadratic friction.

6.2 Tidal Calibrations

Simulations of forced tidal response were performed with both the C2D and FJORD1D models. Time series of surface displacements were provided at each open boundary point in the two models. These were synthesized from harmonic constants (tidal constituent amplitudes and phases) obtained from either the Canadian Hydrographic Service or from a global ocean tidal model developed and run by the U.S. Naval Surface Weapons Center (NSWC) (Schwiderski and Szeto, 1981). The constants from either source were combined to generate elevation time series using

$$\eta(t) = \sum_{j=1}^{n} f_j(t_o) A_j \cos\left\{2\pi[\theta_j(t_o)+\delta_j(t_o)+\sigma_j(t-t_o)-g_j]\right\} \qquad (6.5)$$

where t_o is a reference time, σ_j the constituent frequency, f_j the nodal amplitude correction, δ_j the nodal phase correction, and θ_j the astronomical phase angle. The values A_j and g_j are the corrected amplitude and phase angle for the analyzed constituent. g_j is commonly referred to as the Greenwich phase lag and is the phase angle tabulated in lists of harmonic constants. In the case of the shelf model, the Schwiderski results were used. These consist of 11 harmonic constants for points located at the vertices of a regular grid with a one degree spacing covering all the world's oceans. For simplicity only two constituents were used to generate the boundary elevations. Elevations were calculated using (6.5) and bilinearly interpolated onto the open boundary points of the shelf model. For all inlet models (except system P) the nearest coastal tide gauge station was used to provide harmonic constants for use in reconstructing time series. System P used harmonic constants from the NSWC model because of the lack of an open boundary tide gauge station.

These tidal simulations provided an opportunity to verify the overall correctness of the shelf model bathymetry and to set dissipation levels in the inlet models by adjustment of bottom friction coefficients until calculated phases and amplitudes of the tidal constituents were in good agreement with observations.

(a) The Shelf Model

The C2D model has been carefully calibrated in the Restigouche Estuary at the head of the Baie de Chaleur, N.B., (Hodgins and Hodgins, 1986) where the boundary conditions were accurately specified. In that application the calibration was carried out for current speed and direction at three locations, in addition to water level. The use of currents generally leads to a more accurate specification of bottom friction than calibrating against water level variations alone, and a more critical test of model performance. Verification showed that the model achieved accuracies of 10% to 15% in current speed, and reproduced the measured changes in speed and direction over many tidal cycles well. The model was judged sufficiently accurate in that application that the predicted currents could be used to drive a mud transport model.

In order to provide confidence in the British Columbia shelf set-up--specifically in the landform and bathymetry input--a 5-day tidal simulation was carried out. The model results were harmonically analyzed for comparison with tide gauge station data. For this test, two tidal frequencies were used, the K1 and M2 constituents. These frequencies correspond with the major diurnal and semi-diurnal constituents. The test run was limited to 8 days because of the large size of the model grid and the fine 2.5-km resolution, which result in very long run times for each tidal cycle. The first three days were discarded as these allow initialization transients to propagate out of the solution domain, leaving 5 days for analysis.

The predicted and observed K1 and M2 amplitudes and phases at 10 coastal gauges (Fig. 6.5) are compared in Table 6.2. Confidence in the harmonic constituents calculated from the model output is low because the 5-day time-series is too short for good resolution; in absolute terms, accuracies would not likely exceed 10% in amplitude or 15 degrees of phase. The comparison shows that the model generally reproduces the measured variations from south to north. The greatest error is found in the M2 constituent at the northern gauges 9315 and 9940 in Dixon Entrance, and at 8805 near Cape Caution, where the model tends to overpredict the amplitude. This run was made decoupled from the inlet models, which goes some way in explaining this tendency to overpredict along the coast.

It is expected that better tidal predictions would be obtained through use of the coupled C2D-FJORD1D system model, full specification of boundary constituents, and longer simulation times. Nevertheless, these tidal results confirm that no major errors have been introduced into the model through the landform and bathymetry files, and that the numerical scheme is suitable for tsunami simulations forced along the deep ocean boundaries.

(b) The Inlet Models

The effect of bottom friction in the inlets is more pronounced than on the shelf or in the deep ocean (where friction is often ignored) because of the presence of constrictions and shallower depths. Frictional drag is enhanced at these locations, and hence energy dissipation is increased above normal levels in other reaches of the inlet. This results in decreases in wave amplitude and propagation speed. This dissipation of energy is reflected in the values for constituent amplitudes and phases calculated by harmonic analysis of surface elevation time series measured at tide gauge stations.

Tidal simulations were undertaken in order to adjust friction coefficients at these locations, and thereby match the modelled and measured responses of the inlets. The response is defined to be the tidal constituent amplitudes and phases calculated from a harmonic analysis of model time series.

Harmonic constants (amplitudes and phases) at tide gauge stations located near the open boundary nodes of the inlet models were used to reconstruct time series of surface elevations. These were used to drive the inlet models for 30 day simulations. the major diurnal (K1) and semi-diurnal (M2,S2) constituents were included in the boundary time series.

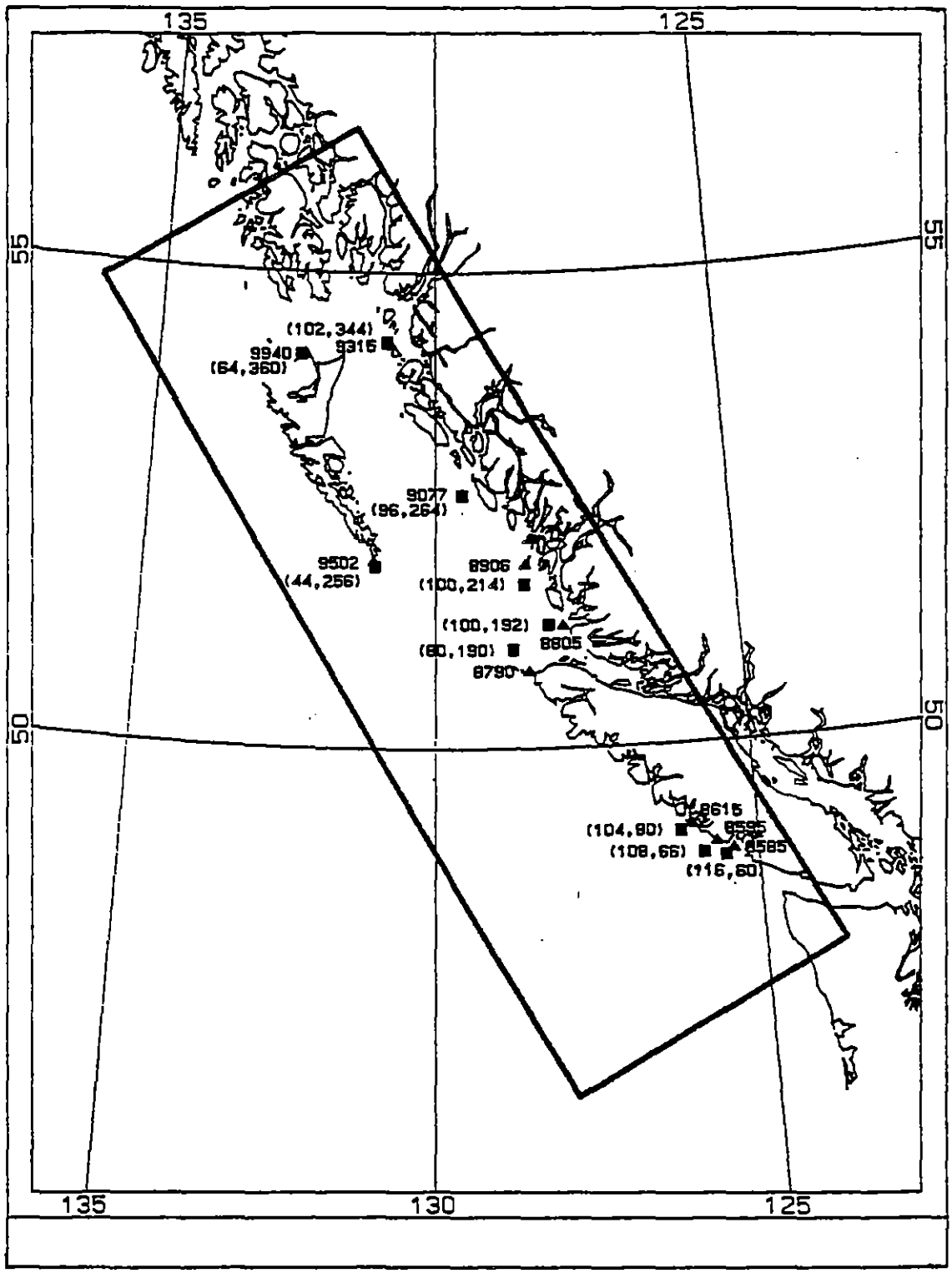

Fig. 6.5 Locations of tide gauge stations (▲) and C2D model grid locations (■) used in the comparison of observed and simulated tidal elevations.

Table 6.2

Harmonic Constants for the K1 and M2 Tidal Constituents at Selected Tide Gauges and C2D Model Grid Locations

Tide Station	C2D Col	C2D Row	K1 Constituent Amplitude (m) Obs	K1 Amplitude (m) C2D	K1 Phase (deg) Obs	K1 Phase (deg) C2D	M2 Constituent Amplitude (m) Obs	M2 Amplitude (m) C2D	M2 Phase (deg) Obs	M2 Phase (deg) C2D
8585	116	60	.39	.21	125	121	.94	.97	3	17
8595	108	66	.38	.21	125	115	.93	.93	4	17
8615	104	80	.39	.20	121	101	.99	.97	8	17
8790	80	190	.44	.40	126	102	1.08	1.19	12	18
8805	100	192	.45	.42	132	106	1.18	1.47	17	26
8906	100	214	.44	.40	126	101	1.08	1.19	12	18
9077	96	264	.45	.44	134	112	1.38	1.57	23	31
9315	102	344	.49	.53	140	125	1.84	2.60	35	56
9502	44	256	.48	.42	138	110	1.05	1.07	32	30
9940	64	360	.46	.45	138	123	1.47	1.74	33	42

Time series were extracted from the model runs at grid points located nearest to tide gauge stations. These were then harmonically analysed and the results for the M2 and K1 constituents plotted against measurements.

Fig. 6.6 to 6.8 present the best fit of the modelled surface elevations to observations obtained by adjusting the bottom friction coefficients. Each symbol corresponds to a different inlet system. Systems not represented were omitted because of the lack of tide gauge data. Panel (a) in each figure shows measured phases plotted against modelled phases. Similarly, panel (b) presents observed and modelled amplitudes, while panel (c) combines the results for both amplitudes and phases. In this figure, differences between observed and modelled amplitudes and phases are plotted against each other. Points closer to the centre represent superior agreement with observed values.

In general, good agreement between modelled and observed amplitudes and phases is found for all three constituents. Some systems exhibit systematic discrepancies that suggest that the values for a constituent amplitude or phase used to generate the boundary condition may not be correct. For example, system K exhibits a consistently smaller amplitude for the K1 constituent (Fig. 6.6(b)). The close grouping of the points suggests that there is an offset in the model amplitude that most likely originates with the boundary data. Similarly, for system P the model phases for K1 are consistently smaller than observed. Again, this is most likely due to the boundary conditions. In general, where points are closely clustered, or fall along a straight line that is parallel to the indicated diagonal, agreement is considered good.

6.3 The 1964 Alaskan Tsunami

The March 28 earthquake presents an excellent opportunity to verify the integrated DOM-C2D-FJORD1D model system using a well documented tsunamigenic event. The most critical component of the simulation--final bottom displacements in the generation zone--are known as well for this earthquake as for any other. Plafker (1969) has constructed contours of final bottom displacements based on surveys of the coastline before and after the earthquake. These were digitized and used to generate displacement values at DOM grid locations in the generation zone (Fig. 6.9).

Table 3.1 lists the tide gauge stations and corresponding models used in the comparison. Fig. 6.10 presents the modelled elevations together with the observed tsunami wave as extracted from tide gauge records. The time of arrival of the initial model wave has been adjusted to synchronize it with the observed wave. The size of this adjustment is indicated on each panel. These time differences average about 6% of the total travel time for the initial wave, and are likely due, for the most part, to differences in the locations of the tide gauge and model output points, and to small errors in specifying arrival times.

Within the constraints imposed on the solutions examined in Fig. 6.10, produced by uncertainties in the initial bottom displacement model, the following conclusions may be drawn: (1) In all cases the initial measured wave had a positive elevation, which varied in amplitude from 5 to 10 cm at Sweeper Cove and Unalaska, to 1.0 to 1.5 m at the other gauge locations, and

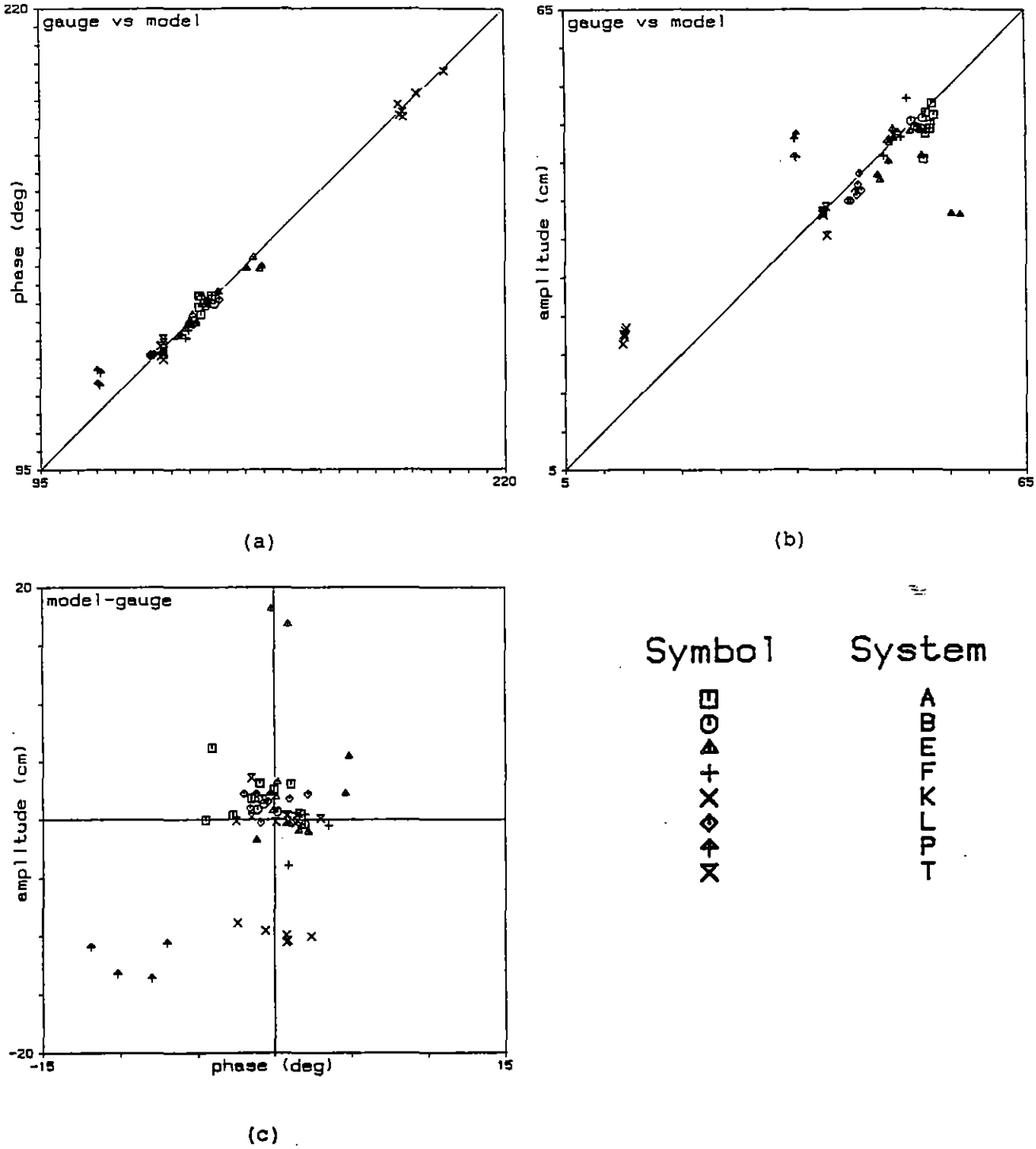

Fig. 6.6 A comparison of K1 tidal constituent amplitudes and phases extracted from measured (gauge) and simulated (model) elevation time-series in the FJORD1D model. (a) phase (gauge versus model); (b) amplitude (gauge versus model); (c) amplitude versus phase (model-gauge).

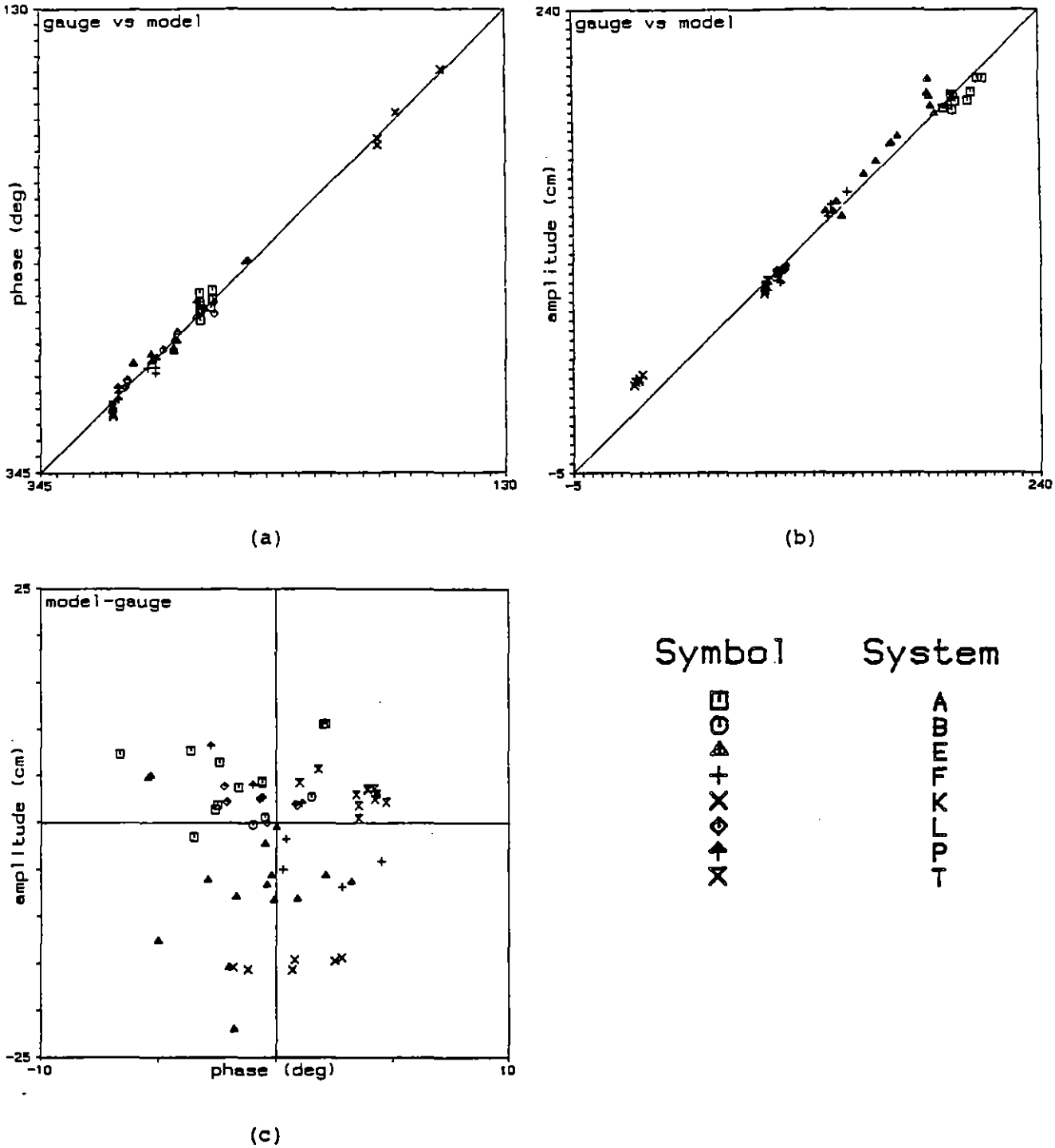

Fig. 6.7 A comparison of M2 tidal constituent amplitudes and phases extracted from measured (gauge) and simulated (model) elevation time-series in the FJORD1D model. (a) phase (gauge versus model); (b) amplitude (gauge versus model); (c) amplitude versus phase (model-gauge).

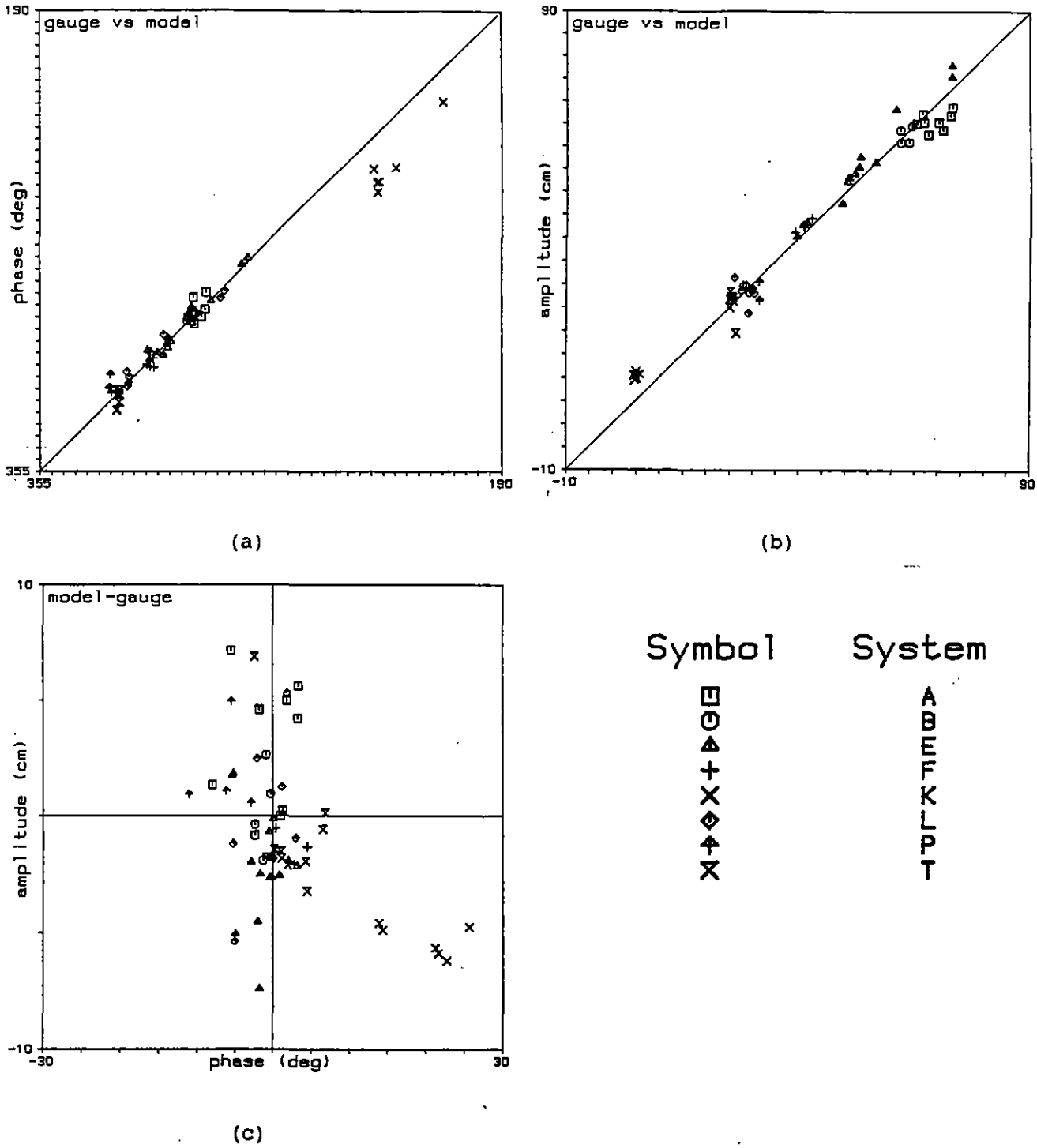

Fig. 6.8 A comparison of S2 tidal constituent amplitudes and phases extracted from measured (gauge) and simulated (model) elevation time-series in the FJORD1D model. (a) phase (gauge versus model); (b) amplitude (gauge versus model); (c) amplitude versus phase (model-gauge).

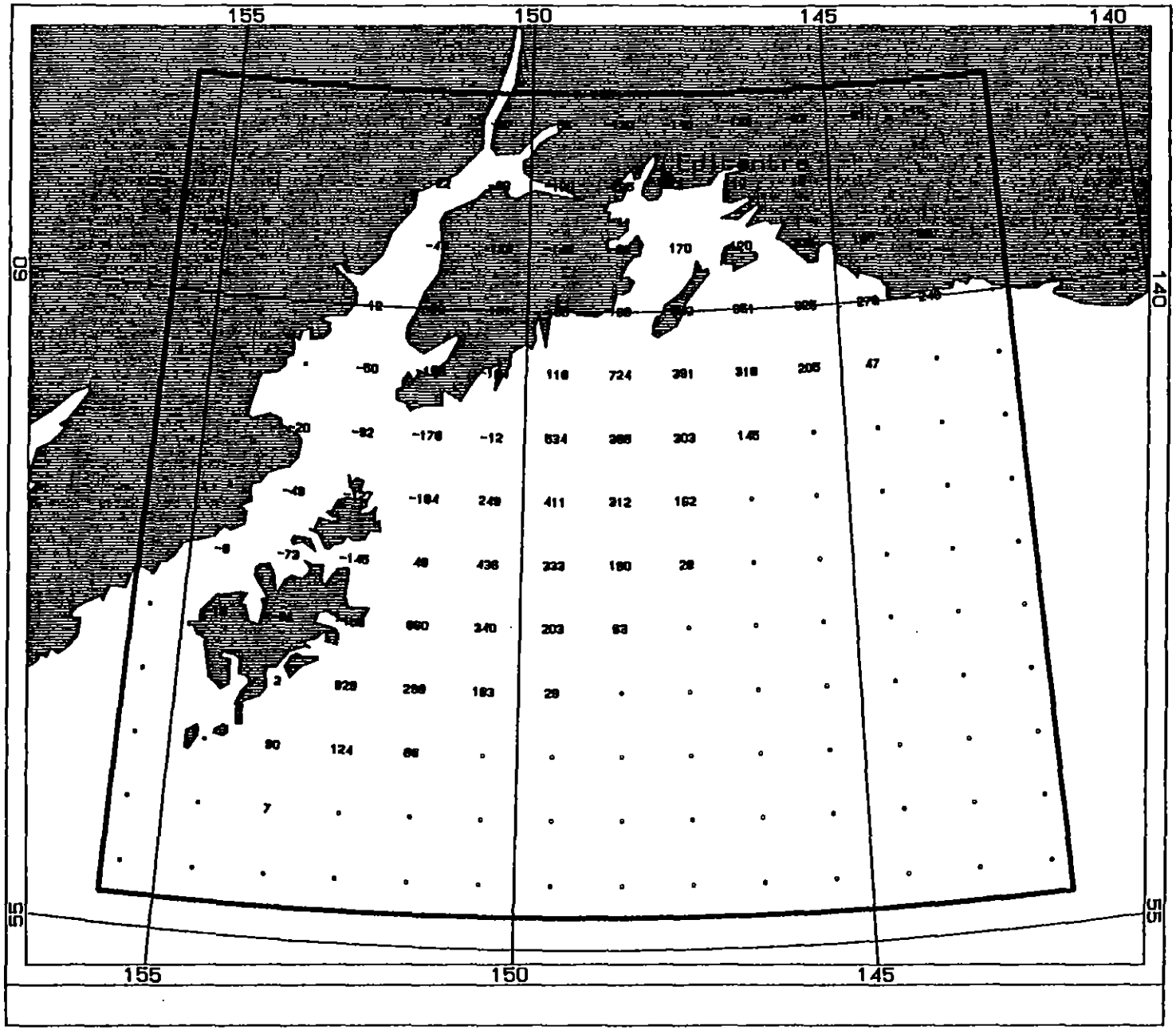

Fig. 6.9 Generation zone (bold rectangle) and bottom displacements (cm) used to simulate the 1964

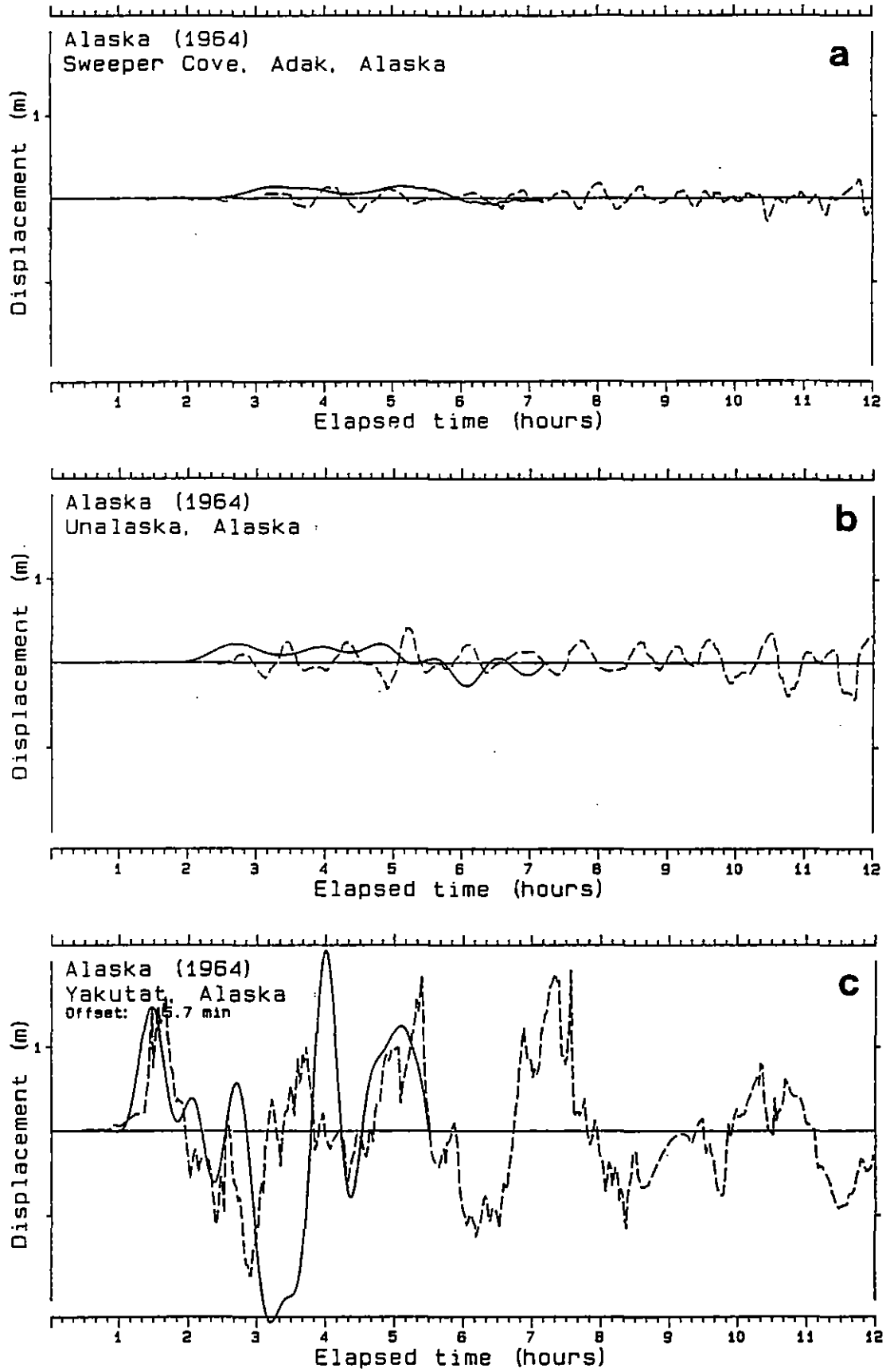

Fig. 6.10 Observed (dashed) and modelled (solid) tsunami wave heights. Station locations and model source are given in Table 3.1.

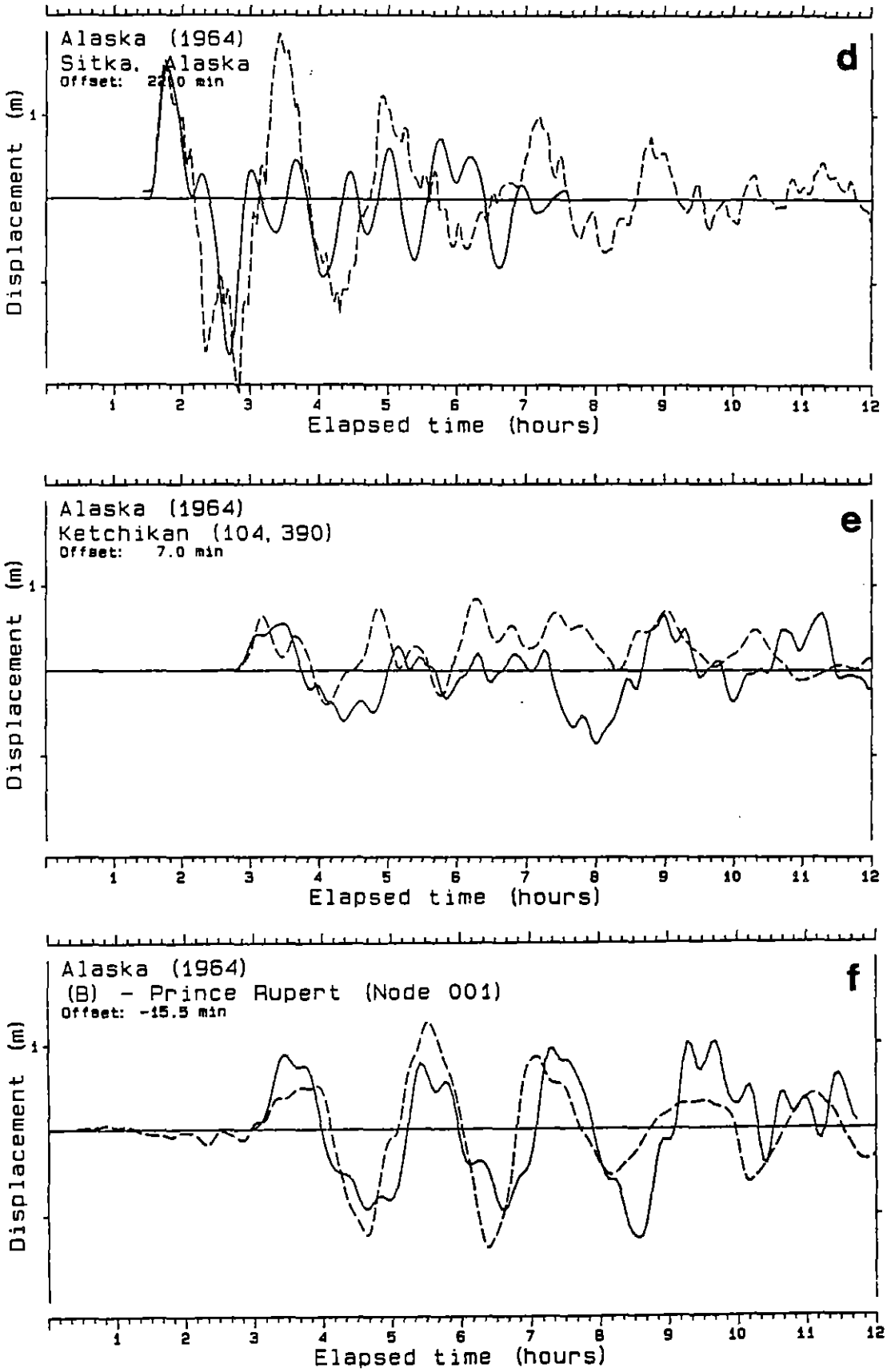

Fig. 6.10 Continued.

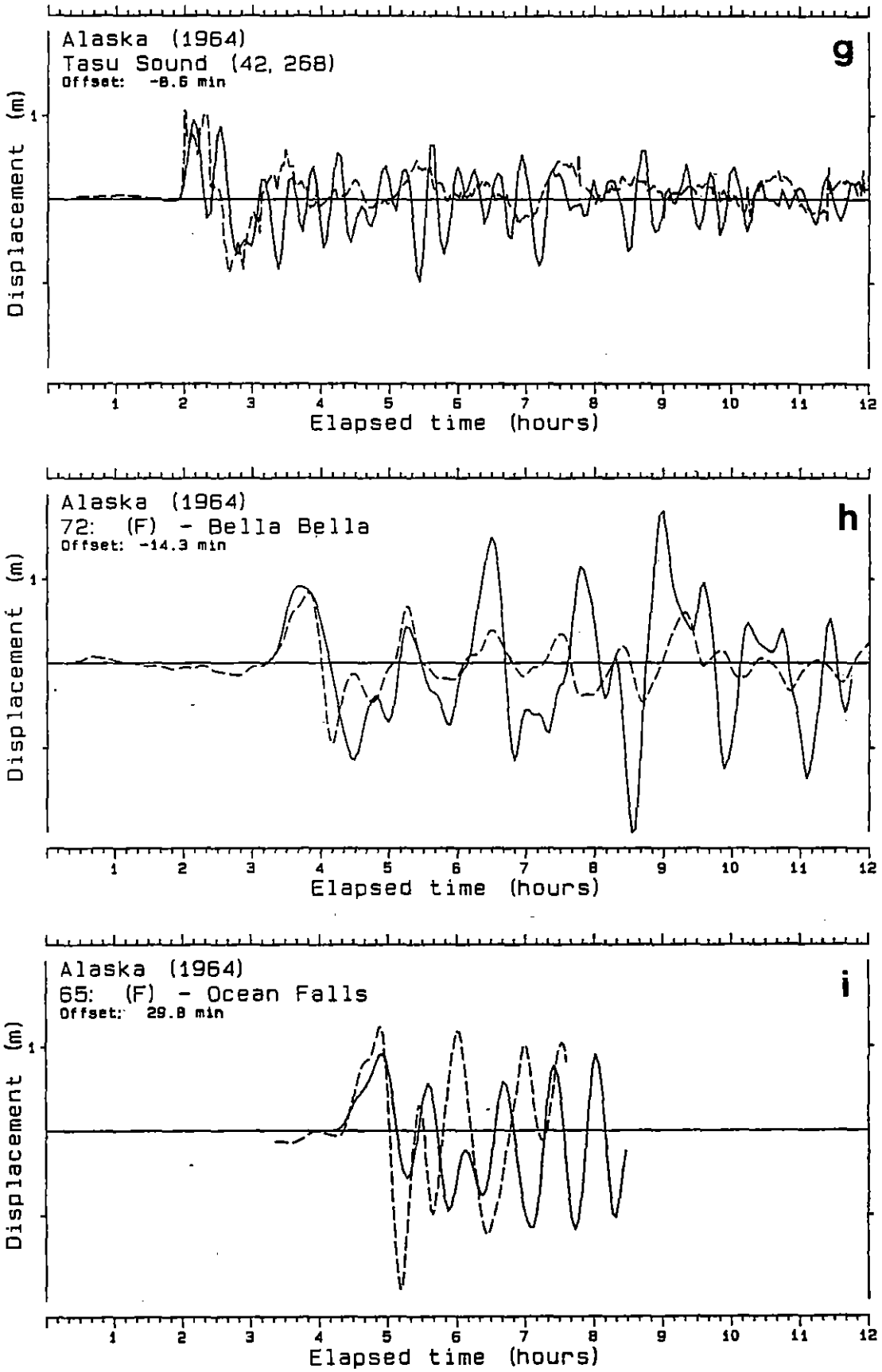

Fig. 6.10 Continued.

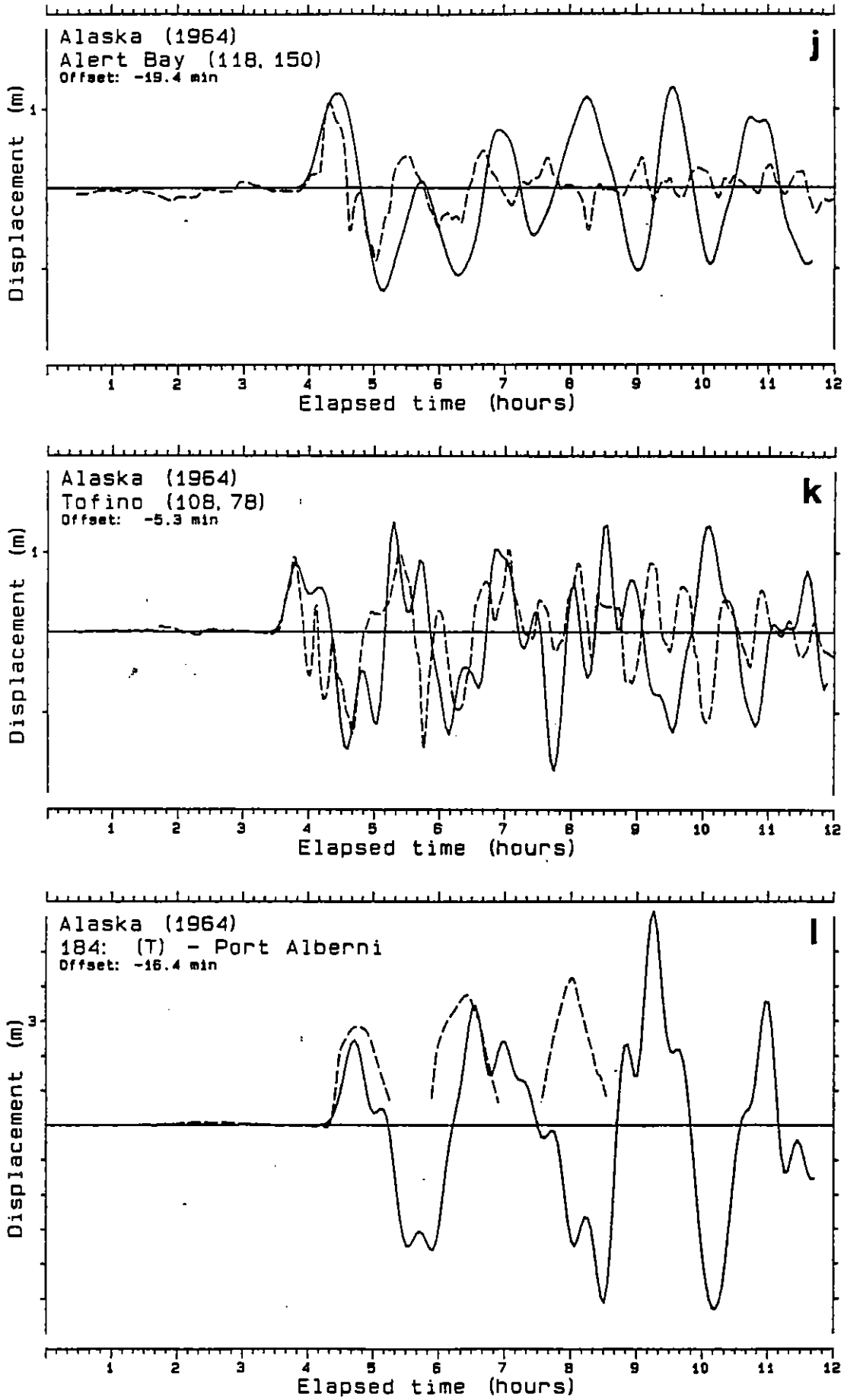

Fig. 6.10 Continued.

to approximately 3 m at Port Alberni. At each location the numerical model reproduced the elevations well. In many locations (Sitka, Ketchikan, Yakutat, Prince Rupert, Alert Bay, Tofino, Tasu Sound and Bella Bella) the model also provided a good estimate of the shape and timing of the following trough. From these results we conclude that the numerical models provide a reliable simulation for the magnitude and shape of the leading wave form.

(2) The degree to which second and subsequent wave forms predicted by the model reproduced the measurements varies depending upon location. Good results were obtained at Prince Rupert and Yakutat; reasonable agreement was found at Tofino. At the other gauge sites (e.g. Tasu Sound) the numerical model results contain moderate amplitude waves at frequencies higher than the incoming tsunami. These are interpreted as reflections within the model produced by the boundary conditions along the coast and at the heads of the inlets. These reflections occur in nature--they are evident in the measured waves at Tofino and Ocean Falls, for example--but are difficult to reproduce precisely in the model at the resolution and boundary treatment adopted here. Nevertheless, if we examine the envelopes of positive and negative amplitudes (crest heights and trough depths around mean water level) the worst conditions are predicted to within an accuracy of approximately 50%, and often much better. Thus we conclude that the model is capable of identifying source regions leading to worst conditions along the coast, of identifying the critical inlet areas in terms of inundation levels, and of providing guidance on expected maximum tsunami water levels and currents. (An overall accuracy of the order of 50% for the model offers a substantial improvement in confidence over conventional statistical methods based on extrapolating measured tsunami levels, or levels derived from earthquake magnitude (e.g. Comer, 1980). In the statistical approaches uncertainty is introduced through the very small number of available observations, or the error of converting between magnitude and tsunami wave amplitude, and through modifying the extreme values at one location into the site of interest at a second location).

The simulation at Port Alberni shows that the first wave is modelled well, but therafter the predicted wave lags the measured wave. The modelled third wave has the largest amplitude (6 m); observations (Wigen and White, 1964) suggest that the third wave was, in fact, the highest at about 4.2 m above the tidal water level. However, the modelled wave lags observations by about one-half a wave period (1 1/4 h). Wigen and White (1964) recognize that the Port Alberni observations are quite imprecise since the gauge at the townsite had broken and these high water values are a synthesis made up from data collected up the Somass River and from eye witness accounts at the town.

The differences in height and timing between the modelled and observed data reflect the fact that Alberni Inlet is nearly resonant with the initial wave (100 to 110 minute period), and the treatment of the reflecting boundary conditions at Port Alberni. Modelled water levels at the head of the inlet could be improved by incorporating a high-resolution model of the flood-dry area in the Somass River valley that allows the tsunami to dissipate some energy by inundating the surrounding land.

7.0 TSUNAMI SIMULATIONS

7.1 Source Region Specifications

Simulations were performed for tsunamis generated at four seismically active regions (Fig. 1.1). Specific locations for each earthquake were selected based on the occurrence of previous great earthquakes or, in the case of the Shumagin Gap, on the hypothesis that a strong earthquake is likely to occur within a few decades. The locations of each earthquake epicentre shown in Fig. 1.1 are provided in Table 7.1.

The simulation results are presented in three ways. First, the behaviour of the tsunami wave field along the outer coast is illustrated in series of contoured water level charts. These charts show how the tsunami levels and currents are modified as the waves cross the continental shelf and enter several prominent inlets. They also illustrate the differences in wave behaviour produced by the different source regions. Second, maximum water levels and currents are tabulated for 185 key locations in British Columbia. These results show which areas are sensitive to tsunamis, and the effects of wave directionality on maximum wave levels at these locations. Finally, time-series graphs of water level variation at 39 special points are discussed. These graphs illustrate the nature of the tsunamis from each source region.

(a) Alaska: Prince William Sound

This is the site of the great earthquake of March 28, 1964 that devastated large parts of Alaska and generated a series of tsunamis that caused damage throughout the Pacific Rim. The mechanism of this earthquake has been studied extensively and it provides the best data on ocean floor displacements. These were determined by Plafker (1969) and form the basis of this simulation. Fig. 7.1 shows contours of final bottom displacements together with values interpolated from these onto the DOM grid (0.5 degree resolution).

Two simulations, denoted by numbers 1a and 1b in Table 7.1, were performed for this generation zone. The first used the bottom displacements as interpolated from measurements. The second set of displacements, 25% greater than the measurments, was used to simulate an extremely large tsunamigenic earthquake and to examine the effect of a known increase in amplitude of bottom motions on the resulting tsunami.

(b) Chile

The bottom displacements used for this simulation were derived from Plafker and Savage (1970) for the 1960 tsunami. This event was selected as a representative large earthquake originating from this area. Fig. 7.2 shows the contours of bottom displacement taken from Plafker and Savage together with values interpolated onto grid points and used in the generation phase of the simulation.

Table 7.1

Locations of Earthquake Epicentres Used for Tsunami Simulations

Number	Longitude	Latitude	Region
1a	147°43.8'W	61°02.4'N	Alaska - Prince William Sound
1b	147°43.8'W	61°02.4'N	Alaska - Prince William Sound
2	74°30.0'W	39°00.0'S	Chile
3	162°00.0'W	54°00.0'N	Shumagin Gap
4	200°24.0'W	52°48.0'N	Kamchatka

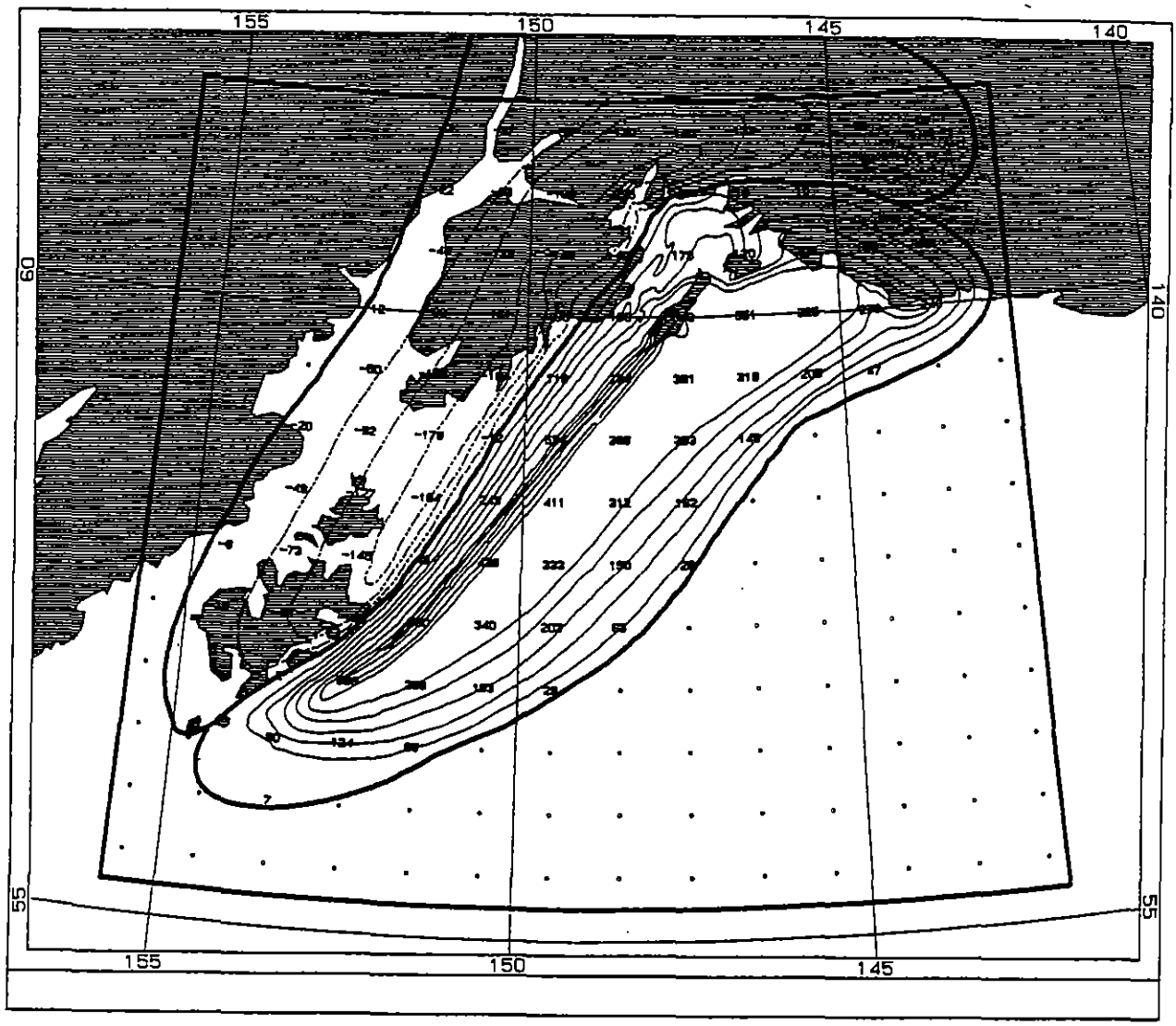

Fig. 7.1 Tsunami generation region for 1964 Alaska earthquake. Contours and numbers represent final bottom displacements (in cm). Dashed lines indicate downthrust; solid lines represent upthrust; and the bold line corresponds to no vertical movement. Contours were digitized from Plafker (1969).

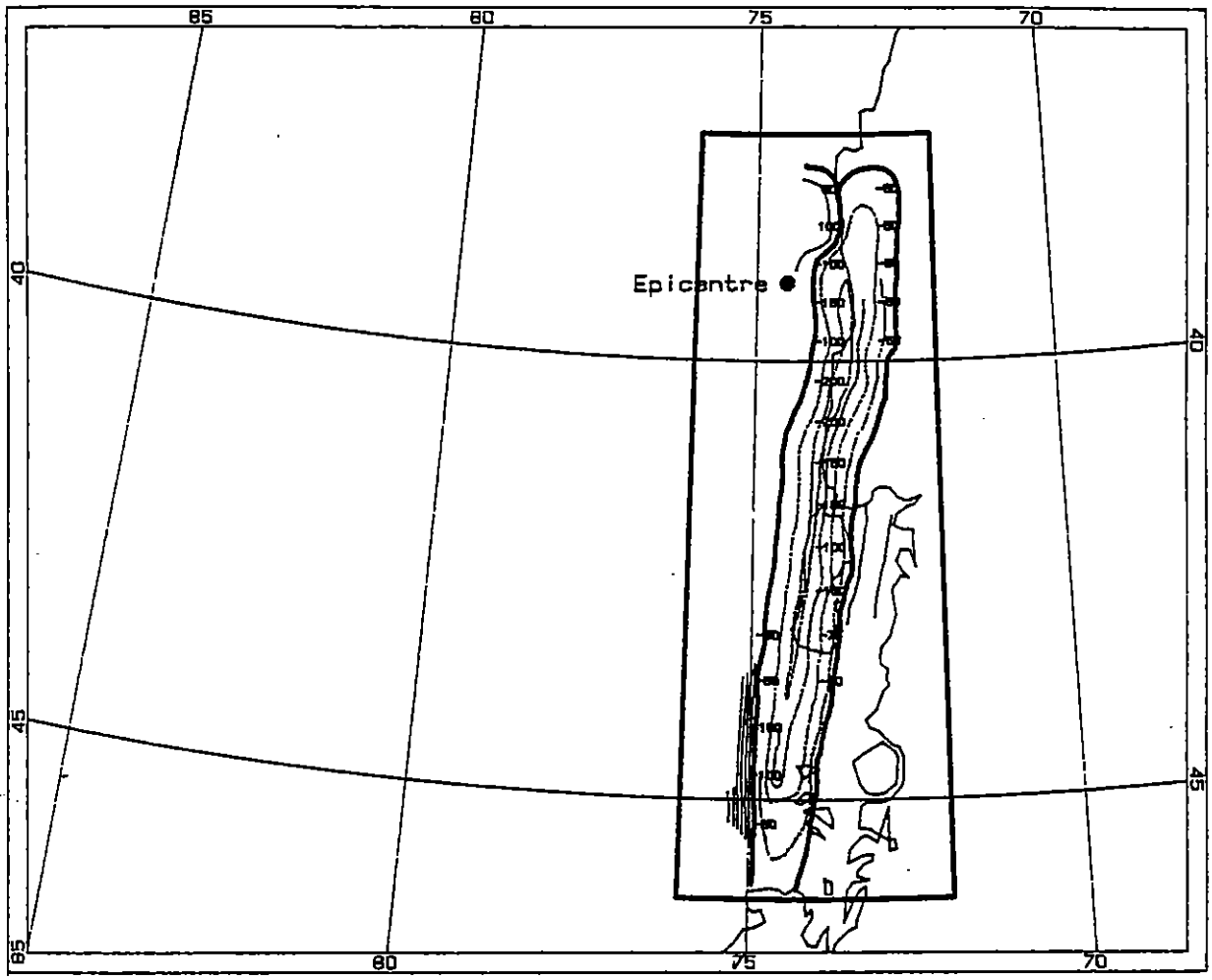

Fig. 7.2 Tsunami generation region for 1960 Chilean earthquake. Contours and numbers represent final bottom displacements (in cm). Dashed lines indicate downthrust; solid lines represent upthrust; and the bold line corresponds to no vertical movement. Contours were digitized from Plafker and Savage (1970).

(c) Shumagin Gap

In a detailed discussion of the seismic potential of the Shumagin Gap, Davies et al. (1981) identified an area near 52°N, 160°W that has not had a major rupture since at least 1900. Adjacent areas are also at possible risk of rupturing should a major earthquake occur in this seismic gap. Fig. 7.3 shows the area that has been used to simulate a major tsunamigenic earthquake in this part of the Aleutian chain. The bottom displacements correspond to a hypothetical maximum upthrust of 10 m. The total volume of water displaced by this final seabed surface is the greatest of all five simulations.

(d) Kamchatka

The final generation zone (Fig. 7.4) was selected to be off the east coast of Kamchatka where, in 1952, a magnitude 8.3 earthquake generated a large tsunami. This site was selected as a representative location for a large tsunamigenic earthquake originating from the northwest Pacific.

The displacement fields for the Shumagin Gap and Kamchatka were specified as regions having an elliptical plan view, with the orientation of the major axis of each ellipse selected to align approximately with the local fault zone. Displacements along lines parallel to the minor axis (i.e., perpendicular to the fault) follow a prescribed form, which was based on the displacement field for the 1964 Alaska earthquake (Plafker, 1969).

The elliptical bottom displacement regions were defined by two focii and a width (length of the minor axis). Along any segment parallel to the minor axis the vertical displacement was specified at 20 equally-spaced locations (Table 7.2). Point 1 corresponds to the landward edge of the ellipse, while point 20 corresponds to the seaward edge.

The parameters for each of the four displacement fields are summarized in Table 7.3. Surface areas reflect the region over which any nonzero displacement takes place. Volumes are calculated using the absolute value of each displacement multiplied by the area of the corresponding DOM grid element.

7.2 Key Output Locations

At 185 locations along the coast of British Columbia (Table 7.4), vulnerable to inundation by tsunamis, simulated water levels and currents have been calculated. These locations have been compiled by consulting hydrographic charts and the British Columbia atlas. The selection criterion was the presence of, or potential for, human activity at each site. Townsites, Indian Reserves, log booming grounds, mill sites, wharves, and parkland are some of the centres of such activity that have been included in the list. The branch and segment number (Br/Seg) or node from the fjord model which is closest to each site is included in the table. These numbers refer back to Fig. 5.10 which shows each of the modelled inlet systems together with node and branch numbers.

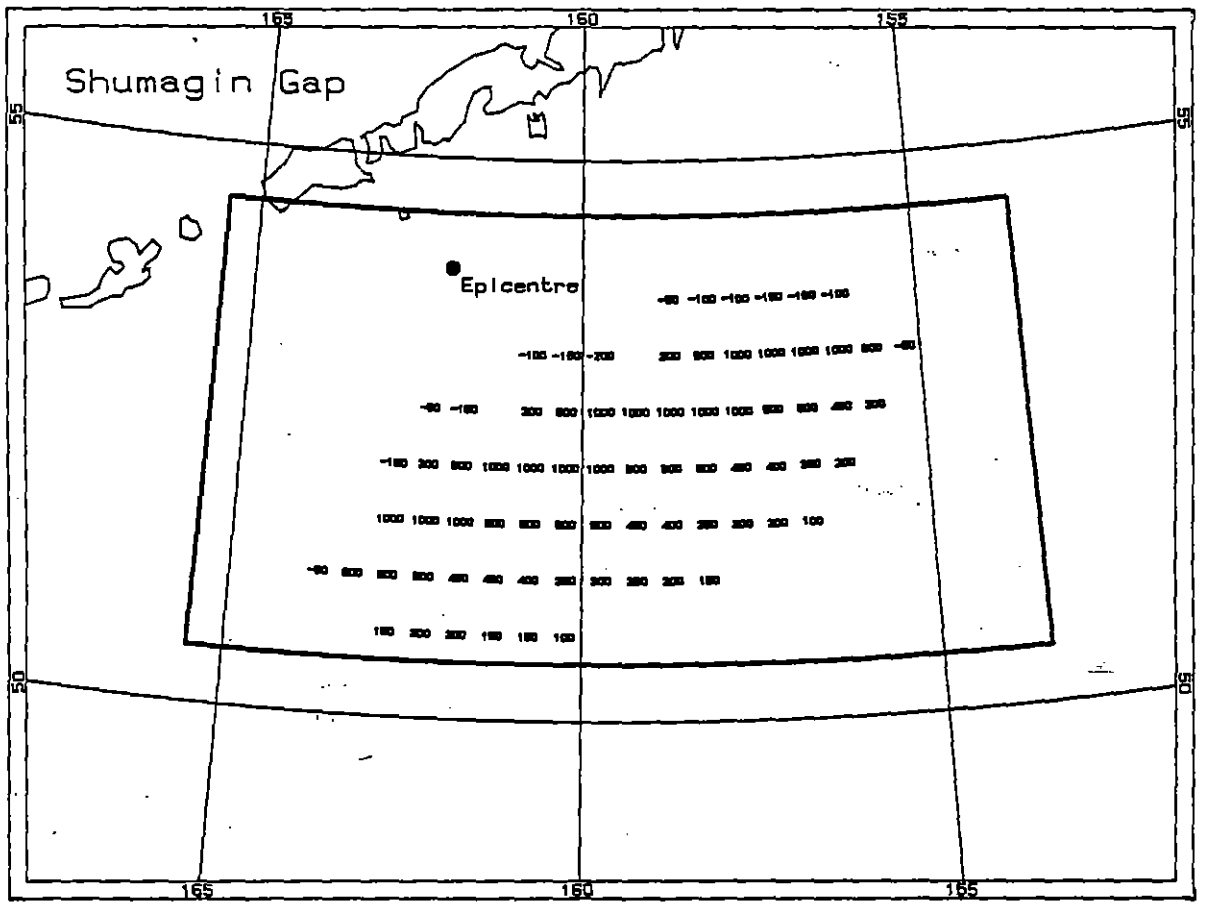

Fig. 7.3 Tsunami generation region for hypothetical earthquake in the Shumagin Gap area of the Aleutian Islands. Values correspond to final bottom displacements (cm).

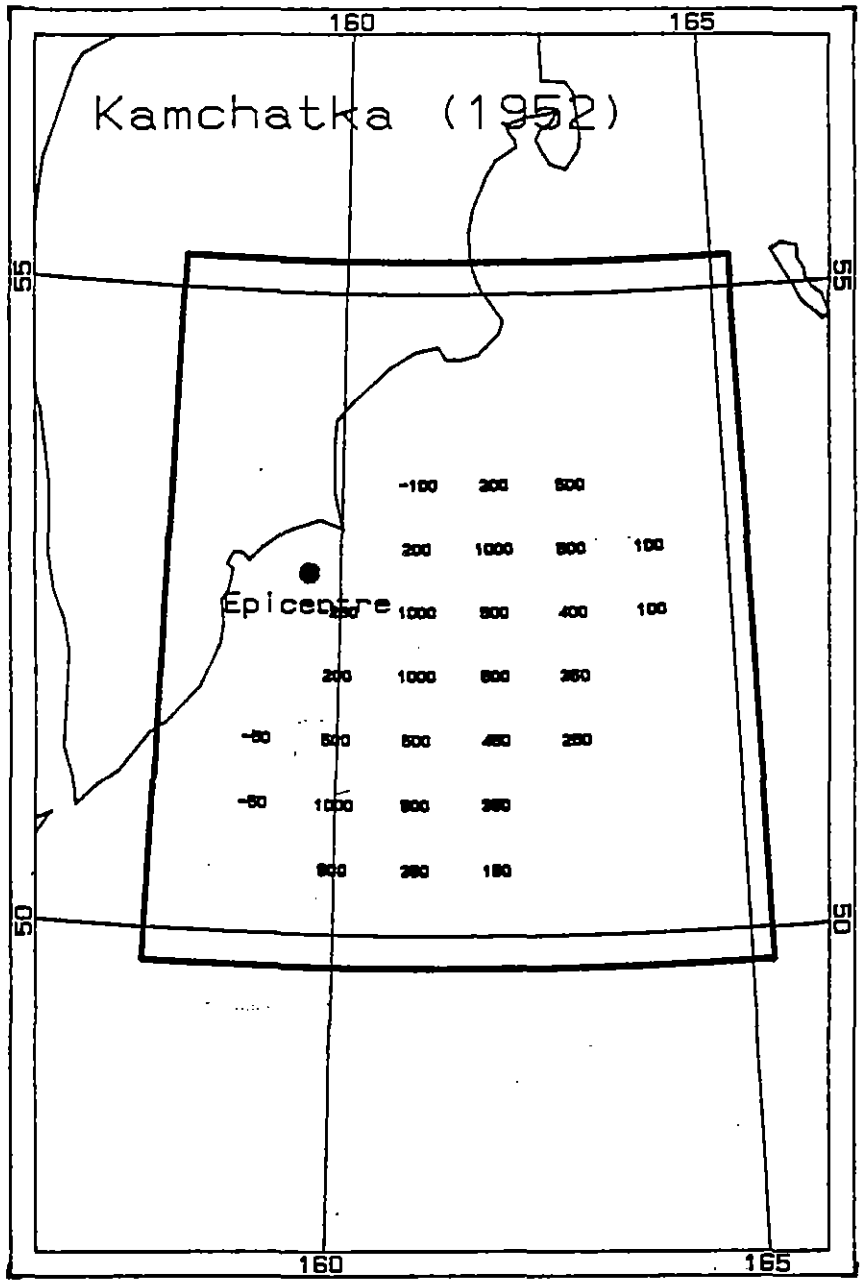

Fig. 7.4 Tsunami generation region for a hypothetical earthquake off the coast of Kamchatka. Location is modelled after the 1952 earthquake. Numbers correspond to final bottom displacements (cm).

Table 7.2

Vertical Displacements for the Elliptical Generation Zones

Point	H (m)	Point	H (m)	Point	H (m)	Point	H (m)	Point	H (m)
1	0.0	2	-0.5	3	-1.0	4	-1.5	5	-2.0
6	0.0	7	2.0	8	5.0	9	10.0	10	10.0
11	5.0	12	4.5	13	4.0	14	3.5	15	3.0
16	2.5	17	2.0	18	1.5	19	1.0	20	0.0

Note: Displacements are along each segment parallel to the minor axis of the ellipse. The landward and seaward edges of the segments correspond to points 1 and 20 respectively.

Table 7.3

Data for Tsunami Generation Regions

Source Number	Region	Data Source or Ellipse Focii	Area (km^2)	Volume (km^3)
1a	Alaska	Plafker (1969)	266,400	446
1b	Alaska	(same as 1a increased by 25%)	266,400	558
2	Chile	Plafker and Savage (1970)	106,400	139
3	Shumagin Gap	156.0°W 53.5°N 163.5°W 51.5°N	141,700	634
4	Kamchatka	196.0°W 55.0°N 203.0°W 50.0°N	98,740	434

Table 7.4

Selected Locations from the Fjord Model

Number	Fjord System (Table 2.1)	Branch/Segment or Node (Fig. 5.10)	Description
1	A	003/004	Indian Reserve
2	A	003/009	Indian Reserve
3	A	003/011	Indian Reserve at Grave Bay - Ensheshese River
4	A	003/017	Indian Reserve near Reservation Point
5	A	004/008	Indian Reserve at head of Quottoon Inlet
6	A	005/003	Indian Reserve / Pile
7	A	005/007	Indian Reserves
8	A	005/008	Indian Reserve
9	A	007/003	Indian Reserve at Union Inlet
10	A	008/004	Indian Reserve at Steamer Passage
11	A	008/005	Indian Reserve at Kumeon Bay
*12	A	009/001	Booming Grounds
13	A	009/009	Booming Grounds
*14	A	009/012	Booming Grounds
15	A	012/001	Indian Reserve
16	A	012/004	Indian Reserve
17	A	013/009	Gwent Cove
18	A	019/001	Arrandale/Indian Reserve at Bay Point
19	A	019/002	Kincolith
20	A	020/004	Indian Reserve
21	A	020/016	Indian Reserve
22	A	020/017	Indian Reserve at Salmon Cove
23	A	020/019	Indian Reserve at Stagoo Creek
24	A	020/024	Indian Reserve
25	A	021/001	Indian Reserve at Perry Bay
*26	A	021/009	Kitsault
*27	A	021/010	Alice Arm/Indian Reserve
28	A	022/002	Anyox
29	A	022/004	Indian Reserve
30	A	022/013	Indian Reserve at head of Hastings Arm
31	A	023/004	Indian Reserve at Whiskey Bay
32	A	024/001	Indian Reserve
33	A	024/039	Indian Reserve at George River
34	A	024/053	Hyder, Alaska
*35	A	024/054	Stewart
*36	A	001	Port Simpson
37	A	004	Indian Reserve near Reservation Point
38	A	006	Indian Reserve at Spakels Point
39	A	008	Indian Reserve
40	B	025/002	Indian Reserve at Venn Passage
41	B	026/004	Oldfield
42	B	027/003	Port Edward
43	B	029/003	Seal Cove

* Sites for which tsunami elevation time-series have been plotted.

Table 7.4

Selected Locations from the Fjord Model (Continued)

Number	Fjord System (Table 2.1)	Branch/Segment or Node (Fig. 5.10)	Description
*44	B	030/001	Prince Rupert/Salt Lake Prov. Park/Damsite
45	B	020	Seal Cove
*46	C	032/013	Last point in Rennell Sound
47	D	033/003	Floats
48	D	034/001	Magneson Point - Westrob Mines/ Causeway/Ramp/Mooring/etc.
*49	D	034/002	Mooring Chain at Hunger Harbour
50	E	037/001	Port Blackney
51	E	048/003	Klemtu
52	E	068/002	Butedale
53	E	085/004	Hartley Bay/Indian Reserve/Public Wharves
54	E	086/011	Kitkiata Inlet/Indian Reserve/Log Dump
55	E	089/030	Kemano Bay/Steamer Landing
56	E	091/009	Kitlope anchorage
57	E	104/006	Kildala Arm
*58	E	107/006	Kitimat
59	E	120/005	Port Essington
60	E	031	Kitkatla
61	E	075	Oona River
62	F	127/019	N. Pulpwoods Ltd./Logging Camp/etc. on S. Bentinck Arm
*63	F	128/008	Bella Coola
64	F	130/026	Kimsquit (abandoned)
*65	F	134/006	Ocean Falls
66	F	138/005	Indian Reserve at Clatse Creek
67	F	139/001	Indian Reserve
68	F	142/001	Shearwater
69	F	142/002	Indian Reserves
70	F	146/001	Indian Reserve
71	F	148/002	Indian Reserve at Kyarti
*72	F	151/005	Bella Bella/New Bella Bella
73	F	166/007	Cabin/Ruins near head of Spiller Inlet
74	F	080	Namu
*75	G	169/005	head of Laredo Inlet
*76	H	174/011	head of Surf Inlet - leads to Belmont Surf Inlet Mine
*77	I	175/003	Duncanby Landing
78	I	175/010	Wadhams/P.O./Union Oil Co.
*79	I	176/009	Dawson Landing/Oil Tanks
80	I	177/004	Brunswick Cannery at Sandell Bay
81	I	177/006	Shell Oil Tanks at Scandinavia Bay
*82	I	178/006	Rivers Inlet Cannery at the head of Rivers Inlet

* Sites for which tsunami elevation time-series have been plotted.

Table 7.4

Selected Locations from the Fjord Model (Continued)

Number	Fjord System (Table 2.1)	Branch/Segment or Node (Fig. 5.10)	Description
83	I	180/007	head of Hardy Inlet
84	I	181/011	head of Moses Inlet
85	I	114	Good Hope
86	J	184/002	Imperial Oil Co. store at Boswell
*87	J	185/009	Nalos Landing
88	J	188/003	last point in Branch 7 - Ahclakerho Channel
89	J	119	Wyclese Indian Reserve
90	K	195/002	Village Cove
91	K	195/003	Village Cove
92	K	197/004	Chief Nollis Bay
*93	K	200/001	Holmes Point
94	K	205/001	Eclipse Narrows
95	K	125	Holmes Point
96	K	129	Eclipse Narrows
97	L	208/005	Indian Reserve
98	L	208/006	Indian Reserve
99	L	208/008	"A" Frame/Log Dump/Wharf at Mahatta River
100	L	210/002	Customs Office
*101	L	212/005	Jeune Landing/Wharf/Piles/"A" Frame
102	L	212/006	Rumble Beach/Yacht Club/Booming Ground
*103	L	212/008	Port Alice
104	L	212/010	Indian Reserve/Booming Ground
105	L	213/001	Indian Reserve
106	L	213/002	Indian Reserve
107	L	213/003	Indian Reserve
*108	L	214/002	Island Copper Mines at Rupert Inlet
109	L	215/002	Coal Harbour
110	L	215/005	Barge/Ramp/Float
111	L	215/016	Indian Reserve
112	L	215/017	Holberg/"A" Frame
113	L	216/001	Indian Reserve
*114	L	216/004	Winter Harbour
115	L	216/005	Indian Reserve/Booming Ground
116	L	134	Gov't Wharf/Float/etc. at Bergh Cove
*117	M	218/002	Klaskino anchorage
118	M	218/006	head of Klaskino Inlet
119	N	219/006	Indian Reserve at head of Ououkinsh Inlet
*120	N	138	Indian Reserve at Byers Cove
*121	O	220/001	Port Langford
122	O	220/005	Indian Reserve at narrows between here and next point
123	O	220/006	Indian Reserve at narrows between here and last point
*124	O	220/008	Indian Reserve at head of Nuchatlitz Inlet

* Sites for which tsunami elevation time-series have been plotted.

Table 7.4

Selected Locations from the Fjord Model (Continued)

Number	Fjord System (Table 2.1)	Branch/Segment or Node (Fig. 5.10)	Description
125	O	139	Indian Reserve
126	P	222/002	Nootka/Piles
127	P	224/001	Indian Reserve/Log Dump at Mooyah Bay
128	P	224/011	Log Dump
*129	P	224/013	Gold River/Tahsis Pulp Mill
130	P	224/017	Indian Reserve/Log Dump at Matchlee Bay
131	P	225/001	Indian Reserve
132	P	226/001	Indian Reserve
133	P	227/002	Indian Reserve
134	P	227/006	Indian Reserves
135	P	227/007	Indian Reserve/Log Dump
136	P	228/002	Plumper Harbour/Log Dump
137	P	229/001	Indian Reserve
138	P	230/004	Indian Reserve/Booming Ground
139	P	230/006	Float/Pier/Booming Ground at Blowhole Bay
140	P	231/001	Boat House/Building/"A" Frame/Booming Ground
*141	P	231/003	Tahsis/Barge/Mooring/Indian Reserve/Float Public Wharves/Booming Ground
142	P	232/001	Indian Reserve/Float
143	P	232/005	Indian Reserve at head of Port Eliza
144	P	234/004	Indian Reserve/Road/Float at Little Espinosa Inlet
145	P	234/006	Indian Reserve
146	P	234/007	Booming Ground/Float
147	P	235/002	Indian Reserve at Graveyard Bay
148	P	235/003	Ehatisaht (abandoned)/Indian Reserve
149	P	236/001	Indian Reserve
150	P	236/003	Float
151	P	236/005	Zeballos/Public Wharves/Indian Reserve/Float/ Seaplane Float
152	P	140	Yuquot/Public Wharves
153	P	141	Indian Reserve at Catala Island
154	P	148	Indian Reserve
155	P	150	Hecate (abandoned)/Esperanza/Ways Float/Imperial Oil/Public Wharves
*156	Q	242/001	Indian Reserve
157	Q	245/003	Indian Reserve at head of Sydney Inlet
*158	Q	246/002	Stewardson Inlet
159	Q	250/002	Indian Reserve at head of Shelter Inlet
160	Q	252/007	Indian Reserve at head of Herbert Inlet at Moyeha Bay/Moyeha River
*161	Q	255/002	Indian Reserve
162	Q	158	Indian Reserve at Megin River
163	Q	159	Ahousat/Public Wharves/Chevron

* Sites for which tsunami elevation time-series have been plotted.

Table 7.4

Selected Locations from the Fjord Model
(Continued)

Number	Fjord System (Table 2.1)	Branch/Segment or Node (Fig. 5.10)	Description
164	R	258/001	Indian Reserve at Toquart River
*165	R	258/005	head of Pipestem Inlet
166	S	259/004	Indian Reserve at Coeur d'Alene Creek
*167	S	259/007	Booms at head of Effingham Inlet
168	S	164	Indian Reserve
169	T	260/002	Indian Reserve
170	T	260/003	Indian Reserve
171	T	260/004	Indian Reserve
*172	T	261/001	Indian Reserves at Rainy Bay and Ecole in Rainy Bay
173	T	262/001	Fishpen/Public Wharves at San Mateo Bay
*174	T	263/001	Green Cove/Piles/Booms
175	T	263/002	Kildonan/Piles/Booms
176	T	263/003	Booms/Indian Reserve at Snug Basin
177	T	264/008	Indian Reserve at Nahmint River
*178	T	264/009	Public Wharves
*179	T	264/011	Sproat Narrows/Piles/Fishpen/Booms
180	T	264/013	Fishpens at Underwood Cove
181	T	264/014	China Creek Provincial Park
182	T	264/016	Floats/Indian Reserve at Stamp Narrows
183	T	264/017	Fog Signal/Indian Reserve at Iso River/Polly Point
*184	T	264/018	Port Alberni
185	T	168	Indian Reserve

* Sites for which tsunami elevation time-series have been plotted.

A subset of 39 of the 185 output points was selected for time-series plots of the simulated tsunami waves. This set includes the major population centres along the British Columbia coast as well as other sites where large amplitude waves were observed in the model output. The 39 locations are indicated in Table 7.4 by asterisks.

7.3 Tsunami Wave Fields

To illustrate wave behaviour along the coast, modelled tsunami wave heights and currents have been plotted at either half-hourly or hourly intervals for each of the four simulations. These have been displayed on two different base maps: one covering the entire coast of British Columbia and a second showing the portion of the coast north of Vancouver Island (Fig. 7.5). Results from the DOM were used for the figures covering the whole coast, while shelf model outputs were used for the high resolution plots of the North Coast.

Each field plot consists of contoured tsunami wave heights and current vectors. These are presented in Fig. 7.6 to 7.12. Wave heights have been contoured using a fixed interval of 25 cm with dashed, solid and bold lines indicating, respectively, negative, positive and zero displacements. Current vector length is proportional to water speed, with the scale given in the lower left corner of each frame. These figures illustrate the spatial distribution of tsunami waves and currents, and shed light on the effect of varying the position and magnitude of the tsunami source on wave heights along the British Columbia coast.

Figures 7.6 to 7.9 show the arrival of the tsunami wave from three of the four source regions to the British Columbia coast. The simulations share certain common features. Wave heights are generally between ± 1 m and current speeds are less than 10 cm/s. Refraction of the tsunami occurs as the wave reaches the shallower water of the continental shelf, and becomes more pronounced as the incident angle becomes more oblique to the NW-SE shelf orientation.

In Fig. 7.6, we can see the wave arriving at 2.01 hours after generation with the leading wave edge being nearly perpendicular to the coastline. As the wave passes the southern tip of the Queen Charlotte Islands at 2.51 hours, it is refracted toward the coast by the decrease in depth over the continental shelf. By 3.01 hours, the leading wave edge is positioned midway along Vancouver Island, and the wave has penetrated into near-coastal waters. The final frame shows that by 3.51 hours the leading wave has reached the Olympic Peninsula.

Fig. 7.7 shows the tsunami from the Shumagin Gap simulation arriving with the wave front nearly parallel to the northern coast. The length of the initial wave decreases noticeably between 2.51 and 3.51 hours as the tsunami travels from deeper to shallower water. The Kamchatka simulation (Fig. 7.8) produced tsunami waves which arrive from approximately the same direction as for the Shumagin Gap simulation. Wave heights are somewhat reduced, however, due to the smaller volume of the initial displacement.

The high resolution field plots (Fig. 7.9 to 7.12) illustrate the evolution of the tsunami as it arrives at the continental shelf and propagates to the

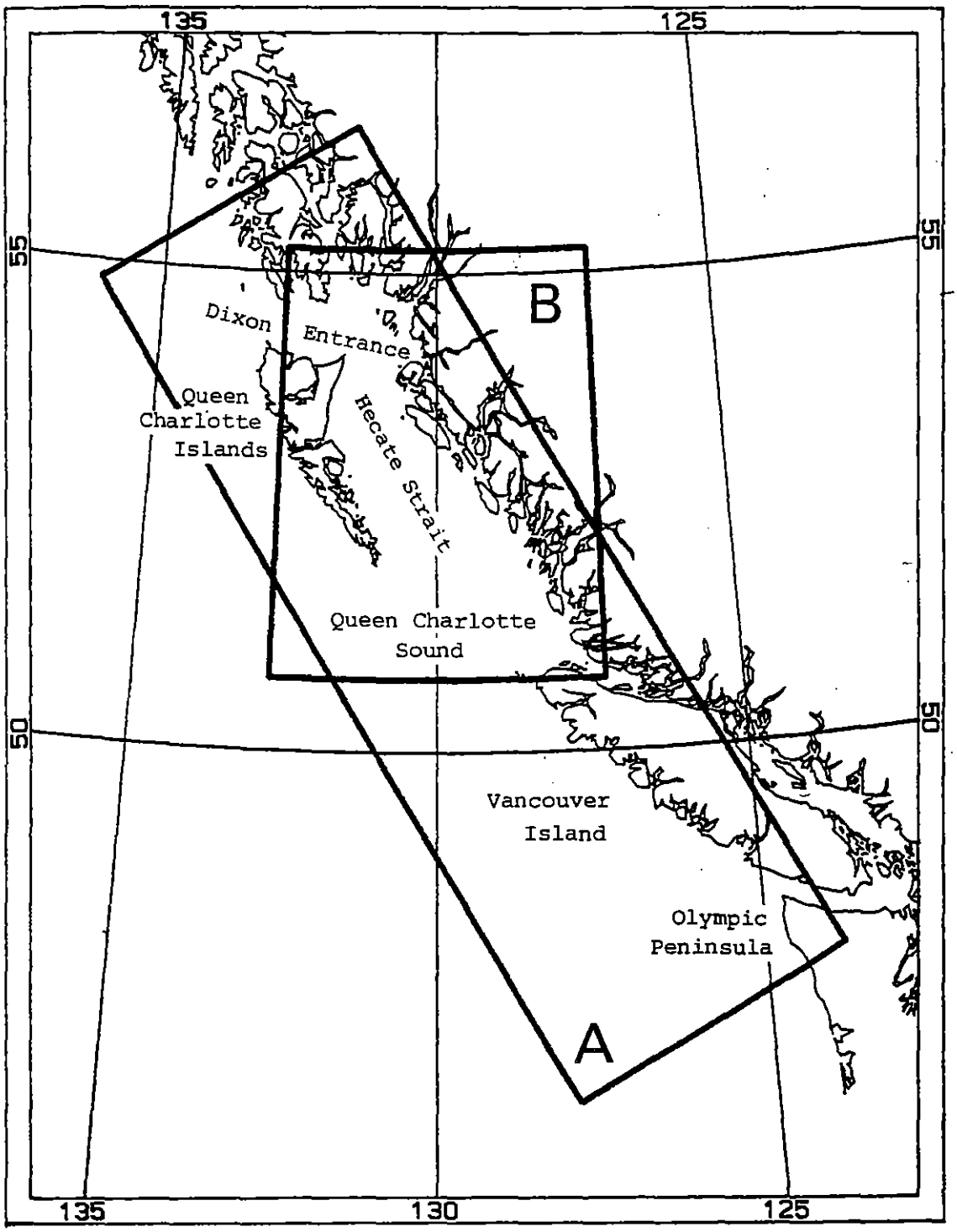

Fig. 7.5 Shelf model grid outline (A) and outline of region used for field plots of northern B.C. coast (B).

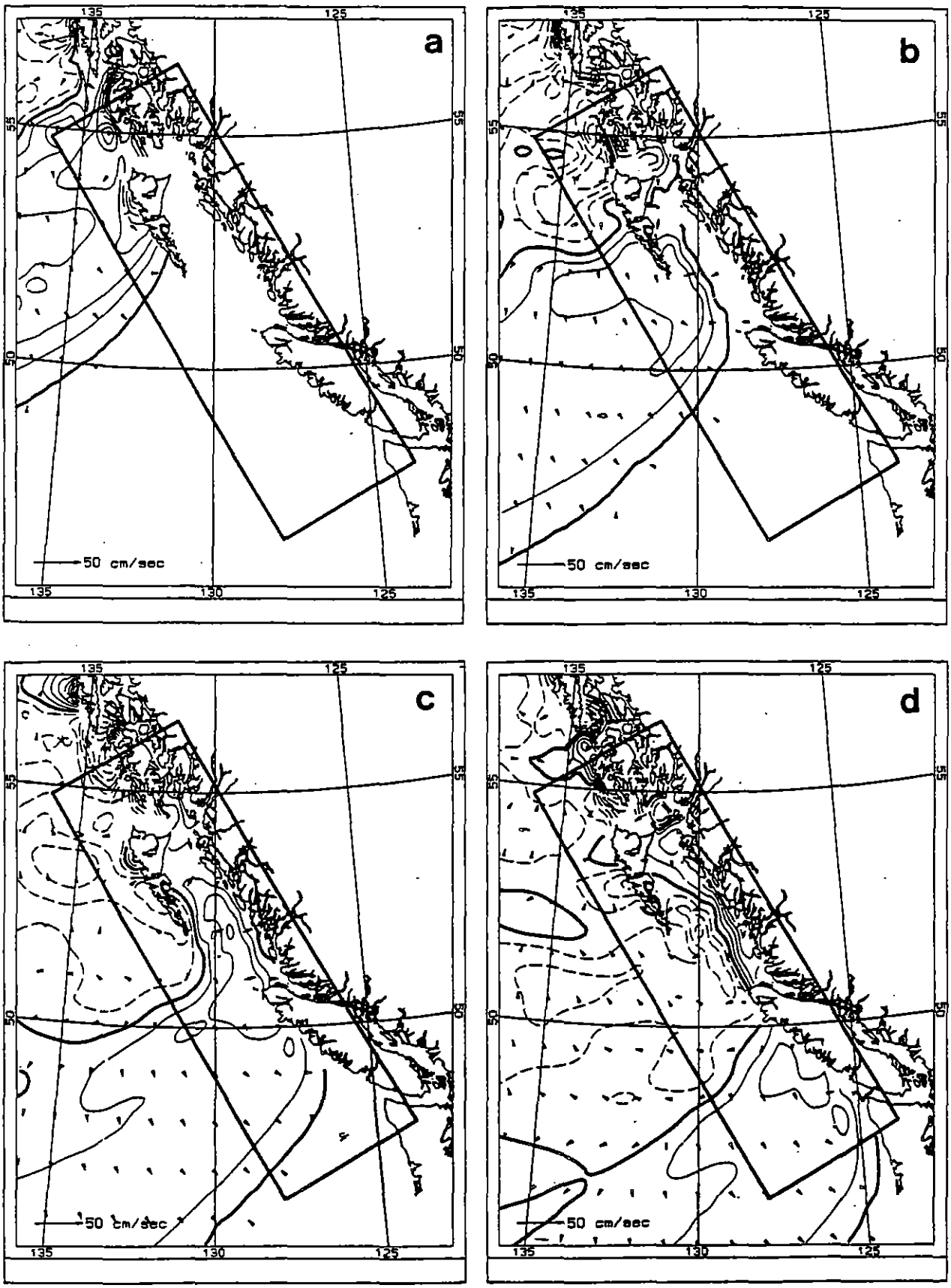

Fig. 7.6 Tsunami wave fields at 0.5 hour intervals for Alaska (x 1.25) simulation. Contour interval is 25 cm. Dashed, solid and bold line correspond respectively to negative, positive and zero displacements.

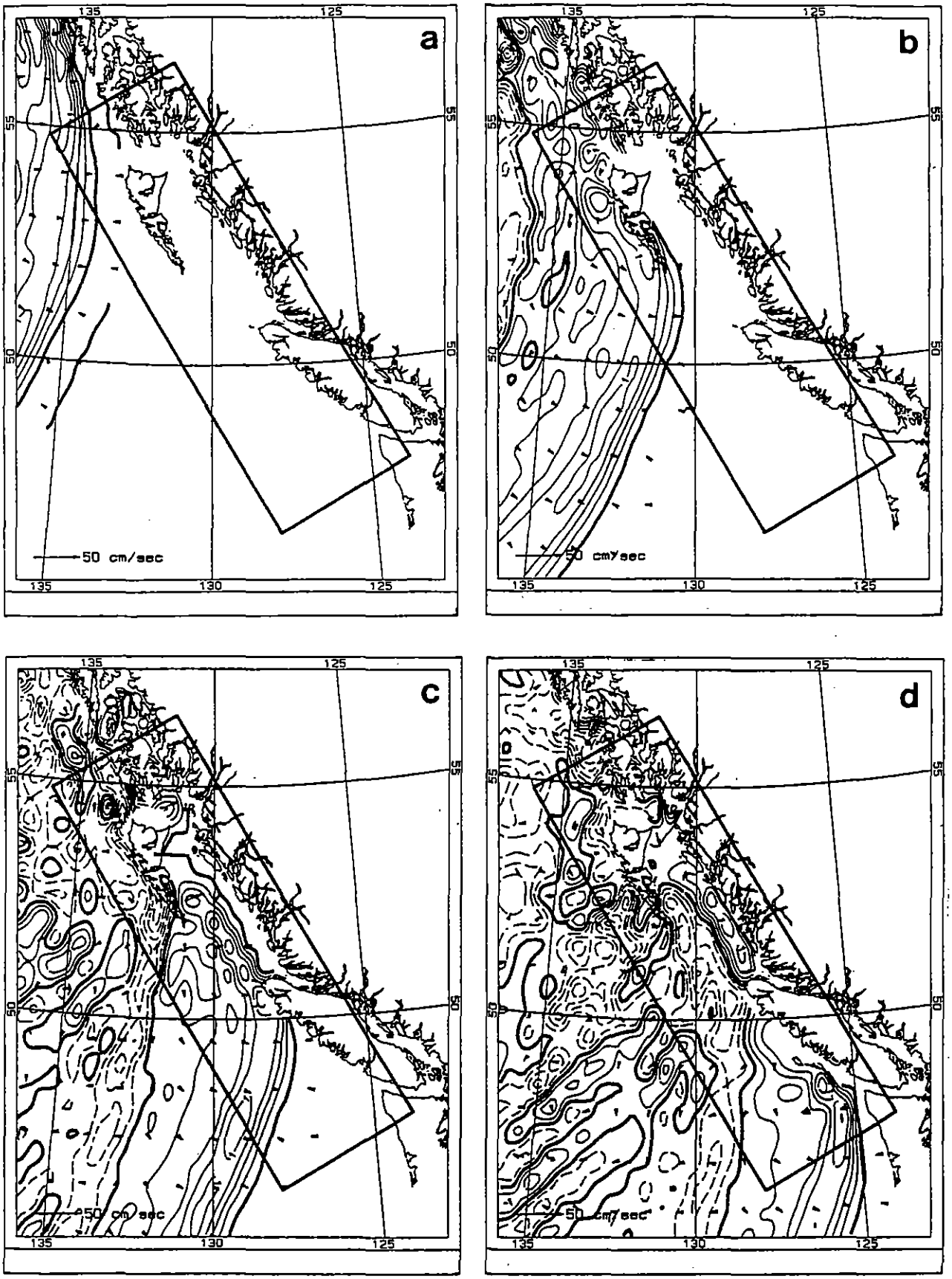

Fig. 7.7 Tsunami wave fields at 0.5 hour intervals for Shumagin Gap simulation. Contour interval is 25 cm. Dashed, solid and bold line correspond respectively to negative, positive and zero displacements.

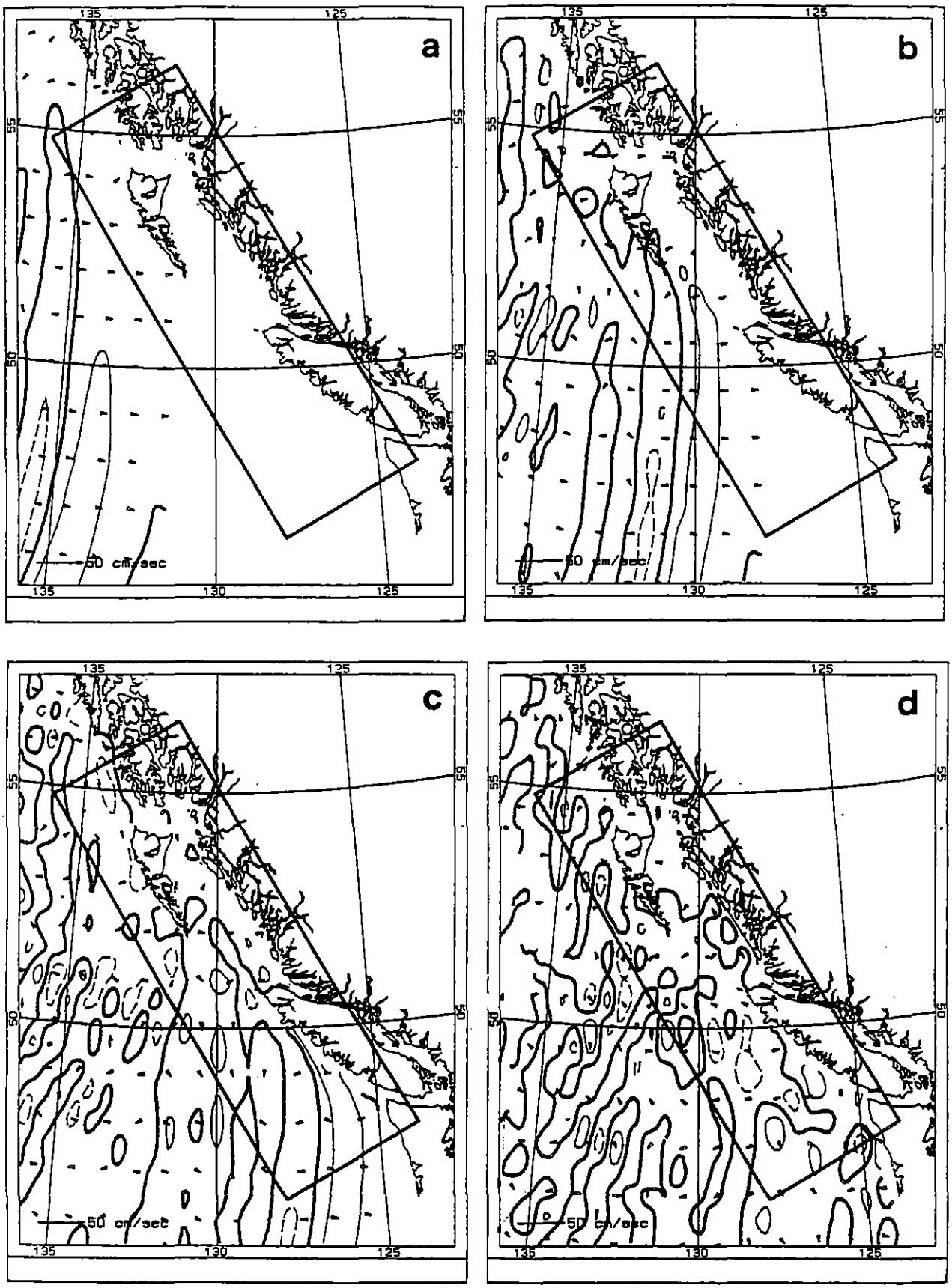

Fig. 7.8 Tsunami wave fields at 0.5 hour intervals for Kamchatka simulation. Contour interval is 25 cm. Dashed, solid and bold line correspond respectively to negative, positive and zero displacements.

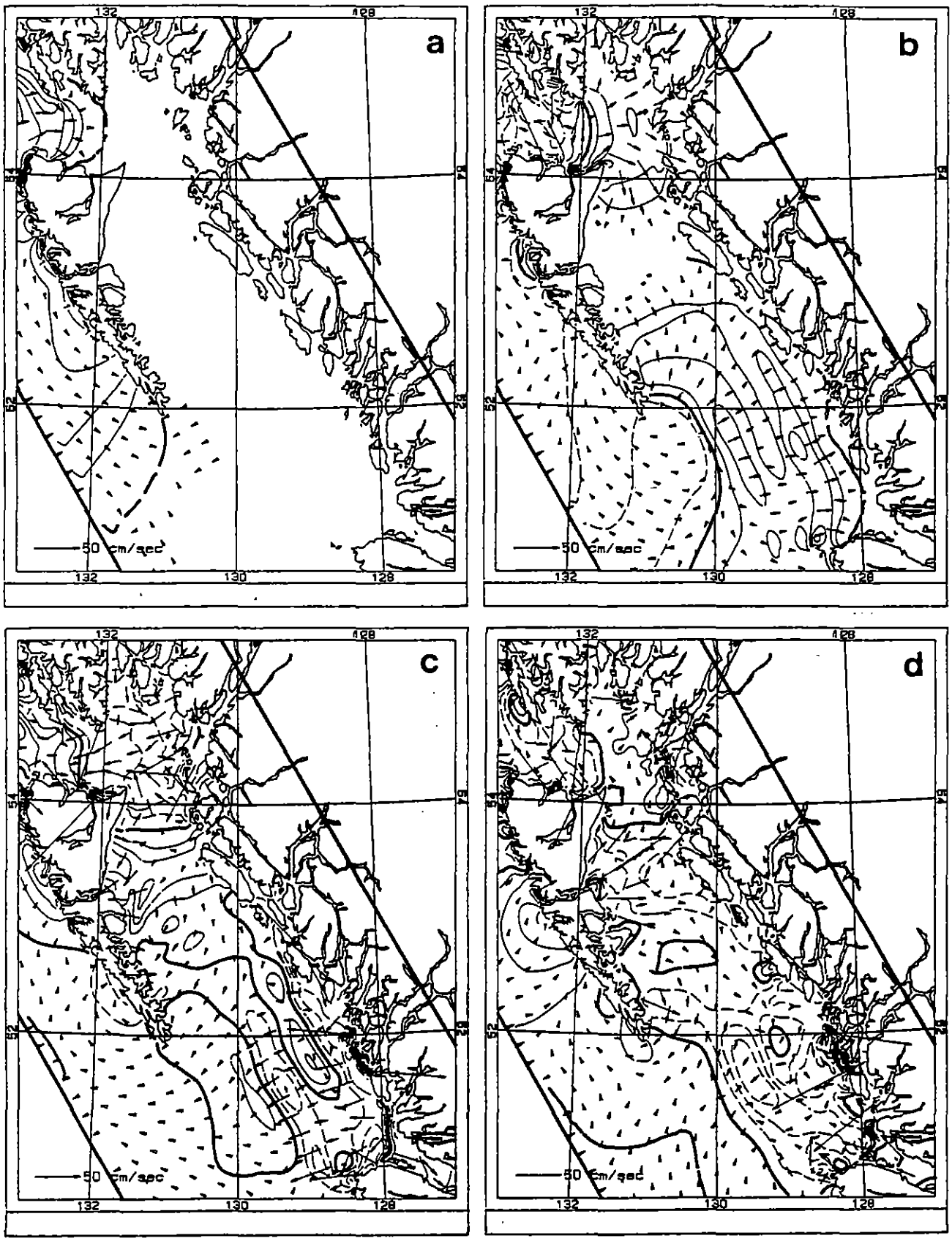

Fig. 7.9 Tsunami wave field and current for north coast of B.C. for Alaska (x 1.25) simulation. Fields are one hour apart beginning 2.11 hours after the earthquake. Contour interval is 25 cm. Dashed, solid and bold line correspond respectively to negative, positive and zero displacements.

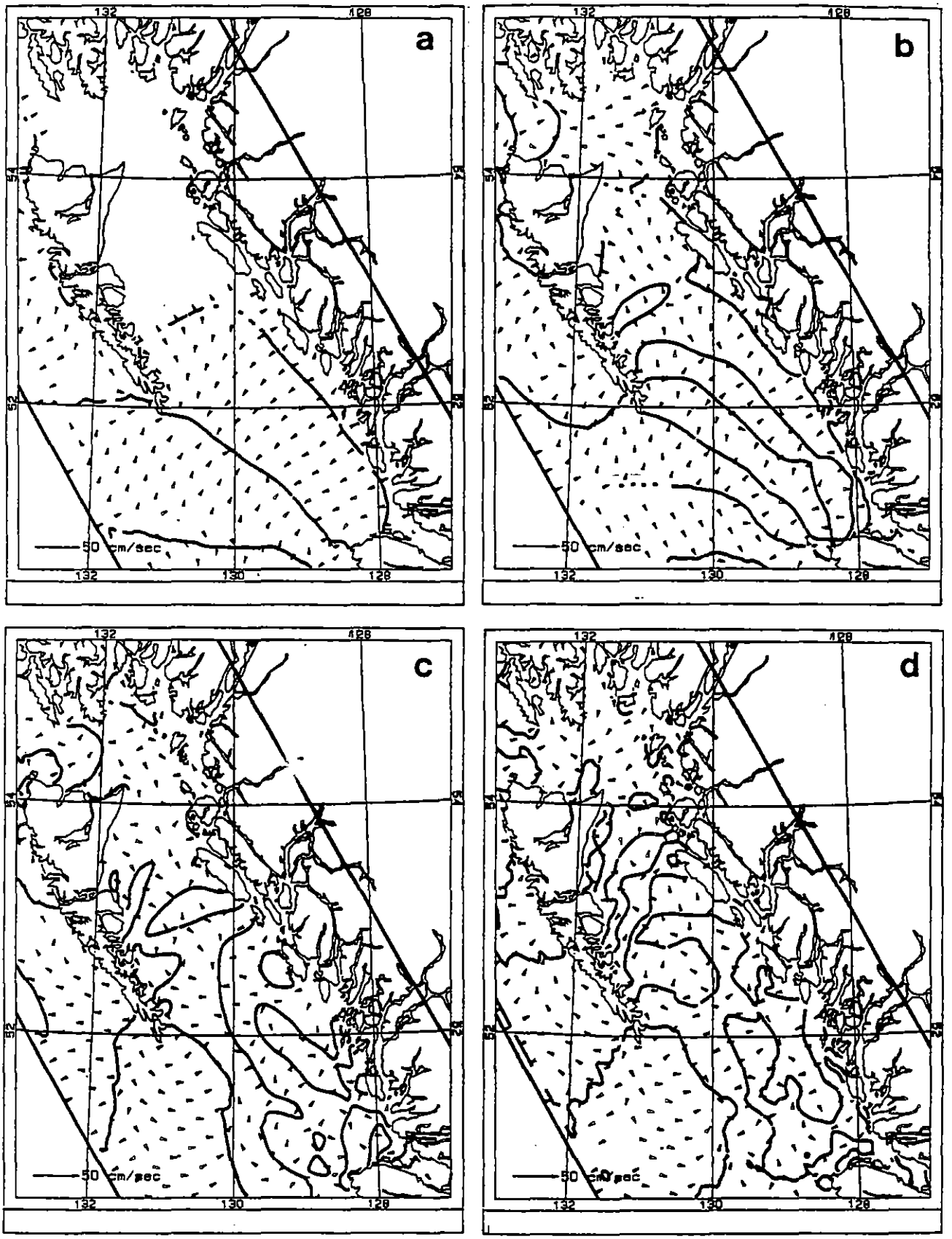

Fig. 7.10 Tsunami wave field and current for north coast of B.C. for Chile simulation. Fields are one hour apart beginning 18.41 hours after the earthquake. Contour interval is 25 cm. Dashed, solid and bold line correspond respectively to negative, positive and zero displacements.

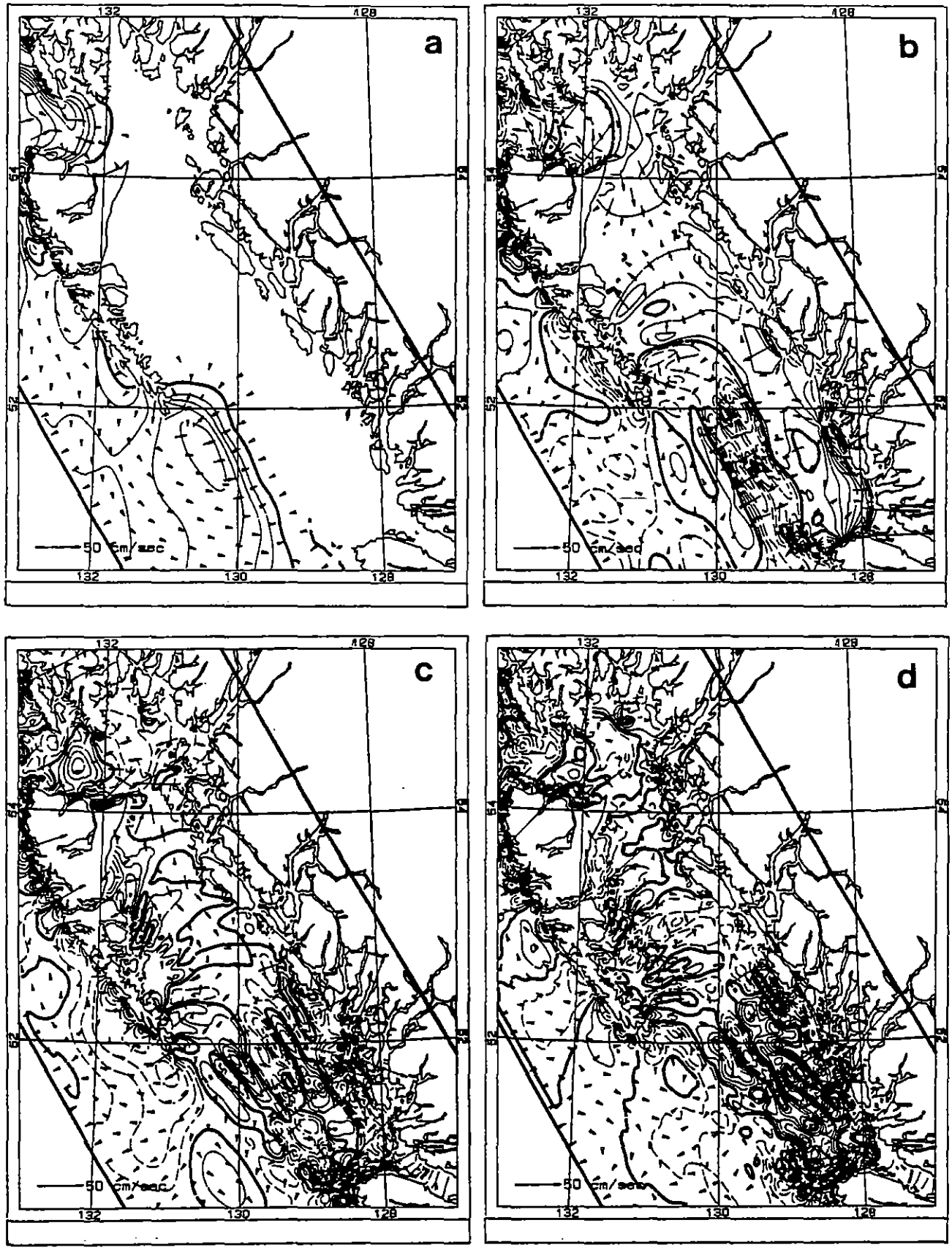

Fig. 7.11 Tsunami wave field and current for north coast of B.C. for Shumagin Gap simulation. Fields are one hour apart beginning 2.68 hours after the earthquake. Contour interval is 25 cm. Dashed, solid and bold line correspond respectively to negative, positive and zero displacements.

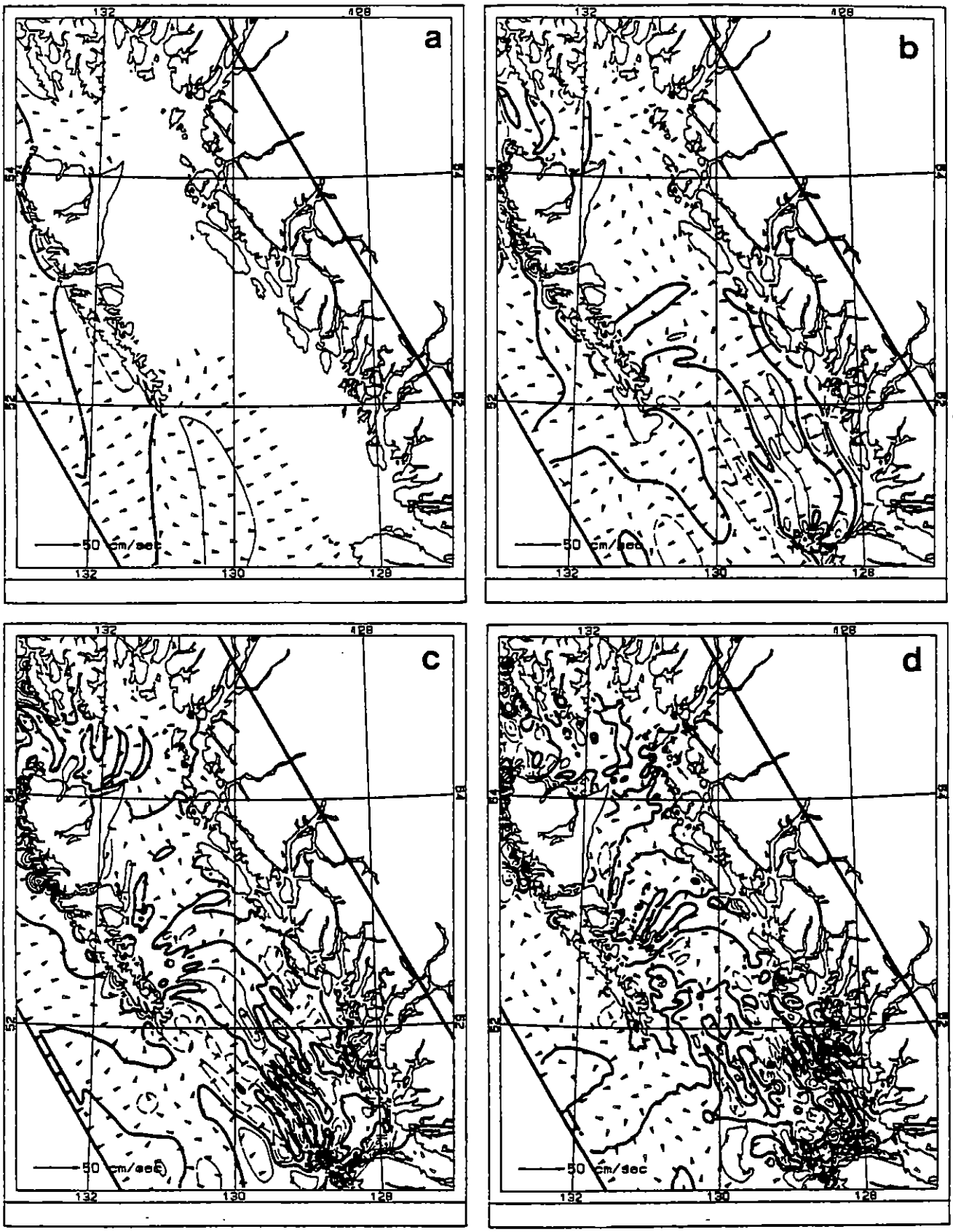

Fig. 7.12 Tsunami wave field and current for north coast of B.C. for Kamchatka simulation. Fields are one hour apart beginning 6.42 hours after the earthquake. Contour interval is 25 cm. Dashed, solid and bold line correspond respectively to negative, positive and zero displacements.

inlet entrances. In each figure, the initial wave can be seen entering through Dixon Entrance to the north, and Queen Charlotte Sound to the south. Subsequently, the two resulting waves interact, resulting in complex patterns of elevation and current.

These plots all show that the leading wave in these tsunamis is spatially coherent as it propagates away from the generation area. In two, Alaska and Shumagin Gap, the leading edge is a wave of depression followed by a much larger (>25 cm) positive wave. In the case of Kamchatka, the leading wave is positive. The crests of the positive first wave are continuous along the arc normal to the propagation vector. However, behind the first wave, water levels are characterized by high frequencies corresponding to the spatially irregular pattern. The high frequency content appears to increase with tsunami amplitude, source distance, and interference from the coastal landforms.

In particular, the Shumagin Gap and Kamchatka simulations show the rapid evolution of high-frequency, large amplitude (about 1 m) waves in the southern portion of Queen Charlotte Sound. The interference pattern is more regular for the Alaska simulation, reflecting its long initial wave length, more oblique angle of incidence to the coast and smoother deep water wave field. The Chilean simulation also produces a complex interference pattern (Fig. 7.10), but one that differs from the other three in that the shorter waves in Queen Charlotte Sound and Hecate Strait, following the leading wave, do not exhibit a distinct shore-parallel orientation and have much smaller amplitudes (<25 cm). These differences are due mainly to the southerly direction of approach and lower deep water amplitudes.

These results lead us to expect differing tsunami behaviour in the fjords. Where the high-frequency energy is incident onto the inlets, then the up-inlet response will reflect their presence. In other areas where the tsunami wave field is smoother and more regular, then we expect less high-frequency energy inside the fjords.

7.4 Maximum Tsunami Water Levels and Currents

At each of the 185 key locations the calculated maximum tsunami wave amplitude and current speed for each simulated source have been listed. These represent maximum (positive) water level and current speed values extracted from the entire length of each simulation, containing four to five waveforms. Results for all five tsunami simulations are presented in Tables 7.5 to 7.11, together with accompanying diagrams that show the locations of each station (Fig. 7.13 to 7.19).

Table 7.5 and Fig. 7.13 give the results for system A which is located at the northern end of the British Columbia coast, and includes Portland Inlet and the town of Stewart (station 35). Maximum wave heights and current speeds occur for the two Alaska tsunamis, with the Shumagin Gap and Kamchatka simulations following in turn. Current speeds are greatest at the entrances to Observatory and Khutzeymateen Inlets, peaking at 2.3 m/s for the Alaska (x 1.25) simulation. Speeds near the heads of the inlets are small, as expected. The Chile tsunami produces negligible water level changes.

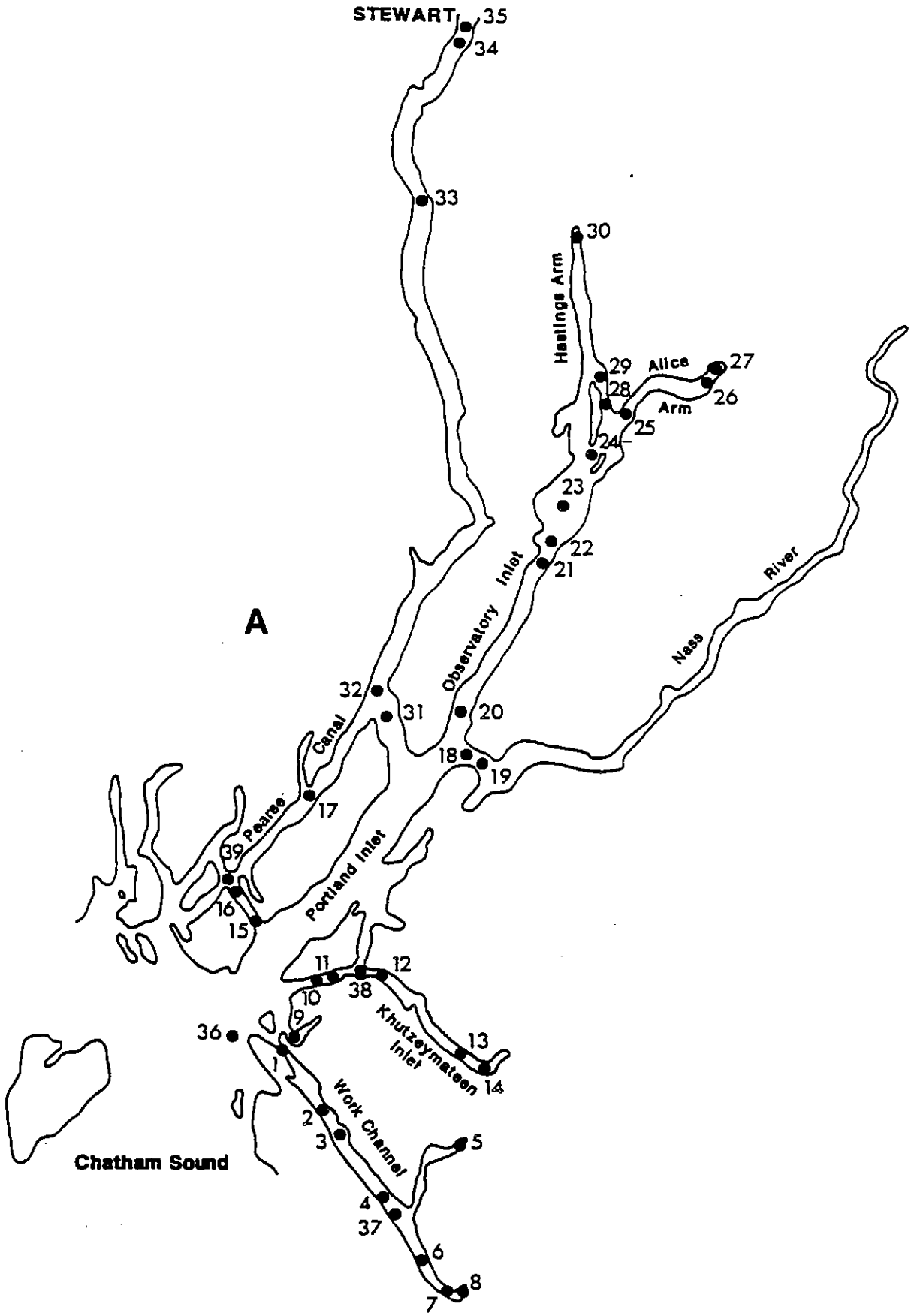

Fig. 7.13 Map showing water level and current locations listed in Table 7.5

Table 7.5

Maximum Tsunami Water Levels and Currents for System A

Location No.	Inlet System	Source Region (Table 7.1) 1a	1b	2	3	4	Source Region (Table 7.1) 1a	1b	2	3	4
		Water Level (m)					Current Speed (m/s)				
1	A	0.6	0.7	0.0	0.6	0.2	1.15	1.32	0.02	1.13	0.41
2	A	0.7	0.9	0.0	0.8	0.3	0.13	0.15	0.00	0.12	0.05
3	A	0.8	0.9	0.0	0.8	0.3	0.12	0.13	0.00	0.11	0.04
4	A	0.8	1.0	0.0	0.8	0.3	0.09	0.10	0.00	0.08	0.03
5	A	1.1	1.3	0.0	0.9	0.4	0.04	0.04	0.00	0.04	0.01
6	A	0.8	1.0	0.0	0.9	0.3	0.08	0.10	0.00	0.09	0.03
7	A	0.9	1.0	0.0	0.9	0.3	0.05	0.06	0.00	0.06	0.02
8	A	0.9	1.1	0.0	0.9	0.3	0.04	0.04	0.00	0.04	0.01
9	A	1.6	1.8	0.0	1.6	0.3	0.59	0.69	0.01	0.64	0.11
10	A	1.7	1.9	0.0	1.7	0.4	1.11	1.27	0.02	0.83	0.20
11	A	1.9	2.1	0.0	1.9	0.4	1.08	1.25	0.01	0.84	0.19
*12	A	2.3	2.6	0.0	2.1	0.5	1.14	1.36	0.02	1.13	0.26
13	A	3.0	3.5	0.0	2.6	0.6	0.18	0.20	0.00	0.20	0.04
*14	A	3.0	3.5	0.0	3.0	0.7	0.10	0.11	0.00	0.12	0.03
15	A	1.2	1.3	0.0	1.1	0.3	0.22	0.26	0.00	0.29	0.07
16	A	1.3	1.5	0.0	1.5	0.5	0.50	0.57	0.01	0.44	0.08
17	A	1.6	1.9	0.0	1.0	0.2	0.30	0.36	0.00	0.32	0.08
18	A	1.4	1.7	0.0	0.9	0.2	0.12	0.15	0.00	0.14	0.04
19	A	1.4	1.7	0.0	0.9	0.2	0.39	0.49	0.01	0.42	0.10
20	A	1.3	1.6	0.0	0.9	0.2	1.87	2.30	0.02	1.69	0.37
21	A	1.9	2.4	0.0	1.7	0.3	0.50	0.62	0.01	0.47	0.10
22	A	2.0	2.5	0.0	1.8	0.3	0.51	0.63	0.01	0.48	0.11
23	A	2.1	2.7	0.0	1.9	0.3	0.17	0.21	0.00	0.16	0.04
24	A	2.3	2.9	0.0	2.1	0.4	0.49	0.60	0.01	0.46	0.11
25	A	1.6	2.0	0.0	1.4	0.3	1.01	1.15	0.03	0.96	0.36
*26	A	1.8	2.2	0.0	1.5	0.4	0.08	0.09	0.00	0.08	0.02
*27	A	1.8	2.2	0.0	1.5	0.4	0.05	0.06	0.00	0.05	0.02
28	A	2.5	3.1	0.0	2.2	0.4	0.23	0.28	0.00	0.20	0.04
29	A	2.7	3.3	0.0	2.2	0.4	0.33	0.41	0.01	0.33	0.07
30	A	2.8	3.4	0.0	2.4	0.5	0.07	0.09	0.00	0.09	0.02
31	A	1.5	1.8	0.0	1.0	0.2	0.42	0.52	0.01	0.44	0.08
32	A	1.6	1.9	0.0	1.1	0.2	0.44	0.54	0.01	0.36	0.08
33	A	2.8	3.4	0.0	1.9	0.3	0.30	0.35	0.00	0.26	0.06
34	A	3.2	4.0	0.0	2.2	0.4	0.17	0.22	0.00	0.19	0.03
*35	A	3.3	4.1	0.0	2.3	0.4	0.23	0.29	0.00	0.25	0.04
*36	A	0.9	1.1	0.0	0.8	0.2	. . . not available . . .				
37	A	0.8	1.0	0.0	0.8	0.3	. . . not available . . .				
38	A	2.1	2.3	0.0	2.0	0.4	. . . not available . . .				
39	A	1.6	1.8	0.0	1.3	0.3	. . . not available . . .				

Notes: * signifies the existence of a corresponding time-series plot.

Water levels are referred to mean water level. The effects of tide must be added to the tsunami levels shown here.

Current speeds represent the rate of water flow averaged over the cross-sectional area of the fjord.

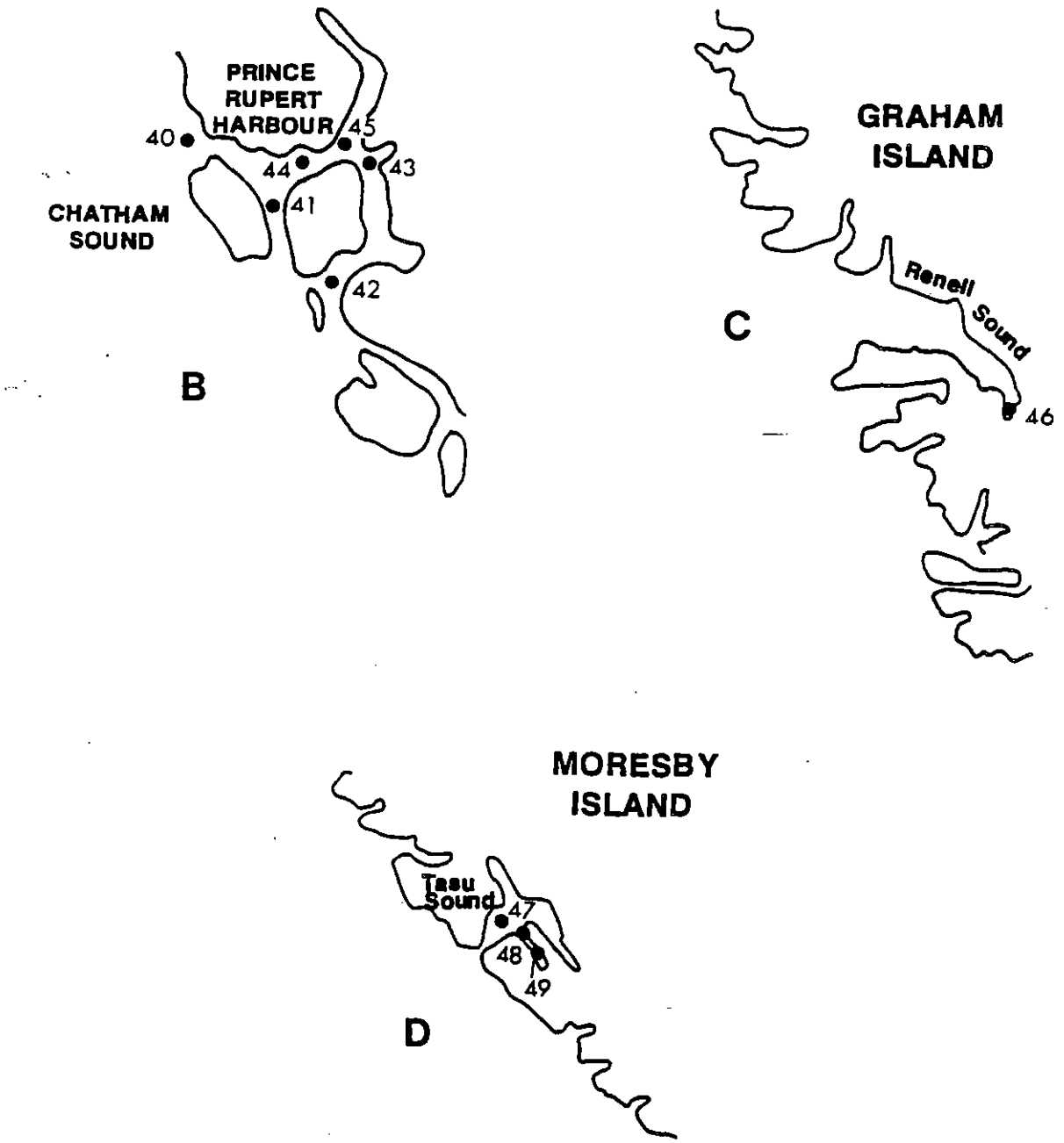

Fig. 7.14 Map showing water level and current locations listed in Table 7.6

Table 7.6

Maximum Tsunami Water Levels and Currents for Systems B, C and D

Location No.	Inlet System	Source Region (Table 7.1) 1a	1b	2	3	4	Source Region (Table 7.1) 1a	1b	2	3	4
		Water Level (m)					Current Speed (m/s)				
40	B	0.7	0.8	0.0	0.7	0.2	0.31	0.35	0.03	0.39	0.12
41	B	1.8	2.2	0.0	1.7	0.3	1.29	1.52	0.04	1.25	0.26
42	B	1.5	1.7	0.0	1.2	0.3	0.94	1.10	0.07	1.40	0.29
43	B	0.7	0.8	0.0	0.6	0.2	0.14	0.16	0.02	0.11	0.05
*44	B	1.9	2.3	0.0	1.7	0.3	0.53	0.61	0.02	0.77	0.12
45	B	2.3	2.7	0.0	1.8	0.3	. . . not available . . .				
46	C	. . . not available . . .									
47	D	1.8	1.9	0.1	2.0	0.7	0.28	0.31	0.03	0.39	0.11
48	D	1.9	2.0	0.1	2.0	0.7	0.12	0.13	0.01	0.24	0.07
*49	D	2.1	2.2	0.2	2.4	0.7	0.24	0.29	0.03	0.54	0.16

Notes: * signifies the existence of a corresponding time-series plot.

Water levels are referred to mean water level. The effects of tide must be added to the tsunami levels shown here.

Current speeds represent the rate of water flow averaged over the cross-sectional area of the fjord.

Results for site 46 at the head of Renell Sound are not available because of limited resolution in the numerical model.

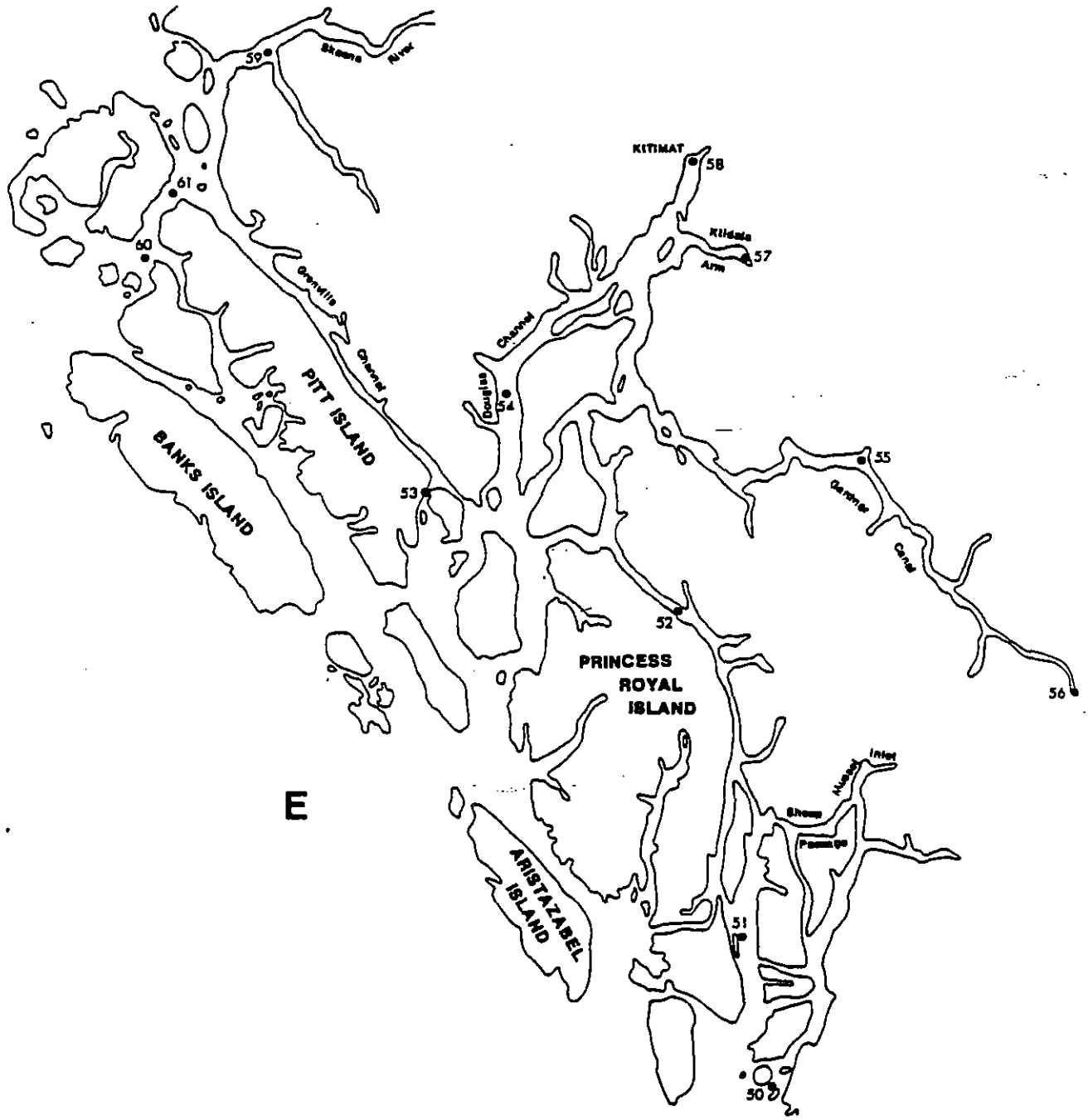

Fig. 7.15 Map showing water level and current locations listed in Table 7.7

Table 7.7

Maximum Tsunami Water Levels and Currents for System E

Location No.	Inlet System	Source Region (Table 7.1) 1a	1b	2	3	4	Source Region (Table 7.1) 1a	1b	2	3	4
		Water Level (m)					Current Speed (m/s)				
50	E	1.4	1.7	0.3	3.5	0.8	0.70	0.84	0.05	0.81	0.36
51	E	2.4	2.9	0.4	4.3	1.3	0.73	0.86	0.17	1.22	0.42
52	E	2.5	3.1	0.1	3.3	0.7	0.47	0.57	0.03	0.62	0.11
53	E	1.1	1.3	0.1	1.0	0.2	0.05	0.06	0.00	0.08	0.03
54	E	1.1	1.4	0.1	1.5	0.5	0.30	0.36	0.01	0.46	0.10
55	E	1.2	1.5	0.1	1.4	0.4	0.12	0.15	0.01	0.18	0.06
56	E	1.8	2.2	0.2	2.3	0.7	0.04	0.05	0.00	0.05	0.03
57	E	1.2	1.5	0.2	2.5	0.8	0.04	0.04	0.01	0.05	0.03
*58	E	1.2	1.4	0.1	1.9	0.4	0.02	0.03	0.00	0.03	0.02
59	E	1.1	1.2	0.1	1.0	0.4	0.25	0.27	0.04	0.28	0.17
60	E	1.3	1.6	0.1	1.3	0.4	. . . not available . . .				
61	E	1.7	1.9	0.0	1.6	0.3	. . . not available . . .				

Notes: * signifies the existence of a corresponding time-series plot.

Water levels are referred to mean water level. The effects of tide must be added to the tsunami levels shown here.

Current speeds represent the rate of water flow averaged over the cross-sectional area of the fjord.

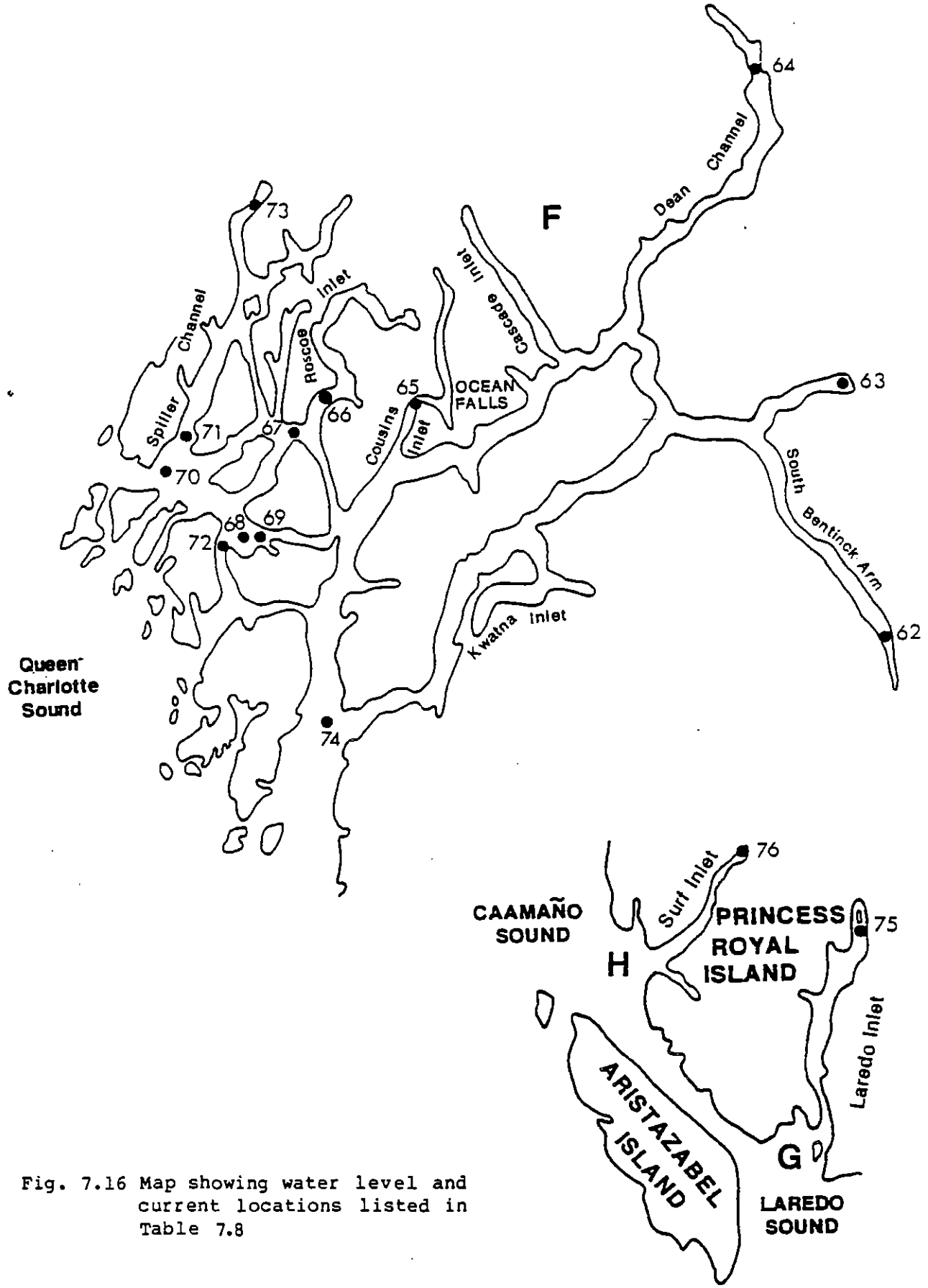

Fig. 7.16 Map showing water level and current locations listed in Table 7.8

Table 7.8

Maximum Tsunami Water Levels and Currents for Systems F, G and H

Location No.	Inlet System	Source Region (Table 7.1) 1a	1b	2	3	4	Source Region (Table 7.1) 1a	1b	2	3	4
		Water Level (m)					Current Speed (m/s)				
62	F	2.0	2.3	0.1	3.0	0.4	0.19	0.22	0.01	0.17	0.07
*63	F	1.5	1.8	0.2	2.2	0.6	0.03	0.03	0.01	0.05	0.01
64	F	1.2	1.5	0.2	2.0	0.3	0.48	0.58	0.07	0.79	0.25
*65	F	2.7	3.3	0.3	4.2	3.1	0.27	0.33	0.03	0.28	0.27
66	F	1.7	2.1	0.1	1.9	0.6	0.84	1.02	0.04	0.67	0.26
67	F	2.0	2.4	0.2	1.1	0.8	1.10	1.34	0.06	1.15	0.30
68	F	1.6	2.0	0.2	2.4	0.7	0.78	0.97	0.07	0.67	0.35
69	F	2.0	2.5	0.2	2.8	0.9	0.74	0.92	0.07	0.82	0.43
70	F	1.6	1.9	0.1	1.9	0.4	0.46	0.55	0.02	0.26	0.15
71	F	1.8	2.1	0.1	2.0	0.6	0.83	1.00	0.05	0.78	0.37
*72	F	1.8	2.2	0.1	2.8	0.7	0.97	1.18	0.12	1.24	0.58
73	F	5.9	7.2	0.3	4.0	3.4	0.54	0.66	0.04	0.35	0.36
74	F	1.0	1.3	0.1	1.2	0.5	. . . not available . . .				
*75	G	3.7	4.4	0.4	5.6	1.5	0.16	0.20	0.03	0.47	0.13
*76	H	2.2	2.5	0.3	3.3	1.5	0.14	0.17	0.02	0.24	0.14

Notes: * signifies the existence of a corresponding time-series plot.

Water levels are referred to mean water level. The effects of tide must be added to the tsunami levels shown here.

Current speeds represent the rate of water flow averaged over the cross-sectional area of the fjord.

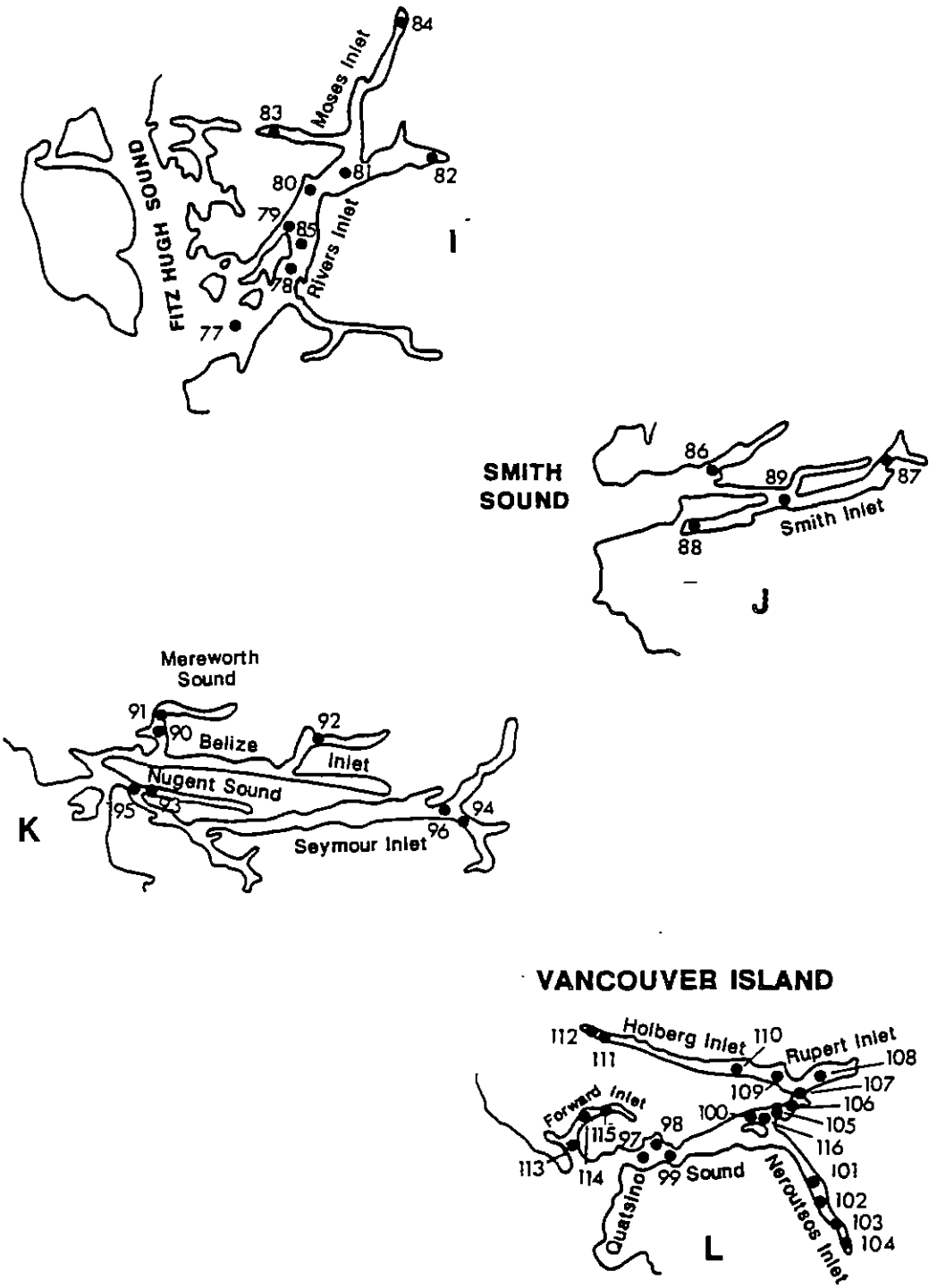

Fig. 7.17 Map showing water level and current locations listed in Table 7.9

Table 7.9

Maximum Tsunami Water Levels and Currents for Systems J, K and L

Location No.	Inlet System	Source Region (Table 7.1) 1a	1b	2	3	4	Source Region (Table 7.1) 1a	1b	2	3	4
		Water Level (m)					Current Speed (m/s)				
*77	I	1.9	2.2	0.1	3.1	1.3	0.75	0.89	0.03	0.83	0.21
78	I	1.8	2.1	0.1	2.7	1.2	0.63	0.73	0.03	0.80	0.19
*79	I	2.3	2.8	0.1	2.8	1.5	1.16	1.43	0.10	1.73	0.52
80	I	2.2	2.7	0.1	2.4	1.2	0.57	0.69	0.03	0.83	0.17
81	I	2.5	3.0	0.1	3.3	1.1	0.60	0.72	0.04	0.85	0.18
*82	I	3.1	3.6	0.2	5.0	1.5	0.08	0.09	0.01	0.11	0.04
83	I	4.7	5.6	0.2	5.3	1.6	0.16	0.18	0.01	0.15	0.05
84	I	5.9	7.2	0.3	9.2	5.1	0.13	0.15	0.01	0.19	0.16
85	I	1.8	2.2	0.1	2.3	1.2	. . . not available . . .				
86	J	3.4	4.1	0.4	4.6	3.5	0.89	1.09	0.16	1.16	0.90
*87	J	7.6	9.3	0.4	8.4	2.2	1.31	1.64	0.25	1.66	0.81
88	J	1.2	1.4	0.2	1.2	0.4	0.03	0.03	0.01	0.04	0.01
89	J	4.9	6.0	0.4	5.0	1.3	. . . not available . . .				
90	K	0.1	0.1	0.0	0.1	0.0	0.07	0.09	0.01	0.13	0.08
91	K	0.1	0.1	0.0	0.1	0.0	0.06	0.07	0.01	0.09	0.08
92	K	0.1	0.1	0.0	0.1	0.0	0.01	0.01	0.00	0.01	0.01
*93	K	0.3	0.3	0.0	0.5	0.2	0.39	0.45	0.04	0.56	0.20
94	K	0.0	0.1	0.0	0.0	0.0	0.01	0.01	0.00	0.01	0.01
95	K	0.3	0.3	0.0	0.6	0.3	. . . not available . . .				
96	K	0.1	0.1	0.0	0.1	0.1	. . . not available . . .				
97	L	1.7	2.1	0.5	7.2	2.4	1.09	1.37	0.14	1.79	1.39
98	L	1.9	2.1	0.5	7.2	2.4	1.18	1.48	0.11	1.66	1.51
99	L	2.2	2.5	0.5	6.1	2.5	1.16	1.40	0.11	2.35	1.40
100	L	2.7	3.5	0.4	6.7	4.0	0.94	1.11	0.19	2.46	0.89
*101	L	3.0	3.7	0.4	5.4	3.6	0.67	0.84	0.10	1.68	1.24
102	L	3.1	3.9	0.3	5.5	4.2	1.03	1.25	0.18	2.65	1.83
*103	L	3.9	4.7	0.5	9.1	7.2	2.77	3.13	0.57	5.76	4.30
104	L	. . . not available . . .									
105	L	3.5	3.9	0.5	8.5	4.2	1.26	1.42	0.30	2.50	1.55
106	L	3.8	4.3	0.7	7.9	4.8	1.41	1.65	0.22	2.84	1.16
107	L	3.3	3.7	0.7	8.1	4.4	2.60	2.92	0.42	4.71	3.00
*108	L	0.7	0.9	0.1	1.2	0.8	0.18	0.21	0.04	0.26	0.17
109	L	0.3	0.4	0.0	0.8	0.4	0.29	0.33	0.02	0.23	0.33
110	L	0.7	0.8	0.1	1.0	0.9	0.26	0.30	0.03	0.25	0.28
111	L	1.2	1.4	0.1	1.3	1.1	0.06	0.07	0.01	0.14	0.06
112	L	2.1	2.3	0.2	3.4	2.3	1.22	1.35	0.18	2.27	1.25
113	L	2.5	2.7	0.3	6.1	2.8	2.04	2.29	0.29	3.72	2.02
*114	L	5.3	6.1	0.8	9.6	6.1	9.47	12.76	0.90	21.42	9.65
115	L	. . . not available . . .									
116	L	2.7	3.2	0.4	7.0	3.7	. . . not available . . .				

Notes: * signifies the existence of a corresponding time-series plot.

Water levels are referred to mean water level. The effects of tide must be added to the tsunami levels shown here.

Current speeds represent the rate of water flow averaged over the cross-sectional area of the fjord.

Results for sites 104 (Neroutsos Inlet) and 115 (Forward Inlet) are not available because of limited resolution in the numerical model.

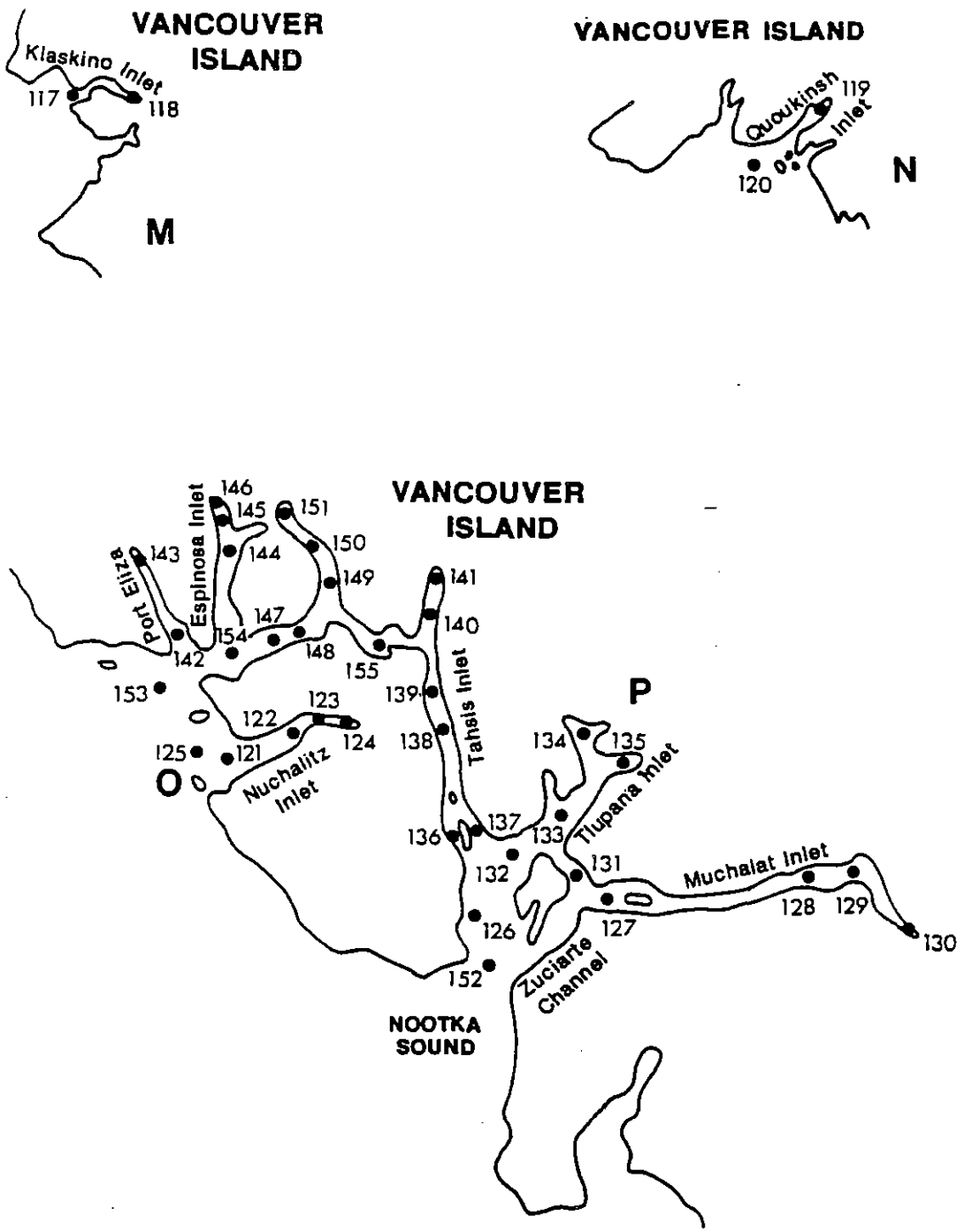

Fig. 7.18 Map showing water level and current locations listed in Table 7.10

Table 7.10

Maximum Tsunami Water Levels and Currents for Systems M, N, O and P

Location No.	Inlet System	Source Region (Table 7.1) 1a	1b	2	3	4	Source Region (Table 7.1) 1a	1b	2	3	4
		Water Level (m)					Current Speed (m/s)				
*117	M	3.0	3.7	0.4	5.5	2.3	2.08	2.40	0.45	2.99	2.32
118	M	4.2	5.0	0.7	5.7	3.7	0.37	0.43	0.09	0.97	0.50
119	N	8.6	10.1	1.2	13.0	4.6	0.80	0.98	0.13	2.29	1.04
*120	N	1.3	1.6	0.3	3.9	1.7	. . . not available . . .				
*121	O	2.1	2.6	0.3	3.3	1.2	0.76	0.91	0.17	1.93	0.98
122	O	3.3	3.8	0.6	4.4	1.7	0.56	0.62	0.12	1.22	0.40
123	O	0.2	0.2	0.0	0.2	0.1	0.02	0.03	0.01	0.04	0.02
*124	O	0.2	0.2	0.0	0.2	0.1	0.00	0.00	0.00	0.01	0.00
125	O	1.9	2.4	0.3	2.9	1.1	. . . not available . . .				
126	P	1.7	2.1	0.2	2.9	2.3	0.74	0.91	0.06	1.76	1.06
127	P	2.4	3.0	0.2	4.5	1.8	1.33	1.64	0.13	2.66	0.47
128	P	5.9	7.3	0.4	10.6	1.6	0.33	0.40	0.04	0.86	0.18
*129	P	6.1	7.5	0.4	10.8	1.7	0.13	0.16	0.02	0.36	0.09
130	P	6.5	8.0	0.4	11.1	2.2	0.22	0.26	0.03	0.68	0.24
131	P	1.9	2.3	0.2	3.0	1.8	1.25	1.53	0.11	2.59	0.80
132	P	1.6	2.0	0.2	4.2	1.8	0.71	0.88	0.06	1.69	0.81
133	P	2.2	2.7	0.2	8.4	3.3	1.14	1.40	0.08	3.53	1.54
134	P	3.5	4.1	0.3	10.3	6.0	0.51	0.63	0.03	1.65	0.87
135	P	3.7	4.3	0.3	11.1	6.4	0.42	0.53	0.03	1.89	0.77
136	P	2.1	2.6	0.2	4.7	2.8	0.51	0.60	0.07	1.85	0.86
137	P	1.8	2.2	0.1	3.5	2.1	1.31	1.62	0.24	2.30	0.64
138	P	1.8	2.1	0.3	2.3	1.2	0.75	0.88	0.11	1.42	0.54
139	P	1.9	2.2	0.3	2.7	1.3	0.31	0.36	0.04	0.75	0.25
140	P	1.9	2.3	0.3	2.9	1.2	0.10	0.12	0.02	0.31	0.12
*141	P	2.0	2.3	0.3	3.1	1.3	0.06	0.08	0.02	0.21	0.08
142	P	1.6	1.9	0.1	3.6	0.9	1.25	1.48	0.20	1.87	1.19
143	P	2.9	3.3	0.5	4.7	2.8	0.49	0.55	0.10	1.18	0.60
144	P	3.8	4.6	0.3	5.2	1.8	0.52	0.63	0.06	1.21	0.38
145	P	4.5	5.4	0.4	6.8	2.2	0.45	0.54	0.05	1.11	0.34
146	P	4.7	5.6	0.4	7.6	2.3	0.36	0.43	0.04	0.91	0.27
147	P	2.2	2.7	0.1	3.4	1.0	0.66	0.82	0.09	1.15	0.61
148	P	2.1	2.7	0.1	3.5	1.0	0.73	0.89	0.10	1.30	0.68
149	P	2.7	3.4	0.3	4.4	2.2	0.48	0.56	0.05	0.97	0.43
150	P	3.4	4.2	0.4	5.3	2.6	0.59	0.68	0.07	1.21	0.53
151	P	3.9	4.8	0.4	6.1	2.9	0.25	0.30	0.03	0.51	0.23
152	P	1.6	1.9	0.2	3.6	2.0	. . . not available . . .				
153	P	1.2	1.6	0.1	3.1	0.9	. . . not available . . .				
154	P	2.2	2.7	0.2	3.2	1.3	. . . not available . . .				
155	P	2.4	3.0	0.3	5.5	2.7	. . . not available . . .				

Notes: * signifies the existence of a corresponding time-series plot.

Water levels are referred to mean water level. The effects of tide must be added to the tsunami levels shown here.

Current speeds represent the rate of water flow averaged over the cross-sectional area of the fjord.

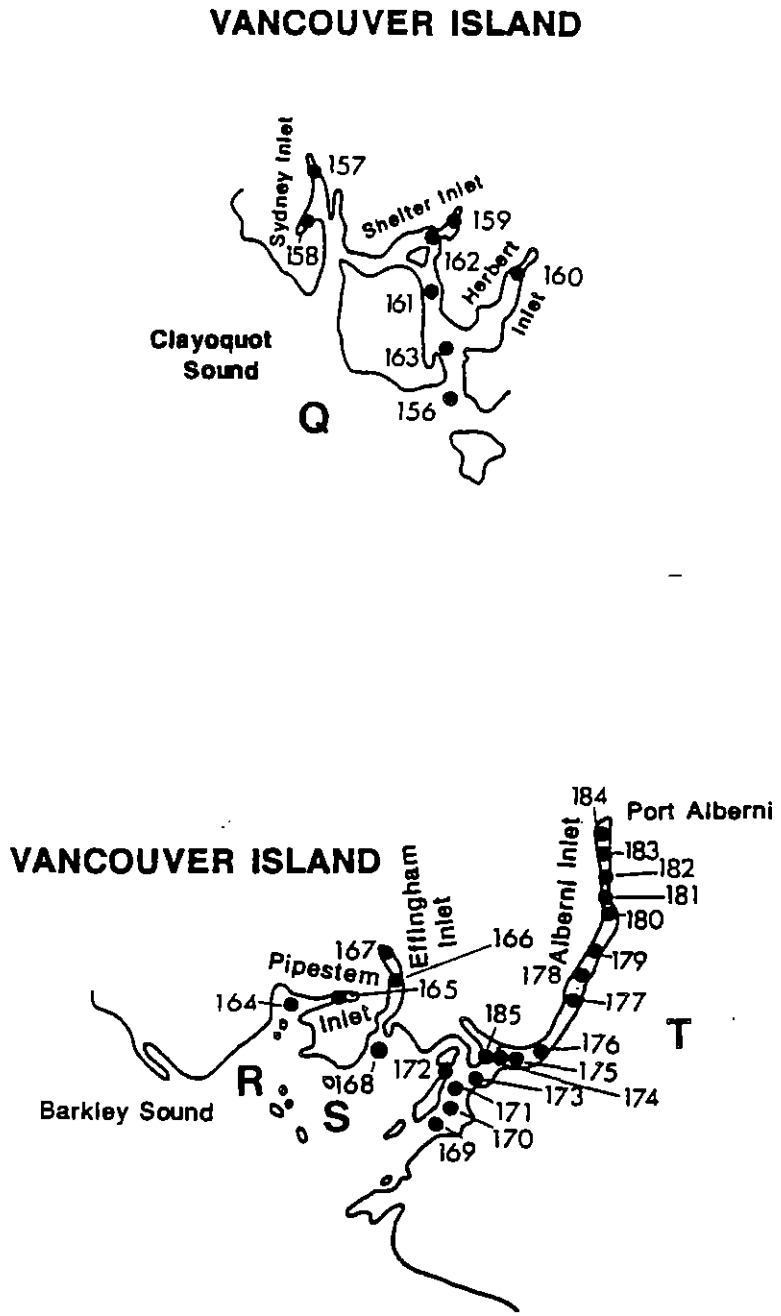

Fig. 7.19 Map showing water level and current locations listed in Table 7.11

Table 7.11

Maximum Tsunami Water Levels and Currents for Systems Q, R, S and T

Location No.	Inlet System	Source Region (Table 7.1) 1a	1b	2	3	4	Source Region (Table 7.1) 1a	1b	2	3	4
		Water Level (m)					Current Speed (m/s)				
*156	Q	0.8	0.9	0.1	1.4	0.6	0.65	0.74	0.09	1.31	0.73
157	Q	1.8	2.3	0.3	3.8	1.4	0.10	0.12	0.03	0.41	0.12
*158	Q	1.7	2.2	0.3	3.1	1.2	0.07	0.08	0.02	0.21	0.08
159	Q	1.1	1.4	0.1	2.8	1.0	0.05	0.06	0.01	0.18	0.05
160	Q	0.8	0.9	0.1	1.5	0.6	0.03	0.04	0.00	0.07	0.02
*161	Q	0.7	0.8	0.1	0.9	0.4	0.29	0.33	0.05	0.35	0.16
162	Q	1.0	1.4	0.1	2.5	0.9	. . . not available . . .				
163	Q	0.8	0.9	0.1	1.1	0.3	0.00	0.00	0.00	0.00	0.00
164	R	2.2	2.7	0.4	7.6	2.9	0.46	0.55	0.11	3.70	1.25
*165	R	3.0	3.6	0.4	5.2	2.3	0.18	0.22	0.06	0.95	0.43
166	S	2.3	3.1	0.3	4.5	1.2	0.22	0.25	0.02	0.33	0.17
*167	S	2.6	3.3	0.3	4.1	1.5	0.13	0.14	0.02	0.25	0.14
168	S	2.0	2.5	0.2	3.1	0.9	. . . not available . . .				
169	T	2.7	3.0	0.2	2.4	1.4	0.74	0.89	0.07	0.93	0.29
170	T	2.7	3.1	0.3	2.5	1.4	0.80	0.94	0.08	1.02	0.30
171	T	2.7	3.1	0.3	2.6	1.3	1.14	1.33	0.12	1.48	0.46
*172	T	2.3	2.6	0.2	3.3	1.0	1.53	1.73	0.13	2.16	1.04
173	T	2.8	3.2	0.3	2.9	1.0	0.99	1.19	0.12	1.46	0.65
*174	T	3.4	4.2	0.4	3.7	1.1	0.72	0.93	0.16	1.43	0.93
175	T	3.8	4.7	0.5	4.1	1.4	0.52	0.67	0.12	1.06	0.69
176	T	4.1	5.1	0.6	4.6	1.8	0.29	0.38	0.07	0.63	0.40
177	T	3.3	4.1	0.3	3.9	2.2	0.40	0.48	0.05	0.58	0.20
*178	T	3.5	4.3	0.3	3.9	2.2	0.80	0.95	0.11	1.51	0.57
*179	T	4.1	5.1	0.4	3.5	1.4	1.15	1.28	0.12	2.47	0.98
180	T	4.2	5.4	0.4	3.8	1.1	0.65	0.79	0.06	1.48	0.61
181	T	4.2	5.3	0.4	3.8	1.2	0.74	0.89	0.08	1.56	0.64
182	T	5.3	6.3	0.5	6.8	2.5	1.65	2.01	0.22	3.46	1.34
183	T	5.7	6.8	0.5	7.5	3.0	1.11	1.35	0.15	2.39	0.86
*184	T	6.2	7.4	0.6	8.3	3.6	0.93	1.17	0.12	2.14	0.67
185	T	3.0	3.4	0.3	3.0	1.1	. . . not available . . .				

Notes: * signifies the existence of a corresponding time-series plot.

Water levels are referred to mean water level. The effects of tide must be added to the tsunami levels shown here.

Current speeds represent the rate of water flow averaged over the cross-sectional area of the fjord.

It is interesting that the Alaska tsunami produces maximum water levels in System A. The Shumagin Gap tsunami is lower, which contrasts with all other systems (except B) where it generally provides the highest water levels. The reason for this difference lies in the shape of the waveforms in relation to the orientation and size of Dixon Entrance. The simulation results suggest that the extreme northern coast appears to be more vulnerable to tsunamis originating from northerly source regions in the Gulf of Alaska than to those with epicentres at more southerly latitudes.

A comparison of wave amplitudes and station locations reveals that the largest waves occur at, or near, the heads of the inlets. This is a general result for the reflecting boundaries imposed on the numerical solutions for each channel and is expected for actual tsunamis. In system A, the model results near the inlet entrance (e.g., stations 1, 15 and 36) are about 1 m; at the inlet head (e.g., stations 27, 30 and 35) wave amplitudes range between 2.8 and 3.3 m.

We note that the actual amplitude values right at inlet heads are sensitive to the reflecting boundary condition and the 2-km grid resolution used in FJORD1D. As a rule they will be overpredicted because the influence of overland flooding on wave dissipation has been neglected. The accuracy of tsunami water level predictions within 5 to 10 km of the heads of each inlet could be improved through use of local area high-resolution models that incorporate flooding and drying, or some other form of relaxation on the total reflective condition.

The maxima for systems B, C and D are given in Table 7.6. System B includes Chatham Sound and Prince Rupert. It is located just south of system A, and exhibits the same relationship between source location and wave heights (stations 40 to 45).

The largest results of all simulations were predicted for system C (Renell Sound) located on the west coast of the Queen Charlotte Islands (Graham Island). Exceptionally large values for both wave height and current speed were found for station 46 at the head of the sound which prompted a closer look at the results for this system. It was determined that the large values were due to the shape of Renell Sound, which resembles a funnel. The cross-sectional area of the inlet decreases rapidly toward the head, resulting in magnification of both currents and wave amplitudes as the wave propagates up the inlet. In the present numerical scheme, the grid spacing of the inlet model (2 km) does not adequately resolve such rapid changes in geometry. For this reason, the simulation results for station 46 have been discarded. A special high-resolution module would be required to yield satisfactory predictions at this location.

We see also that the Shumagin Gap simulation now produces the largest wave amplitudes in Systems C and D, with the Alaska simulations being next in size. Current speeds reach values exceeding 1 m/s at stations 41 and 42.

System E is the largest of those modelled, and contains the city of Kitimat. Maximum wave amplitudes given in Table 7.7 are modest throughout, ranging up to 2.5 m. Current speeds are small as well, being generally less than 1 m/s except at station 51, where a speed of 1.22 m/s is reached in the case of the Shumagin Gap simulation. The Shumagin Gap simulation also gives

generally higher water levels than the other four cases, although there are three minor exceptions (stations 53, 59 and 61). The results suggest that this area is fairly well protected from tsunamis originating from any of the sources selected for this study.

Table 7.8 presents results for systems F, G and H, which includes Ocean Falls. These systems are located to the south of system E and are considerably more exposed--through Queen Charlotte Sound--to tsunamis. This is reflected in the maximum water levels, which are substantially larger than those found further north. Generally the largest waves were produced by the Shumagin simulation, although the largest overall was found at station 73 and was generated by the Alaska simulation. Currents are strongest in the vicinity of stations 66, 67, 71 and 72.

Maximum wave amplitudes and currents for systems I, J, K and L are presented in Table 7.9. Systems I, J and K are on the mainland, just south of system F. System L represents the Rupert-Holberg-Neroutsos Inlet system on the northwest coast of Vancouver Island. Maxima are very small for system K because the entrance to the system is severely constricted, thus blocking the entry of much of the tsunami wave energy. Maxima-reach large values in systems I, J and L, with water levels in excess of 3 m and current speeds greater than 1.5 m/s at many of the stations in these systems. Exceptionally large values for both current and wave height were found at the heads of Forward (stations 114 and 115) and Neroutsos (station 104) Inlets. These results have been set aside for the same reasons cited earlier for Renell Sound. The grid spacing in the model is not fine enough to resolve the rapid changes in bathymetry and width that occur at these locations, nor is the influence of flooding at the inlet head considered.

Table 7.10 presents the maximum modelled wave amplitudes and current speeds for systems M, N, O, and P on the west coast of Vancouver Island. Without exception, the largest waves were generated in the Shumagin Gap simulation, with six values in excess of 10 m, and with current speeds exceeding 2 m/s at several locations. In system N the wave heights at the head of Quoukinsh Inlet are greater by a factor of three to five than those at the entrance, suggesting that local bathymetry is causing the wave to increase in amplitude along the length of the inlet. Large currents (>2 m/s) are found at the entrances to several of the inlets.

The final set of maximum wave heights and current speeds is presented in Table 7.11 for systems Q, R, S and T which includes Alberni Inlet and the city of Port Alberni. The largest amplitudes can be seen to occur for the Shumagin Gap simulation, although several exceptions to this occur. Heights increase toward the head of Alberni Inlet as expected, reaching up to 8.3 m. The differences in maxima for station 164 at the entrance to Pipestem Inlet is particularly striking, as the Shumagin simulation has generated a 7.6 m wave amplitude as opposed to the next largest water level of 2.7 m for the Alaska (x 1.25) simulation.

7.5 Tsunami Time-Series

The time-series graphs for the 39 special locations are contained in Appendix 1. All plots have the same horizontal scale showing the elapsed time (in hours) from the corresponding tsunamigenic earthquake. The

vertical scale shows wave height (in metres) from the mean, undisturbed water level (indicated by the horizontal line). Figure captions give the station number from Table 7.4, the inlet system code in parentheses, and the descriptive station name. The vertical range is nominally ±2 m; however, this has been adjusted upward or downward as required to better present the results for individual stations. Attention should be paid to this fact when examining the plots.

Within each simulation the time-series plots exhibit considerable variability in wave frequency, range, maximum height, and number of the largest wave. At some stations the signal appears regular and lacking high frequency oscillations (e.g., station 49; Alaska 1964). At other locations such as Ocean Falls (65) or in the Quatsino-Neroutsos Inlet system (101, 103) high frequency oscillations appear after the first two waveforms. In general, the tsunami waveform at each point depends strongly on the shape of the forcing wave at the inlet entrance and on local bathymetry, sheltering by islands and headlands, and interactions between incident and reflected waves within the inlet.

7.6 Summary of Results

Tables 7.12 and 7.13 summarize the extreme events to be found in Tables 7.5 through 7.11. Maximum wave heights in excess of 3 m and current speeds greater than 2 m/s have been extracted, and presented together with a location name.

Table 7.12

Summary of Extreme Maximum Tsunami Amplitudes

Location	Maximum Tsunami Height	Source Area
North Coast	3.5 m near the head of Khutzeymateen Inlet	Alaska
	3 to 3.5 m throughout Hastings Arm (north end of Observatory Inlet)	Alaska
	3.5 to 4 m near Stewart	Alaska
North Central Coast	3.5 to 4.5 m west of Princess Royal Island	Shumagin
	4.2 m in Cousins Inlet	Shumagin
	7.2 m at the head of Spiller Channel	Alaska
	5.6 m at the head of Laredo Sound	Shumagin
	3.3 m at the head of Surf Inlet	Shumagin
South Central Coast	3.3 to 9.2 m at the heads of Rivers and Moses Inlets	Shumagin
	6 to 9.3 m in Smith Inlet (increasing toward the head)	Alaska
Northwest coast of Vancouver Island	5.5 to 7.2 m in Quatsino Sound	Shumagin
	up to 9 m in Neroutsos Inlet	Shumagin
	8 to 8.5 m in Quatsino Narrows	Shumagin
	3.4 m at the head of Holberg Inlet	Shumagin
	6 to 7 m in Forward Inlet	
	5 to 6 m in Klaskino Inlet	Shumagin
	> 10 m at the head of Quoukinsh Inlet	Shumagin
Central Coast of Vancouver Island	3.5 to 4.5 m in Nuchalitz Inlet	Shumagin
	4.5 to >10 m in Muchalat and Tlupana inlets (increasing toward heads)	Shumagin
	3.5 to 4.5 m at south end of Tahsis Inlet	Shumagin
	3 m at the head of Tahsis Inlet	Shumagin
	3.6 to 7.6 m in Port Eliza and Espinosa inlets	Shumagin
	3.5 m in Nootka Sound	Shumagin
Southern Coast of Vancouver Island	3 to 4 m in Sydney Inlet	Shumagin
	4 to 8 m in Pipestem and Effingham inlets	Shumagin
	3 to 8 m in Alberni Inlet (increasing toward the head)	Shumagin

Table 7.13

Summary of Extreme Maximum Tsunami Wave Current Speeds

Location	Maximum Tsunami Current	Source Area
North Coast	2.3 m/s at entrance to Observatory Inlet	Alaska
North Central Coast	currents less than 2 m/s	n/a
South Central Coast	currents less than 2 m/s	n/a
Northwest Coast of Vancouver Island	2.5 to 4.7 m/s in Quatsino Narrows	Shumagin
	2.5 to >5 m/s near Port Alice on Neroutsos Inlet	Shumagin
	3 m/s at entrance to Forward Inlet	Shumagin
	3 m/s at entrance to Klaskino Inlet	Shumagin
	2 m/s in Quoukinsh Inlet	Shumagin
Central Coast of Vancouver Island	2.7 m/s at entrance to Muchalat Inlet	Shumagin
	2.5 to 3.5 m/s near entrance to Tlupana Inlet	Shumagin
	2.3 m/s at south end of Tahsis Inlet	Shumagin
Southern Coast of Vancouver Island	3.7 m/s at entrance to Pipestem Inlet	Shumagin
	2 to 3.5 m/s in Alberni Inlet	Shumagin

8.0 CONCLUSIONS AND RECOMMENDATIONS

The vulnerability of Canada's west coast to tsunamis generated in seismically active regions of the Pacific Rim provided the impetus for this study of tsunami hazard in British Columbia. Advanced numerical methods have been used to solve appropriate mathematical equations describing the generation and propagation of tsunamis. Three different computer models have been developed that calculate tsunami wave elevations and currents in the region of generation, along the propagation path across the Pacific Ocean basin, over the continental shelf, and into the complex inlet networks of British Columbia's coastline.

Past tsunamis have arrived at the British Columbia coast from several different source regions. Four of these have been investigated in this study in order to evaluate the potential for damage from a future tsunami. These source regions have been selected on the basis of previous large tsunamis (e.g., the Alaska 1964 earthquake and the Chile 1960 event), or the potential for producing large tsunamis (e.g., the Shumagin Gap). The damage potential from a tsunami is directly related to the amplitude of the largest wave (or waves) and, in some instances, to the magnitude of the associated current. Thus, at 185 key locations along the coast of British Columbia maximum modelled wave amplitude and current speed have been tabulated for each tsunami source. These results have led to the following conclusions:

(1) Generation and propagation of the initial tsunami wave crest to the heads of British Columbia's inlets can be modelled successfully using the mathematical equations and numerical models discussed in this report.

(2) Based on the simulation of the 1964 Alaska tsunami, the following estimates of model accuracy have been made. Wave arrival times are considered accurate to within 2%. Initial wave amplitude is accurate to within 20 cm, and is often much better (assuming the seabed displacement field is known exactly). Subsequent wave amplitudes are accurate to within approximately 50%. Wave period is accurate to within 15%.

(3) Tsunami wave heights are strongly influenced by source location and magnitude. Modelled earthquakes in the Shumagin Gap region of the Aleutian Islands and in the area of the 1964 Alaska earthquake produced the largest waves and strongest currents. These two areas were the closest sources, as well as the largest events modelled.

(4) Scaling the bottom displacement values results in a corresponding, approximately linear, scaling of wave heights; i.e., for a particular source area, a 20% increase in the amplitude of water displaced by the earthquake results in a 20% increase in maximum water levels.

(5) Chile, the furthest source point, produced the smallest waves, and is not considered a probable source of tsunamis greater than 1.5 m amplitude in the coastal inlets.

(6) The highest crest in a series of tsunami waves is often not the first to arrive. Consequently, the behaviour of a series of waves inside the

inlets must be predicted, which demands, in turn, a realistic treatment of boundary conditions, most especially the reflection condition at the landward end. More accurate modelling of extreme water levels near inlet heads that exhibit significant absorption of wave energy, or flooding of dry ground will require fine resolution, one- or two-dimensional submodels covering the area near the head of the inlet.

(7) In general, the largest modelled tsunamis resulted from a simulated earthquake in the Shumagin Gap region of the Aleutian Islands. The exception to this was along the extreme north coast of British Columbia where larger wave heights may be expected from a strong earthquake near the site of the Alaskan earthquake of 1964.

(8) Maximum modelled water levels vary significantly from one region to another along the coast. The following list summarizes the results for six geographic zones indicating critical areas that are subject to high water levels. In most cases (exceptions noted), these estimates are based on the occurrence of a very large tsunamigenic earthquake in the Shumagin Gap region of the Aleutian Islands.

- North Coast, Chatham Sound: (largest waves from the Alaska source location) generally from 3 to 4 m in Observatory Inlet; 4 m at Stewart; 3.5 m at other inlet heads.

- West Coast of Graham Island: extreme water levels exceeding 8 to 10 m at the head of Renell Sound. The shape of this inlet amplifies the wave energy.

- North Central Coast, Caamano Sound to Milbanke Sound: 3.5 to 4.5 m in Princess Royal Channel; up to 7 m at the head of Spiller Channel; amplitudes ranging between 4 and 6 m at Ocean Falls and in Laredo Inlet.

- South Central Coast, off Fitz Hugh Sound and Smith Sound: up to 9 m at the heads of Smith Inlet and Moses Inlet.

- Northwest Coast of Vancouver Island, Quatsino Sound: 5.5 to 7 m in Quatsino Sound; up to 9 m in Neroutsos Inlet; 8.5 m in Quatsino Narrows.

- Central Coast of Vancouver Island, Checloset Bay to Nootka Sound: extreme water levels of 10 m or more at the head of Quoukinsh Inlet; up to 10 m at heads of Machalat and Tlupana Inlets; up to 7 or 8 m in Espinosa Inlet; 4.5 to 5 m at Port Eliza.

- South Coast of Vancouver Island, Clayoquot Sound to Barkley Sound: 3 to 4 m in Sydney Inlet; up to 8 m at the head of Alberni Inlet, 7 to 8 m in Pipestem Inlet, and 4 to 4.5 m in Effingham Inlet.

(9) The principal limitation to estimating tsunami wave heights more accurately for particular sources is the uncertainty associated with specifying the final bottom displacements that will result for an earthquake occurring at that source.

(10) The model developed in this study runs slower than real-time because of its implementation on a microprocessor. It is suitable for tsunami hindcasting, but not for real-time forecasting. However, it provides reasonably accurate estimates of arrival time and the tsunami effect all along the coast for the first few waveforms; this is a great deal more information than is presently available from tsunami forecasting systems. Restructuring of the software and installation on a supercomputer could, conceivably, overcome the constraint of long execution times, and permit forecasting of expected tsunami wave heights for real tsunamigenic events. The usefulness of such a system would depend on a reasonably accurate model for bottom displacements. An elliptical model oriented along known fault lines in the source areas, with displaced volume related to earthquake magnitude would provide a useful starting point.

We have demonstrated that numerical models can be used to successfully estimate tsunami water levels and currents in British Columbia's inlets starting from distant source points. The critical input to the model is the ground motion resulting from the earthquake: its maximum displacement and volume are the important parameters. It is difficult at present to specify these parameters with precision in a predictive sense (i.e., for earthquakes that have not yet occurred). Furthermore, it is very difficult to associate a probability of occurrence with these parameters at each potential earthquake location. Nevertheless, an assessment of tsunami risk along the British Columbia coast requires this type of information in conjuction with the numerical model.

Improvements can also be made to the numerical models and their application in the inlets, designed to increase the accuracy of the results. Such improvements are focused on the continental shelf and the inlet systems. The deep ocean model performance appears satisfactory as formulated.

The foregoing considerations lead to recommendations in six areas:

(1) Research to improve understanding of earthquake ground motion is recommended. The objectives of such research include parameterization of the types of motion that are possible in each potential earthquake area, and the probability of occurrence of the parameter values. Given the likelihood that destructive tsunamis will originate around the northern Pacific Rim, attention should initially be directed at source points there.

(2) This study has considered distant earthquakes; however, it has been hypothesized that a local earthquake in the Fuca plate subduction zone could also generate a severe tsunami. This type of event could be modelled using the techniques developed here. Simulation of locally-generated tsunamis, originating at locations with a high likelihood of seismic activity, is recommended. Such simulations would provide greater confidence in the maximum wave amplitudes developed in this study.

(3) Improvements in model accuracy should focus, as a first priority, on the treatment of flooding/drying areas within the inlet systems. In most of the inlets examined in this study, local-area high-resolution

models are required, typically at the inlet head, to refine the water level criteria.

(4) As a second step, water level accuracy in certain systems, which are close to resonance, would be improved by higher resolution of the entrance to the inlet and improved coupling between the shelf and fjord models. A case in point is Barkley Sound, a complicated area composed of many small islands and deep channels, with multiple connections to Alberni Inlet. This system is only partially resolved in the present model.

(5) Further evaluation of tsunami water levels should also consider the influence of tides. Tidal forcing applied along the shelf model boundary can be coupled with tsunami levels from the deep ocean model to give a combined simulation over the shelf and up into the fjords. Simulations can be phased to combine tidal high water with the tsunami crest elevations, providing an estimate of maximum probable combined water level in a dynamically coupled calculation. This type of modelling should be done in conjunction with improved treatment of flooding in the inlets.

(6) The feasibility of developing a real-time tsunami forecasting system using an adaptation of the present model should be considered. Execution time on a mainframe supercomputer (such as a CRAY XMP or a CYBER 205) would be short enough to allow prediction of wave heights for actual tsunamigenic events, including consideration of accurate tidal fluctuations. The critical component of such a system would be the prescribed bottom displacement field used to initiate the propagation of the tsunami. Simple transfer functions relating earthquake magnitude and area to displacement volume may be adequate to provide reasonable estimates of maximum expected water levels along the British Columbia coast. The first steps in such a feasibility study would be to investigate the effect of source parameterization (shape, area, orientation, and volume of water) on calculated water levels, and to establish the expected forecast lead times for earthquakes in Alaska and the Aleutian Islands, using a supercomputer.

9.0 REFERENCES

Abbott, M.B., 1975. Method of Characteristics. Chapter 3 in Unsteady Flow in Open Channels (Mahmood, K. and V. Yevjevich, Ed.). Water Resources Publications, Colorado, 63-88.

Chwang, A.T. and H. Power, 1983. Focusing and Reflection of a Cylindrical Solitary Wave, in Tsunamis: Their Science and Engineering (Lida, K. and T. Iwasaki, Ed.). Terra Scientific Publishing Company, Tokyo, 251-263.

Comer, R.P., 1980. Tsunami Height and Earthquake Magnitude: Theoretical Basis of an Empirical Relation. Geophys. Res. Letters, 7(6), 445-448.

Crean, P.B., 1976. Numerical Model studies of the Tides Between Vancouver Island and the Mainland Coast. J. Fish Res. Board Can., 33, 2340-2344.

Davies, J., L. Sykes, L. House and K. Jacob, 1981. Shumagin Seismic Gap, Alaska Peninsula: History of Great Earthquakes, Tectonic Setting, and Evidence for High Seismic Potential. J. Geophys. Res., 86(B5), 3821-3855.

Dronkers, J.J., 1964. Tidal Computations in Rivers and Coastal Waters. North Holland Publishing Co., Amsterdam.

Flather, R.A. and N.S. Heaps, 1975. Tidal Computations for Morecambe Bay. Geophys. J. R. Astr. Soc., 42, 489-517.

Hammack, J.L., 1973. A Note on Tsunamis: Their Generation and Propagation in an Ocean of Uniform Depth. J. Fluid Mech., 60(4), 769-799.

Henry, R.F. and T.S. Murty, 1973. Resonance Periods of Multi-Branched Inlets with Tsunami Amplification. Trans. Tsunami Symmp., XV General Assembly I.U.G.G., Moscow (August 1971), Yuzhno-Sakhalinsk.

Hodgins, D.O. and S.L.M. Hodgins, 1986. Dalhousie Harbour Siltation Study, Physical Oceanographic Program (1985) and Numerical Hydraulic Modelling. Subcontractor report prepared for Public Works Canada on behalf of Eastern Designers & Company Limited, Fredericton, N.B.

Hodgins, S.L.M., 1977. An Improved Computational Method for The Shallow Water Wave Equations Based on the Leendertse (1967) Finite Difference Scheme. SINTEF Report No. STF60 A77058, River and Harbour Laboratory, Trondheim, Norway.

Hwang, L. and D. Divoky, 1970. Tsunami Generation. J. Geophys. Res., 75(33), 6802-6817.

Ippen, A.T., 1966. Estuary and Coastline Hydrodynamics. McGraw-Hill Book Company, Inc., New York.

Leendertse, J.J., 1967. Aspects of a Computational Method for Long-period Water-wave Propagation. The Rand Corp RM-5294-PR.

Marshall, Macklin Monaghan, 1986. Development Management in Tsunami Hazard Areas of Port Alberni. Consultants report prepared for the City of Port Alberni.

Peregrine, D.H., 1967. Long Waves on a Beach. J. Fluid Mech., 27(4), 815-927.

Plafker, G., 1969. Tectonics of the March 27, 1964 Alaska Earthquake. Geological Survey Professional Paper 543-I, U.S. Government Printing Office, Washington.

Plafker, G. and J.C. Savage, 1970. Mechanism of the Chilean Earthquakes of May 21 and 22, 1960. Geolog. Soc. Am. Bull., 81, 1001-1030.

Power, H. and A.T. Chwang, 1984. On Reflection of a Planar Solitary Wave at a Vertical Wall. Wave Motion (6), 183-195.

Seabra-Santos, F.J., 1985. Contribution a l'Etude des Ondes de Gravite Bidimensionelles en Eau Peu Profonde. Ph.D. thesis, Grenoble, France.

Schwiderski, E.W. and L.T. Szeto, 1981. The NSWC Global Ocean Tide Data Tape (GOTD), Its Features and Application, Random-Point Tide Program. Naval Surface Weapons Center, Report NSWC TR 81-254.

Spaeth, M.G. and S.C. Berkman, 1967 The Tsunami of March 28, 1964, as Recorded at Tide Stations. Coast and Geodetic Survey Technical Bulletin No. 33, U.S. Department of Commerce, Environmental Science Services Administration, Rockville, Md.

Ursell, F., 1953. The Long-wave Paradox in the Theory of Gravity Waves. Proc. Camb. Phil. Soc., 49, 685-694.

Wigen, S.O., 1981. Historical Study of Tsunamis at Tofino, Canada. Presented at the International Tsunami Symposium, 1981 I.U.G.G. Tsunami Commission. (Subsequently published 1983 in Tsunamis: Their Science and Engineering (Lida, K. and T. Iwasaki, Ed.), Terra Scientific Publishing Company, Tokyo, 105-119.)

Wigen, S.O. and W.R.H. White, 1964. Tsunami of March 27-29, 1964 West Coast of Canada. Unpublished report of the Department of Mines and Technical Surveys, Ottawa.

APPENDIX 1

Time-series water level plots for selected locations along the British Columbia Coast.

(refer to Fig. 7.13 to 7.19 for a map showing these locations)

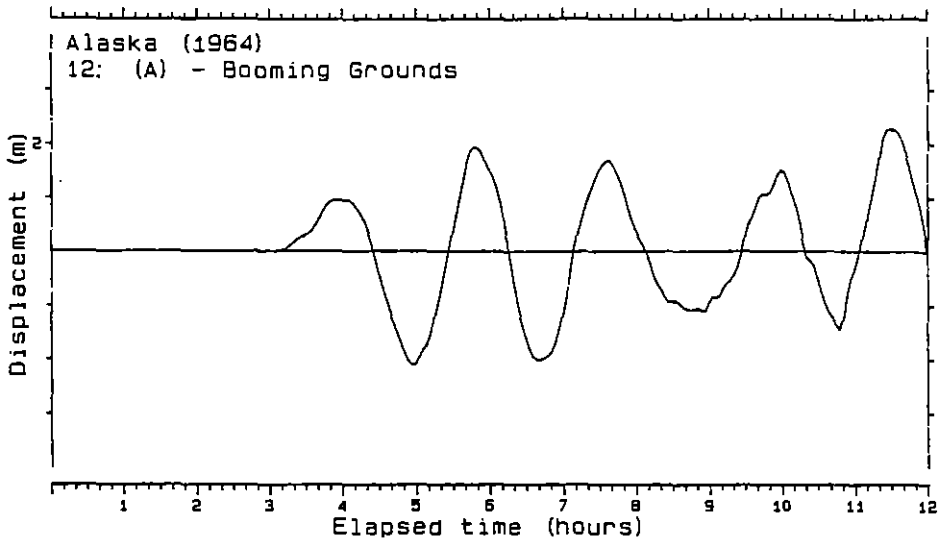
Alaska (1964)
12: (A) - Booming Grounds
Displacement (m)
2
1 2 3 4 5 6 7 8 9 10 11 12
Elapsed time (hours)

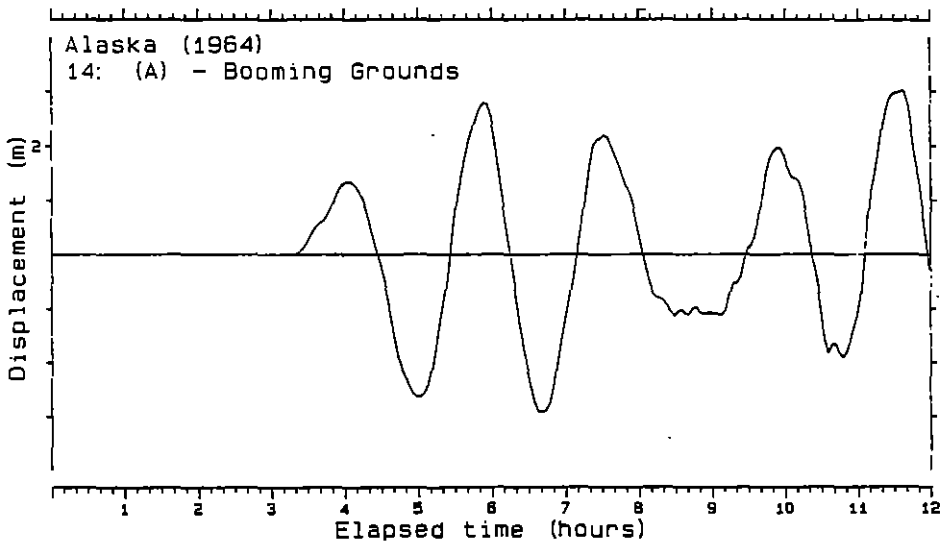
Alaska (1964)
14: (A) - Booming Grounds
Displacement (m)
2
1 2 3 4 5 6 7 8 9 10 11 12
Elapsed time (hours)

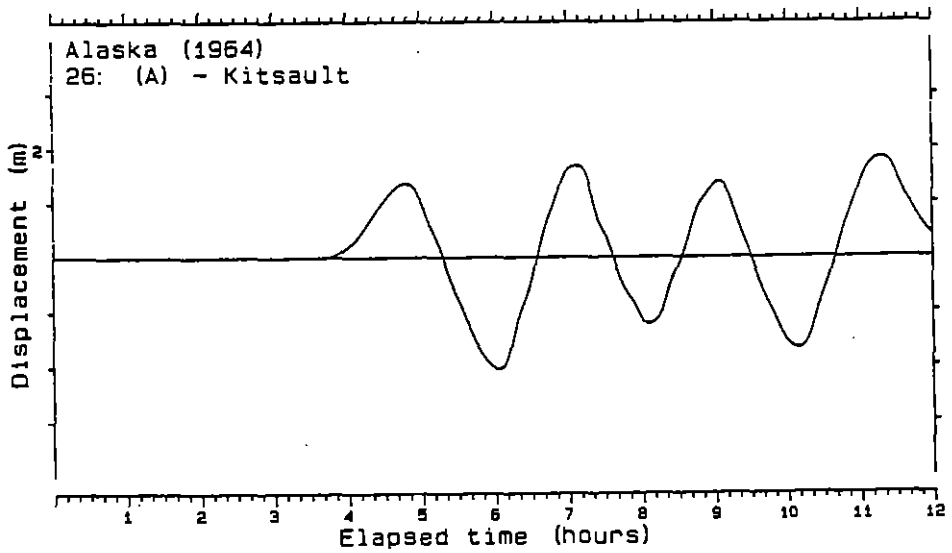
Alaska (1964)
26: (A) - Kitsault
Displacement (m)
2
1 2 3 4 5 6 7 8 9 10 11 12
Elapsed time (hours)

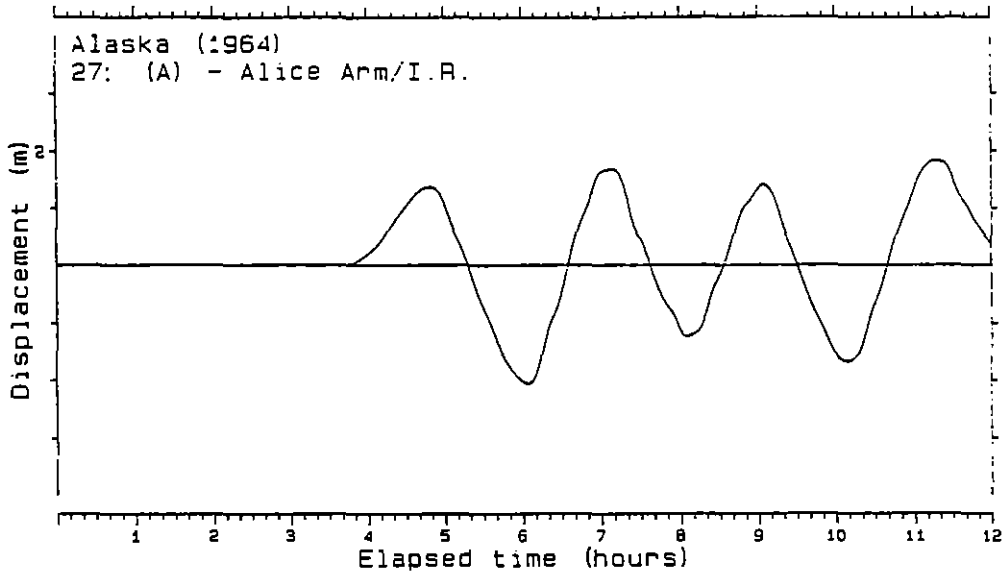
Alaska (1964)
27: (A) - Alice Arm/I.R.
Displacement (m)
2
1 2 3 4 5 6 7 8 9 10 11 12
Elapsed time (hours)

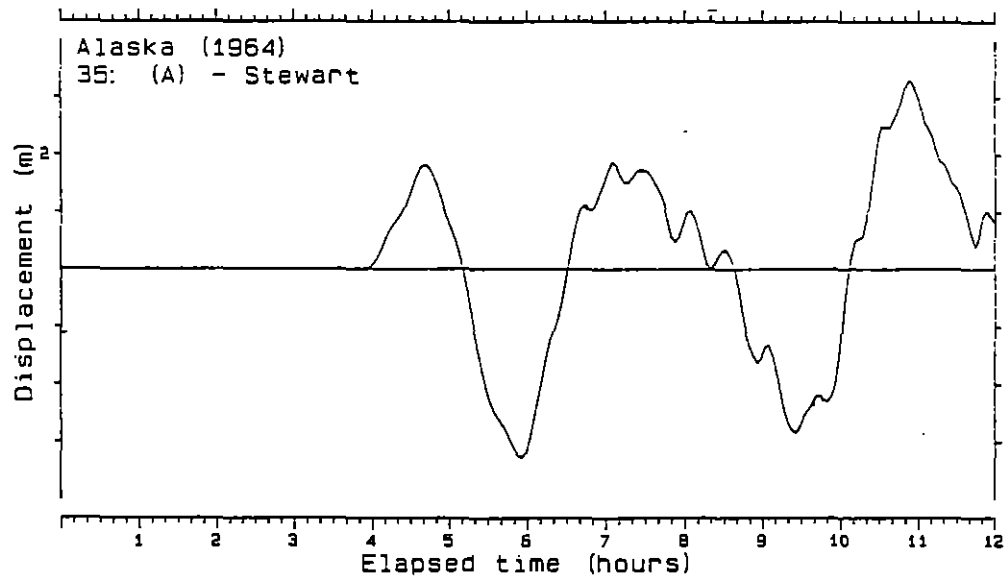
Alaska (1964)
35: (A) - Stewart
Displacement (m)
2
1 2 3 4 5 6 7 8 9 10 11 12
Elapsed time (hours)

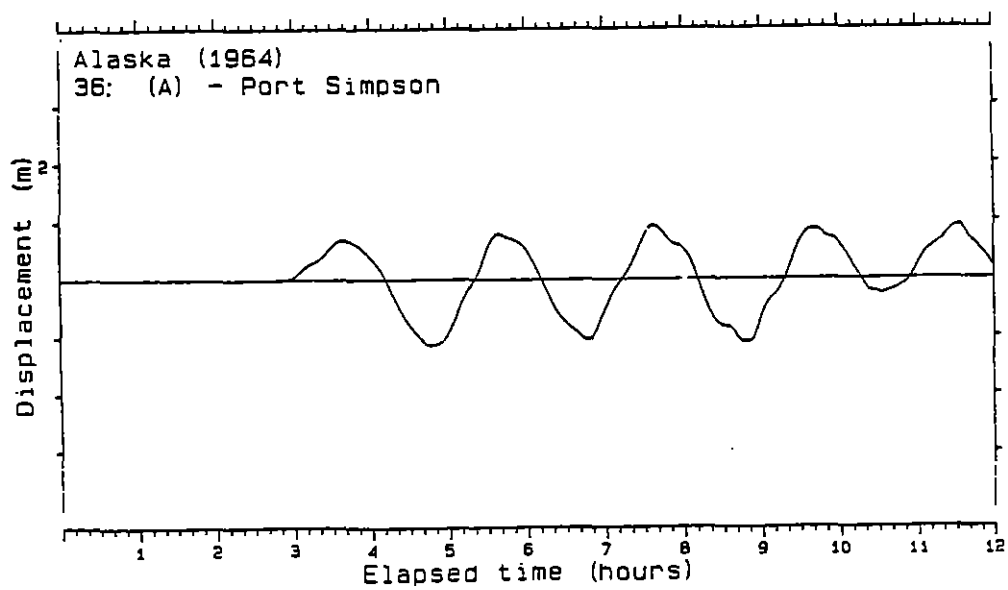
Alaska (1964)
36: (A) - Port Simpson
Displacement (m)
2
1 2 3 4 5 6 7 8 9 10 11 12
Elapsed time (hours)

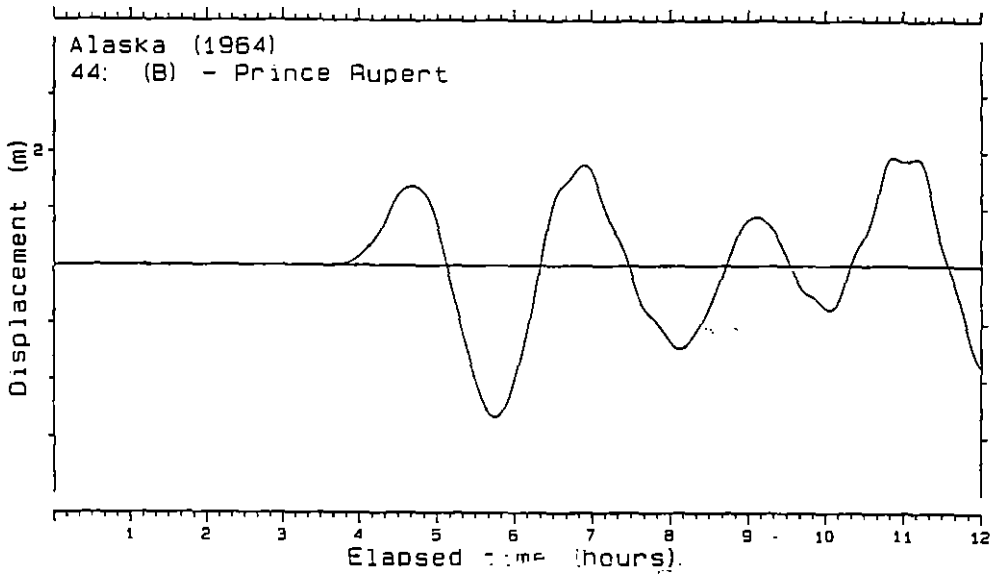
Alaska (1964)
44: (B) - Prince Rupert
Displacement (m)
2
1 2 3 4 5 6 7 8 9 10 11 12
Elapsed time (hours)

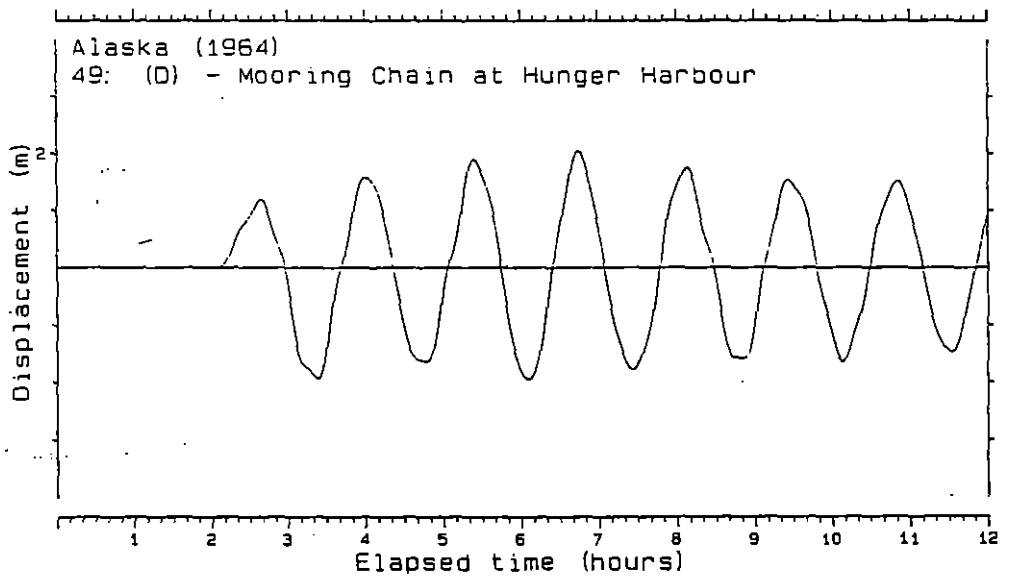
Alaska (1964)
49: (D) - Mooring Chain at Hunger Harbour
Displacement (m)
2
1 2 3 4 5 6 7 8 9 10 11 12
Elapsed time (hours)

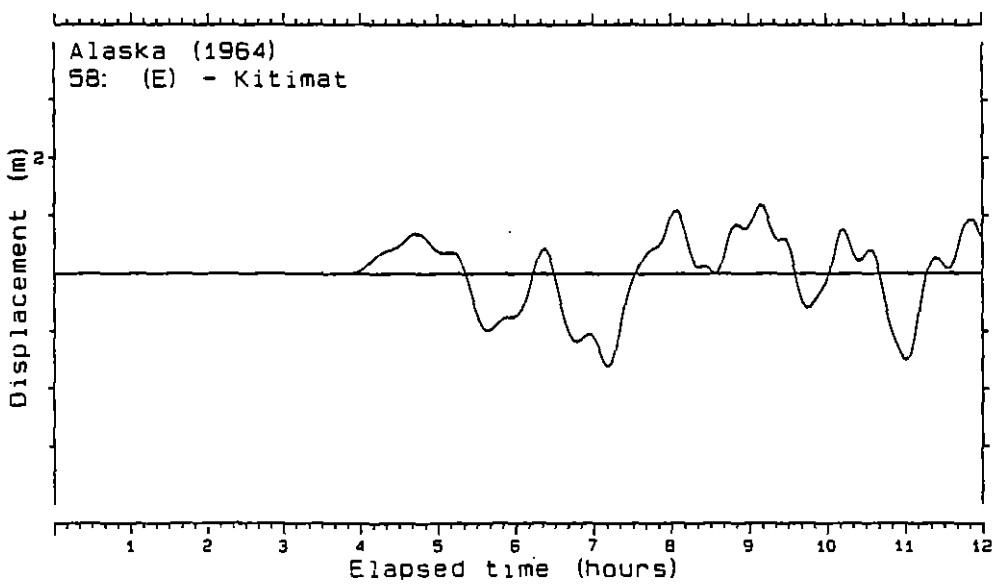
Alaska (1964)
58: (E) - Kitimat
Displacement (m)
2
1 2 3 4 5 6 7 8 9 10 11 12
Elapsed time (hours)

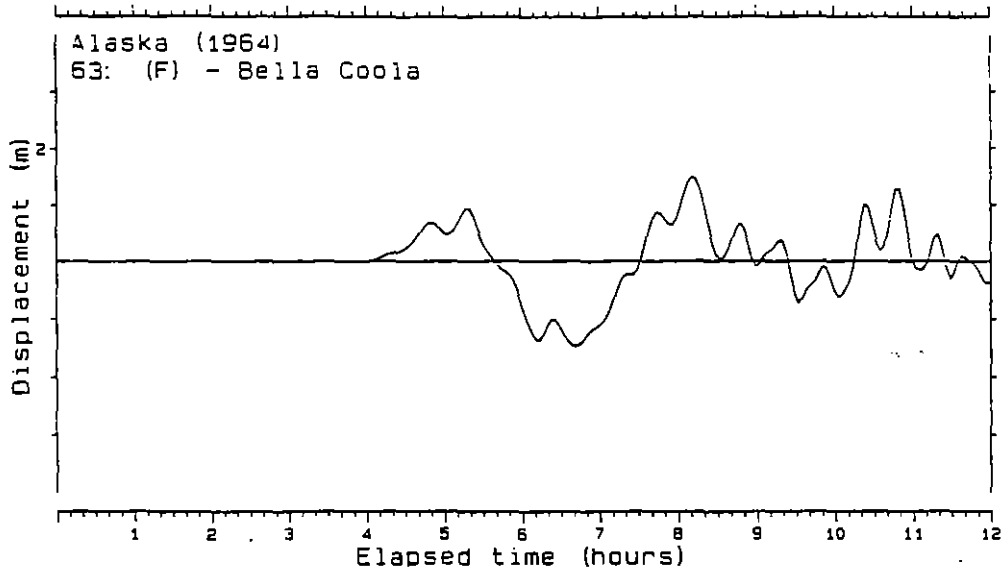
Alaska (1964)
63: (F) - Bella Coola
Displacement (m)
2
1 2 3 4 5 6 7 8 9 10 11 12
Elapsed time (hours)

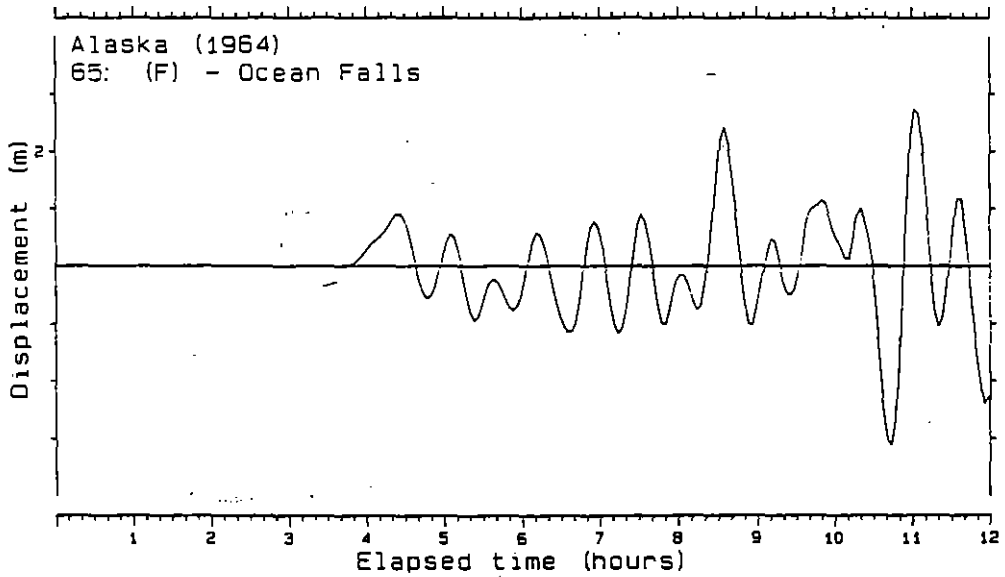
Alaska (1964)
65: (F) - Ocean Falls
Displacement (m)
2
1 2 3 4 5 6 7 8 9 10 11 12
Elapsed time (hours)

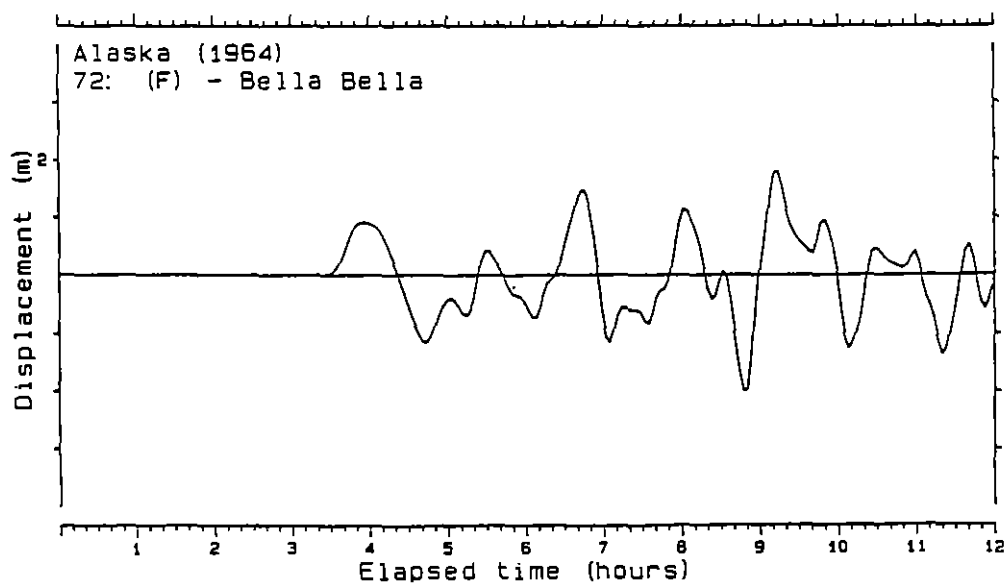
Alaska (1964)
72: (F) - Bella Bella
Displacement (m)
2
1 2 3 4 5 6 7 8 9 10 11 12
Elapsed time (hours)

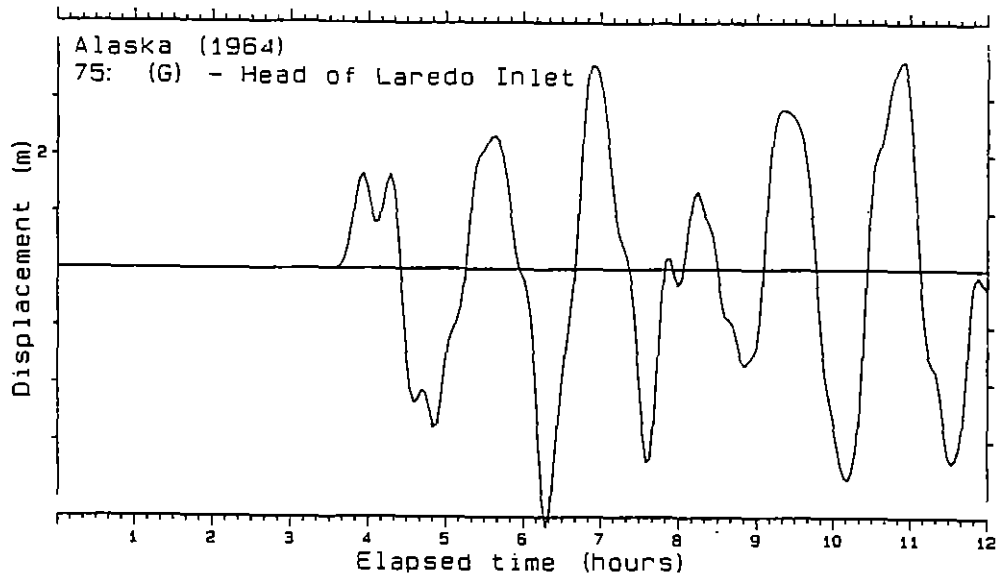
Alaska (1964)
75: (G) - Head of Laredo Inlet
Displacement (m)
2
1 2 3 4 5 6 7 8 9 10 11 12
Elapsed time (hours)

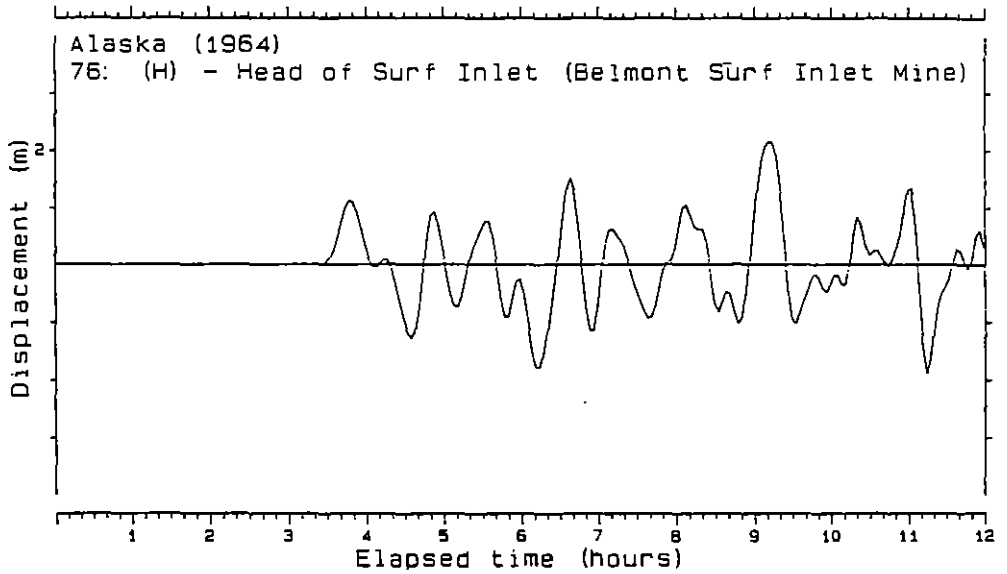
Alaska (1964)
76: (H) - Head of Surf Inlet (Belmont Surf Inlet Mine)
Displacement (m)
2
1 2 3 4 5 6 7 8 9 10 11 12
Elapsed time (hours)

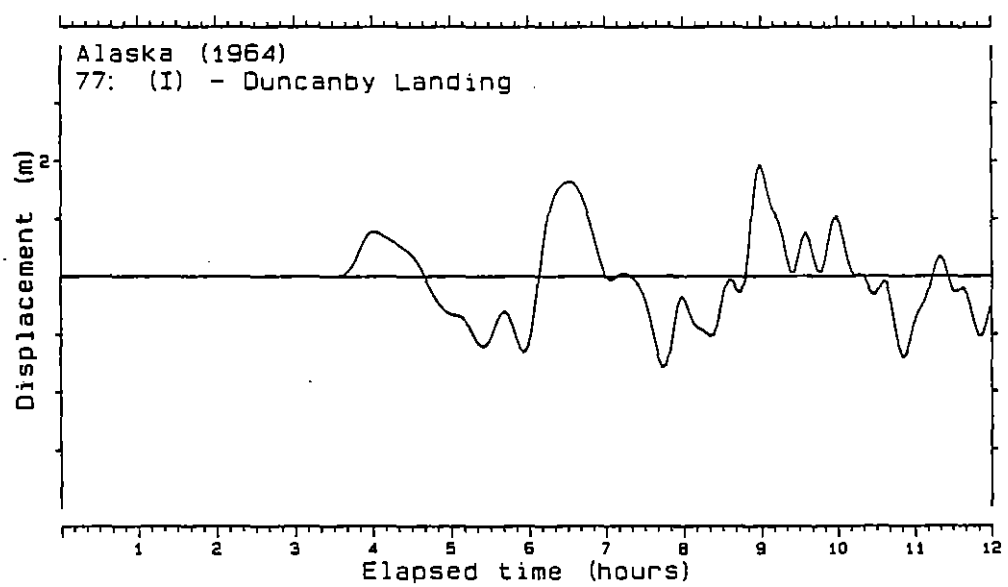
Alaska (1964)
77: (I) - Duncanby Landing
Displacement (m)
2
1 2 3 4 5 6 7 8 9 10 11 12
Elapsed time (hours)

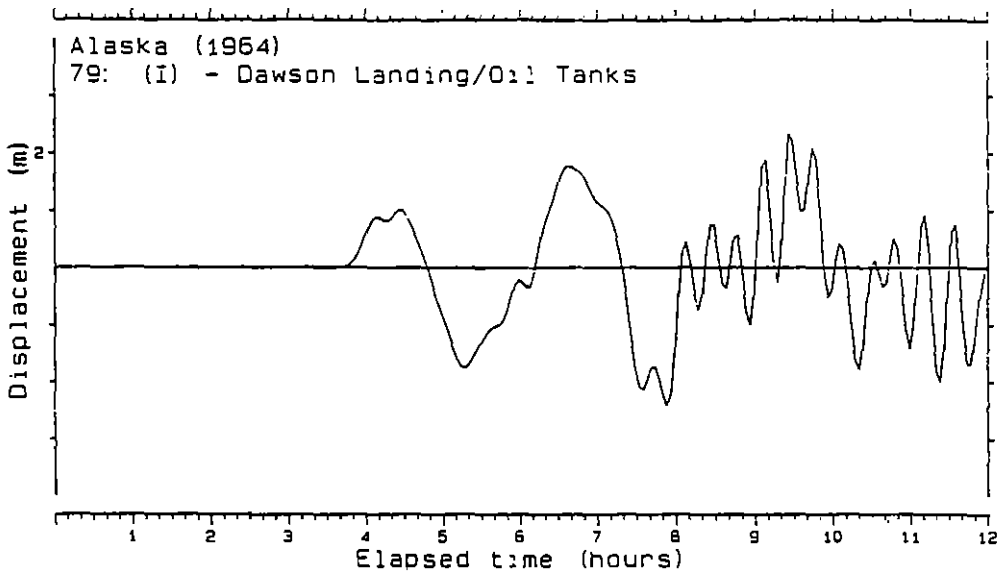
Alaska (1964)
79: (I) - Dawson Landing/Oil Tanks
Displacement (m)
2
1 2 3 4 5 6 7 8 9 10 11 12
Elapsed time (hours)

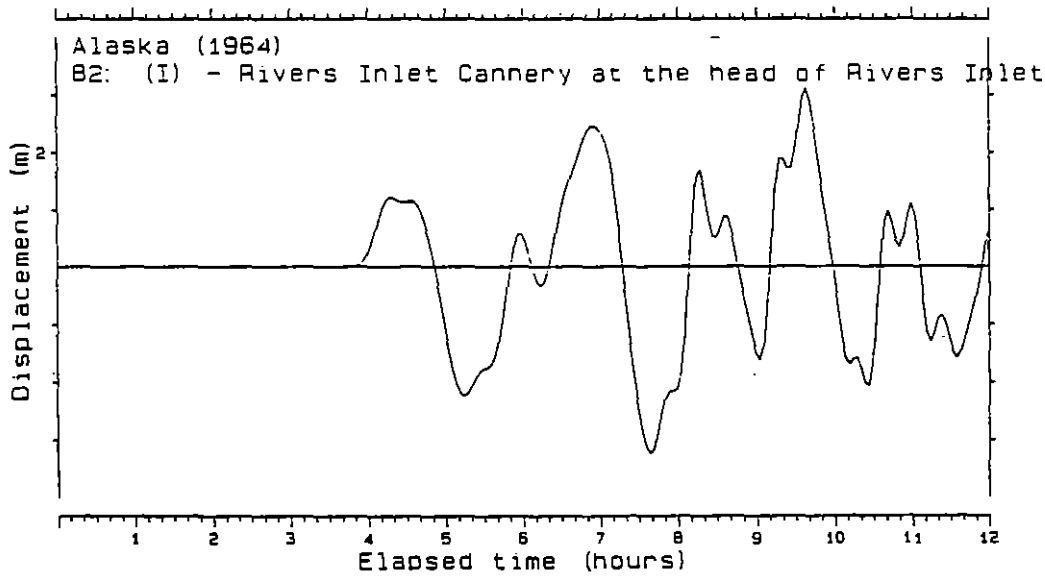
Alaska (1964)
82: (I) - Rivers Inlet Cannery at the head of Rivers Inlet
Displacement (m)
2
1 2 3 4 5 6 7 8 9 10 11 12
Elapsed time (hours)

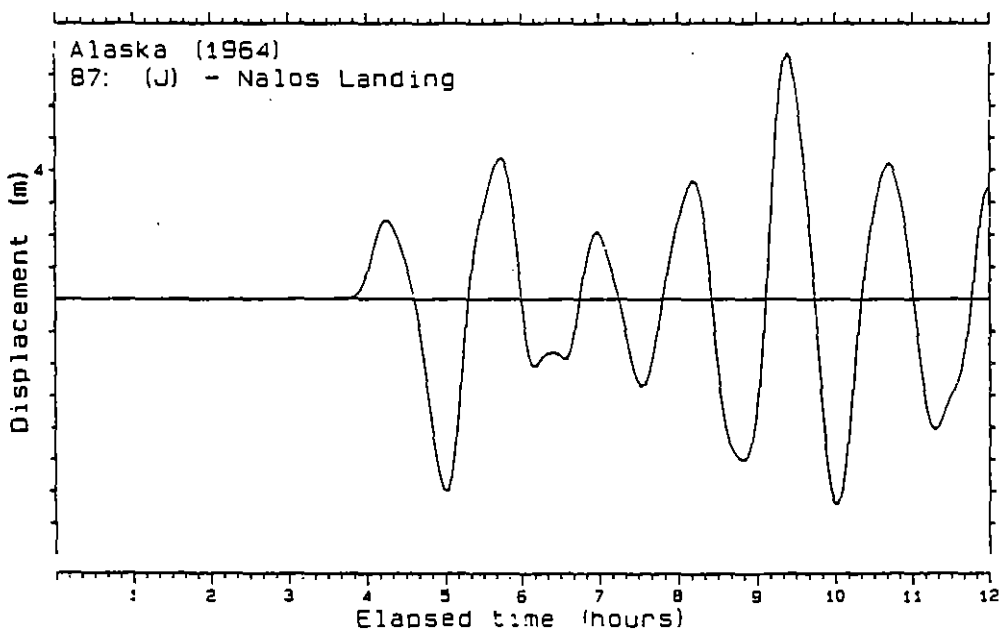
Alaska (1964)
87: (J) - Nalos Landing
Displacement (m)
4
1 2 3 4 5 6 7 8 9 10 11 12
Elapsed time (hours)

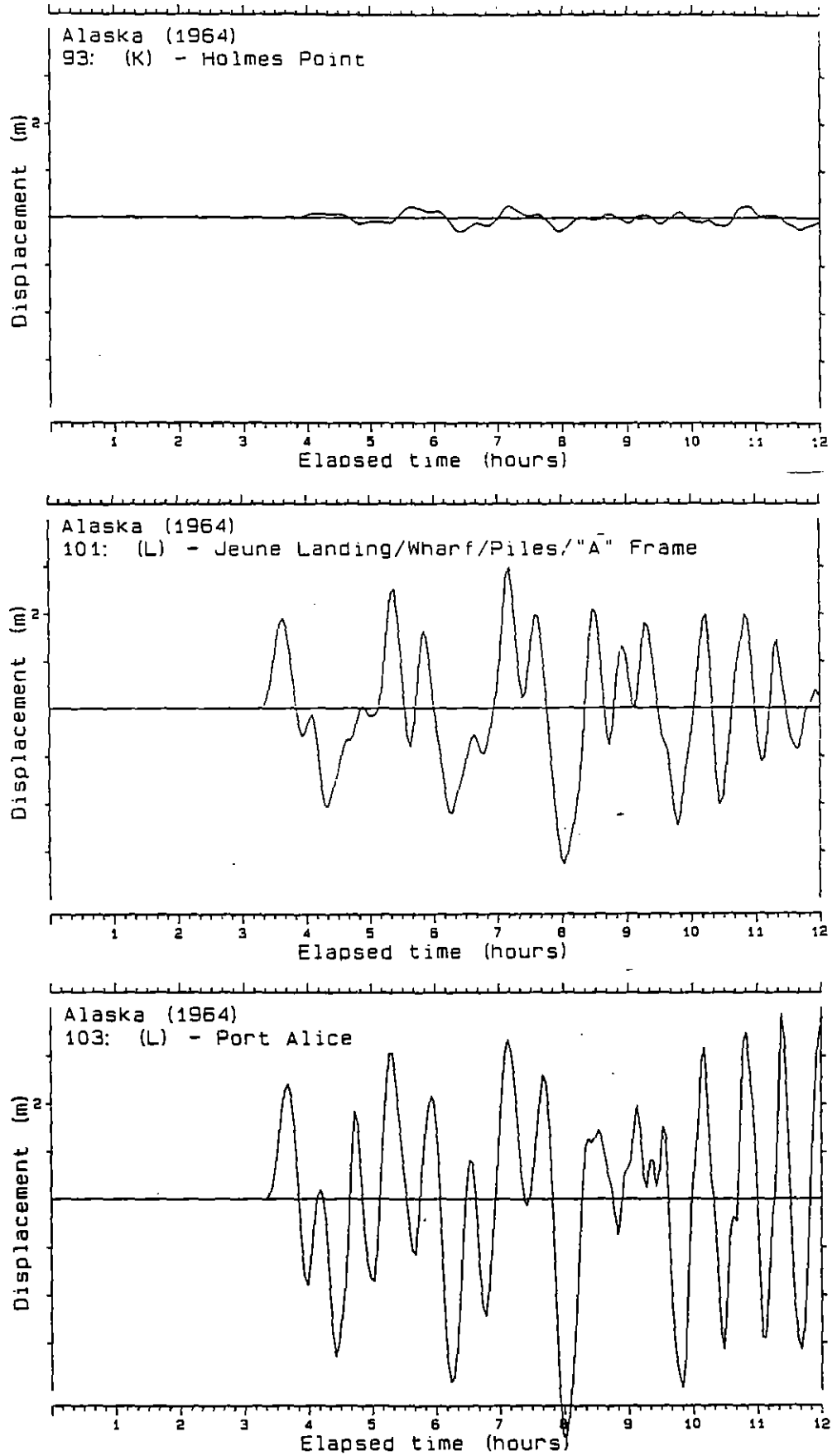
Alaska (1964)
93: (K) - Holmes Point
Displacement (m)
2
1 2 3 4 5 6 7 8 9 10 11 12
Elapsed time (hours)
Alaska (1964)
101: (L) - Jeune Landing/Wharf/Piles/"A" Frame
Displacement (m)
2
1 2 3 4 5 6 7 8 9 10 11 12
Elapsed time (hours)
Alaska (1964)
103: (L) - Port Alice
Displacement (m)
2
1 2 3 4 5 6 7 8 9 10 11 12
Elapsed time (hours)

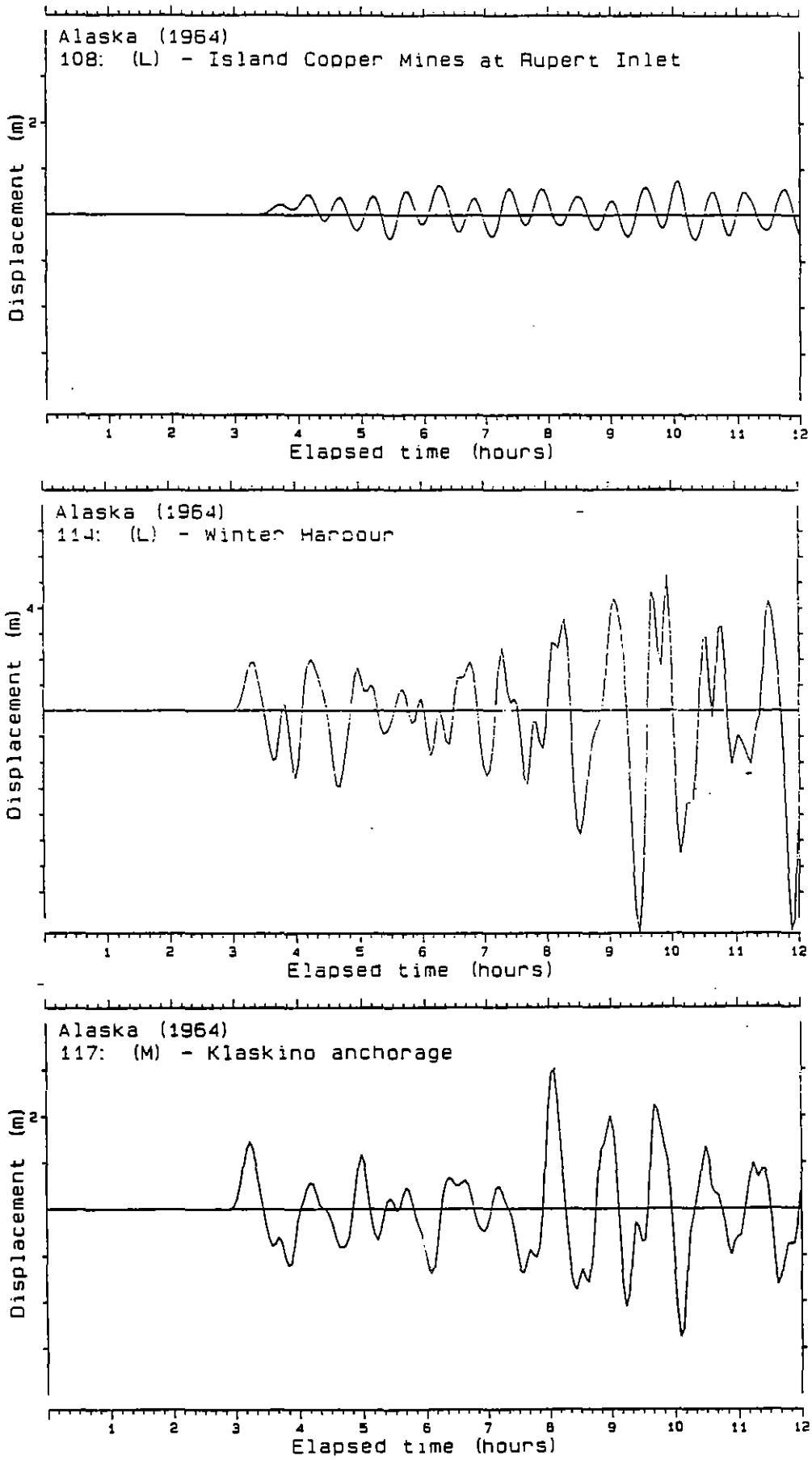
Alaska (1964)
108: (L) - Island Copper Mines at Rupert Inlet
Displacement (m)
2
1 2 3 4 5 6 7 8 9 10 11 12
Elapsed time (hours)
Alaska (1964)
114: (L) - Winter Harbour
Displacement (m)
4
1 2 3 4 5 6 7 8 9 10 11 12
Elapsed time (hours)
Alaska (1964)
117: (M) - Klaskino anchorage
Displacement (m)
2
1 2 3 4 5 6 7 8 9 10 11 12
Elapsed time (hours)

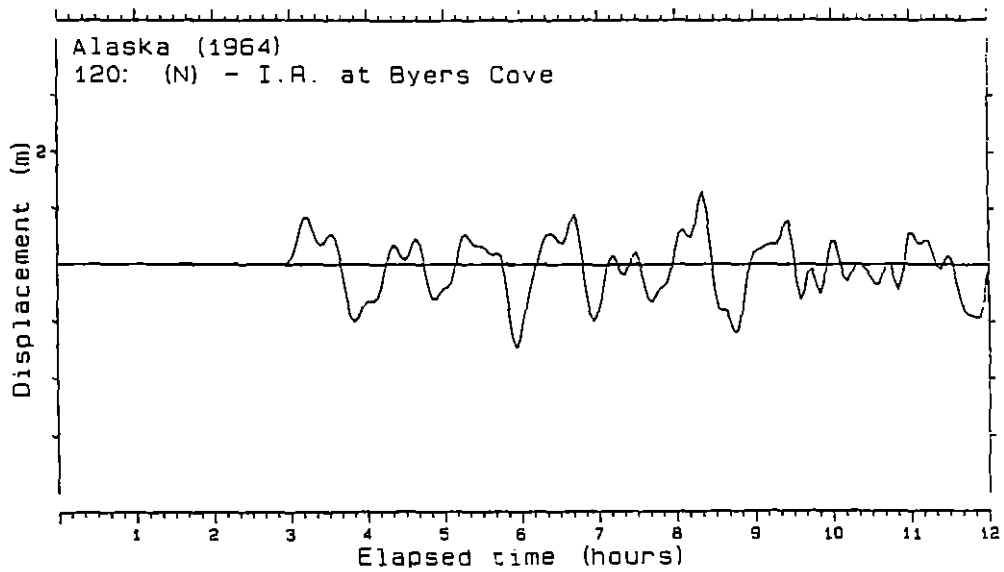
Alaska (1964)
120: (N) - I.R. at Byers Cove
Displacement (m)
2
1 2 3 4 5 6 7 8 9 10 11 12
Elapsed time (hours)

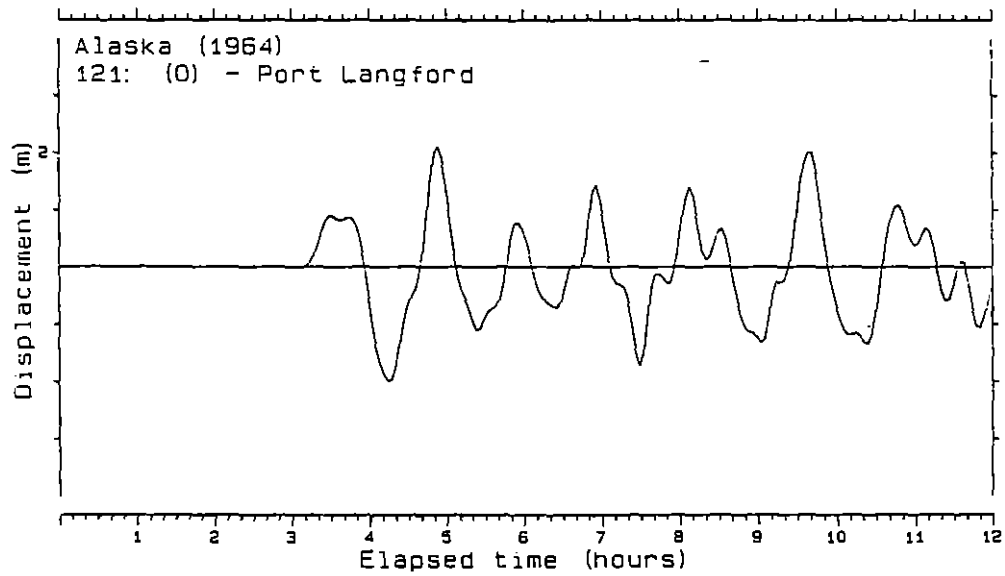
Alaska (1964)
121: (0) - Port Langford
Displacement (m)
2
1 2 3 4 5 6 7 8 9 10 11 12
Elapsed time (hours)

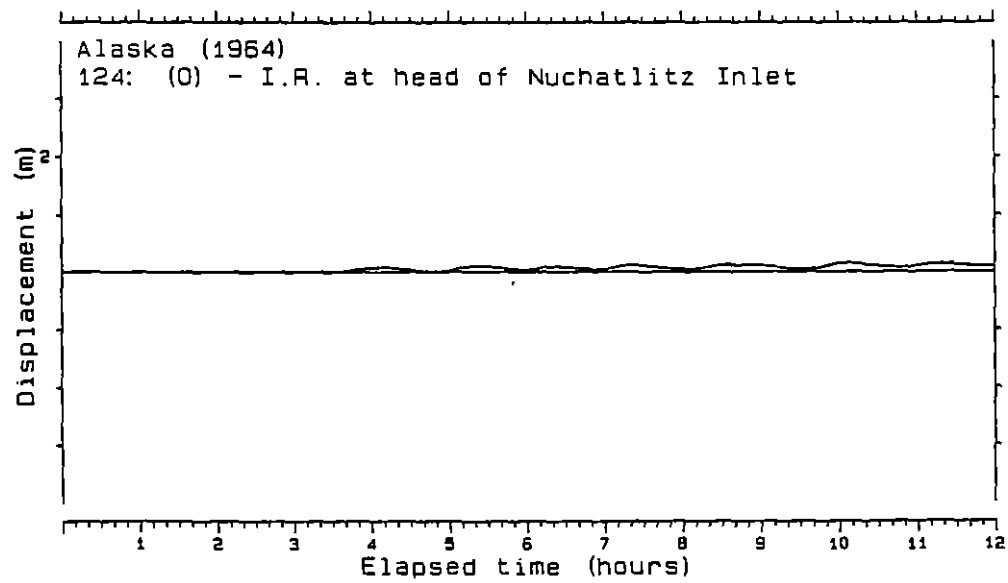
Alaska (1964)
124: (0) - I.R. at head of Nuchatlitz Inlet
Displacement (m)
2
1 2 3 4 5 6 7 8 9 10 11 12
Elapsed time (hours)

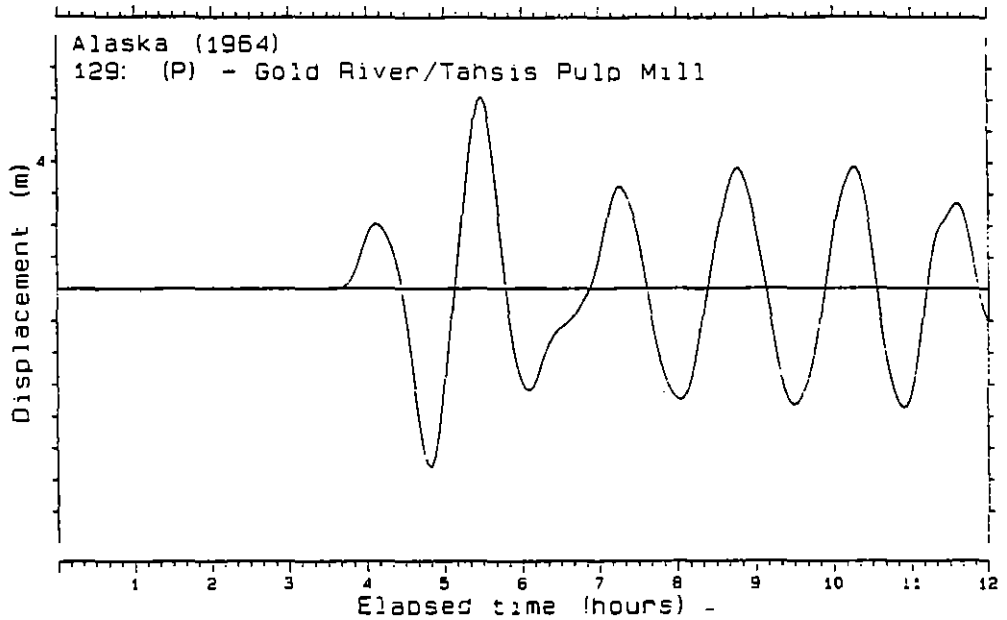
Alaska (1964)
129: (P) - Gold River/Tahsis Pulp Mill
Displacement (m)
4
1 2 3 4 5 6 7 8 9 10 11 12
Elapsed time (hours)

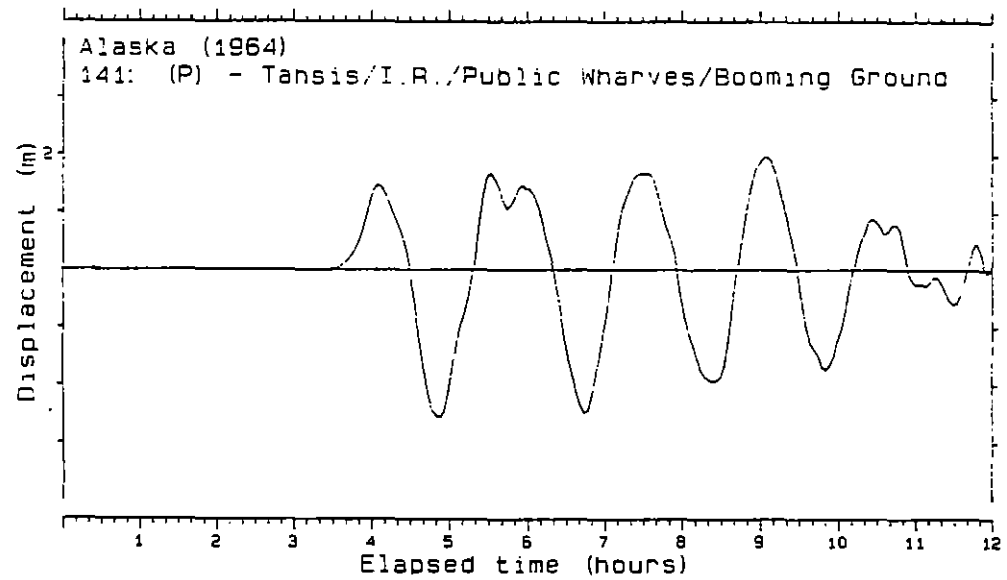
Alaska (1964)
141: (P) - Tahsis/I.R./Public Wharves/Booming Ground
Displacement (m)
2
1 2 3 4 5 6 7 8 9 10 11 12
Elapsed time (hours)

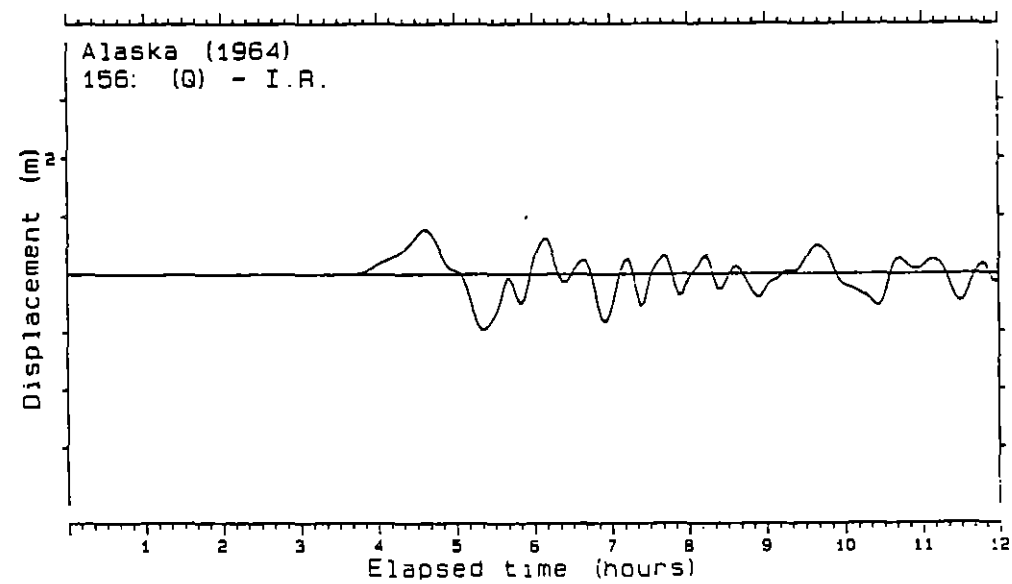
Alaska (1964)
156: (Q) - I.R.
Displacement (m)
2
1 2 3 4 5 6 7 8 9 10 11 12
Elapsed time (hours)

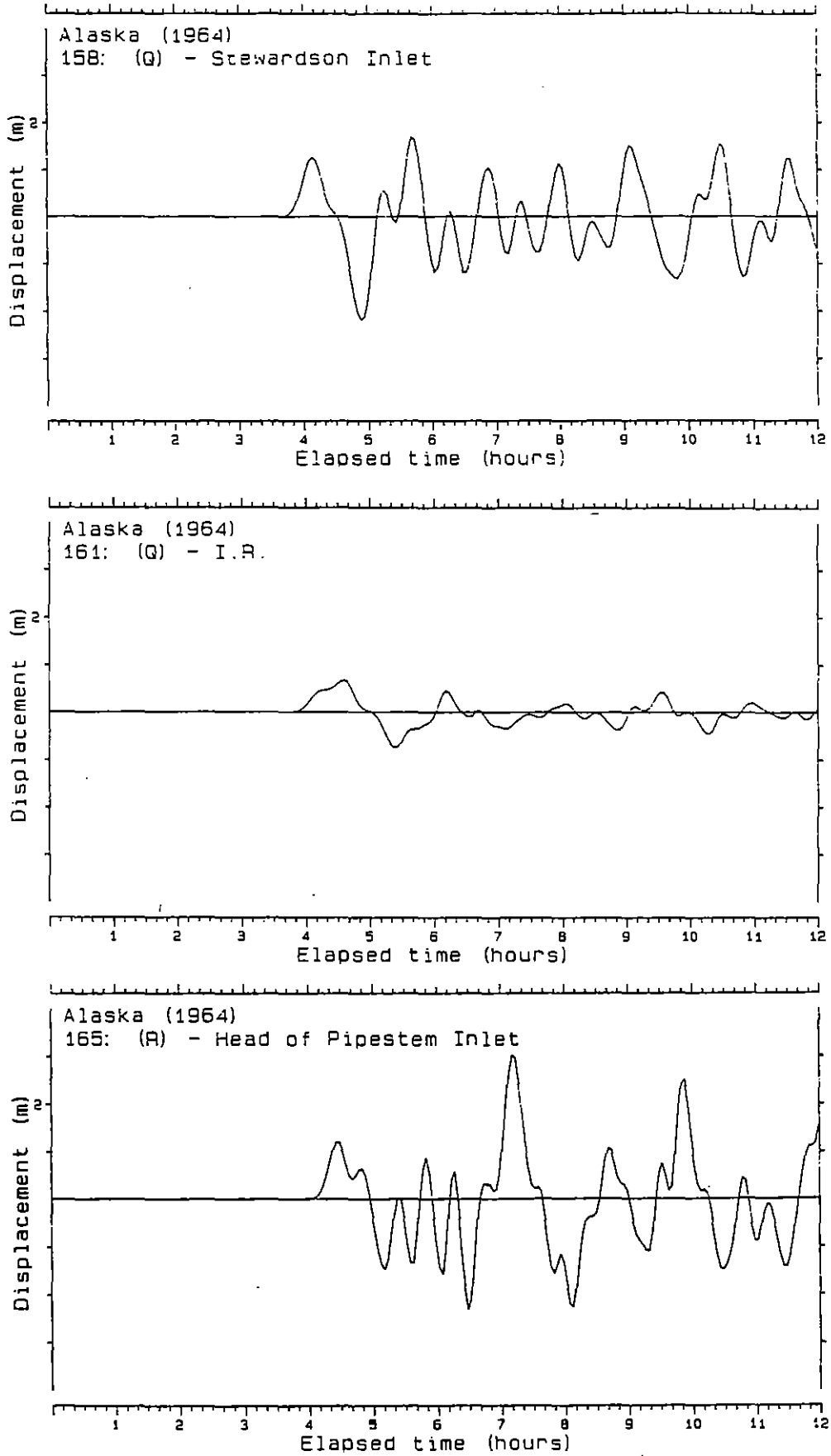
Alaska (1964)
158: (Q) - Stewardson Inlet
Displacement (m)
2
1 2 3 4 5 6 7 8 9 10 11 12
Elapsed time (hours)
Alaska (1964)
161: (Q) - I.R.
Displacement (m)
2
1 2 3 4 5 6 7 8 9 10 11 12
Elapsed time (hours)
Alaska (1964)
165: (A) - Head of Pipestem Inlet
Displacement (m)
2
1 2 3 4 5 6 7 8 9 10 11 12
Elapsed time (hours)

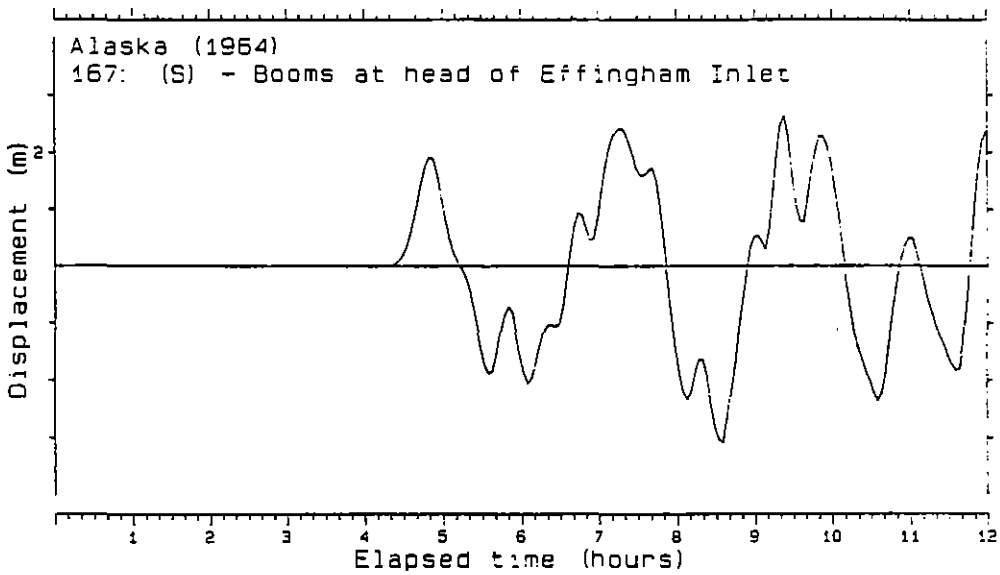
Alaska (1964)
167: (S) - Booms at head of Effingham Inlet
Displacement (m)
2
1 2 3 4 5 6 7 8 9 10 11 12
Elapsed time (hours)

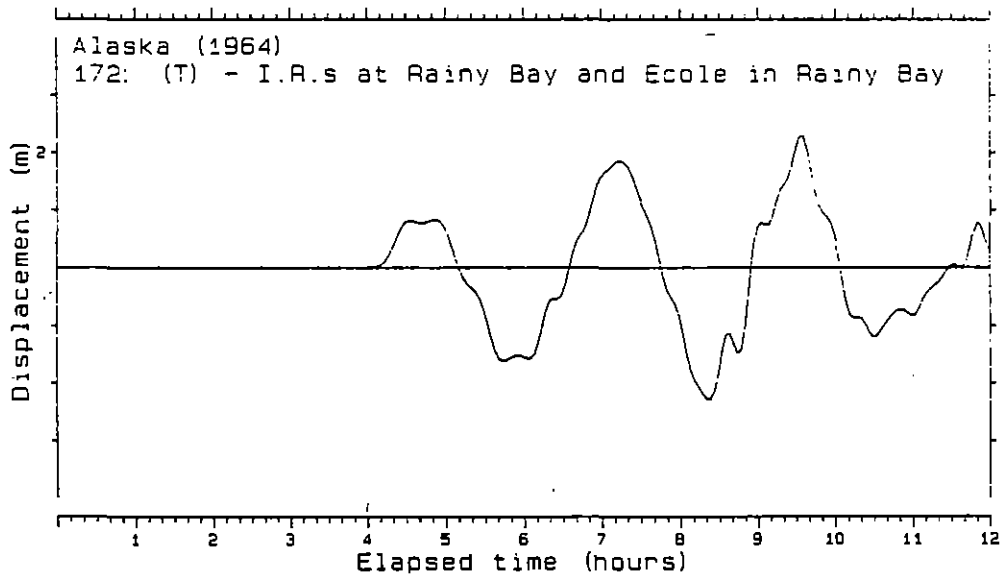
Alaska (1964)
172: (T) - I.R.s at Rainy Bay and Ecole in Rainy Bay
Displacement (m)
2
1 2 3 4 5 6 7 8 9 10 11 12
Elapsed time (hours)

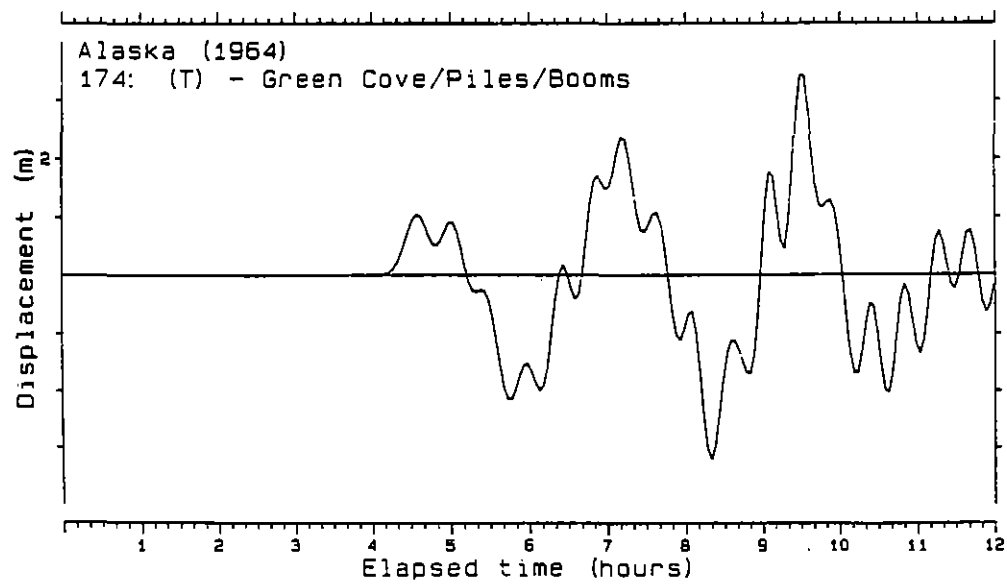
Alaska (1964)
174: (T) - Green Cove/Piles/Booms
Displacement (m)
2
1 2 3 4 5 6 7 8 9 10 11 12
Elapsed time (hours)

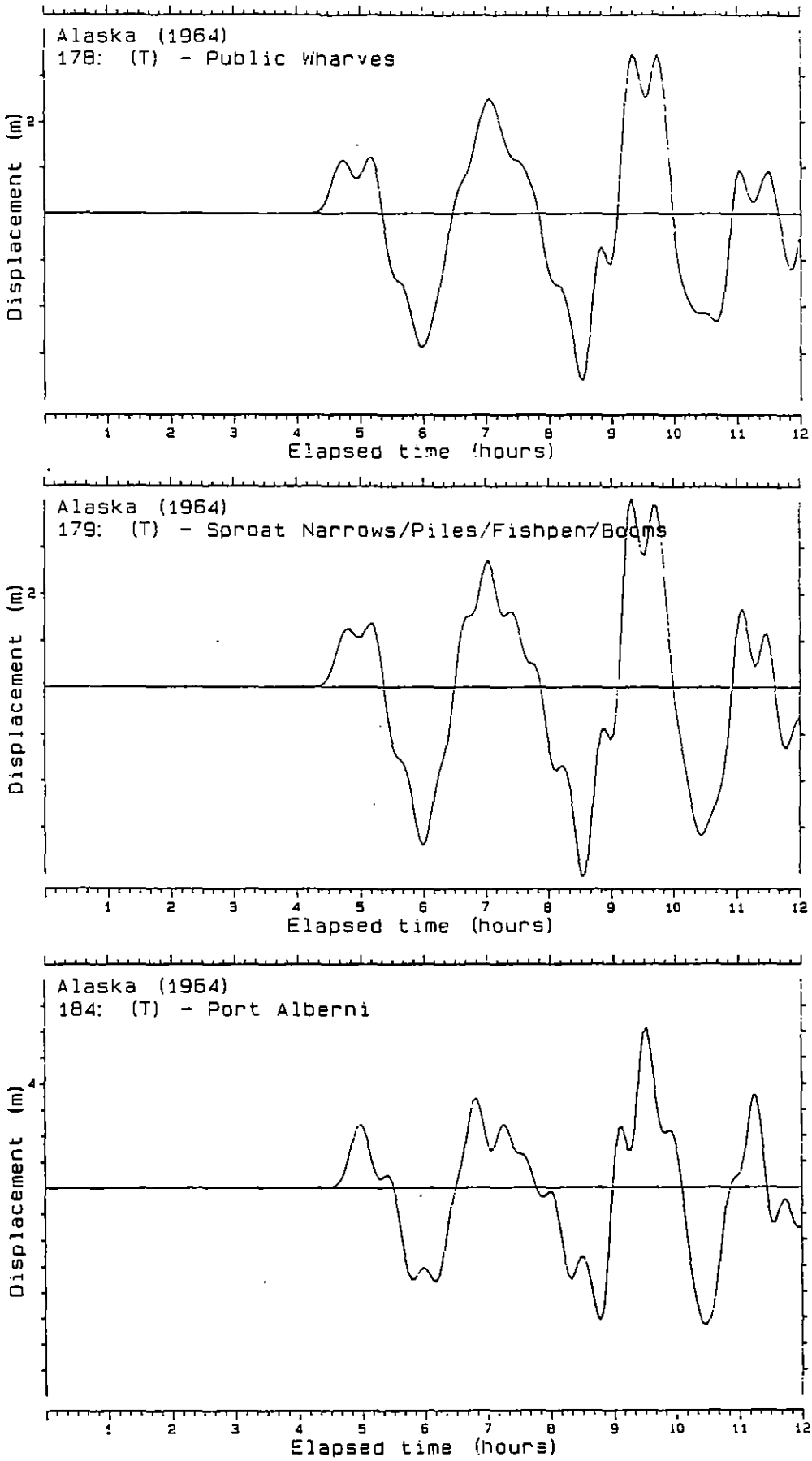
Alaska (1964)
178: (T) - Public Wharves
Displacement (m)
2
1 2 3 4 5 6 7 8 9 10 11 12
Elapsed time (hours)
Alaska (1964)
179: (T) - Sproat Narrows/Piles/Fishpen/Booms
Displacement (m)
2
1 2 3 4 5 6 7 8 9 10 11 12
Elapsed time (hours)
Alaska (1964)
184: (T) - Port Alberni
Displacement (m)
4
1 2 3 4 5 6 7 8 9 10 11 12
Elapsed time (hours)

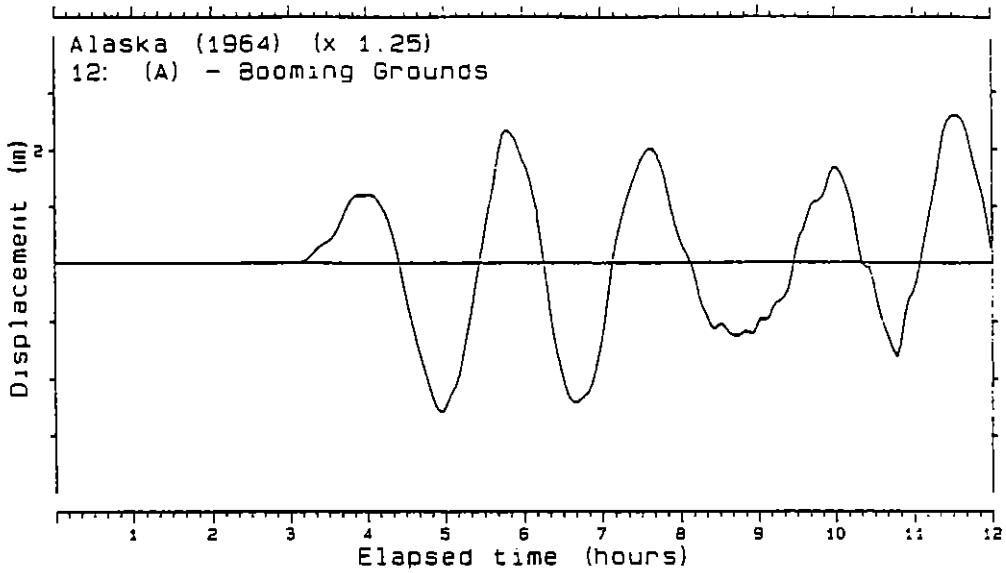
Alaska (1964) (x 1.25)
12: (A) - Booming Grounds
Displacement (m)
2
1 2 3 4 5 6 7 8 9 10 11 12
Elapsed time (hours)

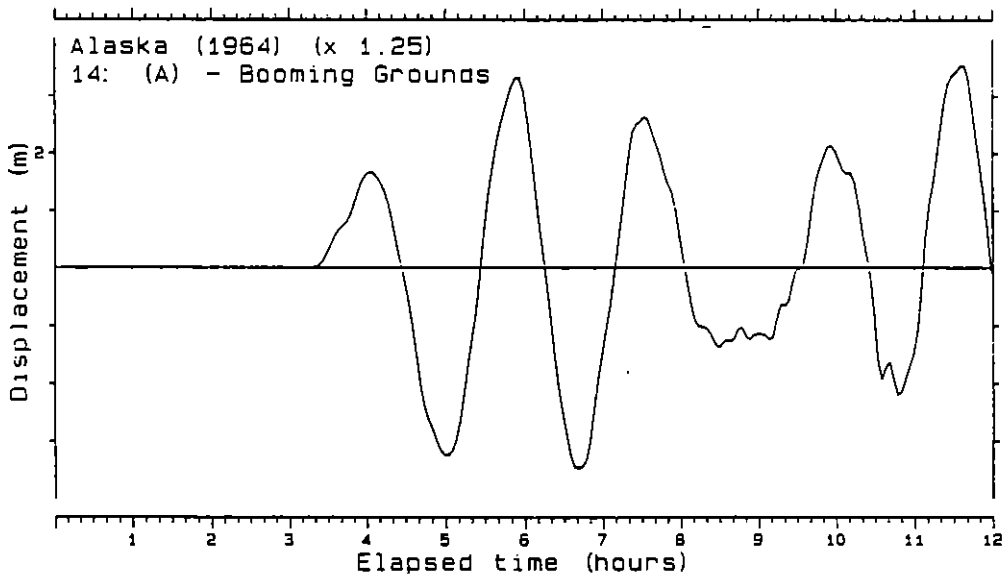
Alaska (1964) (x 1.25)
14: (A) - Booming Grounds
Displacement (m)
2
1 2 3 4 5 6 7 8 9 10 11 12
Elapsed time (hours)

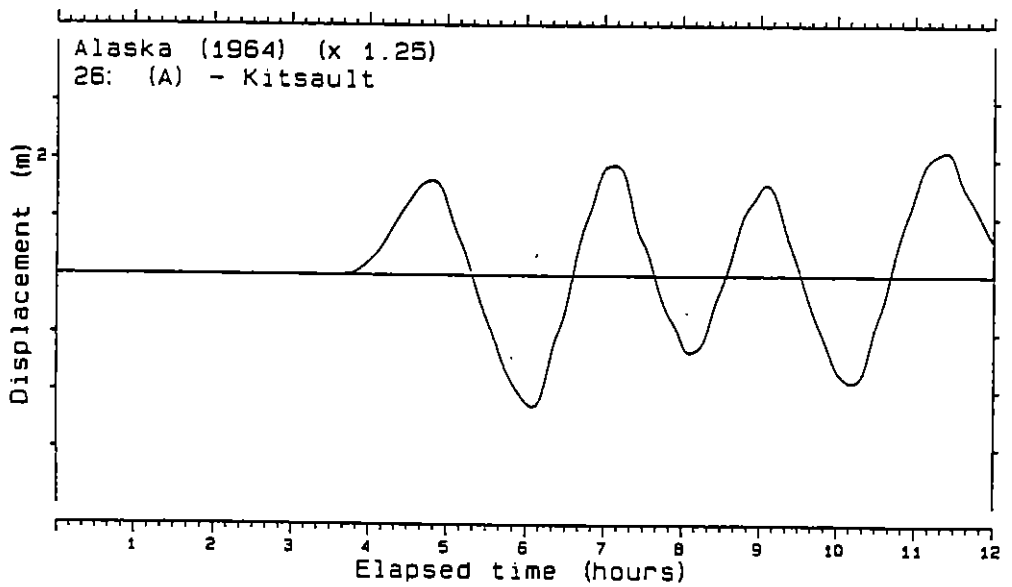
Alaska (1964) (x 1.25)
26: (A) - Kitsault
Displacement (m)
2
1 2 3 4 5 6 7 8 9 10 11 12
Elapsed time (hours)

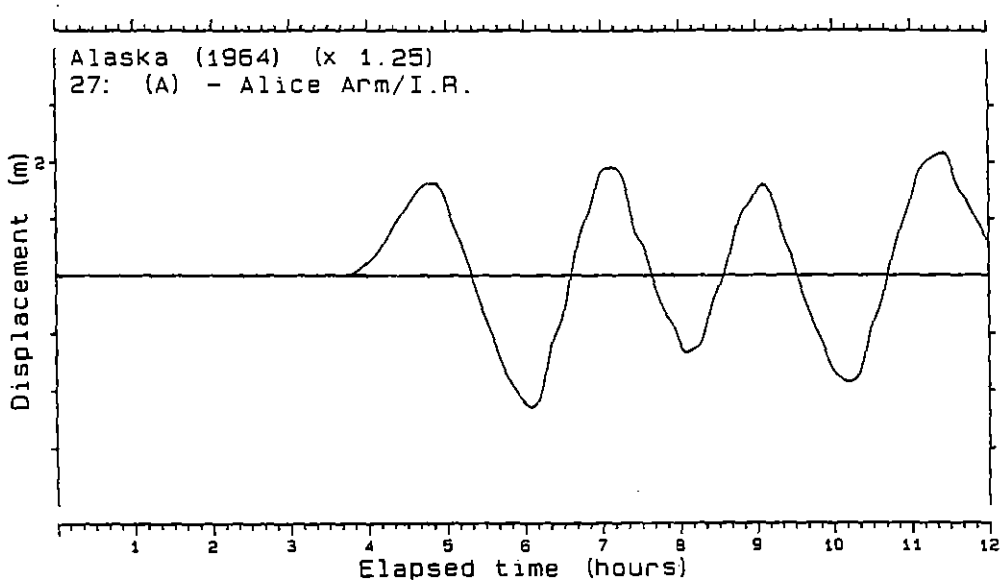
Alaska (1964) (x 1.25)
27: (A) - Alice Arm/I.R.
Displacement (m)
2
1 2 3 4 5 6 7 8 9 10 11 12
Elapsed time (hours)

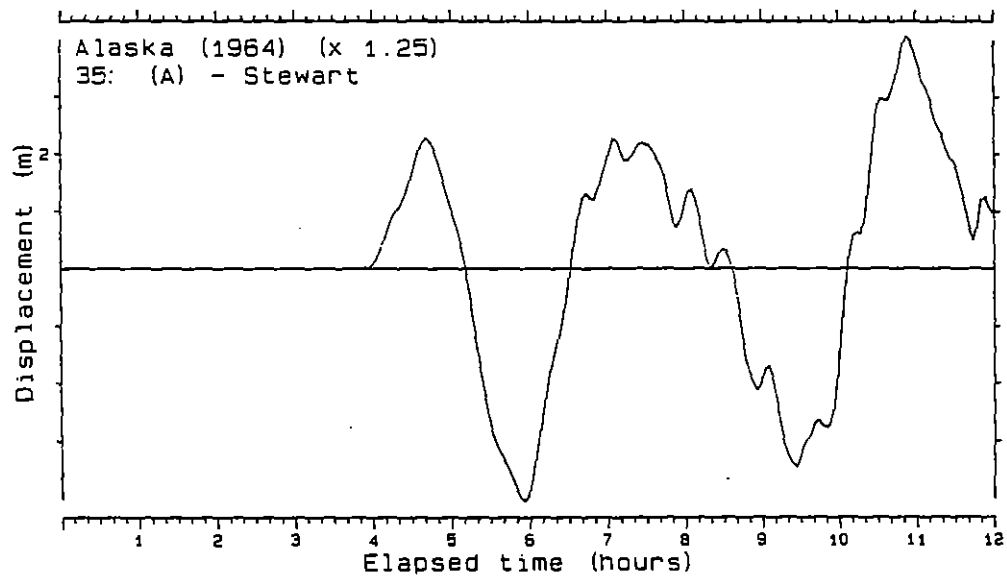
Alaska (1964) (x 1.25)
35: (A) - Stewart
Displacement (m)
2
1 2 3 4 5 6 7 8 9 10 11 12
Elapsed time (hours)

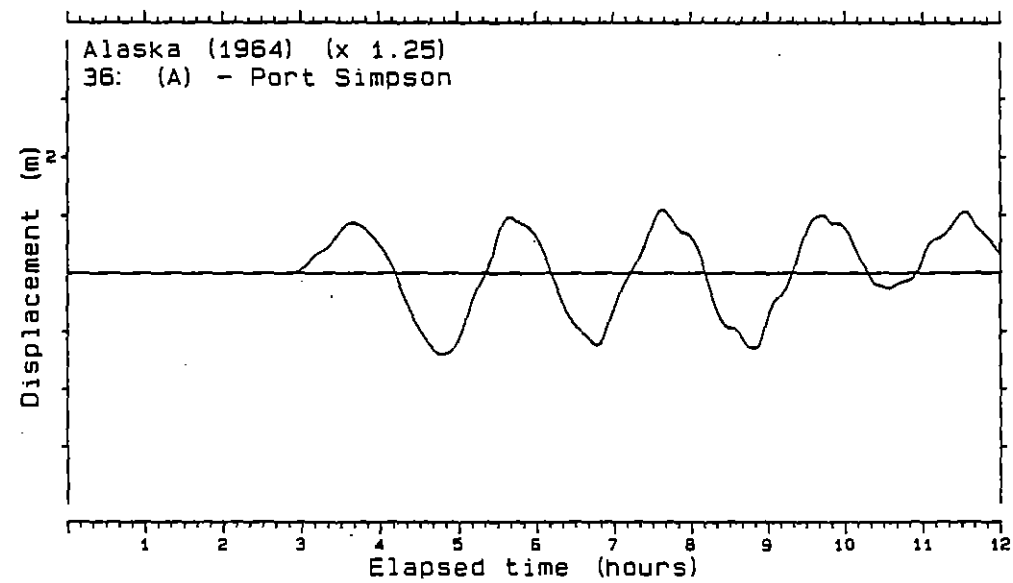
Alaska (1964) (x 1.25)
36: (A) - Port Simpson
Displacement (m)
2
1 2 3 4 5 6 7 8 9 10 11 12
Elapsed time (hours)

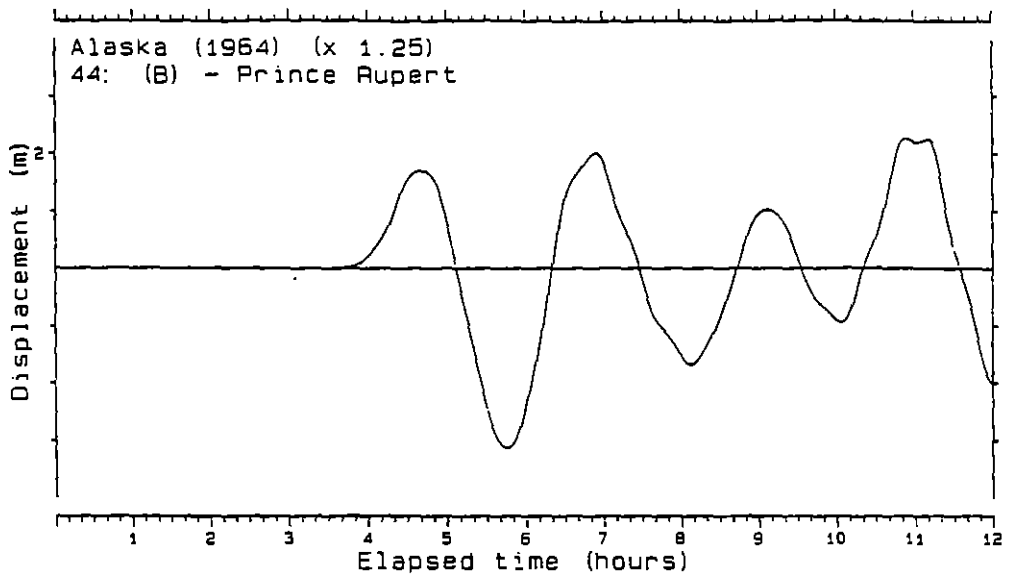
Alaska (1964) (x 1.25)
44: (B) - Prince Rupert
Displacement (m)
2
1 2 3 4 5 6 7 8 9 10 11 12
Elapsed time (hours)

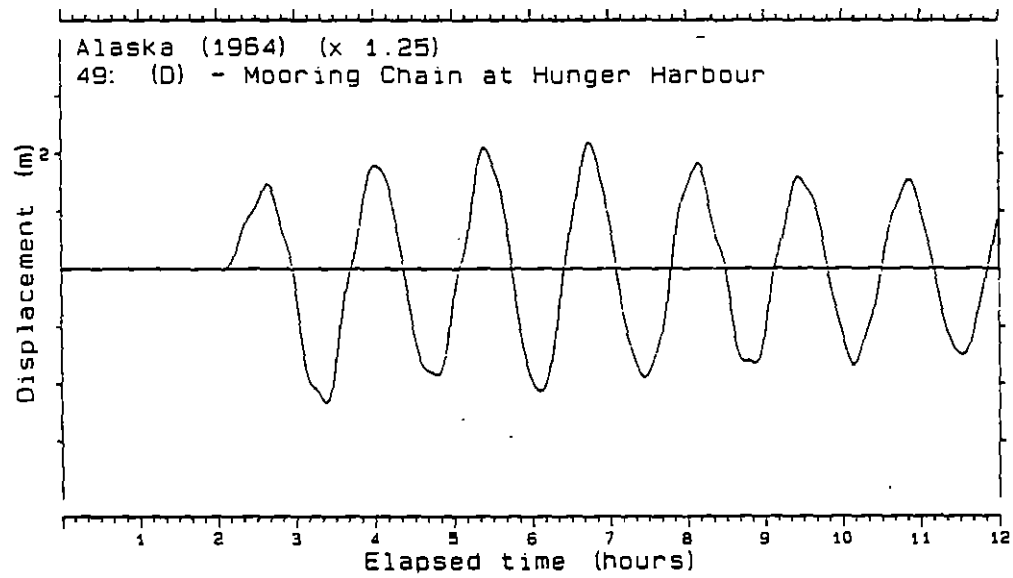
Alaska (1964) (x 1.25)
49: (D) - Mooring Chain at Hunger Harbour
Displacement (m)
2
1 2 3 4 5 6 7 8 9 10 11 12
Elapsed time (hours)

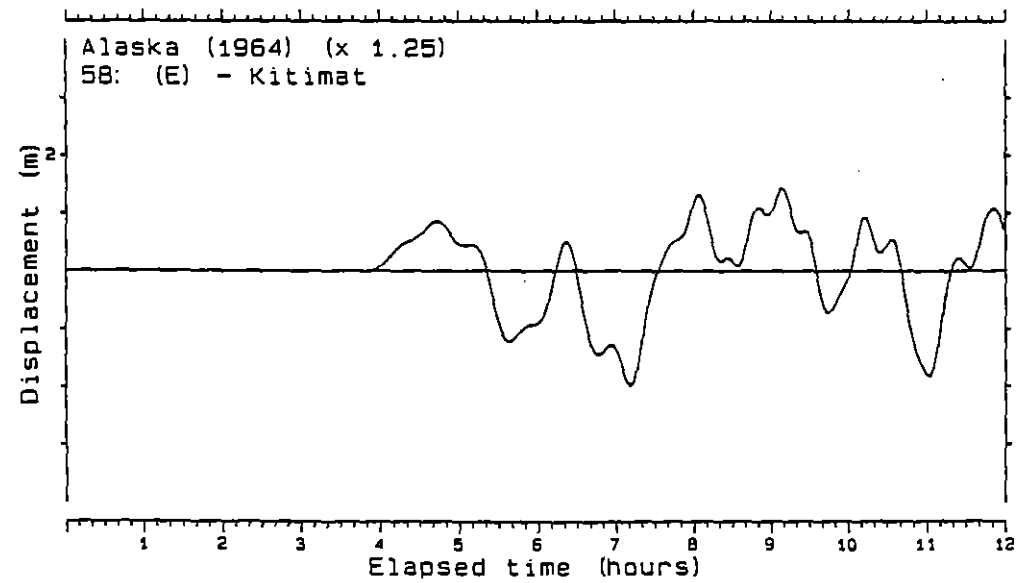
Alaska (1964) (x 1.25)
58: (E) - Kitimat
Displacement (m)
2
1 2 3 4 5 6 7 8 9 10 11 12
Elapsed time (hours)

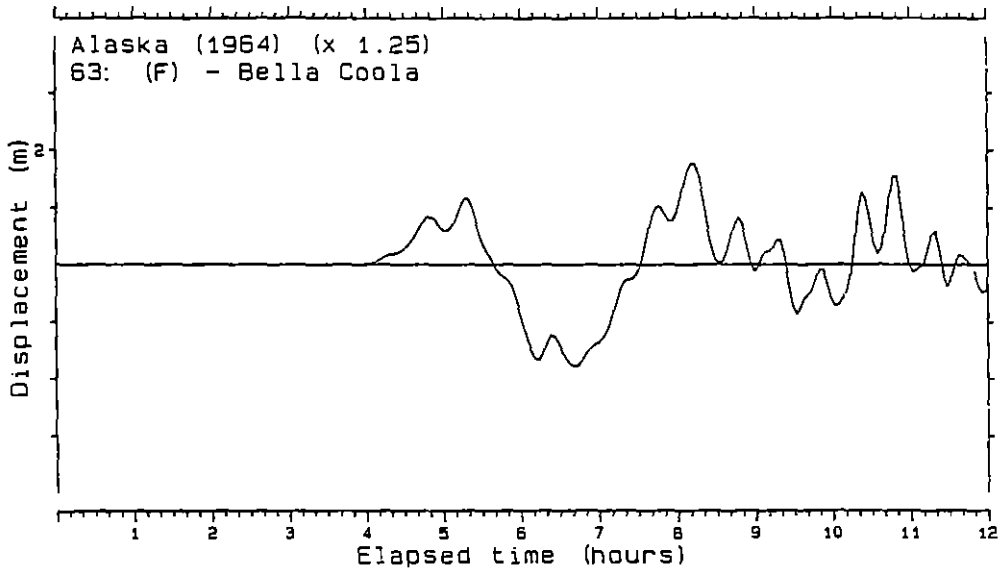
Alaska (1964) (x 1.25)
63: (F) - Bella Coola
Displacement (m)
2
1 2 3 4 5 6 7 8 9 10 11 12
Elapsed time (hours)

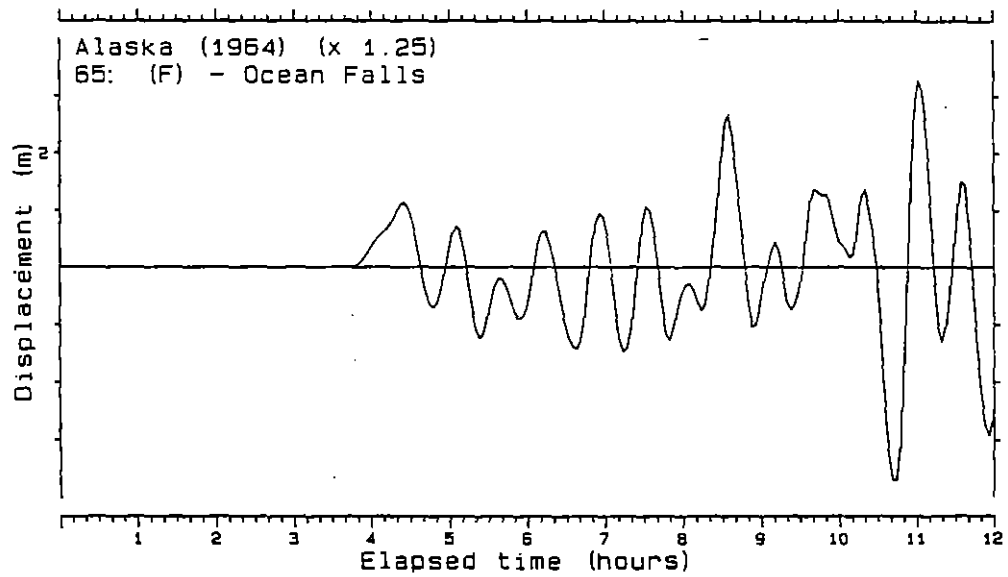
Alaska (1964) (x 1.25)
65: (F) - Ocean Falls
Displacement (m)
2
1 2 3 4 5 6 7 8 9 10 11 12
Elapsed time (hours)

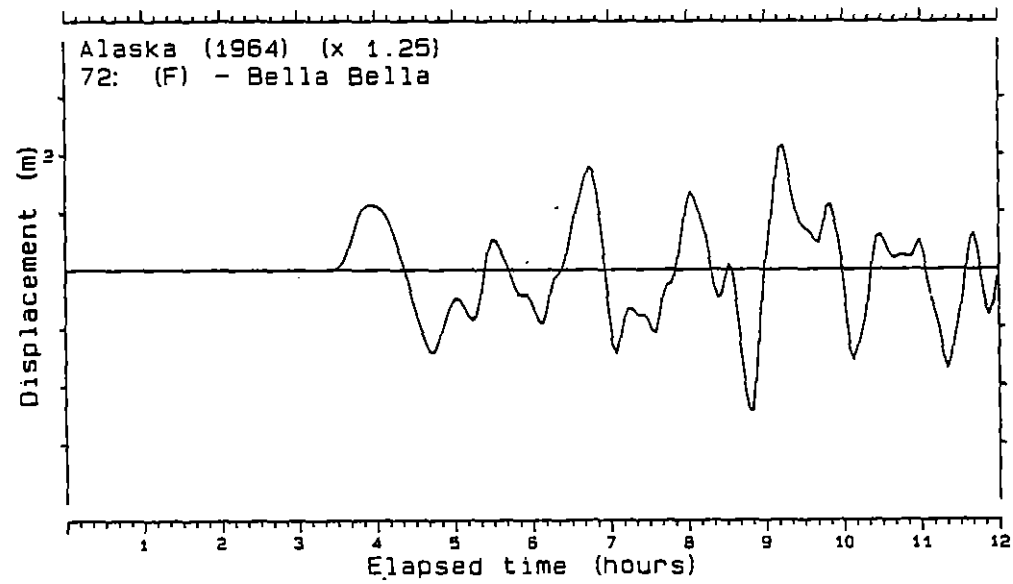
Alaska (1964) (x 1.25)
72: (F) - Bella Bella
Displacement (m)
2
1 2 3 4 5 6 7 8 9 10 11 12
Elapsed time (hours)

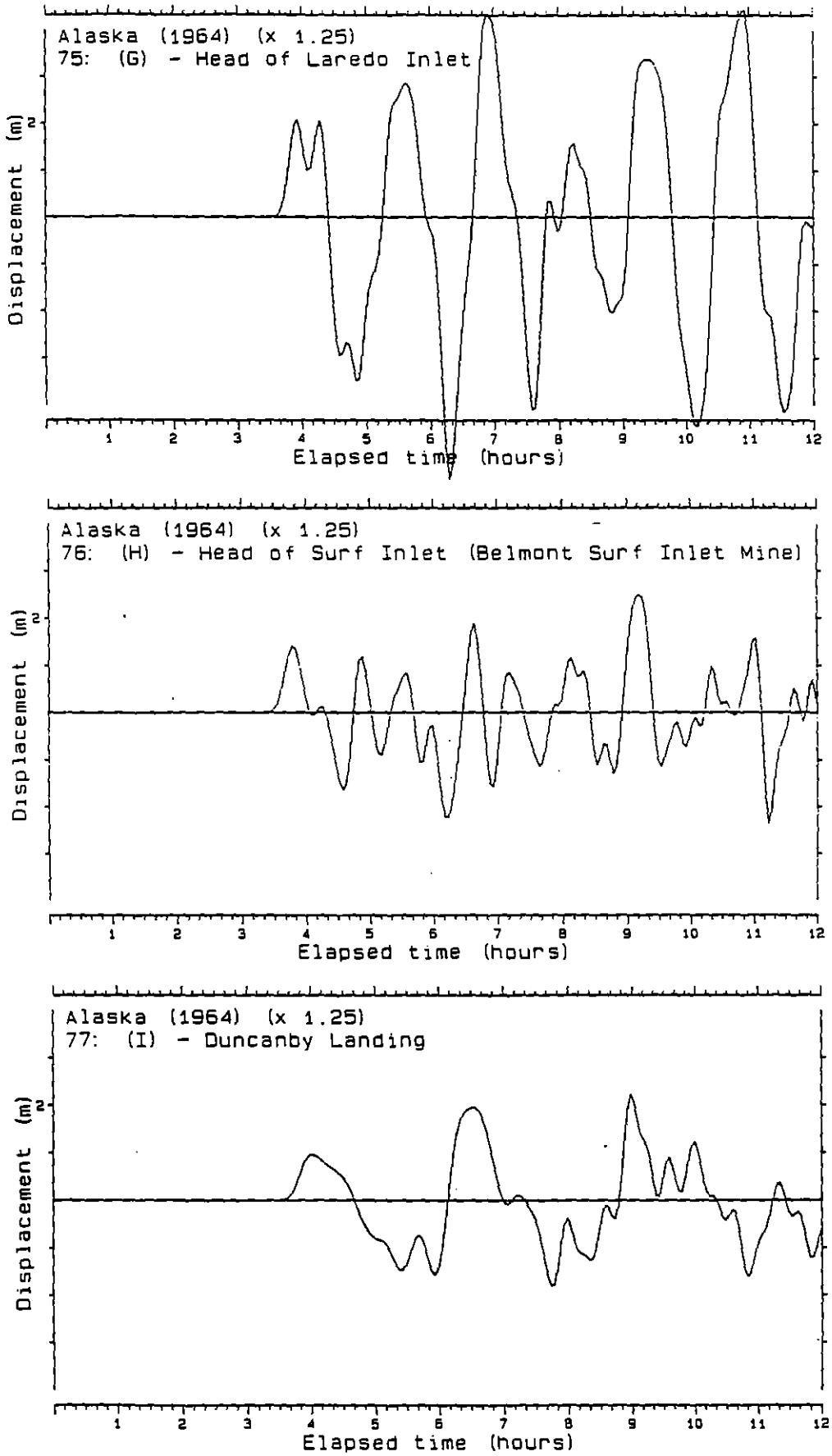
Alaska (1964) (x 1.25)
75: (G) - Head of Laredo Inlet
Displacement (m)
2
1 2 3 4 5 6 7 8 9 10 11 12
Elapsed time (hours)
Alaska (1964) (x 1.25)
76: (H) - Head of Surf Inlet (Belmont Surf Inlet Mine)
Displacement (m)
2
1 2 3 4 5 6 7 8 9 10 11 12
Elapsed time (hours)
Alaska (1964) (x 1.25)
77: (I) - Duncanby Landing
Displacement (m)
2
1 2 3 4 5 6 7 8 9 10 11 12
Elapsed time (hours)

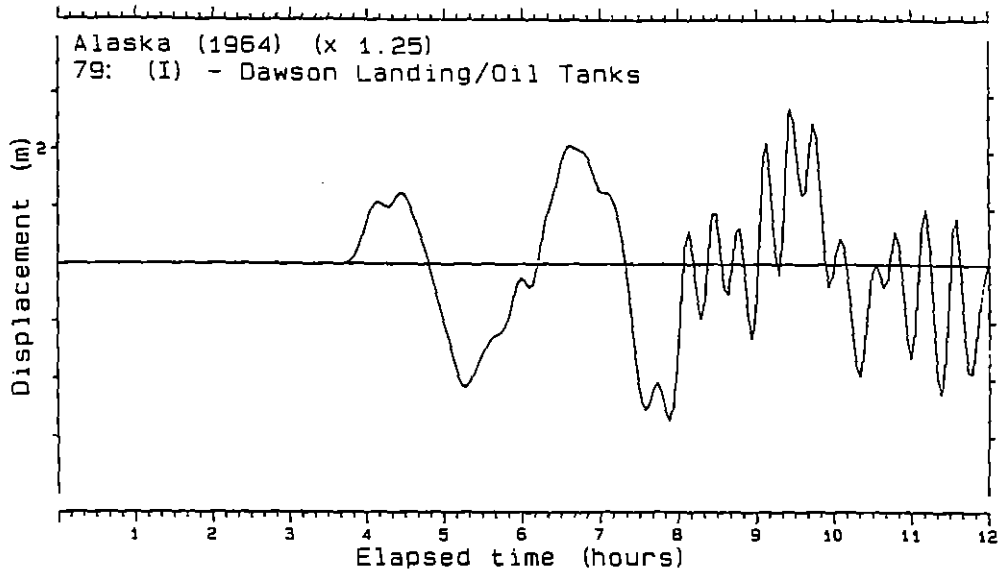
Alaska (1964) (x 1.25)
79: (I) - Dawson Landing/Oil Tanks
Displacement (m)
2
1 2 3 4 5 6 7 8 9 10 11 12
Elapsed time (hours)

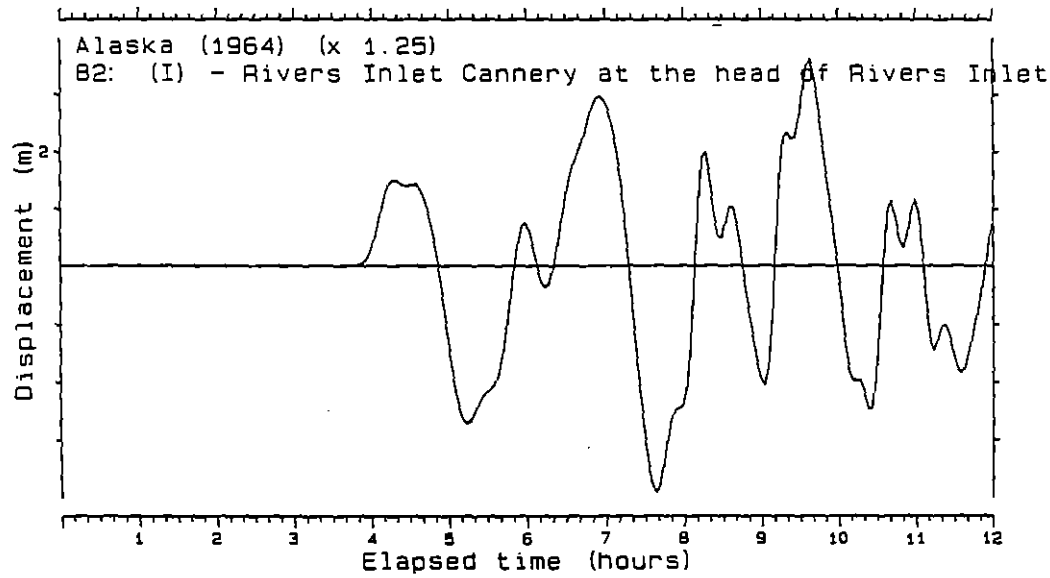
Alaska (1964) (x 1.25)
82: (I) - Rivers Inlet Cannery at the head of Rivers Inlet
Displacement (m)
2
1 2 3 4 5 6 7 8 9 10 11 12
Elapsed time (hours)

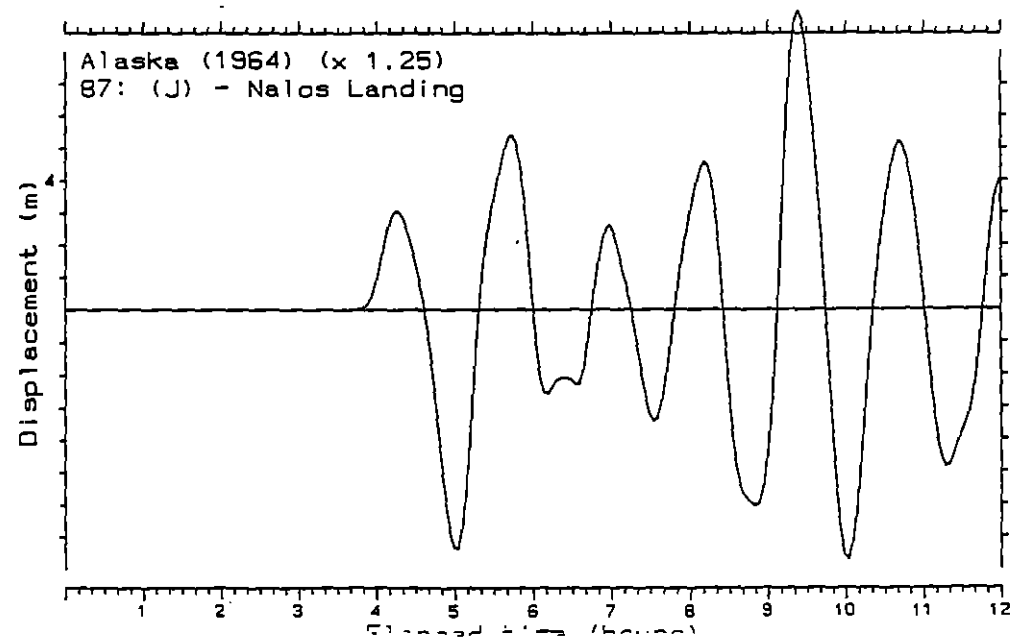
Alaska (1964) (x 1.25)
87: (J) - Nalos Landing
Displacement (m)
4
1 2 3 4 5 6 7 8 9 10 11 12

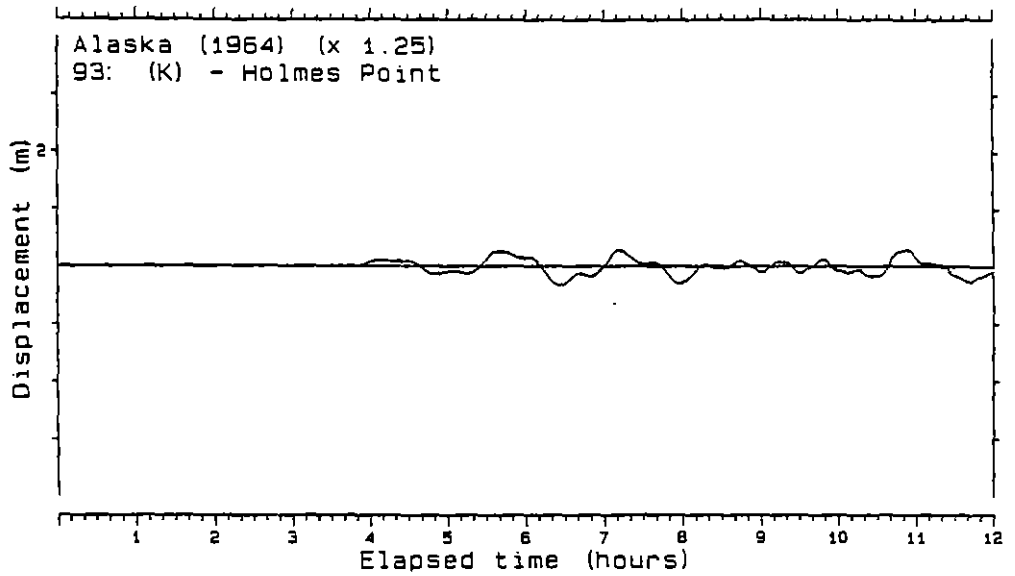
Alaska (1964) (x 1.25)
93: (K) - Holmes Point
Displacement (m)
2
1 2 3 4 5 6 7 8 9 10 11 12
Elapsed time (hours)

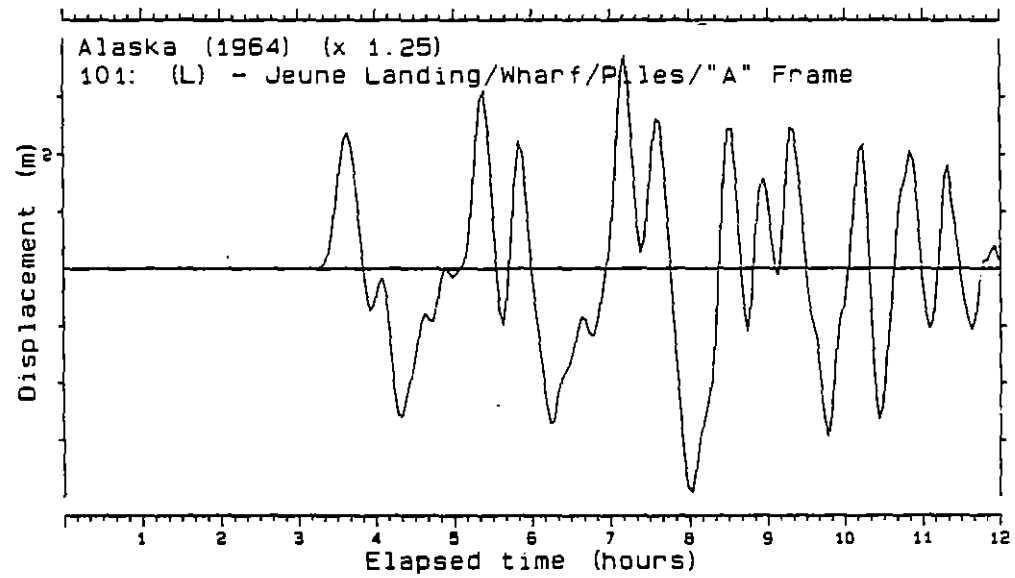
Alaska (1964) (x 1.25)
101: (L) - Jeune Landing/Wharf/Piles/"A" Frame
Displacement (m)
2
1 2 3 4 5 6 7 8 9 10 11 12
Elapsed time (hours)

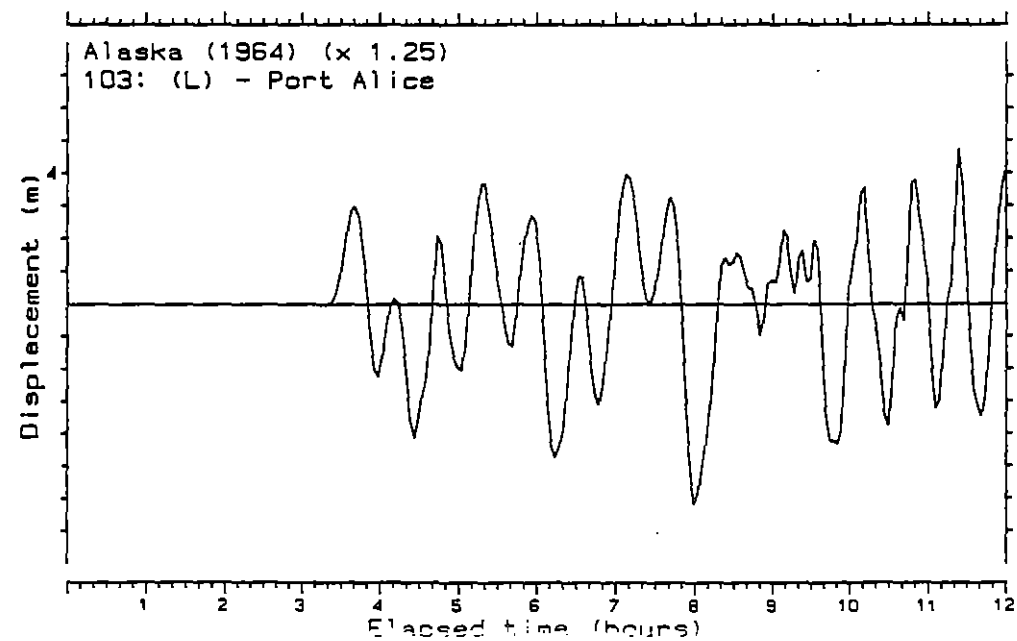
Alaska (1964) (x 1.25)
103: (L) - Port Alice
Displacement (m)
4
1 2 3 4 5 6 7 8 9 10 11 12
Elapsed time (hours)

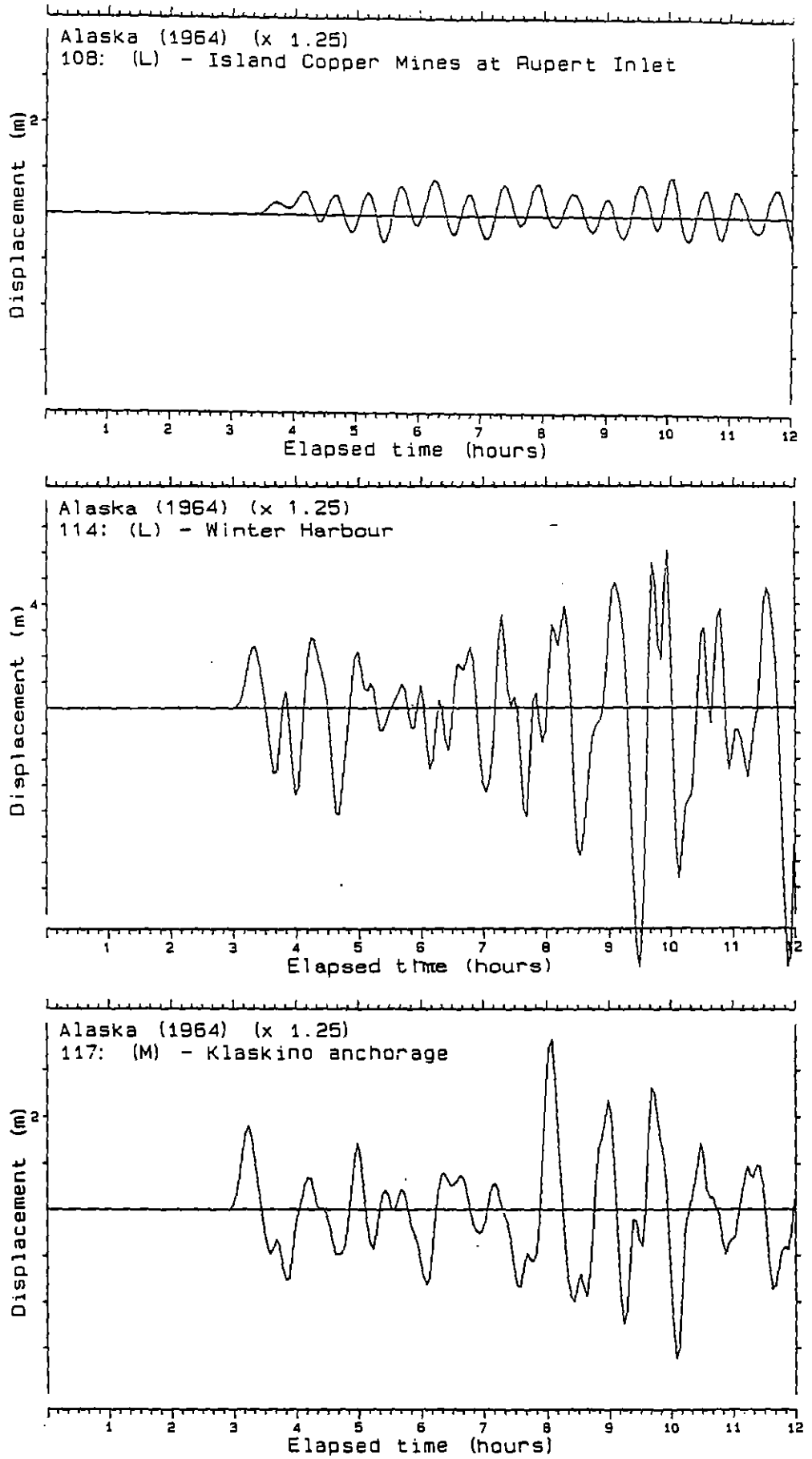
Alaska (1964) (x 1.25)
108: (L) - Island Copper Mines at Rupert Inlet
Displacement (m)
2
1 2 3 4 5 6 7 8 9 10 11 12
Elapsed time (hours)
Alaska (1964) (x 1.25)
114: (L) - Winter Harbour
Displacement (m)
4
1 2 3 4 5 6 7 8 9 10 11 12
Elapsed time (hours)
Alaska (1964) (x 1.25)
117: (M) - Klaskino anchorage
Displacement (m)
2
1 2 3 4 5 6 7 8 9 10 11 12
Elapsed time (hours)

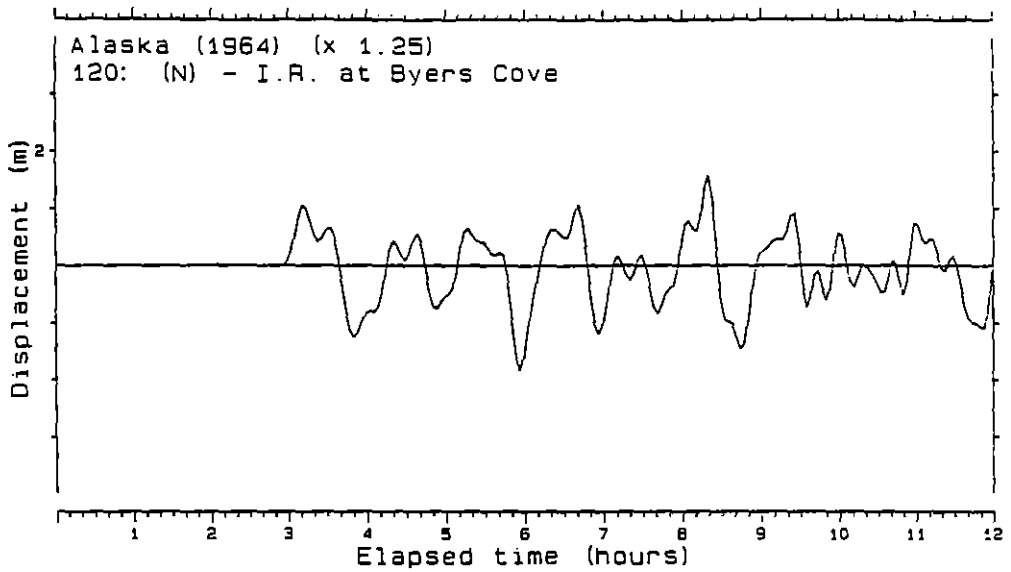
Alaska (1964) (x 1.25)
120: (N) - I.R. at Byers Cove
Displacement (m)
2
1 2 3 4 5 6 7 8 9 10 11 12
Elapsed time (hours)

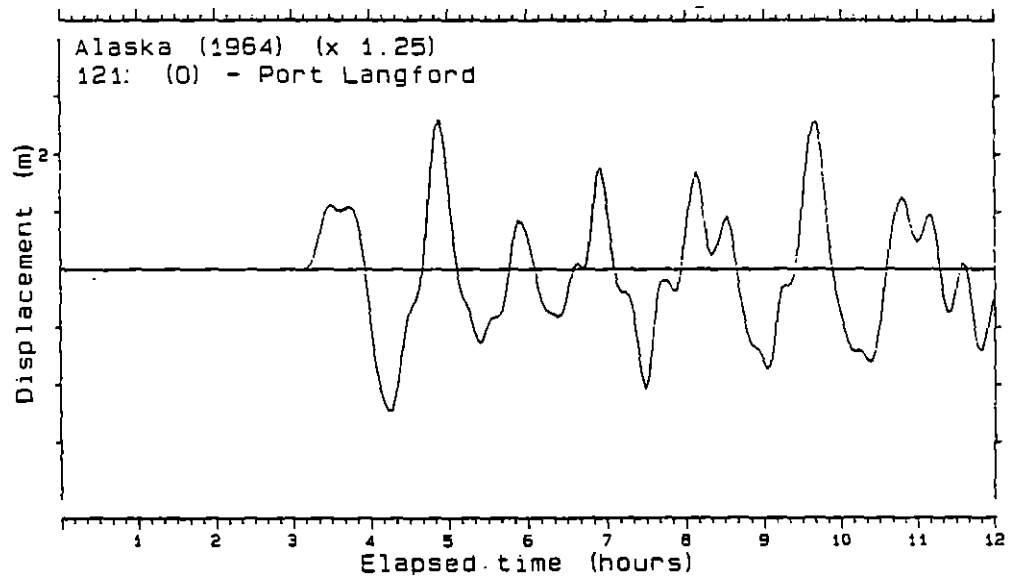
Alaska (1964) (x 1.25)
121: (0) - Port Langford
Displacement (m)
2
1 2 3 4 5 6 7 8 9 10 11 12
Elapsed time (hours)

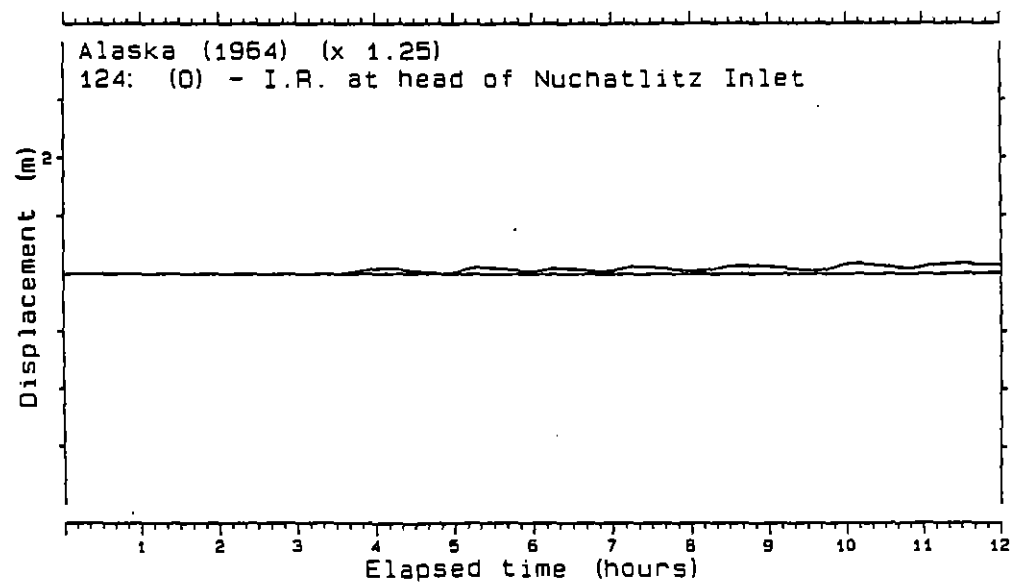
Alaska (1964) (x 1.25)
124: (0) - I.R. at head of Nuchatlitz Inlet
Displacement (m)
2
1 2 3 4 5 6 7 8 9 10 11 12
Elapsed time (hours)

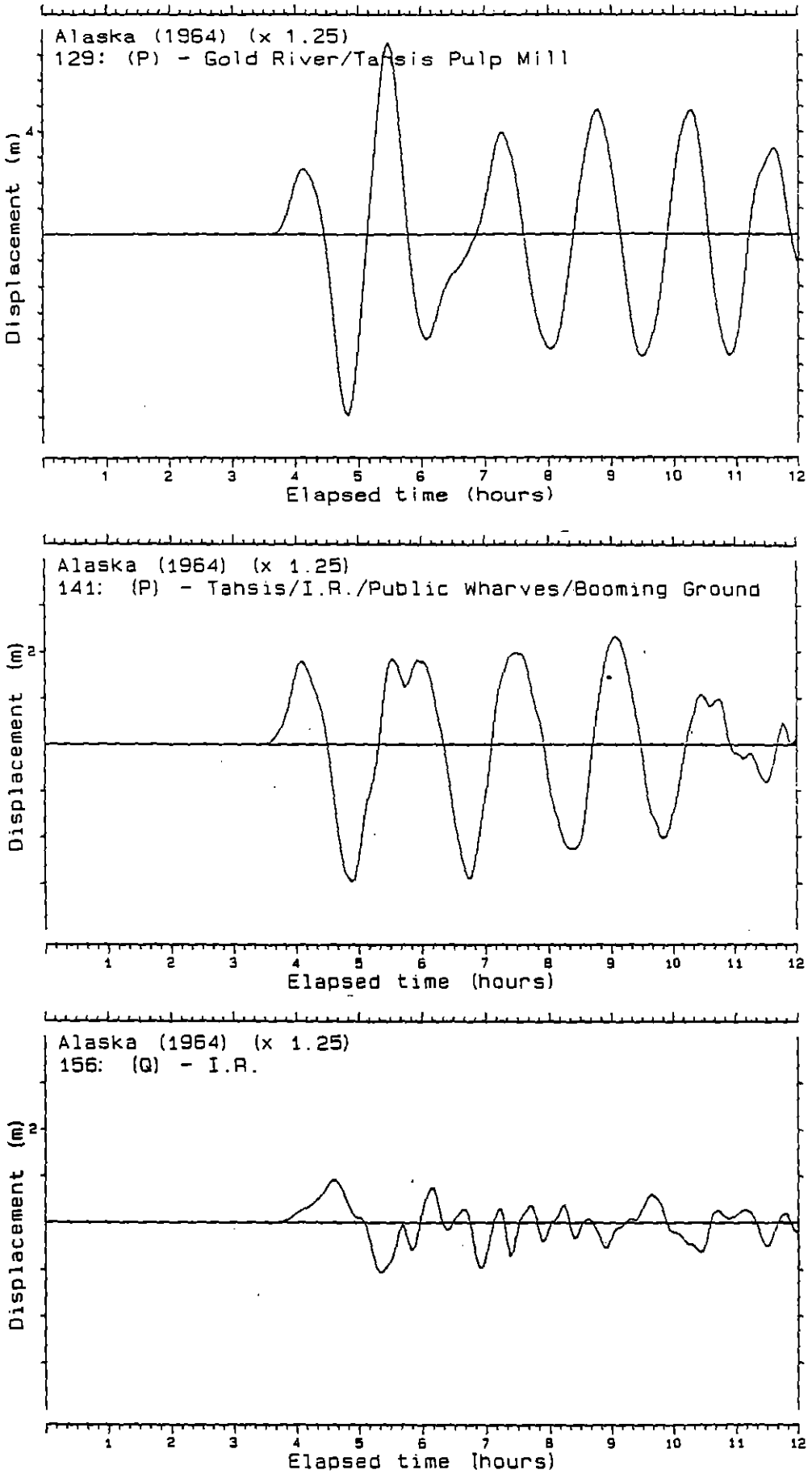
Alaska (1964) (x 1.25)
129: (P) - Gold River/Tahsis Pulp Mill
Displacement (m)
4
1 2 3 4 5 6 7 8 9 10 11 12
Elapsed time (hours)
Alaska (1964) (x 1.25)
141: (P) - Tahsis/I.R./Public Wharves/Booming Ground
Displacement (m)
2
1 2 3 4 5 6 7 8 9 10 11 12
Elapsed time (hours)
Alaska (1964) (x 1.25)
156: (Q) - I.R.
Displacement (m)
2
1 2 3 4 5 6 7 8 9 10 11 12
Elapsed time (hours)

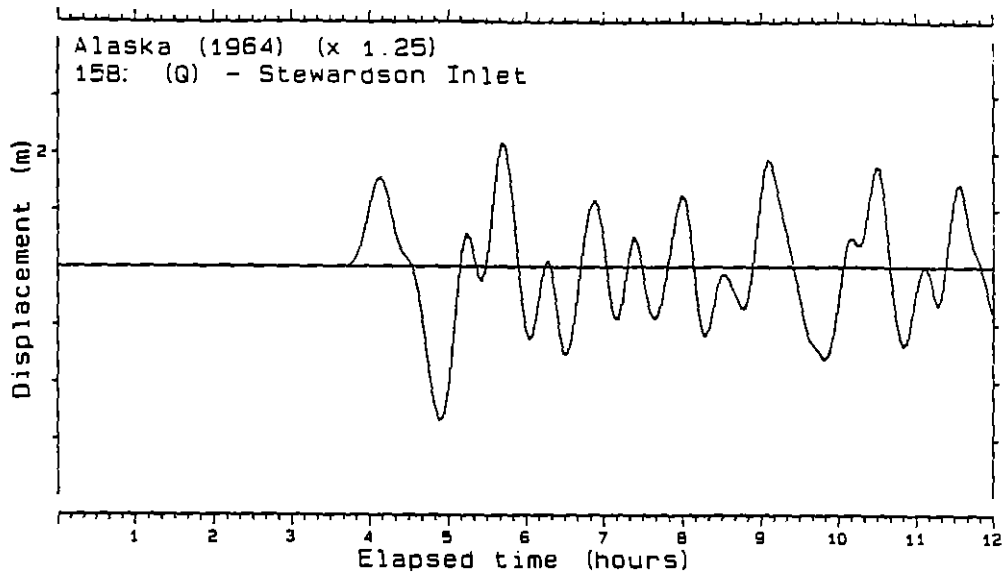
Alaska (1964) (x 1.25)
158: (Q) - Stewardson Inlet
Displacement (m)
2
1 2 3 4 5 6 7 8 9 10 11 12
Elapsed time (hours)

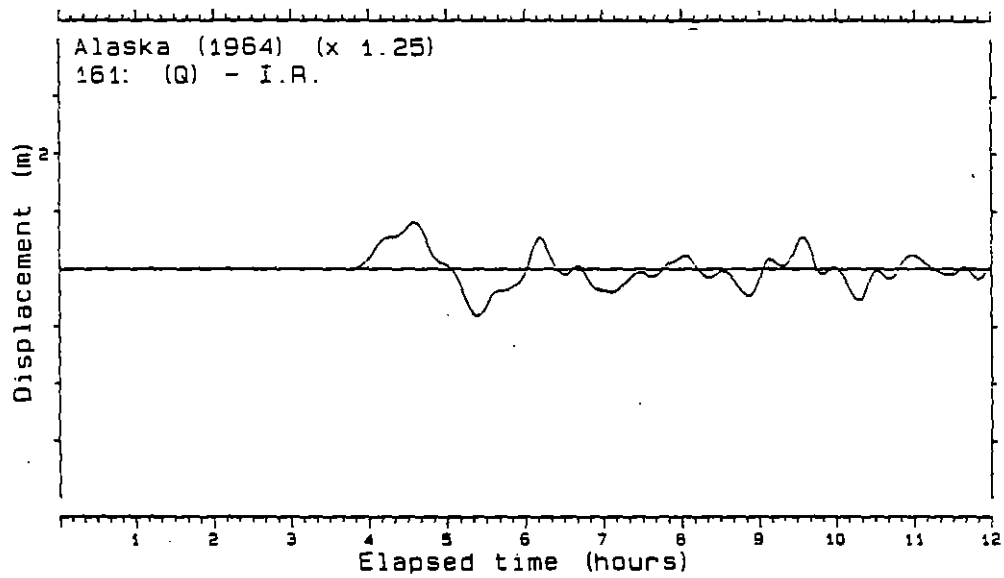
Alaska (1964) (x 1.25)
161: (Q) - I.R.
Displacement (m)
2
1 2 3 4 5 6 7 8 9 10 11 12
Elapsed time (hours)

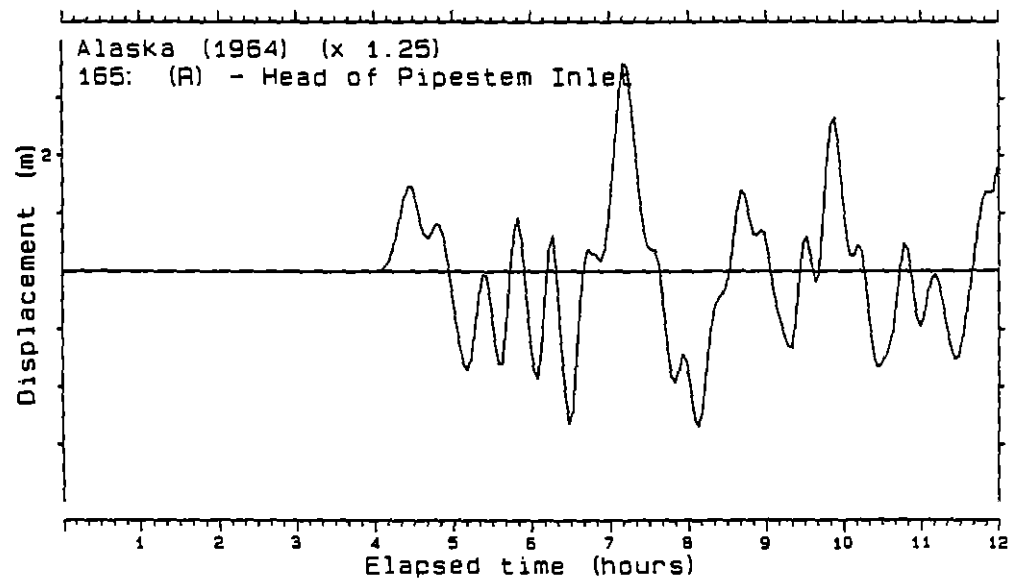
Alaska (1964) (x 1.25)
165: (R) - Head of Pipestem Inlet
Displacement (m)
2
1 2 3 4 5 6 7 8 9 10 11 12
Elapsed time (hours)

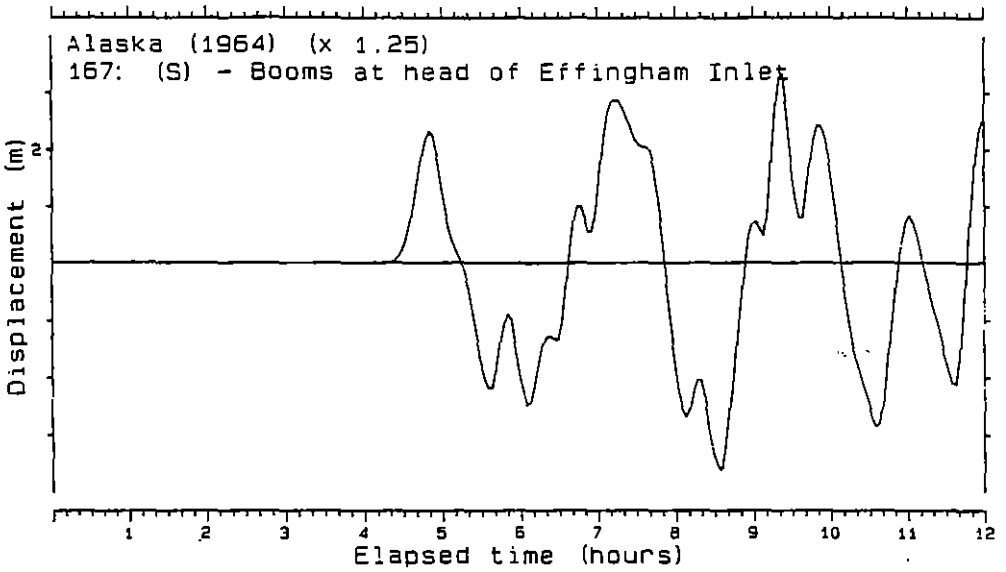
Alaska (1964) (x 1.25)
167: (S) - Booms at head of Effingham Inlet
Displacement (m)
2
1 2 3 4 5 6 7 8 9 10 11 12
Elapsed time (hours)

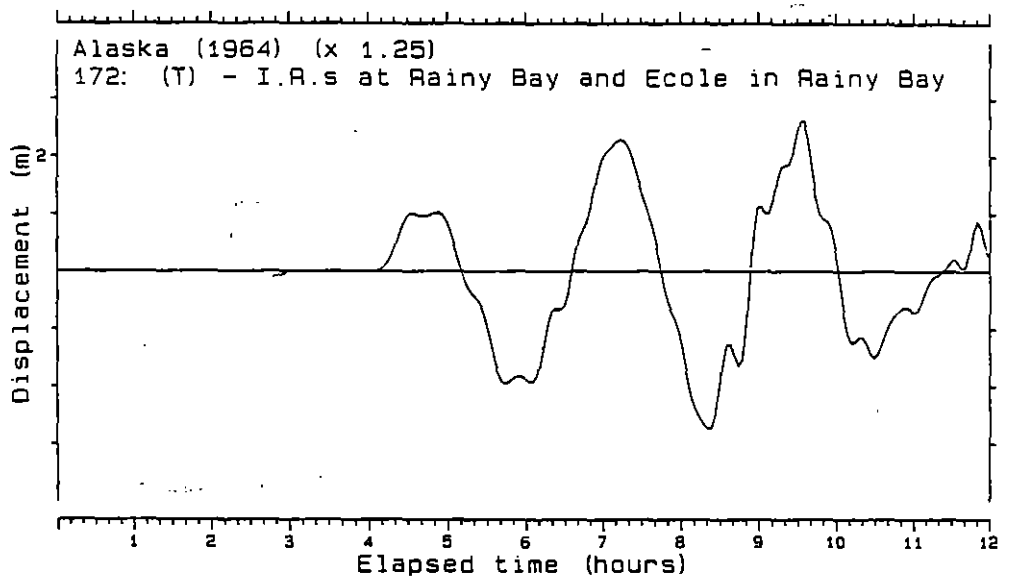
Alaska (1964) (x 1.25)
172: (T) - I.R.s at Rainy Bay and Ecole in Rainy Bay
Displacement (m)
2
1 2 3 4 5 6 7 8 9 10 11 12
Elapsed time (hours)

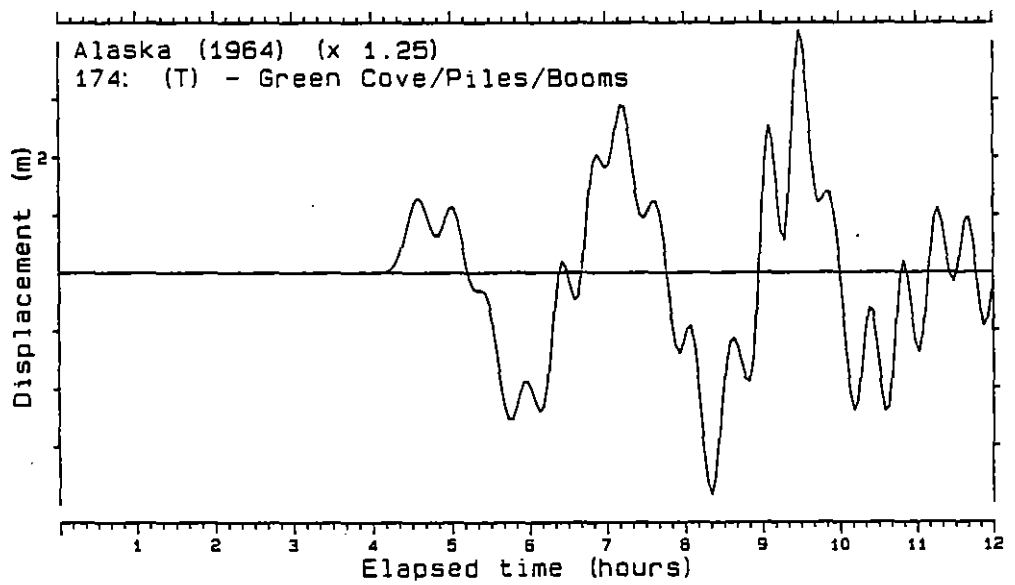
Alaska (1964) (x 1.25)
174: (T) - Green Cove/Piles/Booms
Displacement (m)
2
1 2 3 4 5 6 7 8 9 10 11 12
Elapsed time (hours)

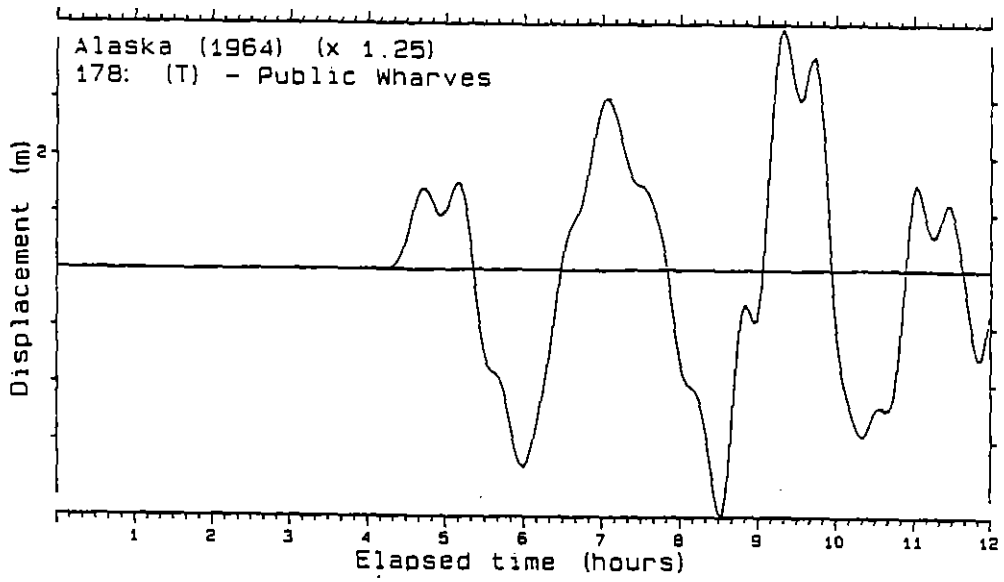
Alaska (1964) (x 1.25)
178: (T) - Public Wharves
Displacement (m)
2
1 2 3 4 5 6 7 8 9 10 11 12
Elapsed time (hours)

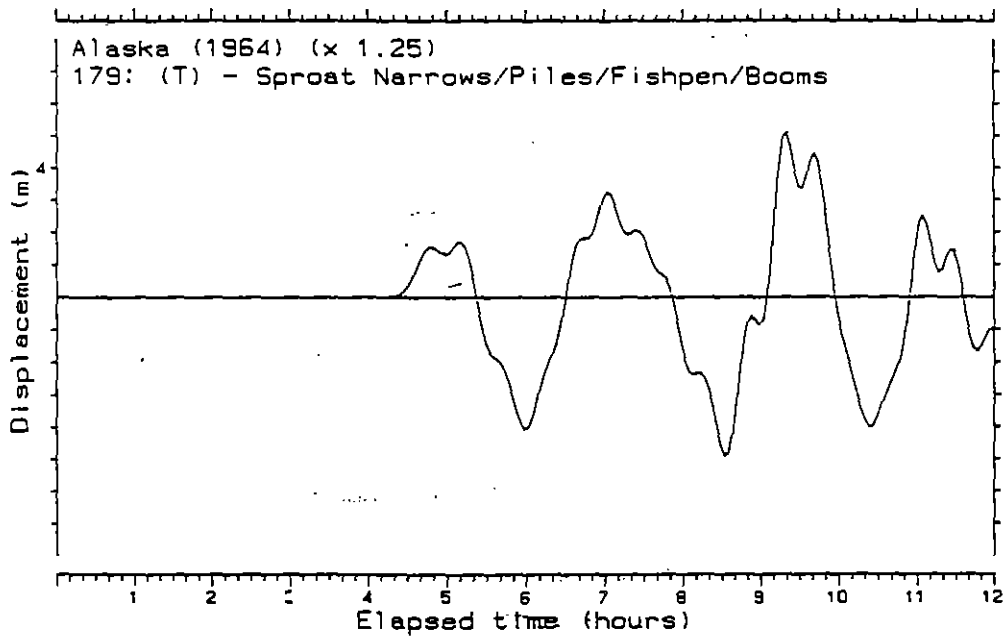
Alaska (1964) (x 1.25)
179: (T) - Sproat Narrows/Piles/Fishpen/Booms
Displacement (m)
4
1 2 3 4 5 6 7 8 9 10 11 12
Elapsed time (hours)

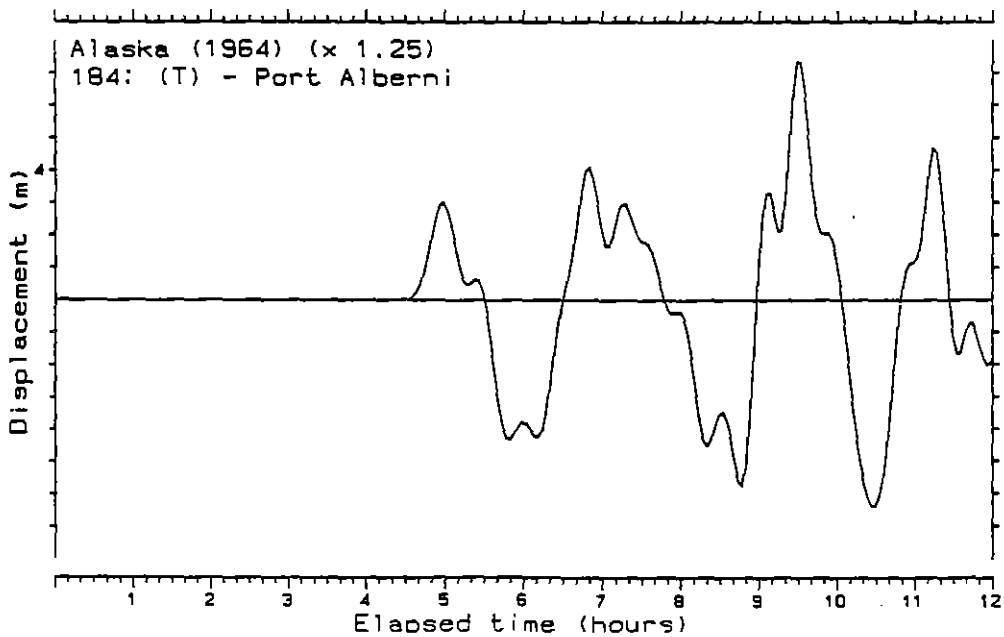
Alaska (1964) (x 1.25)
184: (T) - Port Alberni
Displacement (m)
4
1 2 3 4 5 6 7 8 9 10 11 12
Elapsed time (hours)

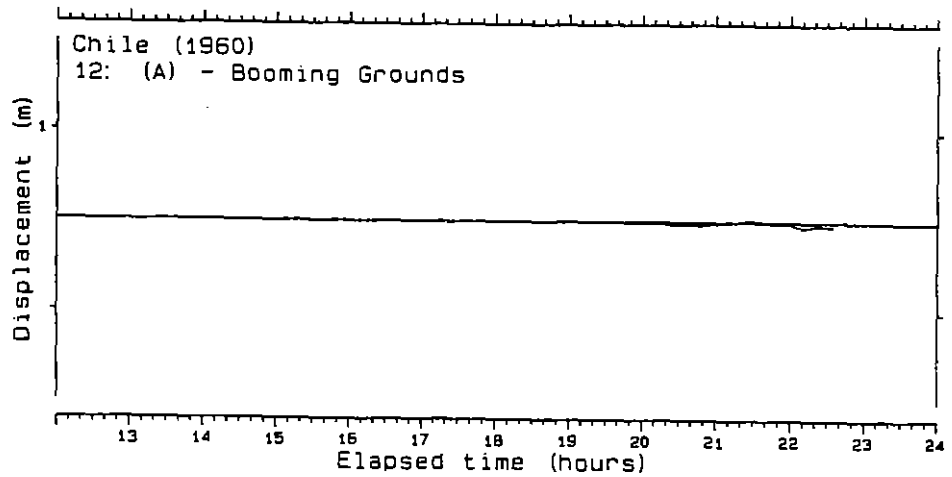
Chile (1960)
12: (A) - Booming Grounds
Displacement (m)
1
13 14 15 16 17 18 19 20 21 22 23 24
Elapsed time (hours)

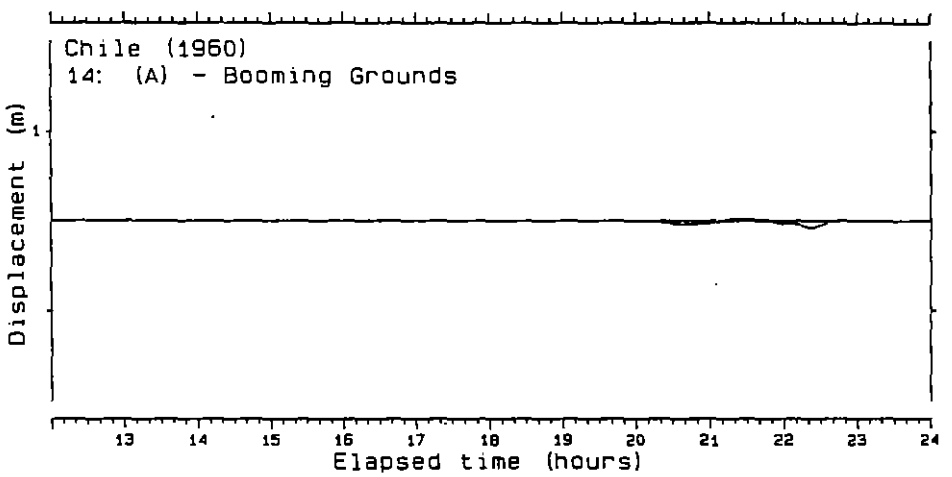
Chile (1960)
14: (A) - Booming Grounds
Displacement (m)
1
13 14 15 16 17 18 19 20 21 22 23 24
Elapsed time (hours)

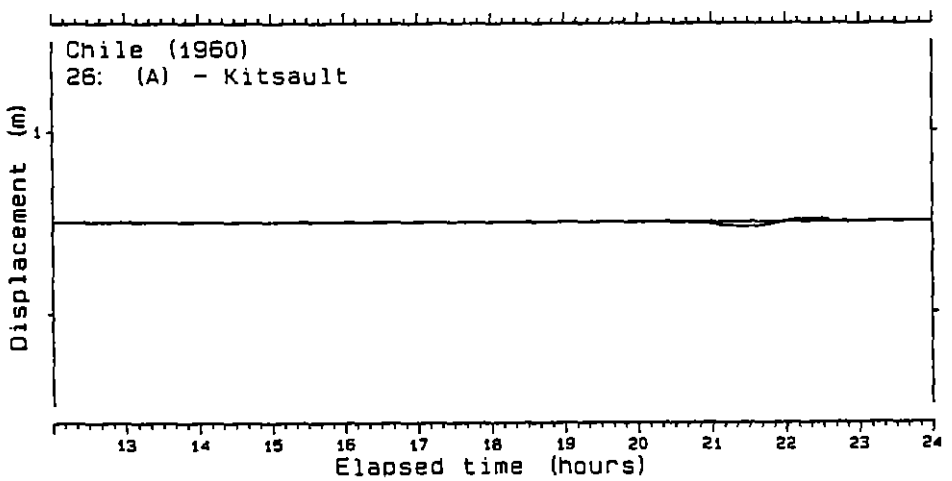
Chile (1960)
26: (A) - Kitsault
Displacement (m)
1
13 14 15 16 17 18 19 20 21 22 23 24
Elapsed time (hours)

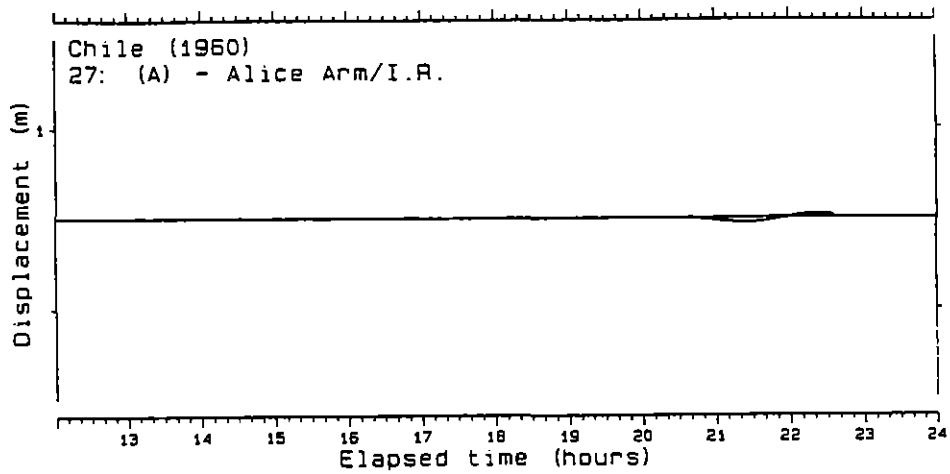
Chile (1960)
27: (A) - Alice Arm/I.R.
Displacement (m)
1
13 14 15 16 17 18 19 20 21 22 23 24
Elapsed time (hours)

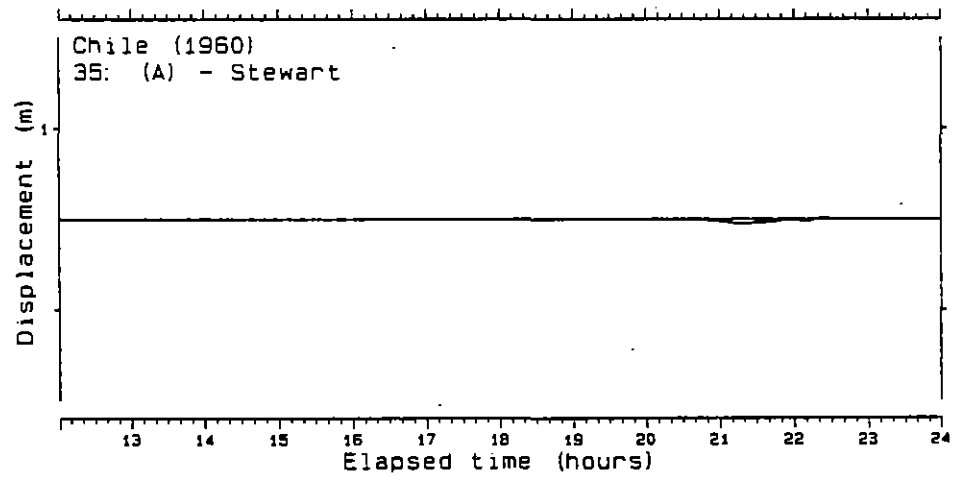
Chile (1960)
35: (A) - Stewart
Displacement (m)
1
13 14 15 16 17 18 19 20 21 22 23 24
Elapsed time (hours)

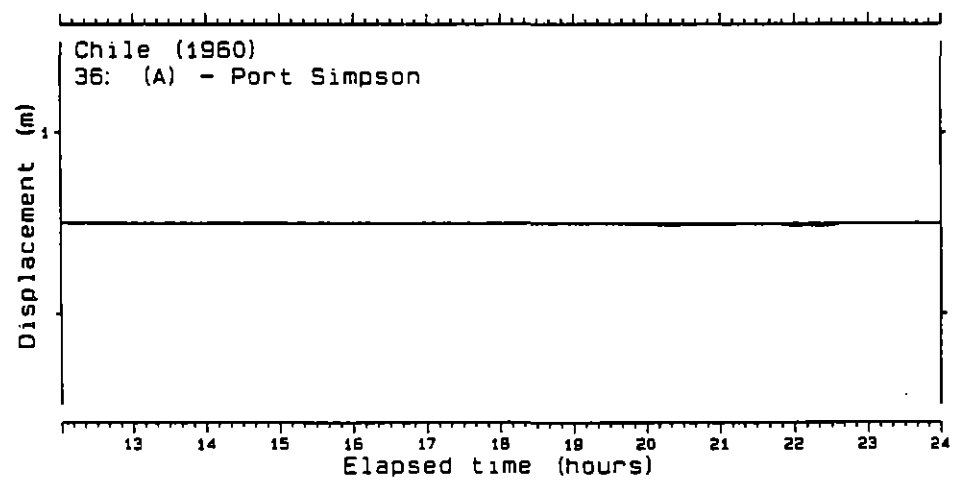
Chile (1960)
36: (A) - Port Simpson
Displacement (m)
1
13 14 15 16 17 18 19 20 21 22 23 24
Elapsed time (hours)

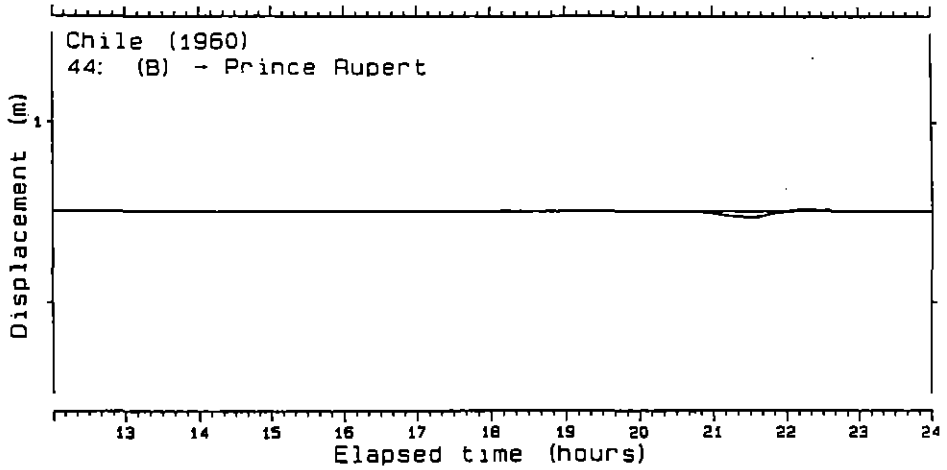
Chile (1960)
44: (B) - Prince Rupert
Displacement (m)
1
13 14 15 16 17 18 19 20 21 22 23 24
Elapsed time (hours)

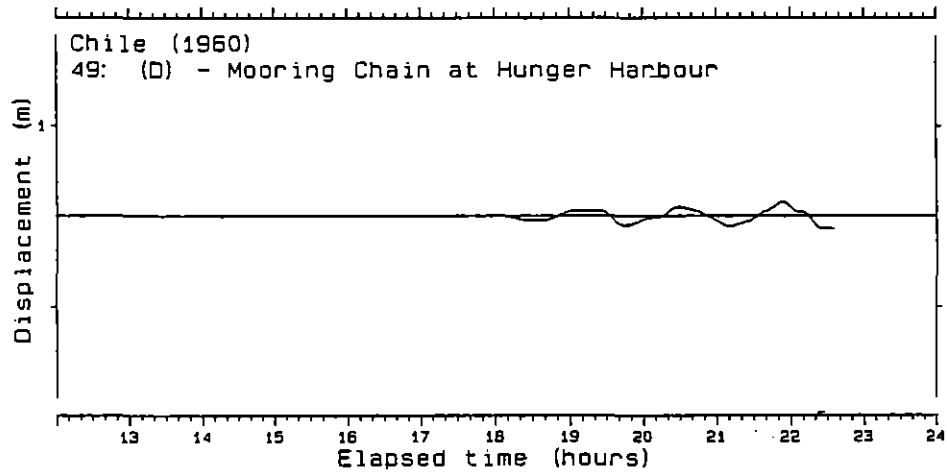
Chile (1960)
49: (D) - Mooring Chain at Hunger Harbour
Displacement (m)
1
13 14 15 16 17 18 19 20 21 22 23 24
Elapsed time (hours)

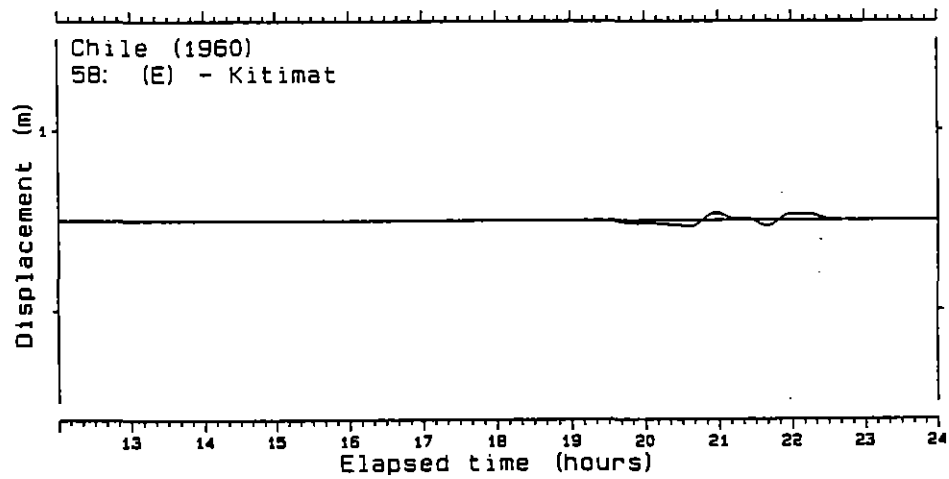
Chile (1960)
58: (E) - Kitimat
Displacement (m)
1
13 14 15 16 17 18 19 20 21 22 23 24
Elapsed time (hours)

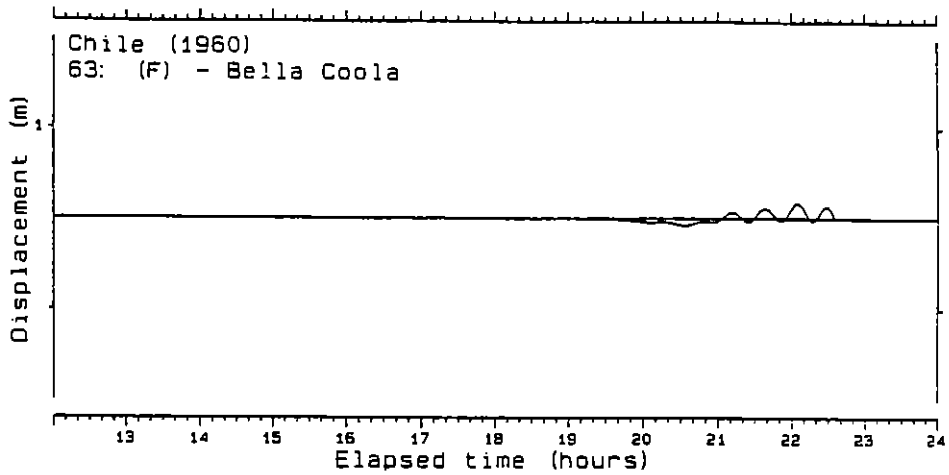
Chile (1960)
63: (F) - Bella Coola
Displacement (m)
1
13 14 15 16 17 18 19 20 21 22 23 24
Elapsed time (hours)

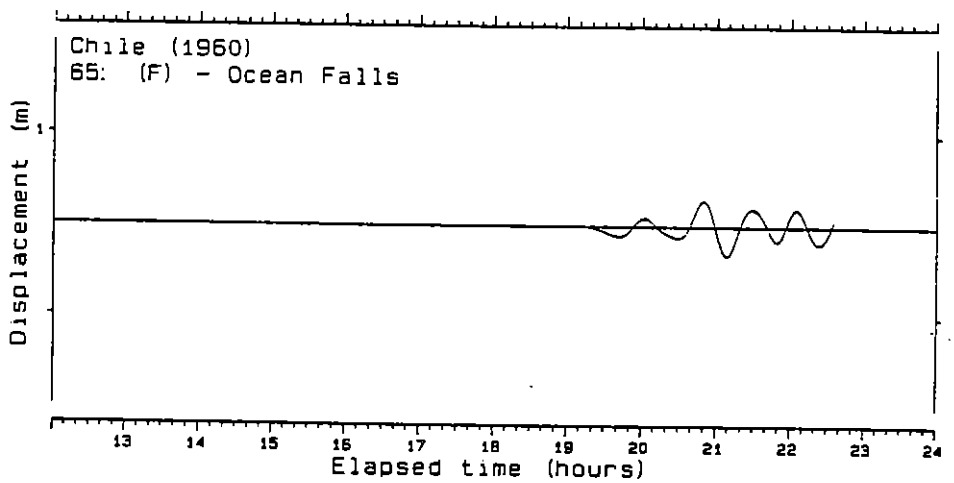
Chile (1960)
65: (F) - Ocean Falls
Displacement (m)
1
13 14 15 16 17 18 19 20 21 22 23 24
Elapsed time (hours)

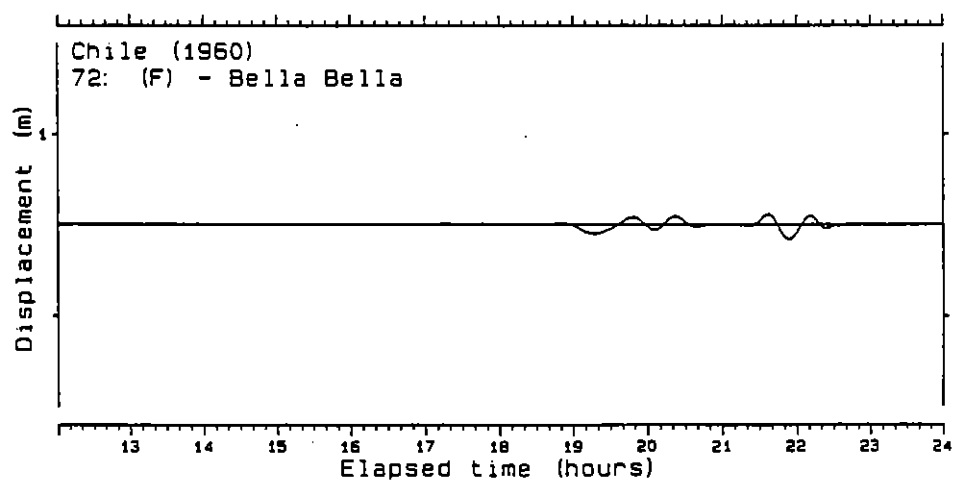
Chile (1960)
72: (F) - Bella Bella
Displacement (m)
1
13 14 15 16 17 18 19 20 21 22 23 24
Elapsed time (hours)

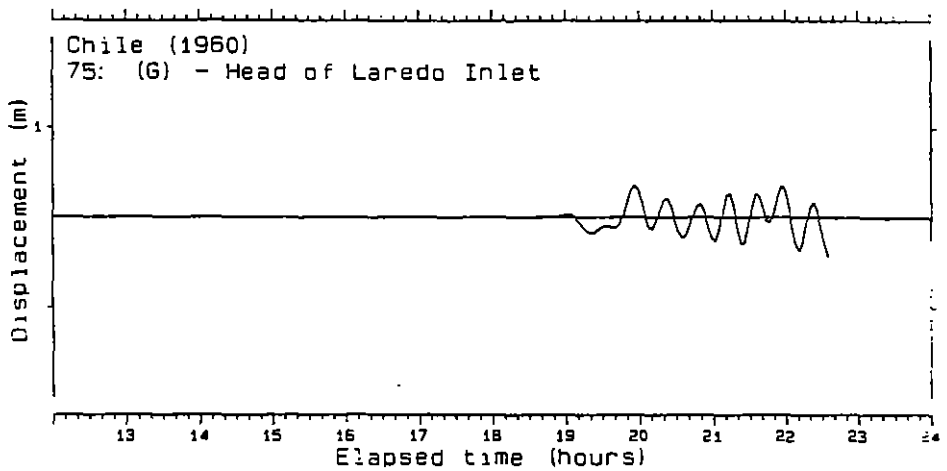
Chile (1960)
75: (G) - Head of Laredo Inlet
Displacement (m)
1
13 14 15 16 17 18 19 20 21 22 23 24
Elapsed time (hours)

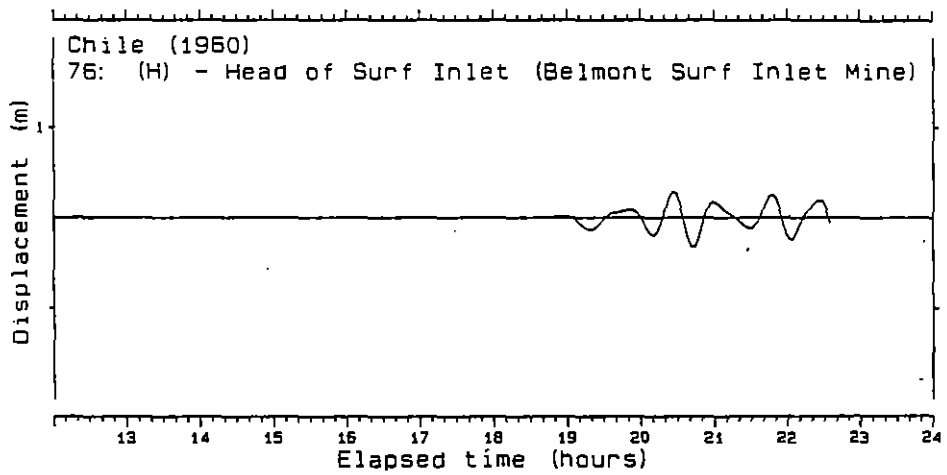
Chile (1960)
76: (H) - Head of Surf Inlet (Belmont Surf Inlet Mine)
Displacement (m)
1
13 14 15 16 17 18 19 20 21 22 23 24
Elapsed time (hours)

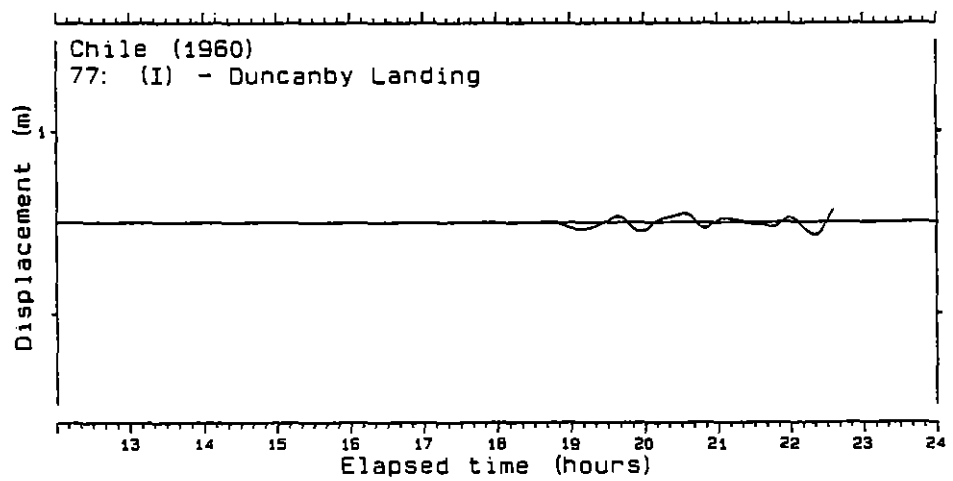
Chile (1960)
77: (I) - Duncanby Landing
Displacement (m)
1
13 14 15 16 17 18 19 20 21 22 23 24
Elapsed time (hours)

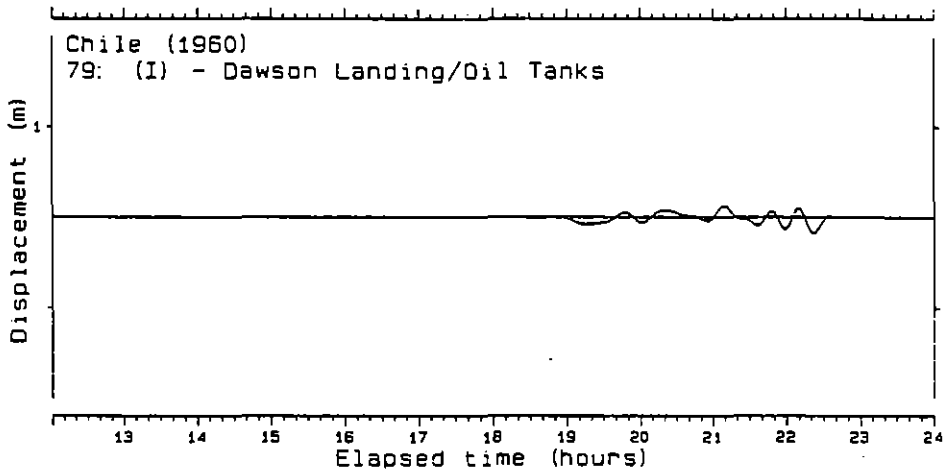
Chile (1960)
79: (I) - Dawson Landing/Oil Tanks
Displacement (m)
1
13 14 15 16 17 18 19 20 21 22 23 24
Elapsed time (hours)

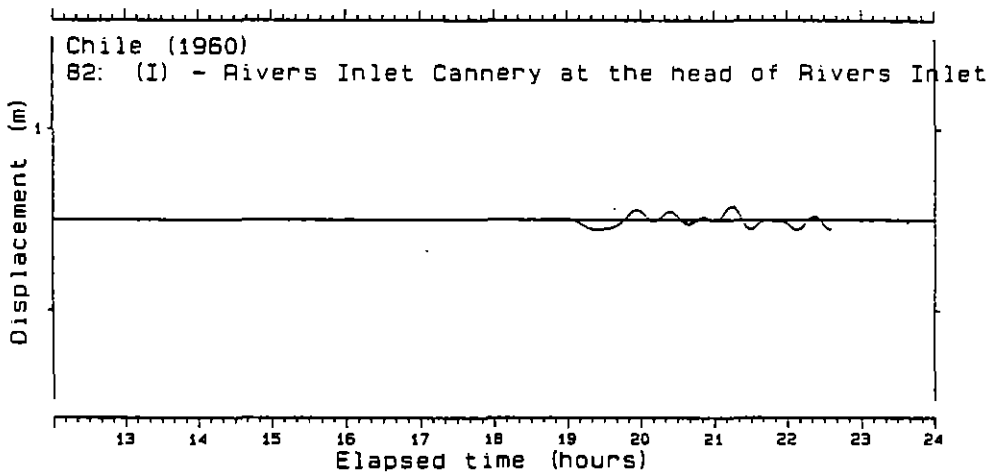
Chile (1960)
82: (I) - Rivers Inlet Cannery at the head of Rivers Inlet
Displacement (m)
1
13 14 15 16 17 18 19 20 21 22 23 24
Elapsed time (hours)

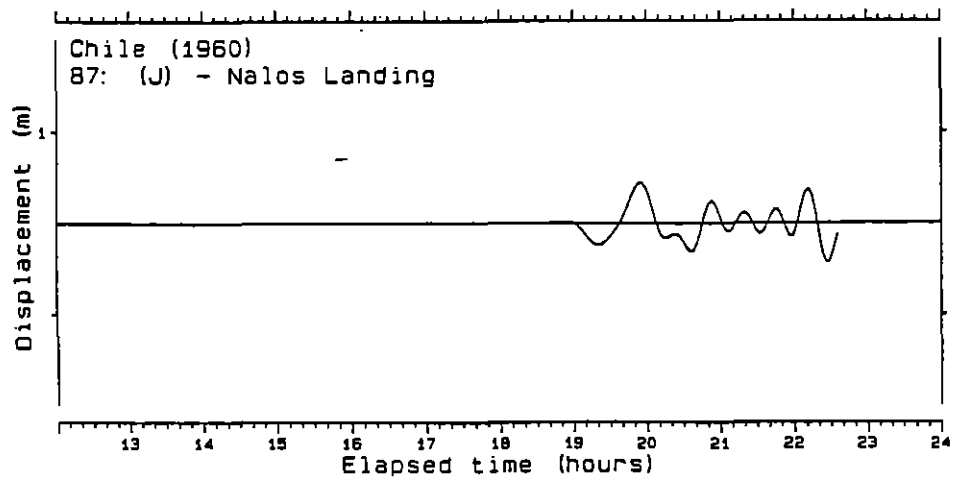
Chile (1960)
87: (J) - Nalos Landing
Displacement (m)
1
13 14 15 16 17 18 19 20 21 22 23 24
Elapsed time (hours)

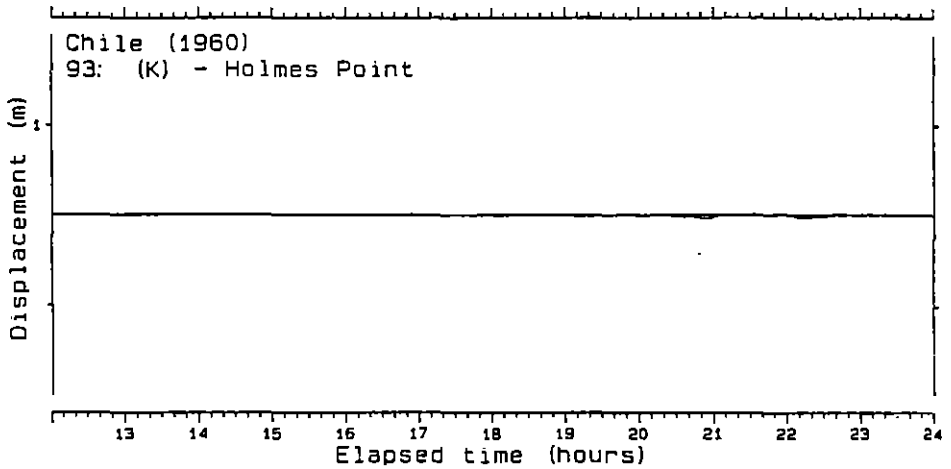
Chile (1960)
93: (K) - Holmes Point
Displacement (m)
1
13 14 15 16 17 18 19 20 21 22 23 24
Elapsed time (hours)

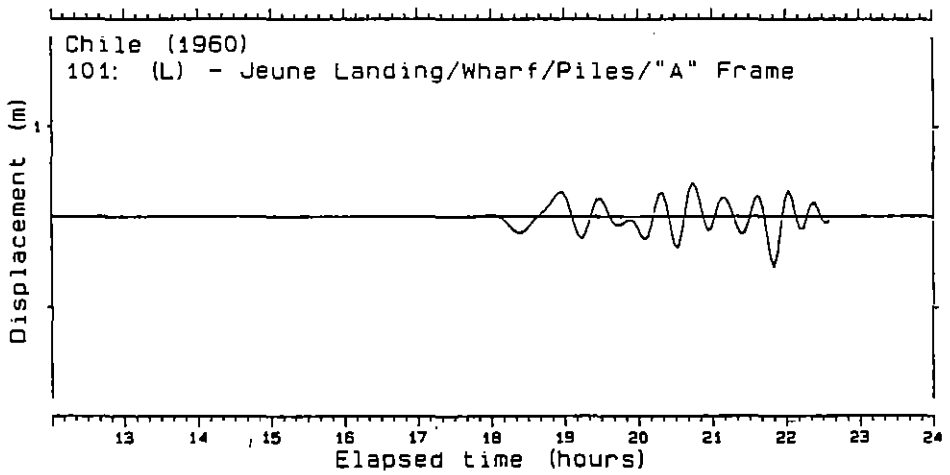
Chile (1960)
101: (L) - Jeune Landing/Wharf/Piles/"A" Frame
Displacement (m)
1
13 14 15 16 17 18 19 20 21 22 23 24
Elapsed time (hours)

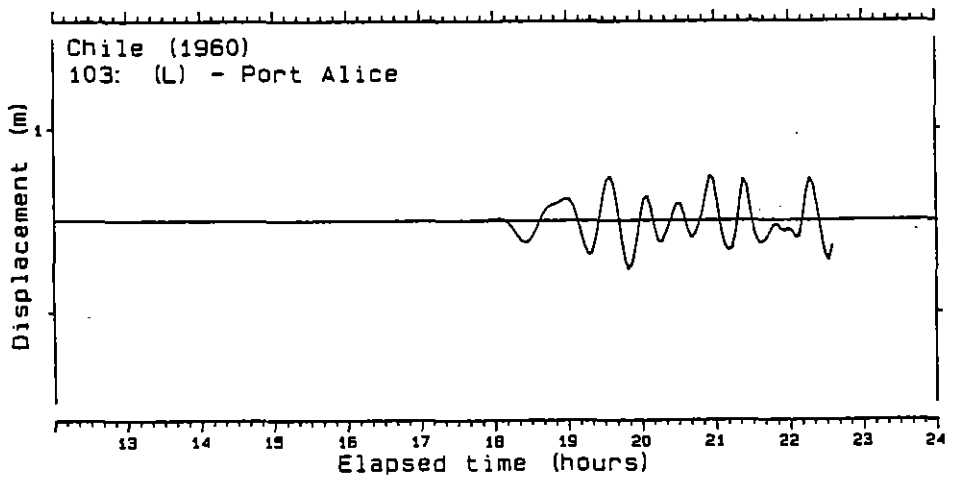
Chile (1960)
103: (L) - Port Alice
Displacement (m)
1
13 14 15 16 17 18 19 20 21 22 23 24
Elapsed time (hours)

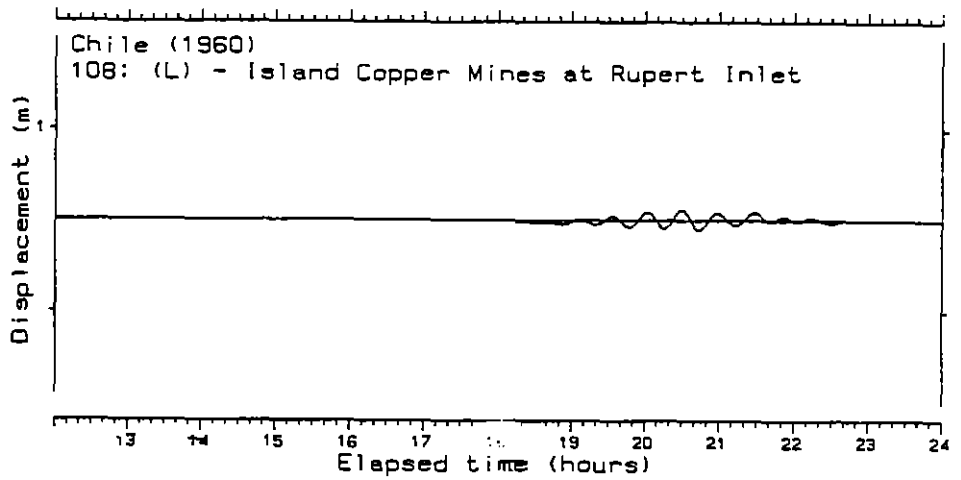
Chile (1960)
108: (L) - Island Copper Mines at Rupert Inlet
Displacement (m)
1
13
15
16
17
19
20
21
22
23
24
Elapsed time (hours)

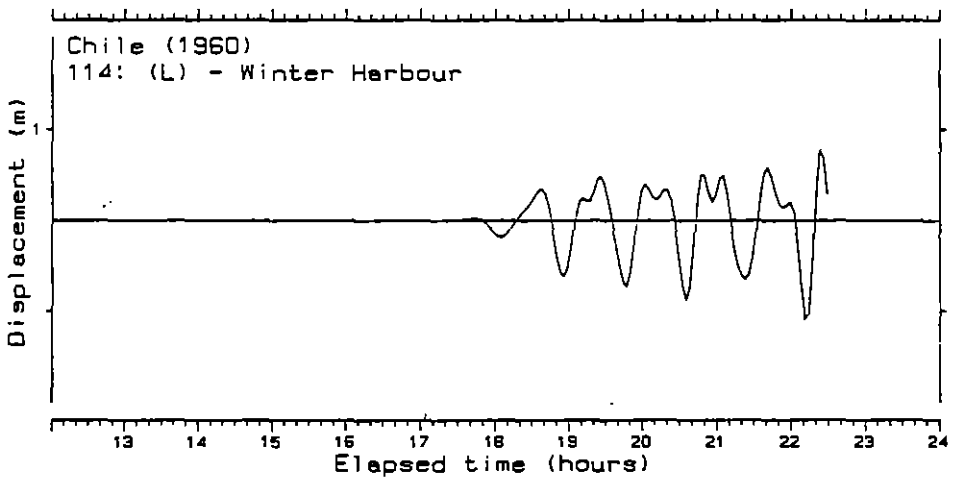
Chile (1960)
114: (L) - Winter Harbour
Displacement (m)
1
13
14
15
16
17
18
19
20
21
22
23
24
Elapsed time (hours)

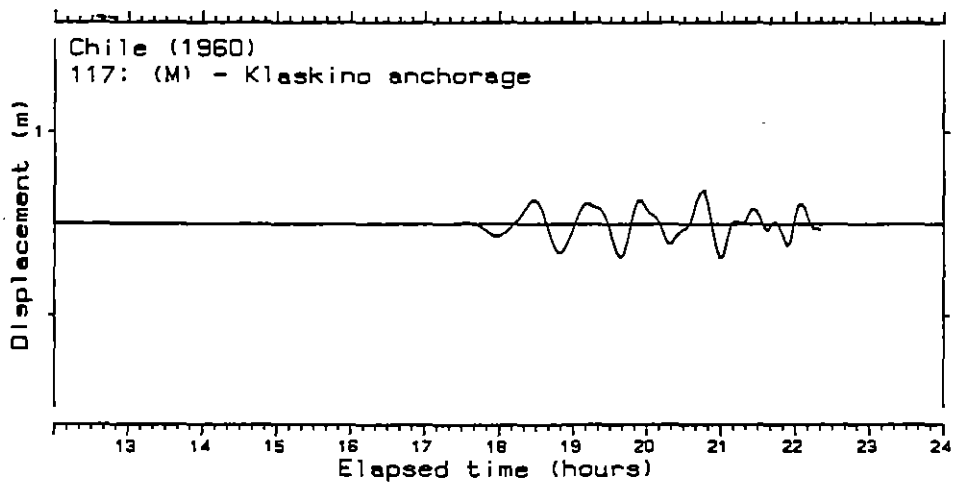
Chile (1960)
117: (M) - Klaskino anchorage
Displacement (m)
1
13
14
15
16
17
18
19
20
21
22
23
24
Elapsed time (hours)

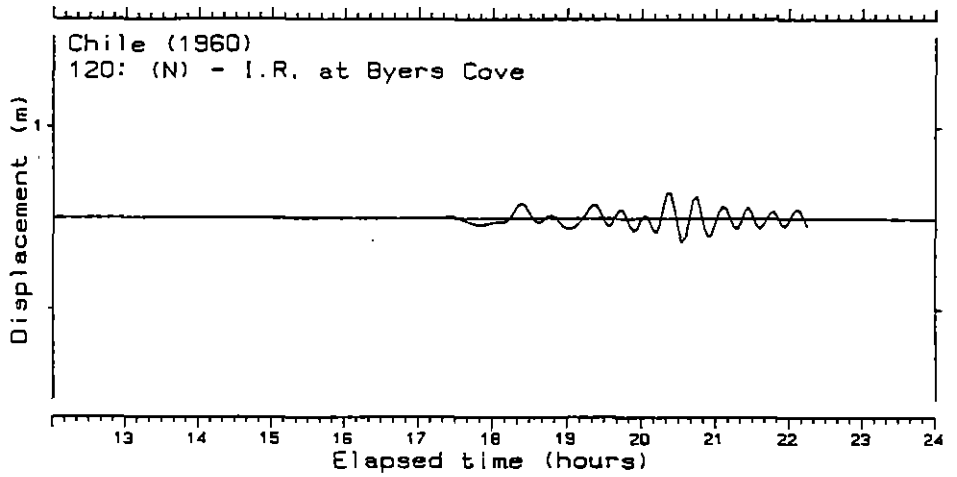
Chile (1960)
120: (N) - I.R. at Byers Cove
Displacement (m)
1
13 14 15 16 17 18 19 20 21 22 23 24
Elapsed time (hours)

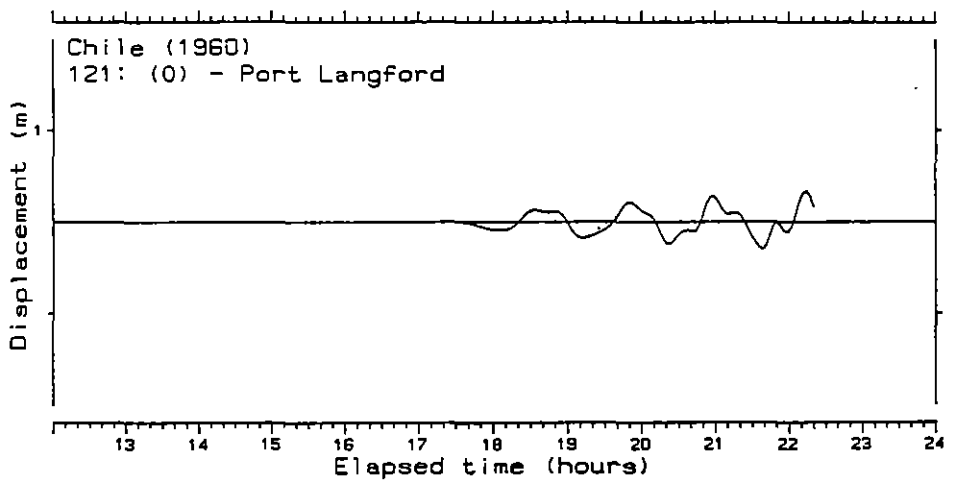
Chile (1960)
121: (0) - Port Langford
Displacement (m)
1
13 14 15 16 17 18 19 20 21 22 23 24
Elapsed time (hours)

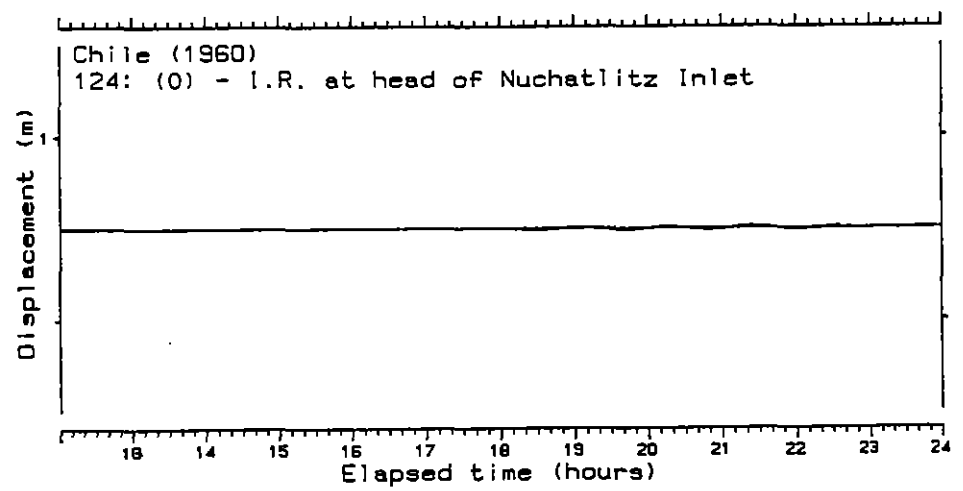
Chile (1960)
124: (0) - I.R. at head of Nuchatlitz Inlet
Displacement (m)
1
13 14 15 16 17 18 19 20 21 22 23 24
Elapsed time (hours)

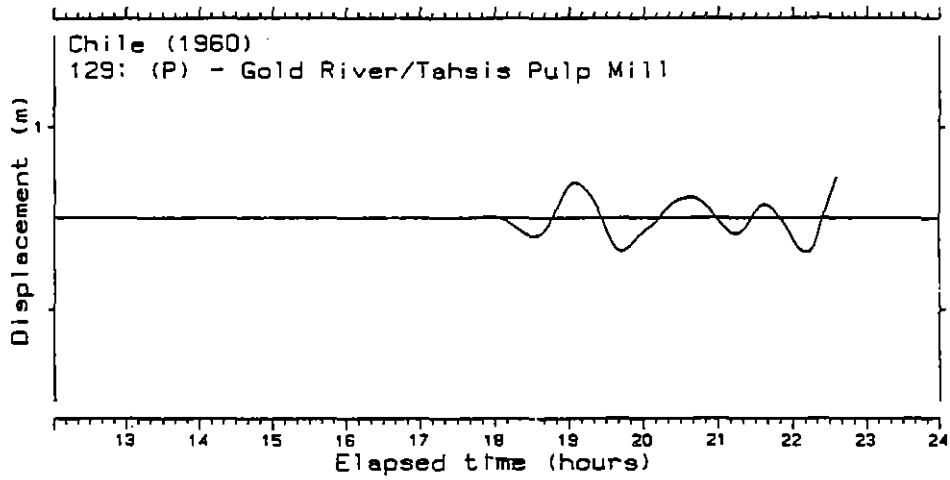
Chile (1960)
129: (P) - Gold River/Tahsis Pulp Mill
Displacement (m)
1
13 14 15 16 17 18 19 20 21 22 23 24
Elapsed time (hours)

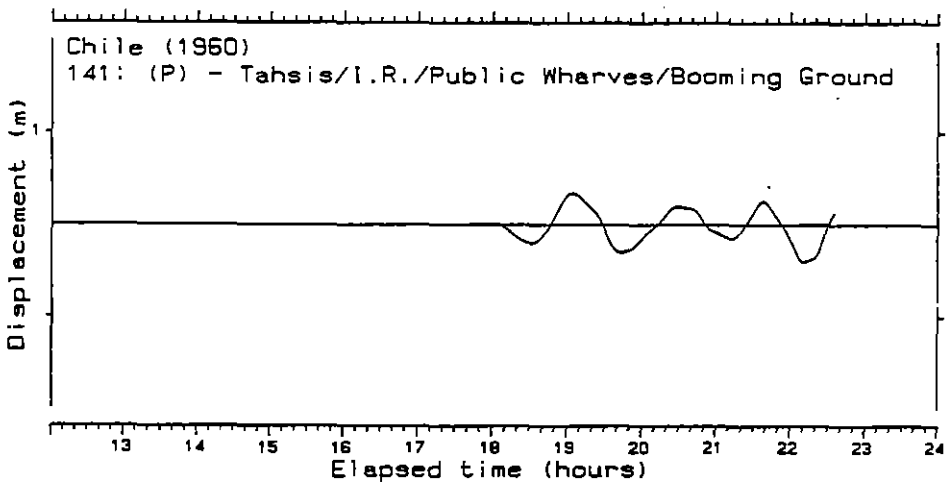
Chile (1960)
141: (P) - Tahsis/I.R./Public Wharves/Booming Ground
Displacement (m)
1
13 14 15 16 17 18 19 20 21 22 23 24
Elapsed time (hours)

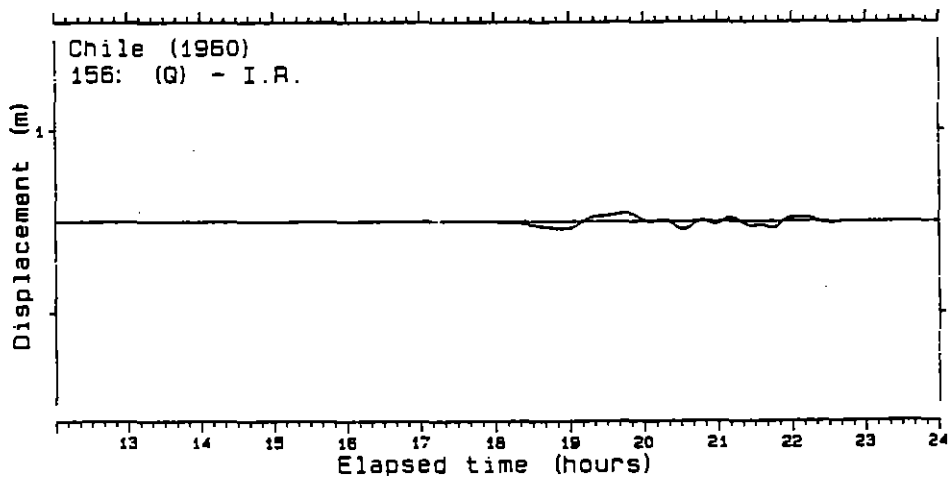
Chile (1960)
156: (Q) - I.R.
Displacement (m)
1
13 14 15 16 17 18 19 20 21 22 23 24
Elapsed time (hours)

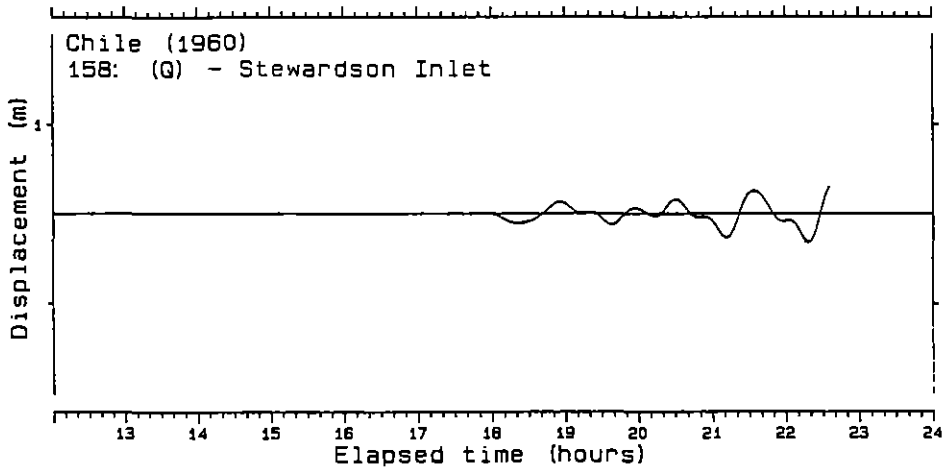
Chile (1960)
158: (Q) - Stewardson Inlet
Displacement (m)
1
13 14 15 16 17 18 19 20 21 22 23 24
Elapsed time (hours)

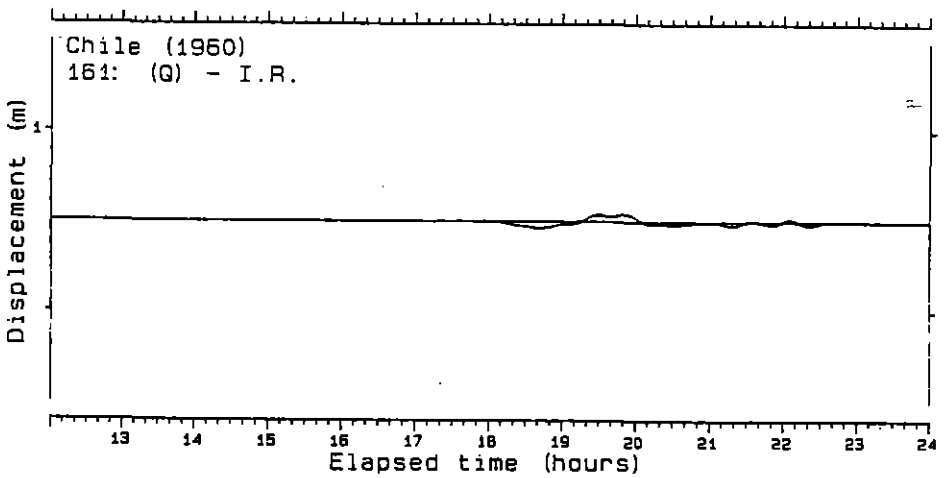
Chile (1960)
161: (Q) - I.R.
Displacement (m)
1
13 14 15 16 17 18 19 20 21 22 23 24
Elapsed time (hours)

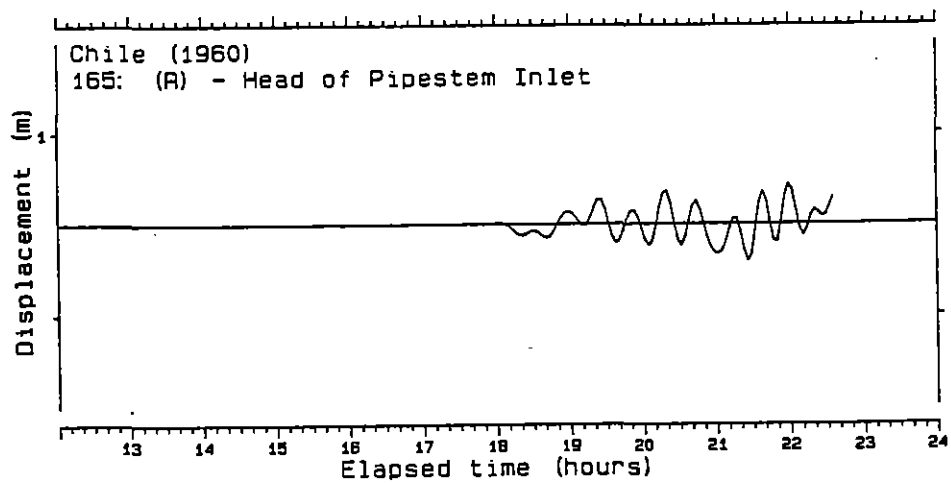
Chile (1960)
165: (R) - Head of Pipestem Inlet
Displacement (m)
1
13 14 15 16 17 18 19 20 21 22 23 24
Elapsed time (hours)

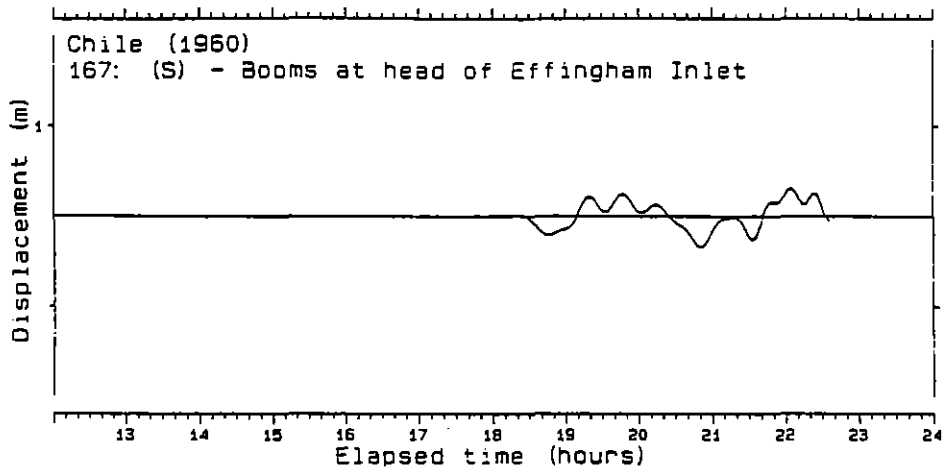
Chile (1960)
167: (S) - Booms at head of Effingham Inlet
Displacement (m)
1
13 14 15 16 17 18 19 20 21 22 23 24
Elapsed time (hours)

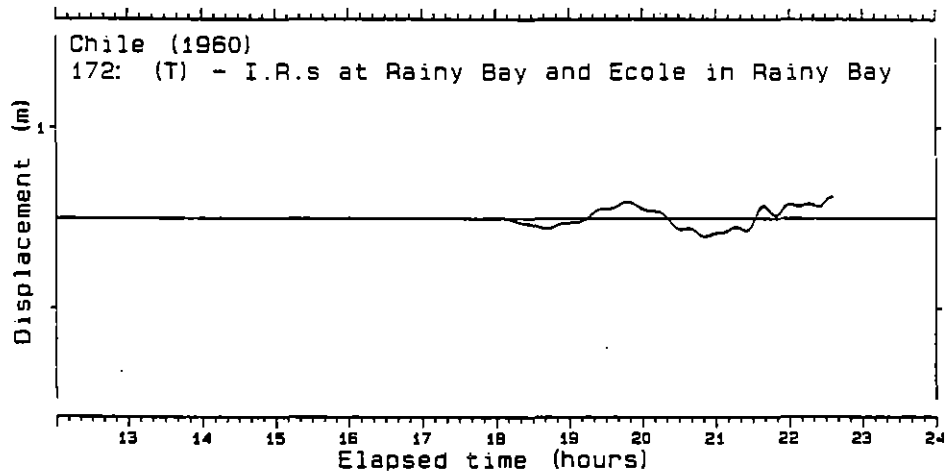
Chile (1960)
172: (T) - I.R.s at Rainy Bay and Ecole in Rainy Bay
Displacement (m)
1
13 14 15 16 17 18 19 20 21 22 23 24
Elapsed time (hours)

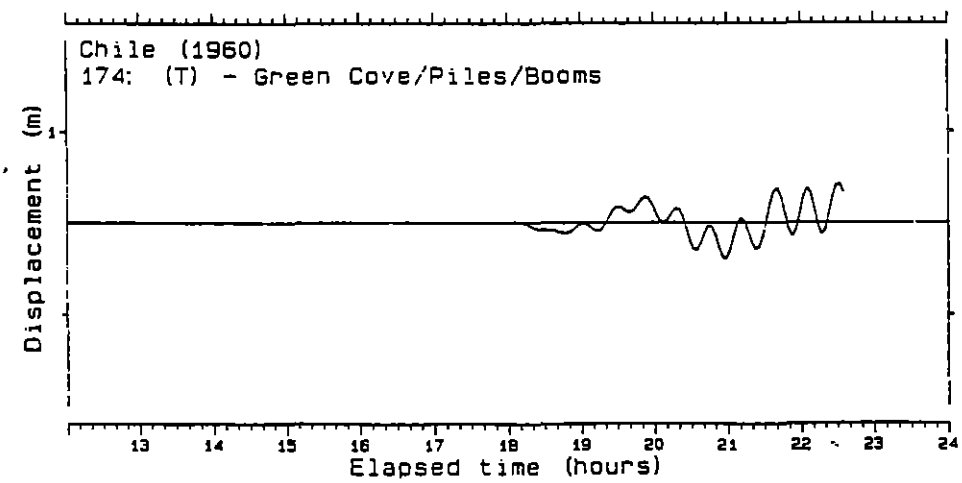
Chile (1960)
174: (T) - Green Cove/Piles/Booms
Displacement (m)
1
13 14 15 16 17 18 19 20 21 22 23 24
Elapsed time (hours)

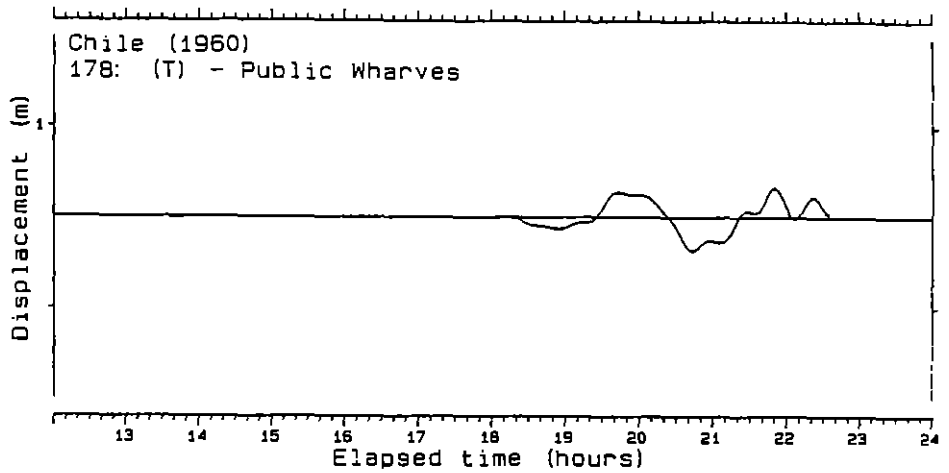
Chile (1960)
178: (T) - Public Wharves
Displacement (m)
1
13 14 15 16 17 18 19 20 21 22 23 24
Elapsed time (hours)

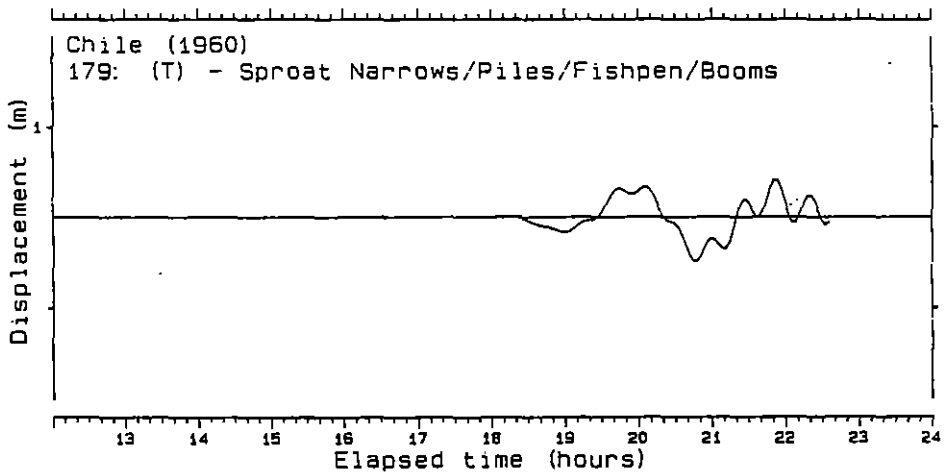
Chile (1960)
179: (T) - Sproat Narrows/Piles/Fishpen/Booms
Displacement (m)
1
13 14 15 16 17 18 19 20 21 22 23 24
Elapsed time (hours)

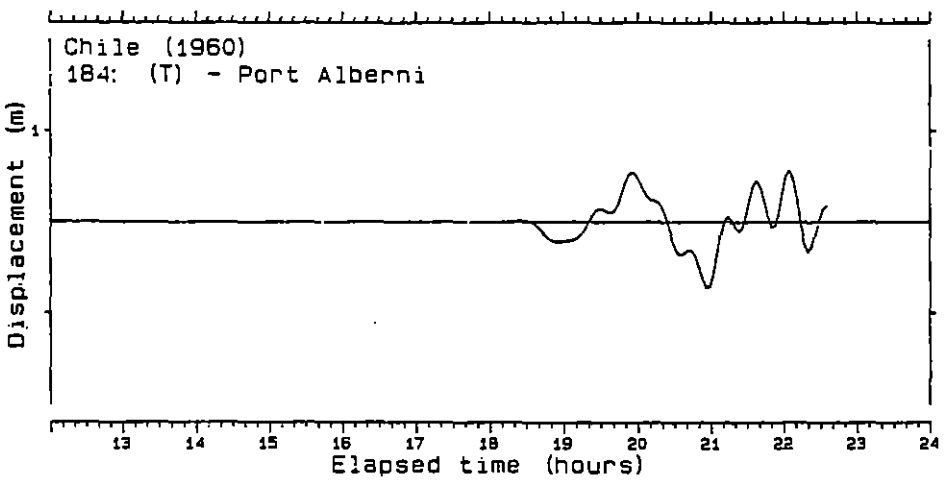
Chile (1960)
184: (T) - Port Alberni
Displacement (m)
1
13 14 15 16 17 18 19 20 21 22 23 24
Elapsed time (hours)

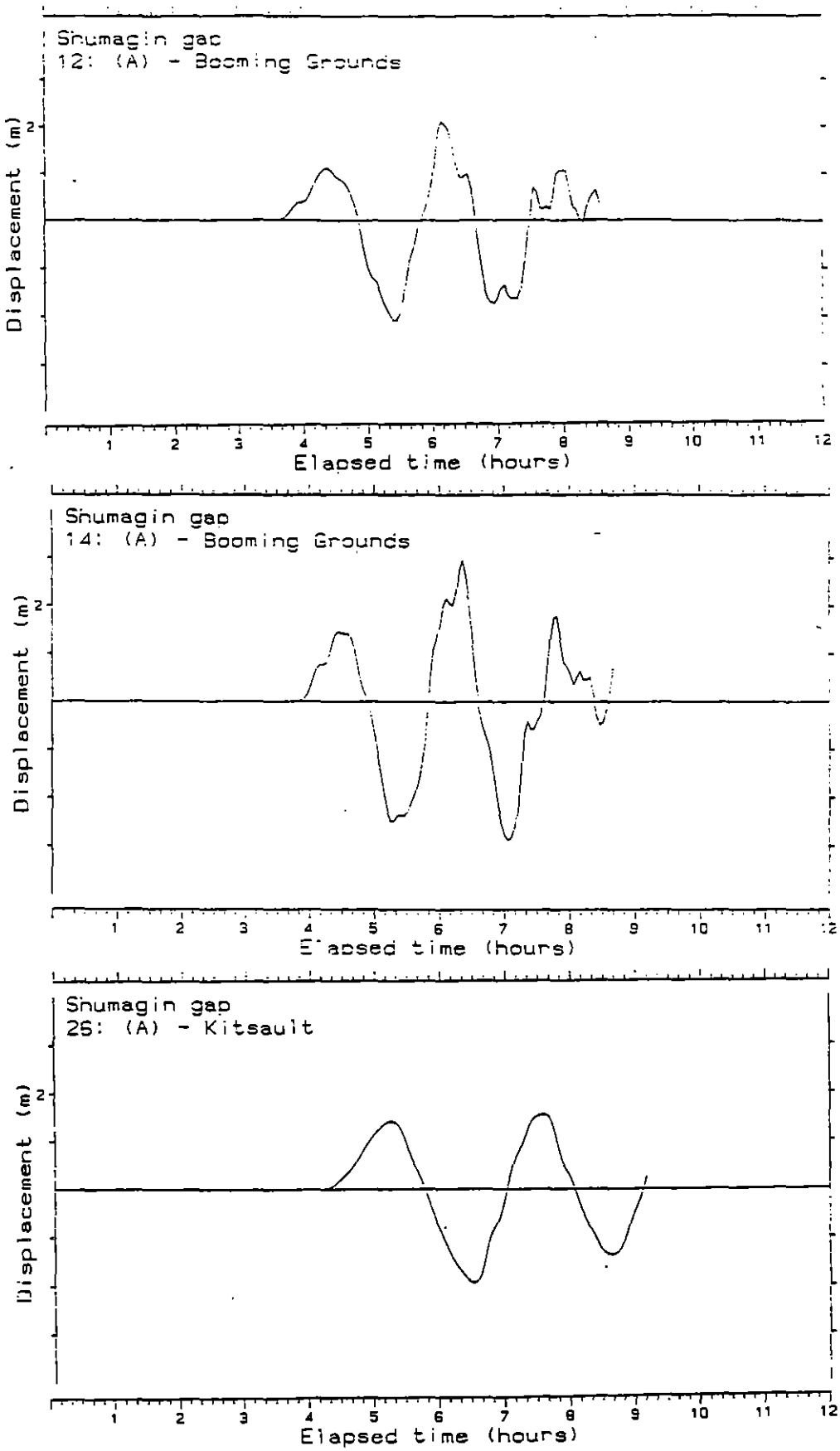
Shumagin gap
12: (A) - Booming Grounds
Displacement (m)
2
1 2 3 4 5 6 7 8 9 10 11 12
Elapsed time (hours)
Shumagin gap
14: (A) - Booming Grounds
Displacement (m)
2
1 2 3 4 5 6 7 8 9 10 11 12
Elapsed time (hours)
Shumagin gap
26: (A) - Kitsault
Displacement (m)
2
1 2 3 4 5 6 7 8 9 10 11 12
Elapsed time (hours)

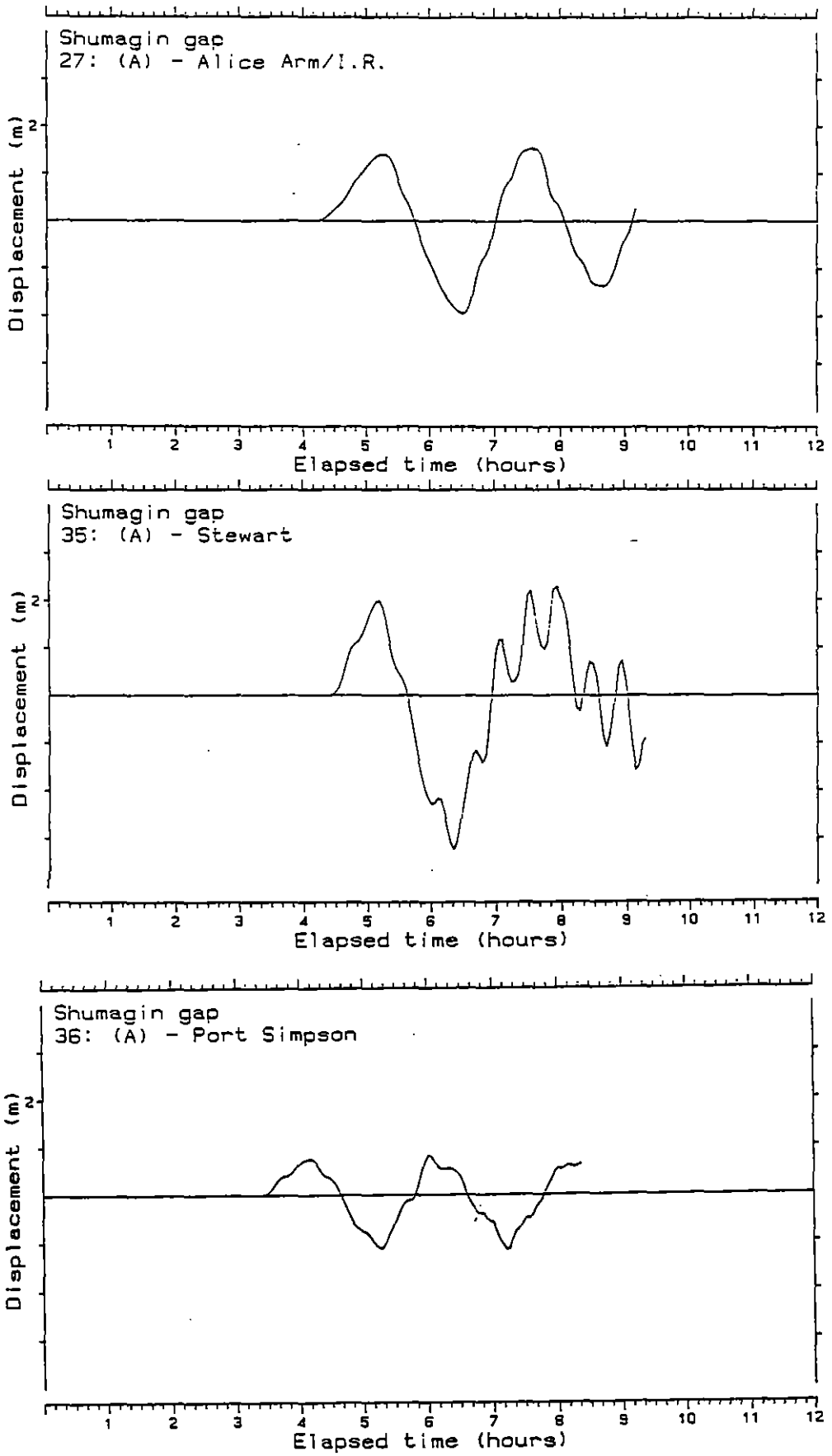
Shumagin gap
27: (A) - Alice Arm/I.R.
Displacement (m)
2
1 2 3 4 5 6 7 8 9 10 11 12
Elapsed time (hours)
Shumagin gap
35: (A) - Stewart
Displacement (m)
2
1 2 3 4 5 6 7 8 9 10 11 12
Elapsed time (hours)
Shumagin gap
36: (A) - Port Simpson
Displacement (m)
2
1 2 3 4 5 6 7 8 9 10 11 12
Elapsed time (hours)

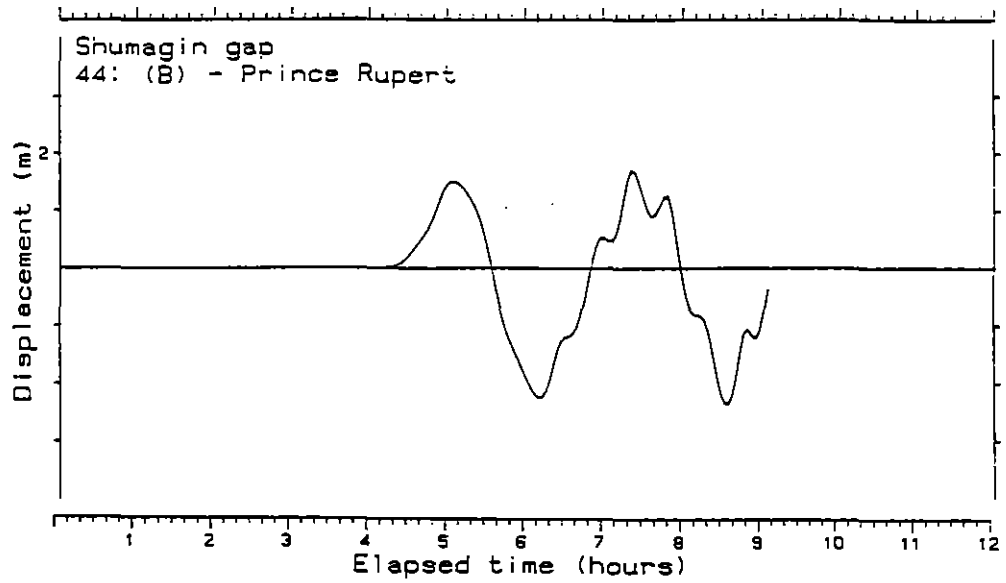
Shumagin gap
44: (B) - Prince Rupert
Displacement (m)
2
1 2 3 4 5 6 7 8 9 10 11 12
Elapsed time (hours)

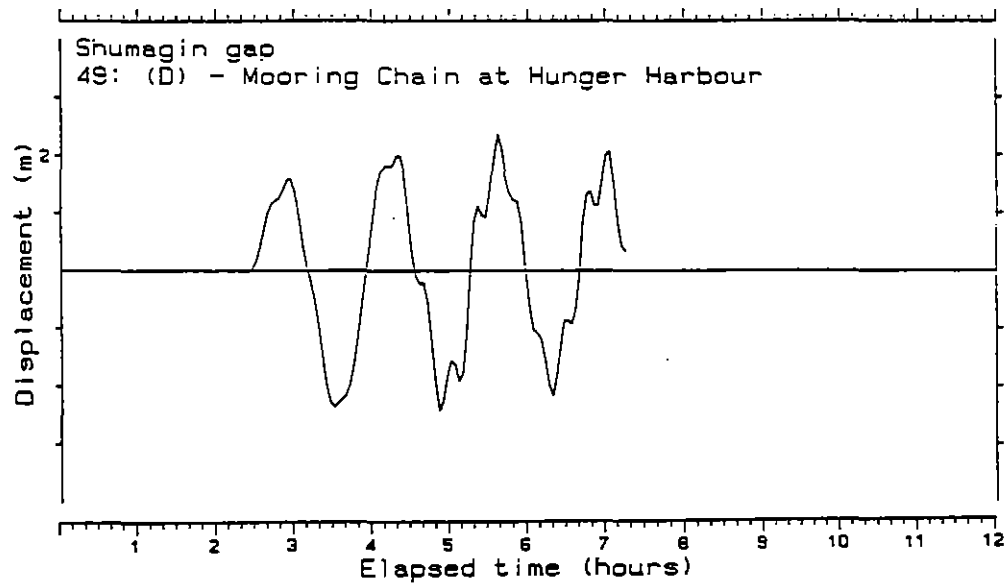
Shumagin gap
49: (D) - Mooring Chain at Hunger Harbour
Displacement (m)
2
1 2 3 4 5 6 7 8 9 10 11 12
Elapsed time (hours)

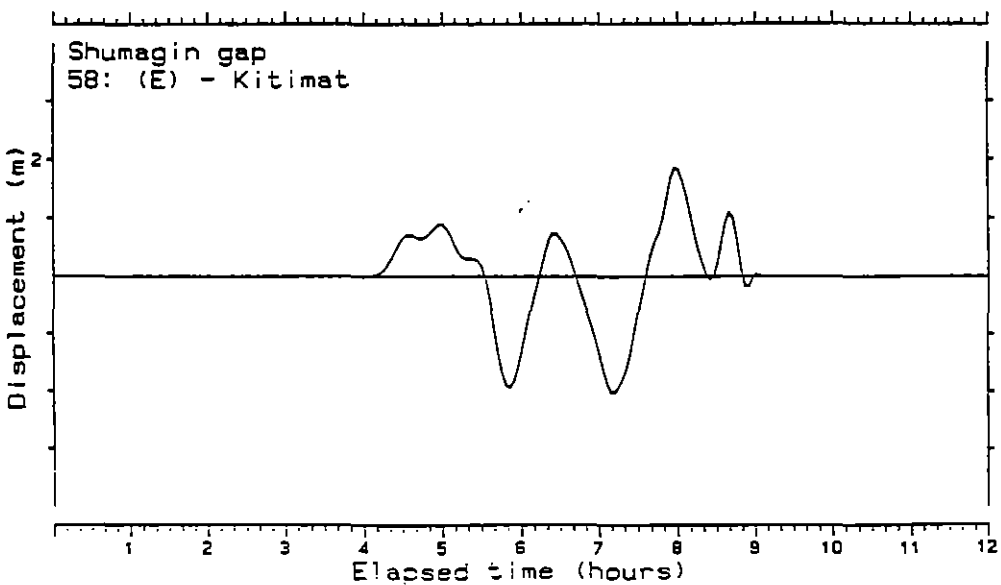
Shumagin gap
58: (E) - Kitimat
Displacement (m)
2
1 2 3 4 5 6 7 8 9 10 11 12
Elapsed time (hours)

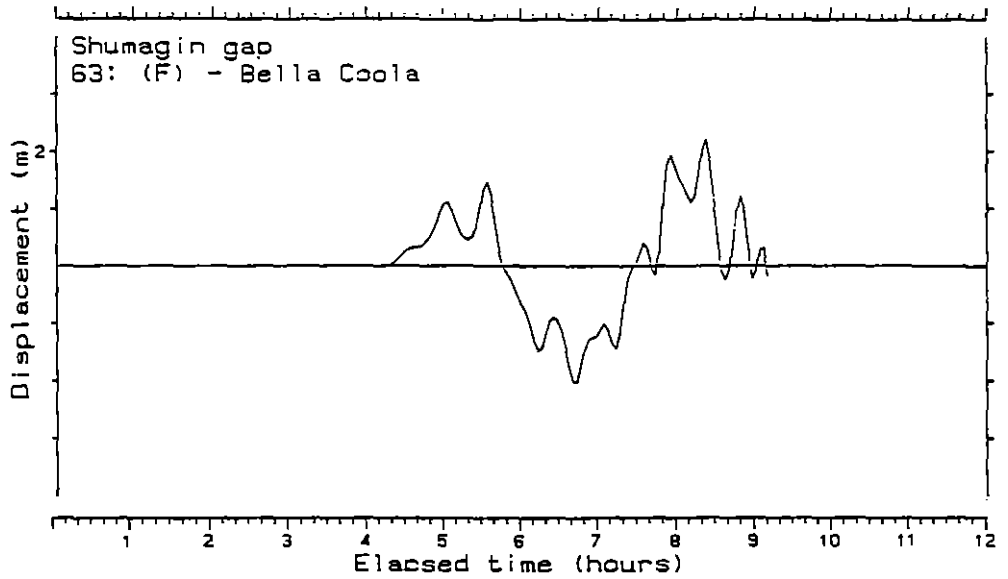
Shumagin gap
63: (F) - Bella Coola
Displacement (m)
2
1 2 3 4 5 6 7 8 9 10 11 12
Elapsed time (hours)

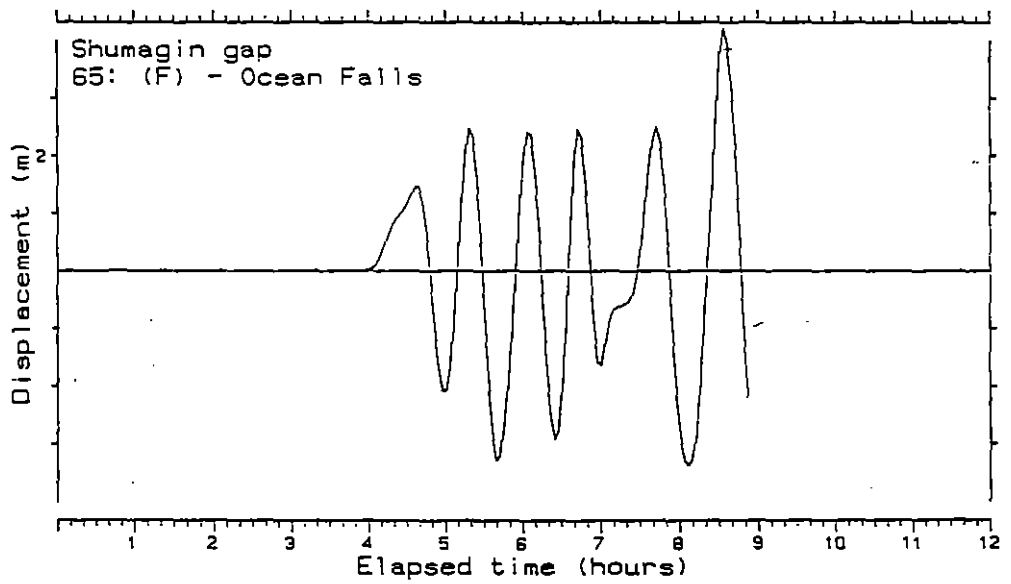
Shumagin gap
65: (F) - Ocean Falls
Displacement (m)
2
1 2 3 4 5 6 7 8 9 10 11 12
Elapsed time (hours)

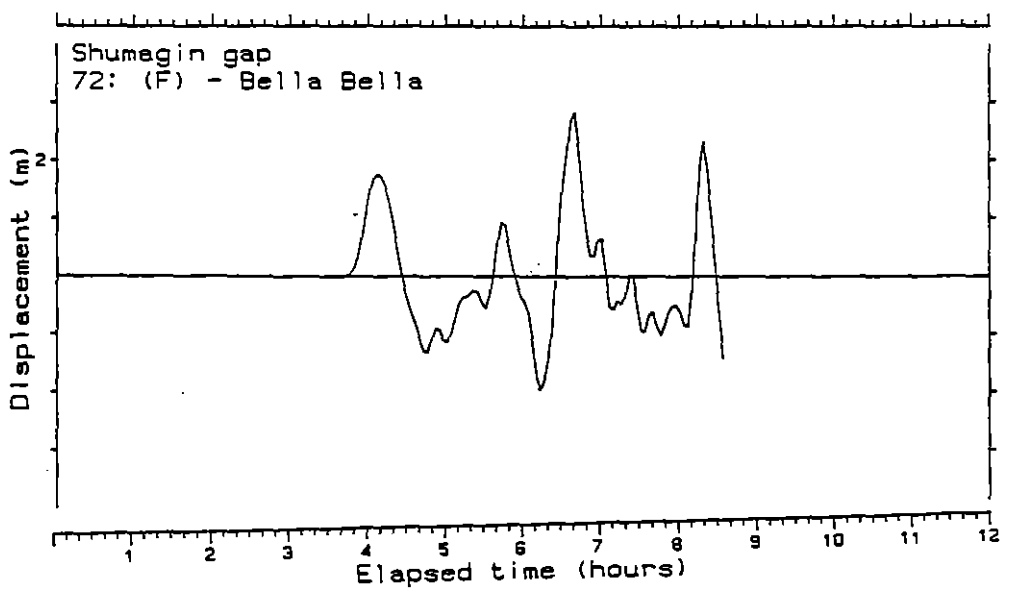
Shumagin gap
72: (F) - Bella Bella
Displacement (m)
2
1 2 3 4 5 6 7 8 9 10 11 12
Elapsed time (hours)

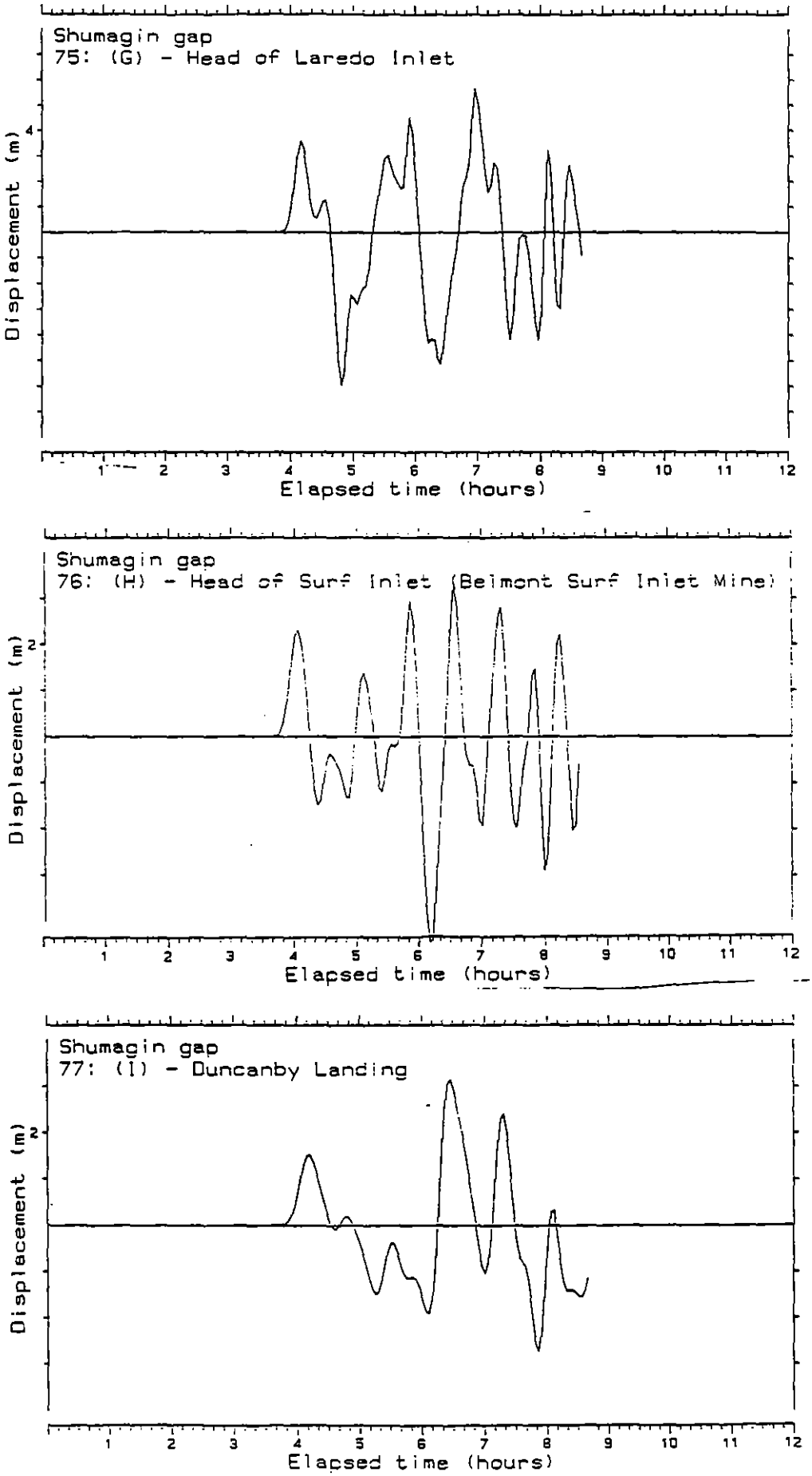
Shumagin gap
75: (G) - Head of Laredo Inlet
Displacement (m)
4
1 2 3 4 5 6 7 8 9 10 11 12
Elapsed time (hours)
Shumagin gap
76: (H) - Head of Surf Inlet (Belmont Surf Inlet Mine)
Displacement (m)
2
1 2 3 4 5 6 7 8 9 10 11 12
Elapsed time (hours)
Shumagin gap
77: (I) - Duncanby Landing
Displacement (m)
2
1 2 3 4 5 6 7 8 9 10 11 12
Elapsed time (hours)

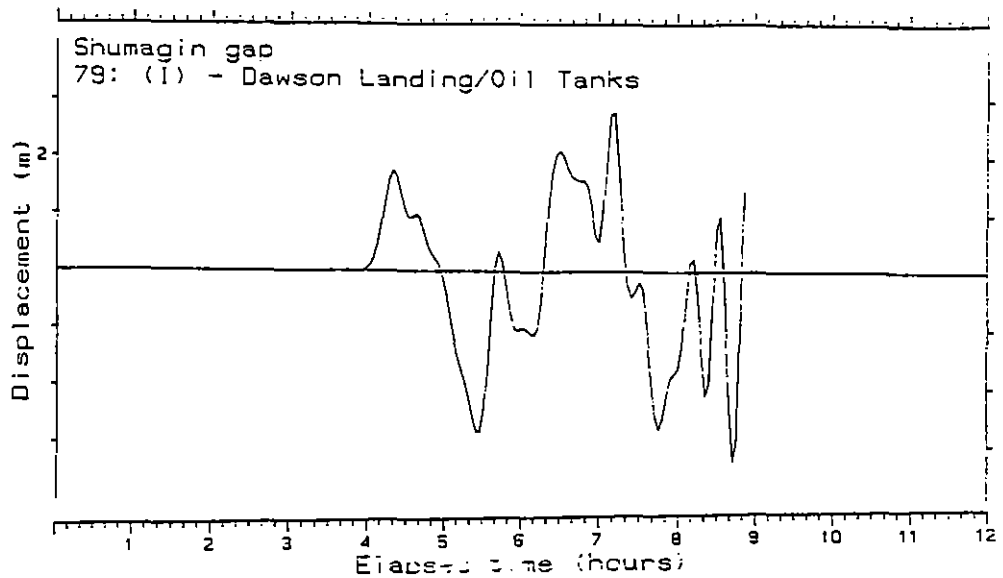
Shumagin gap
79: (I) - Dawson Landing/Oil Tanks
Displacement (m)
2
1 2 3 4 5 6 7 8 9 10 11 12
Elapsed time (hours)

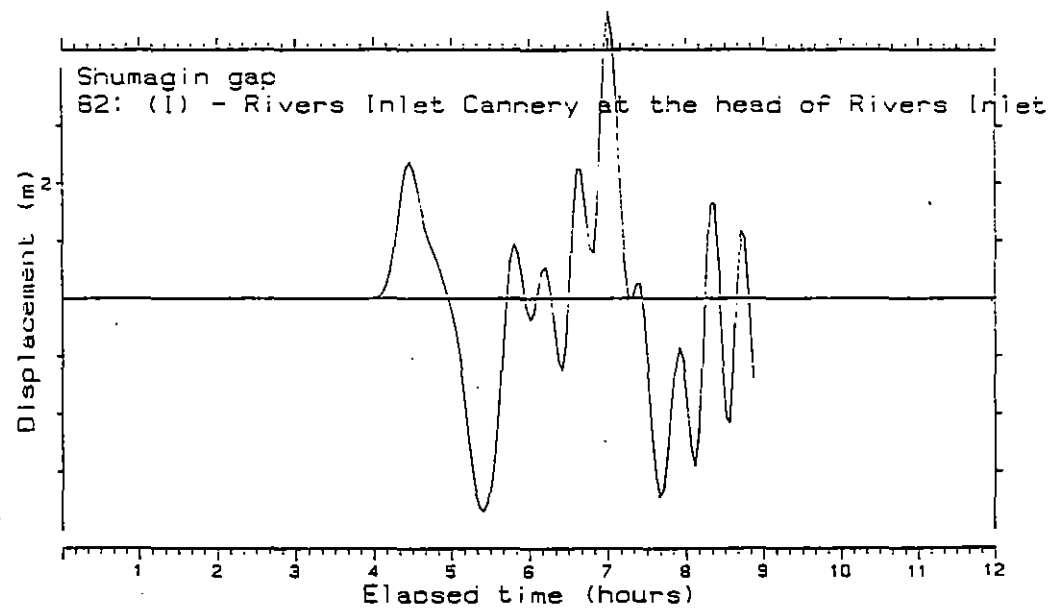
Shumagin gap
82: (I) - Rivers Inlet Cannery at the head of Rivers Inlet
Displacement (m)
2
1 2 3 4 5 6 7 8 9 10 11 12
Elapsed time (hours)

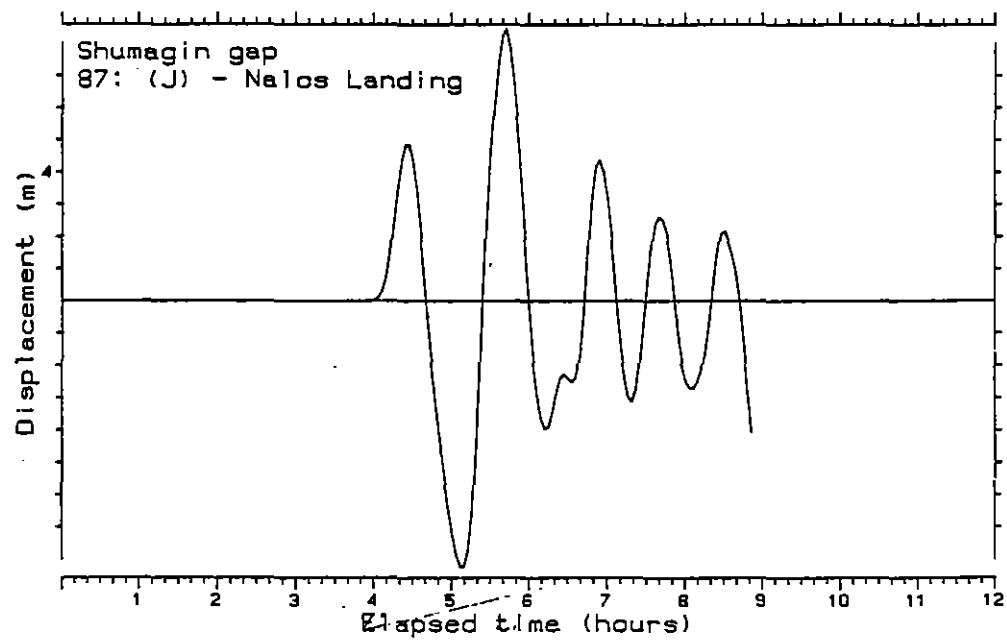
Shumagin gap
87: (J) - Nalos Landing
Displacement (m)
4
1 2 3 4 5 6 7 8 9 10 11 12
Elapsed time (hours)

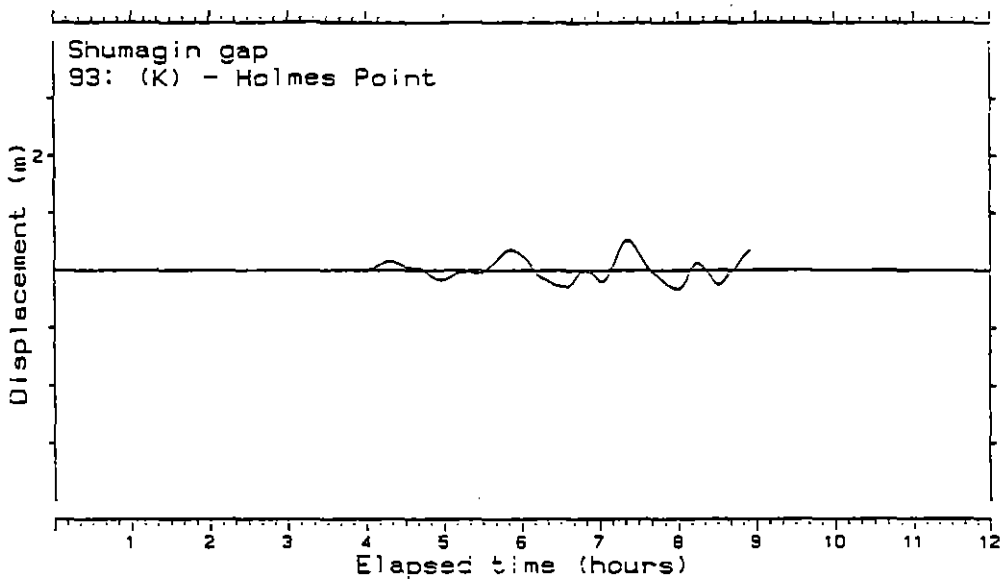
Shumagin gap
93: (K) - Holmes Point
Displacement (m)
2
1 2 3 4 5 6 7 8 9 10 11 12
Elapsed time (hours)

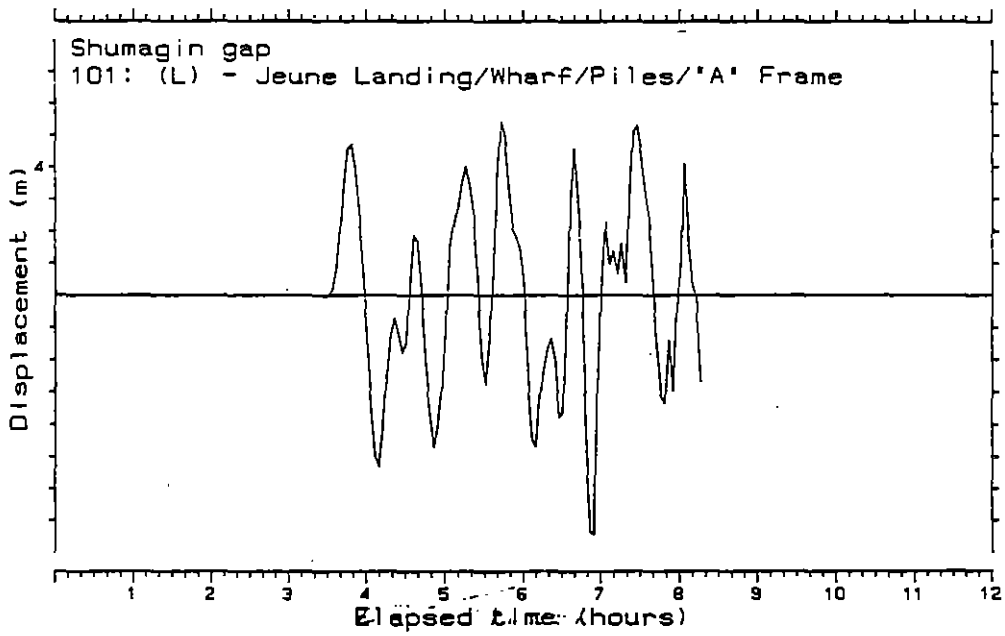
Shumagin gap
101: (L) - Jeune Landing/Wharf/Piles/"A" Frame
Displacement (m)
4
1 2 3 4 5 6 7 8 9 10 11 12
Elapsed time (hours)

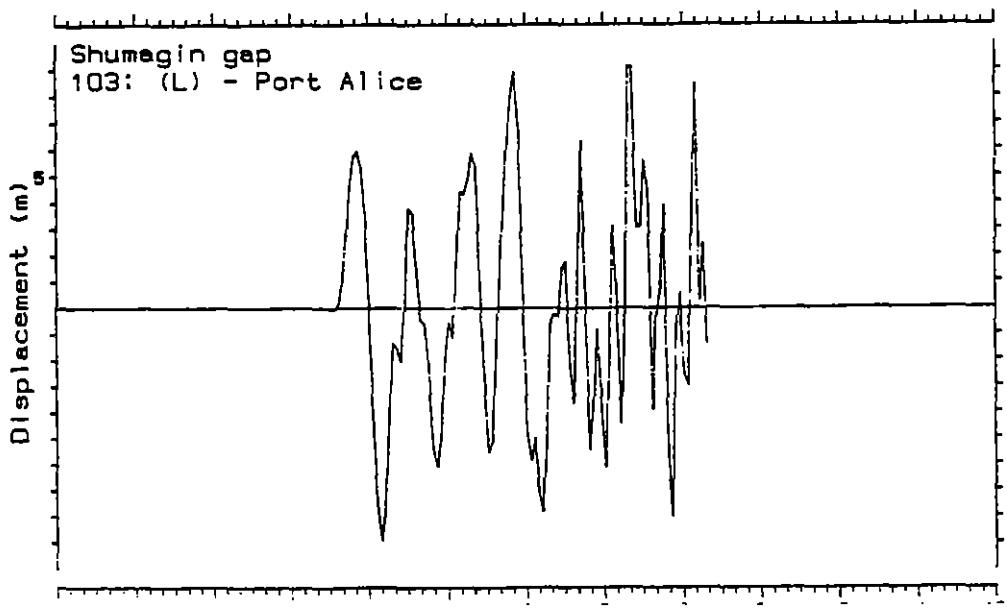
Shumagin gap
103: (L) - Port Alice
Displacement (m)
5

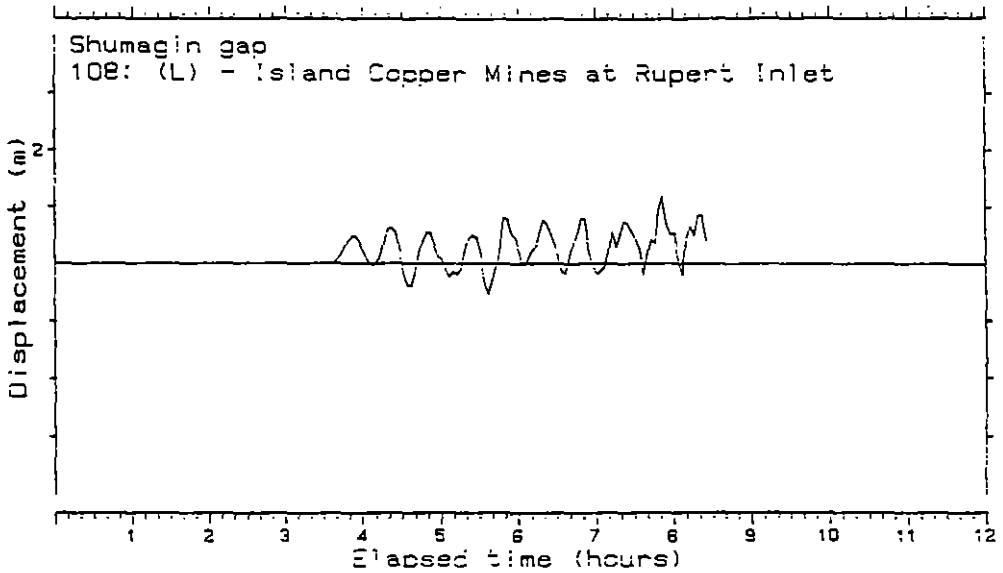
Shumagin gap
108: (L) - Island Copper Mines at Rupert Inlet
Displacement (m)
2
1 2 3 4 5 6 7 8 9 10 11 12
Elapsed time (hours)

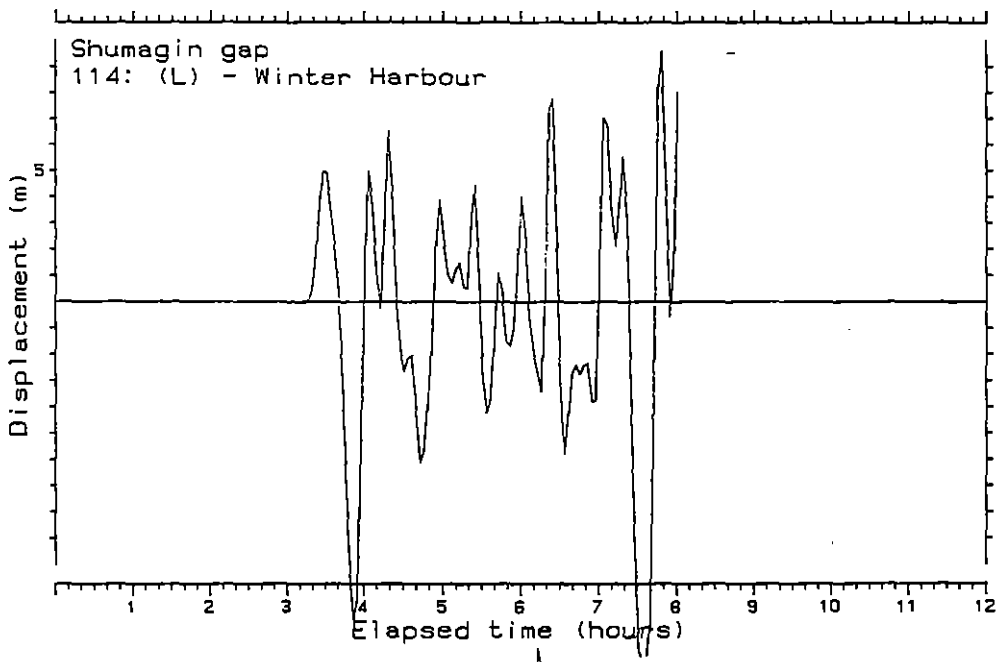
Shumagin gap
114: (L) - Winter Harbour
Displacement (m)
5
1 2 3 4 5 6 7 8 9 10 11 12
Elapsed time (hours)

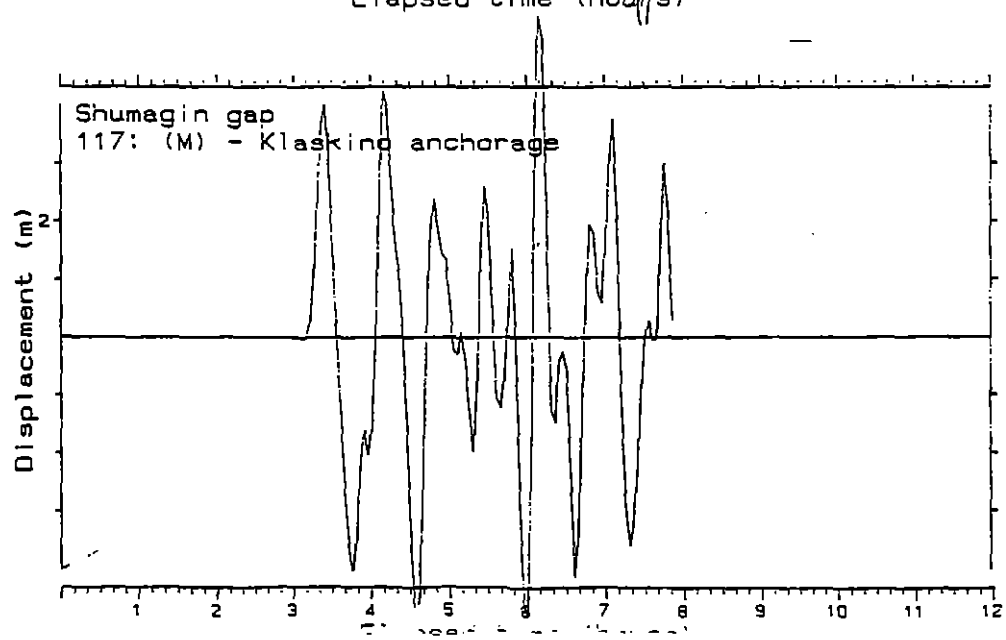
Shumagin gap
117: (M) - Klaskino anchorage
Displacement (m)
2
1 2 3 4 5 6 7 8 9 10 11 12

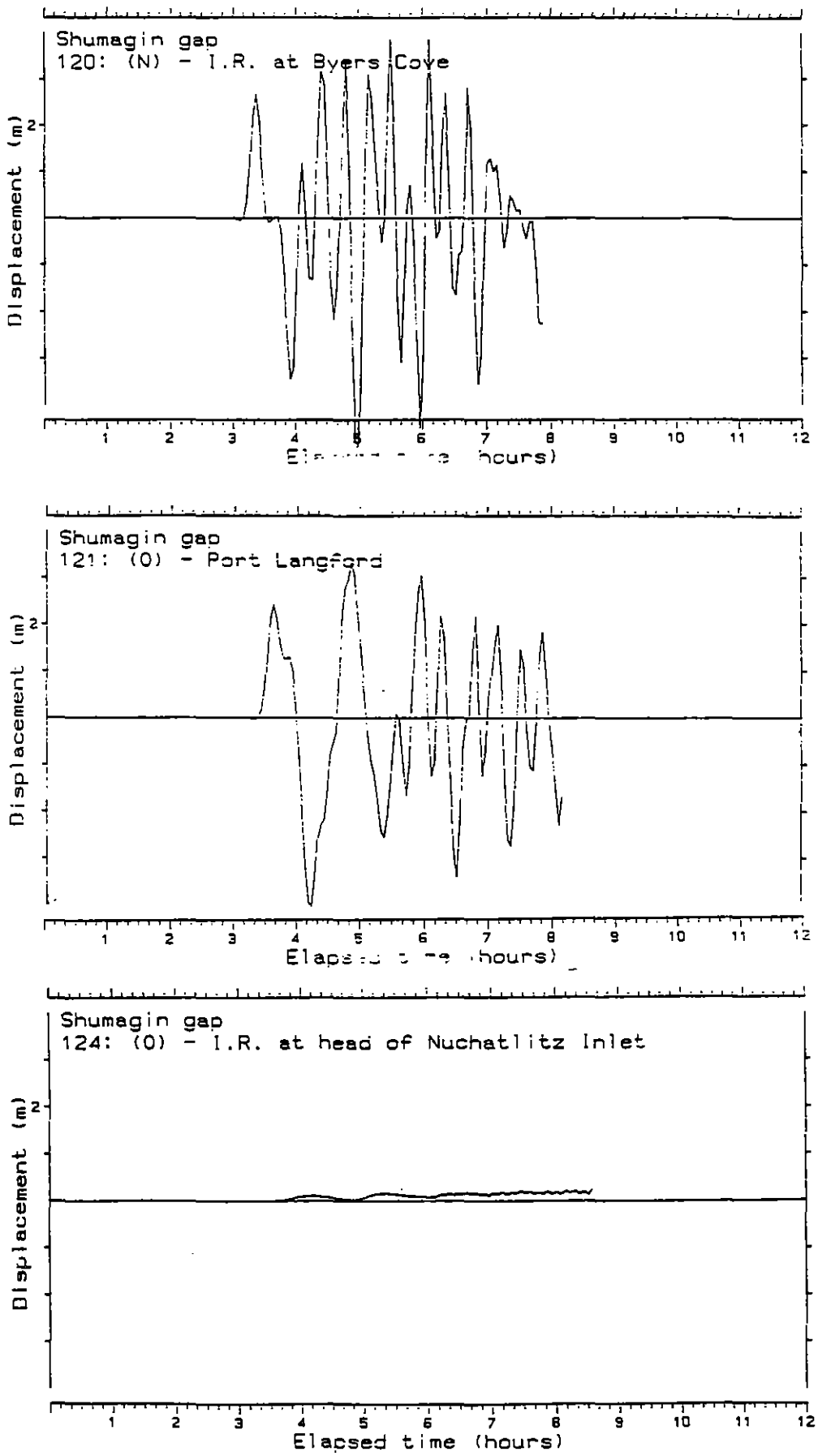
Shumagin gap
120: (N) - I.R. at Byers Cove
Displacement (m)
2
1 2 3 4 5 6 7 8 9 10 11 12
hours)
Shumagin gap
121: (0) - Port Langford
Displacement (m)
2
1 2 3 4 5 6 7 8 9 10 11 12
hours)
Shumagin gap
124: (0) - I.R. at head of Nuchatlitz Inlet
Displacement (m)
2
1 2 3 4 5 6 7 8 9 10 11 12
Elapsed time (hours)

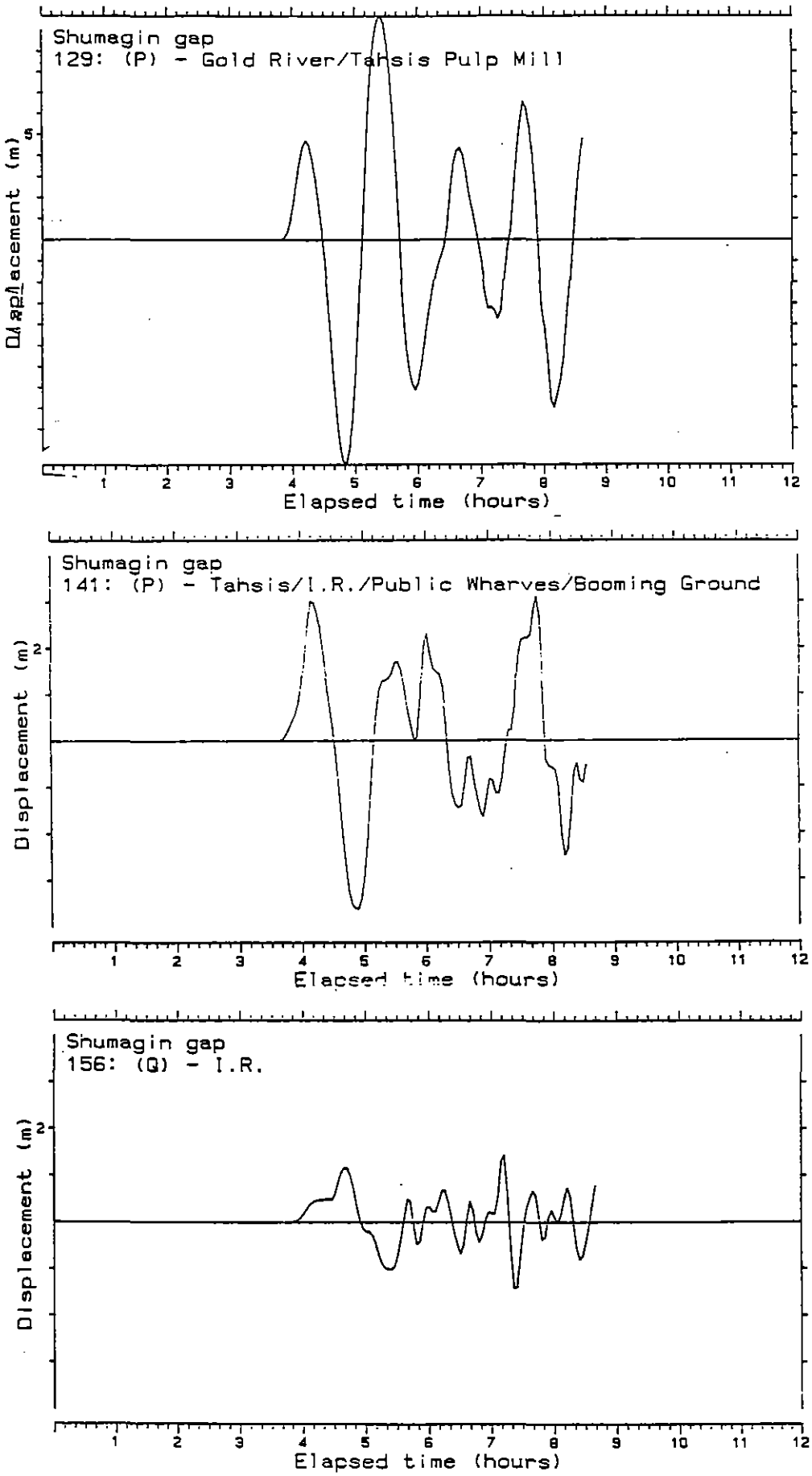
Shumagin gap
129: (P) - Gold River/Tahsis Pulp Mill
Displacement (m)
5
1 2 3 4 5 6 7 8 9 10 11 12
Elapsed time (hours)
Shumagin gap
141: (P) - Tahsis/I.R./Public Wharves/Booming Ground
Displacement (m)
2
1 2 3 4 5 6 7 8 9 10 11 12
Elapsed time (hours)
Shumagin gap
156: (Q) - I.R.
Displacement (m)
2
1 2 3 4 5 6 7 8 9 10 11 12
Elapsed time (hours)

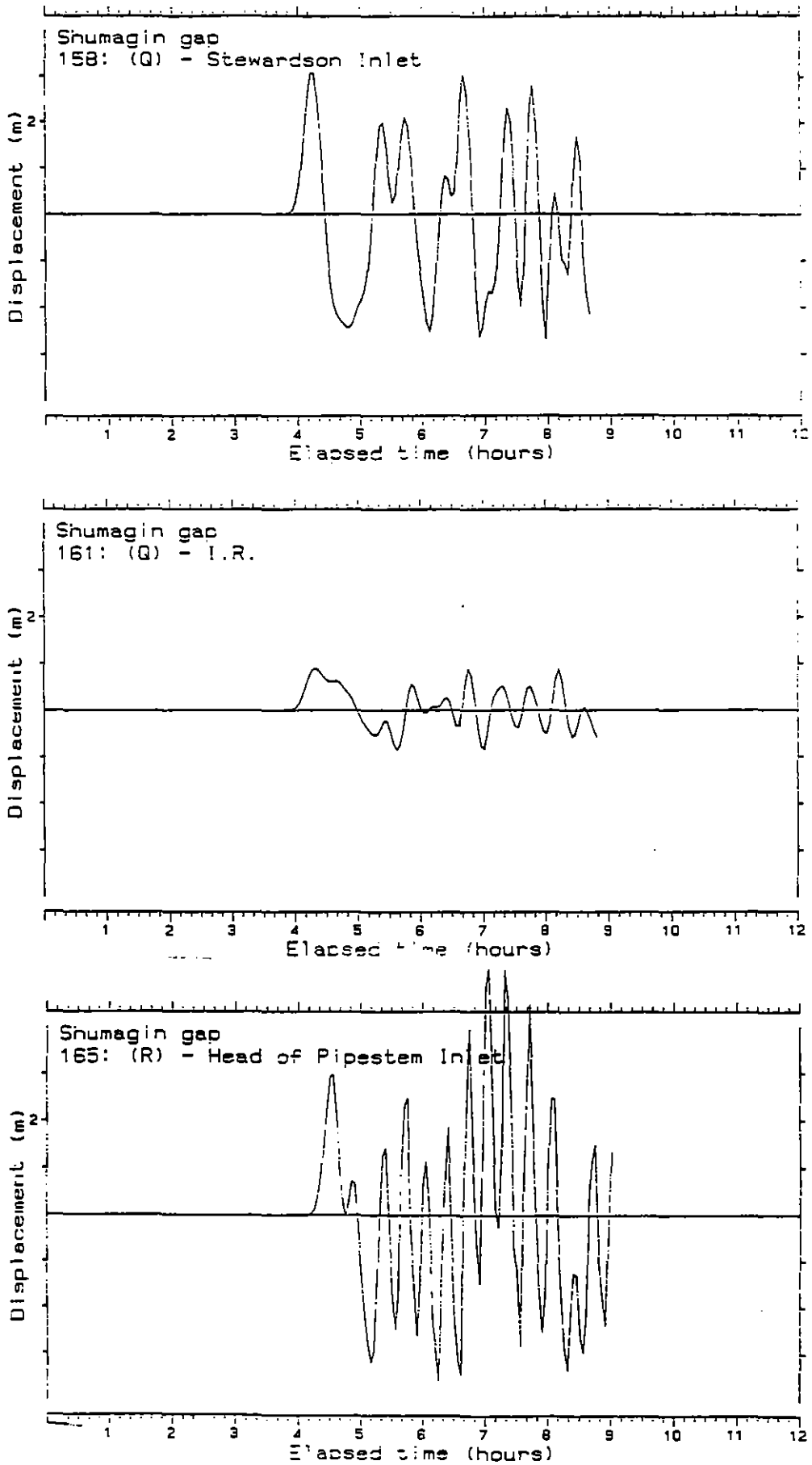
Shumagin gap
158: (Q) - Stewardson Inlet
Displacement (m)
2
1 2 3 4 5 6 7 8 9 10 11 12
Elapsed time (hours)
Shumagin gap
161: (Q) - I.R.
Displacement (m)
2
1 2 3 4 5 6 7 8 9 10 11 12
Elapsed time (hours)
Shumagin gap
165: (R) - Head of Pipestem Inlet
Displacement (m)
2
1 2 3 4 5 6 7 8 9 10 11 12
Elapsed time (hours)

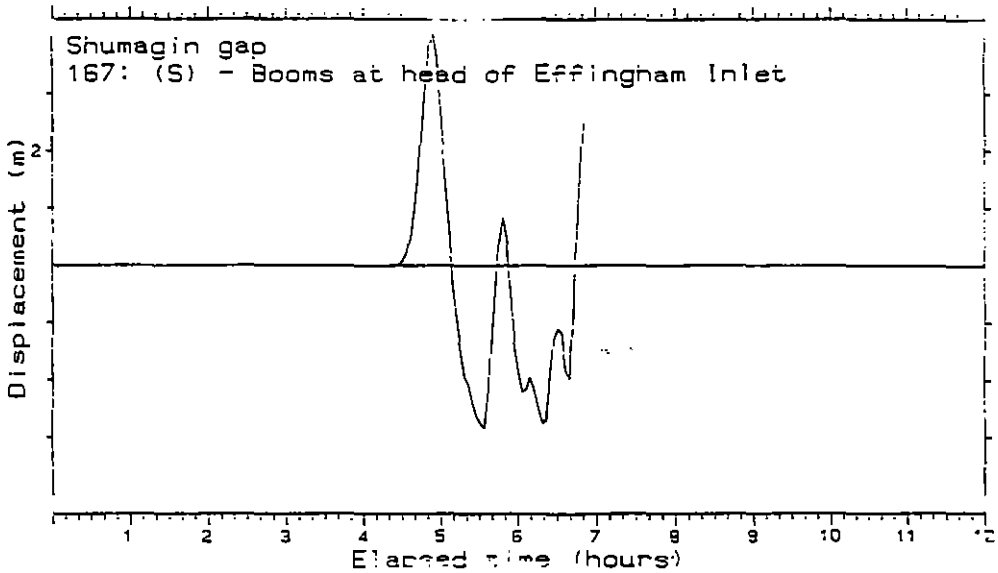
Shumagin gap
167: (S) - Booms at head of Effingham Inlet
Displacement (m)
2
1 2 3 4 5 6 7 8 9 10 11 12
Elapsed time (hours)

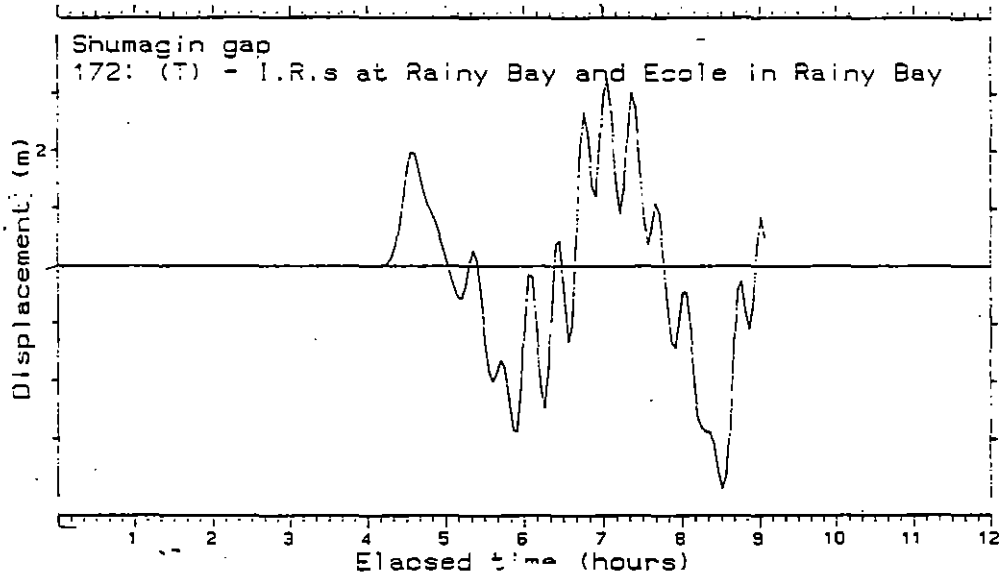
Shumagin gap
172: (T) - I.R.s at Rainy Bay and Ecole in Rainy Bay
Displacement (m)
2
1 2 3 4 5 6 7 8 9 10 11 12
Elapsed time (hours)

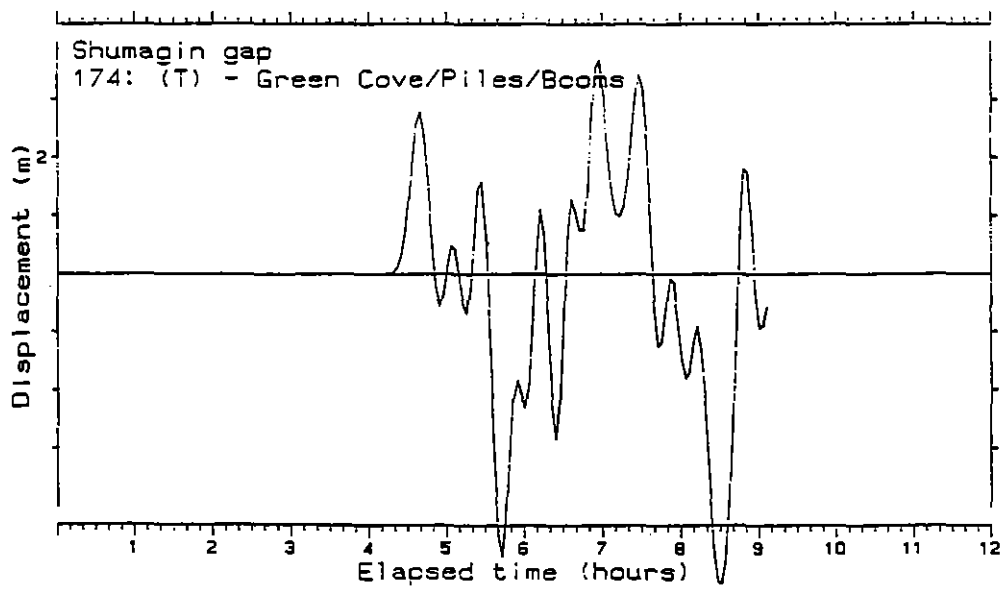
Shumagin gap
174: (T) - Green Cove/Piles/Booms
Displacement (m)
2
1 2 3 4 5 6 7 8 9 10 11 12
Elapsed time (hours)

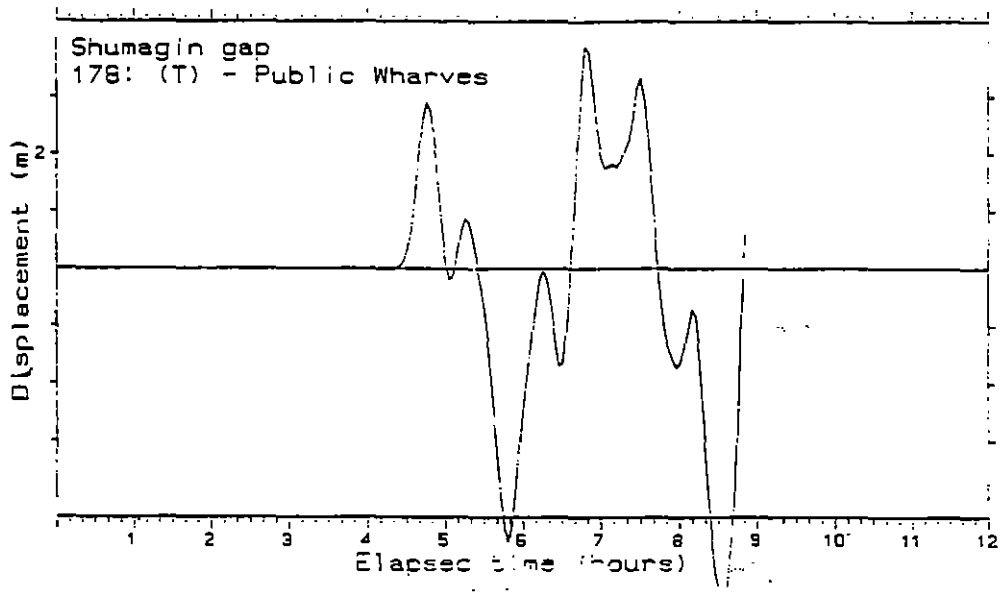
Shumagin gap
178: (T) - Public Wharves
Displacement (m)
2
1 2 3 4 5 6 7 8 9 10 11 12
Elapsed time (hours)

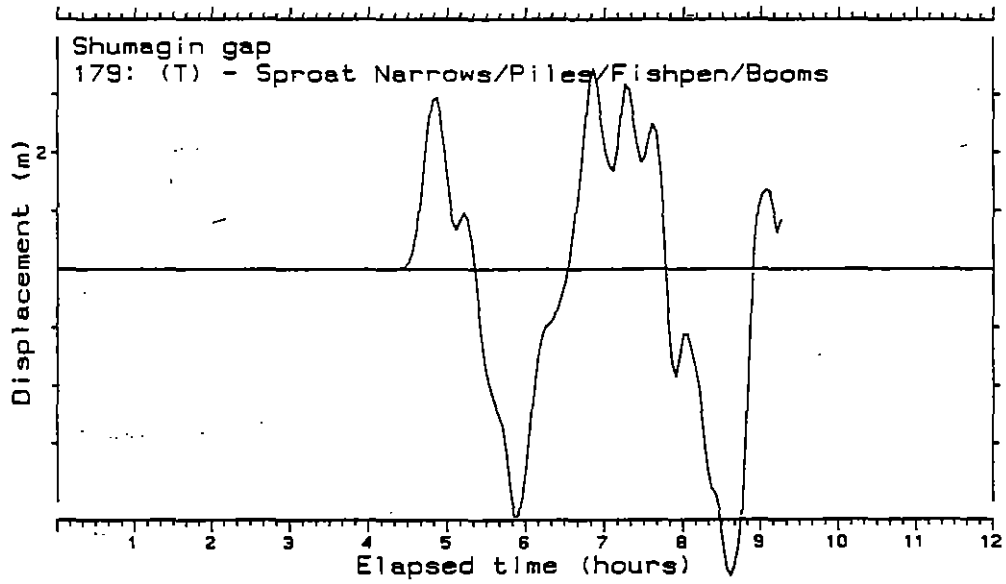
Shumagin gap
179: (T) - Sproat Narrows/Piles/Fishpen/Booms
Displacement (m)
2
1 2 3 4 5 6 7 8 9 10 11 12
Elapsed time (hours)

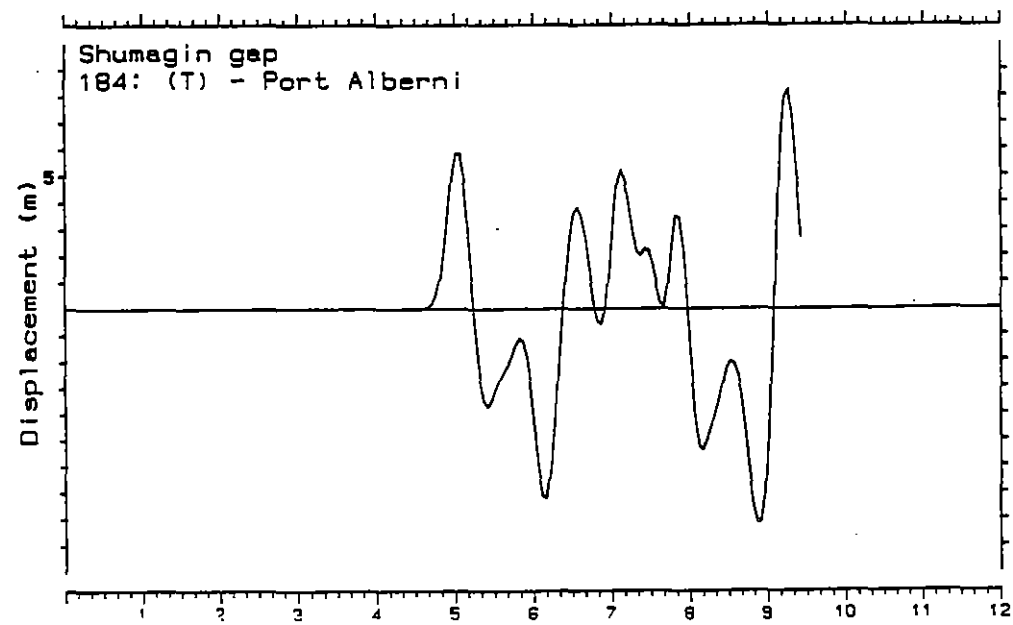
Shumagin gap
184: (T) - Port Alberni
Displacement (m)
5
1 2 3 4 5 6 7 8 9 10 11 12

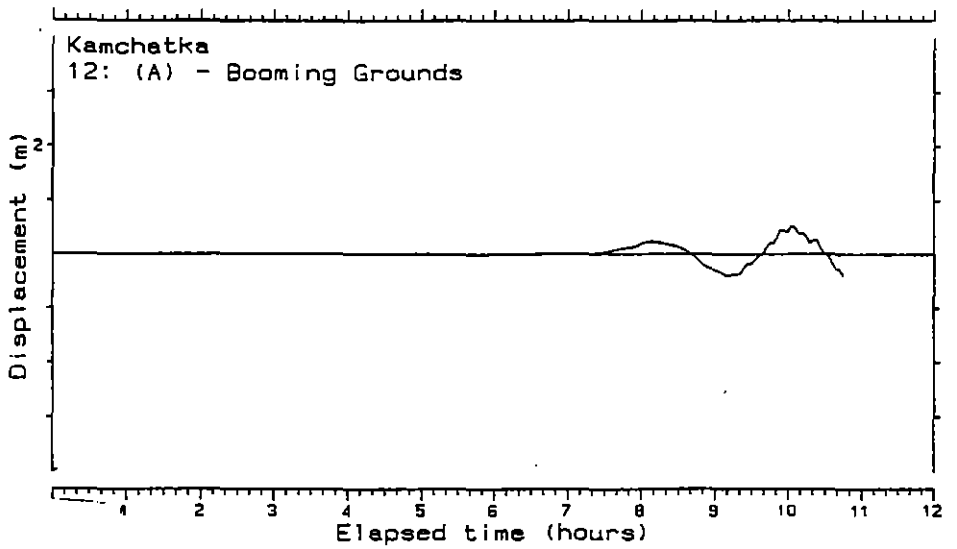
Kamchatka
12: (A) - Booming Grounds
Displacement (m)
2
1
2
3
4
5
6
7
8
9
10
11
12
Elapsed time (hours)

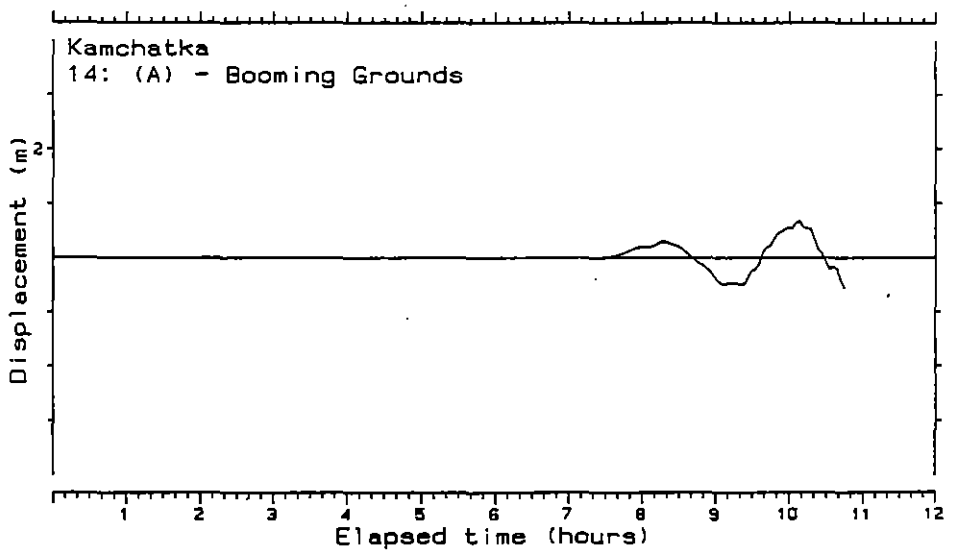
Kamchatka
14: (A) - Booming Grounds
Displacement (m)
2
1
2
3
4
5
6
7
8
9
10
11
12
Elapsed time (hours)

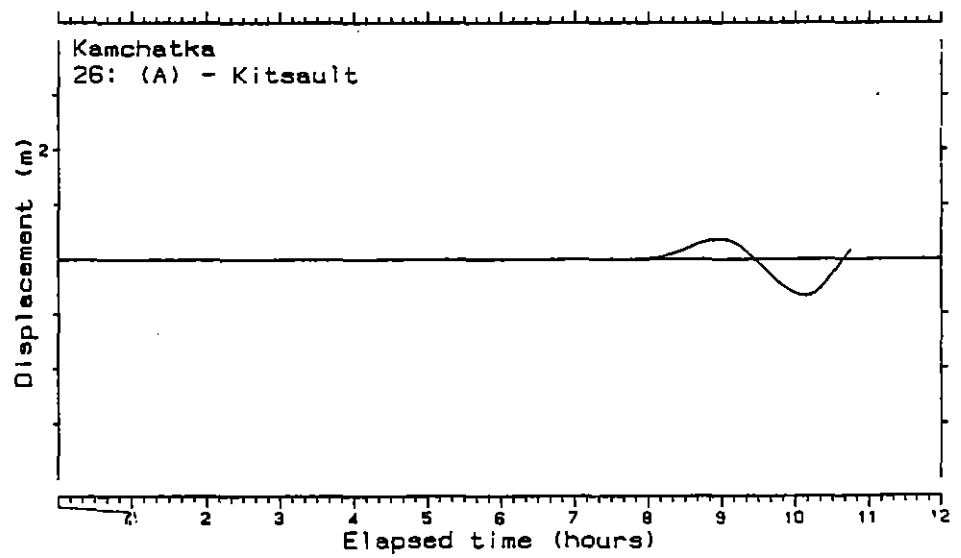
Kamchatka
26: (A) - Kitsault
Displacement (m)
2
1
2
3
4
5
6
7
8
9
10
11
12
Elapsed time (hours)

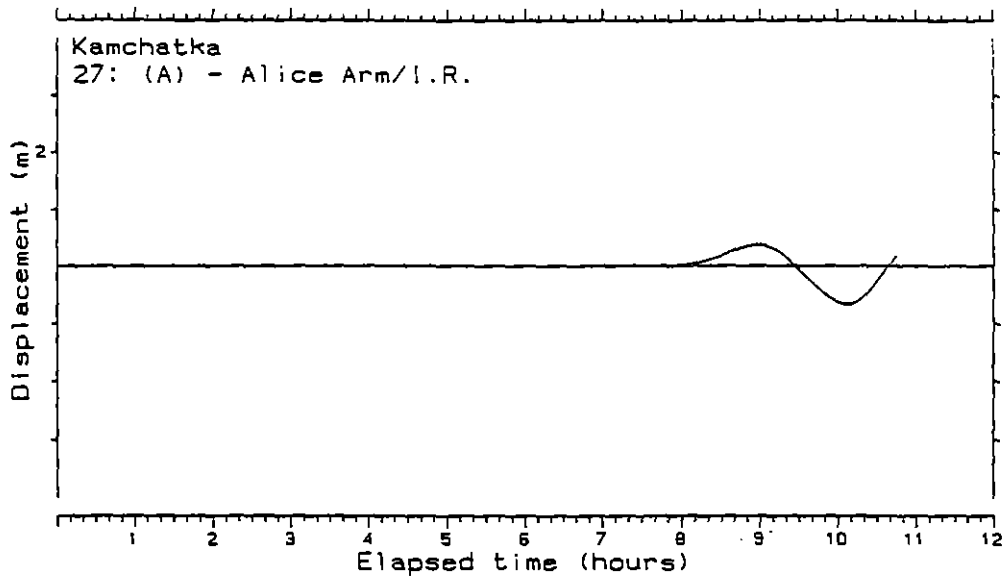
Kamchatka
27: (A) - Alice Arm/I.R.
Displacement (m)
2
1 2 3 4 5 6 7 8 9 10 11 12
Elapsed time (hours)

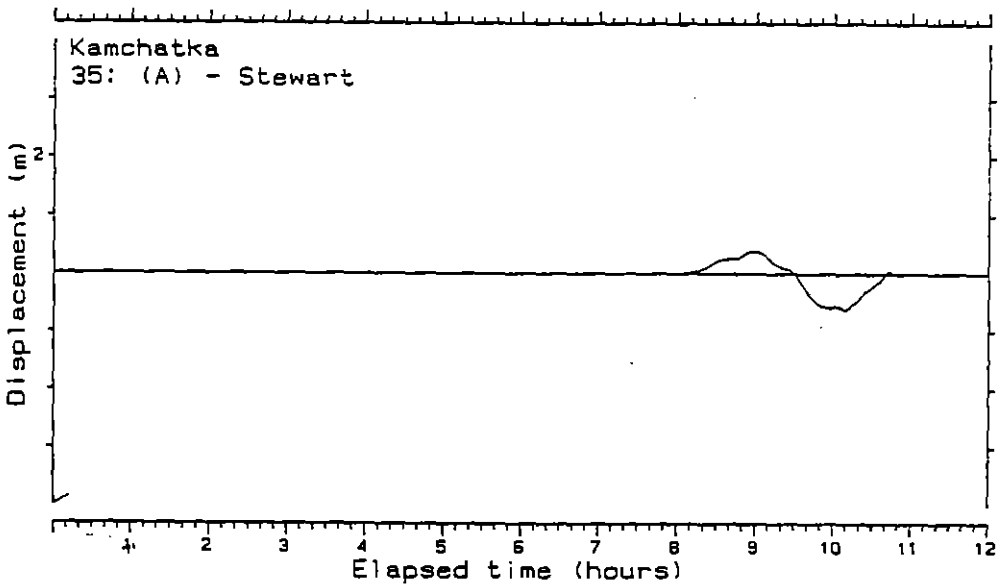
Kamchatka
35: (A) - Stewart
Displacement (m)
2
1 2 3 4 5 6 7 8 9 10 11 12
Elapsed time (hours)

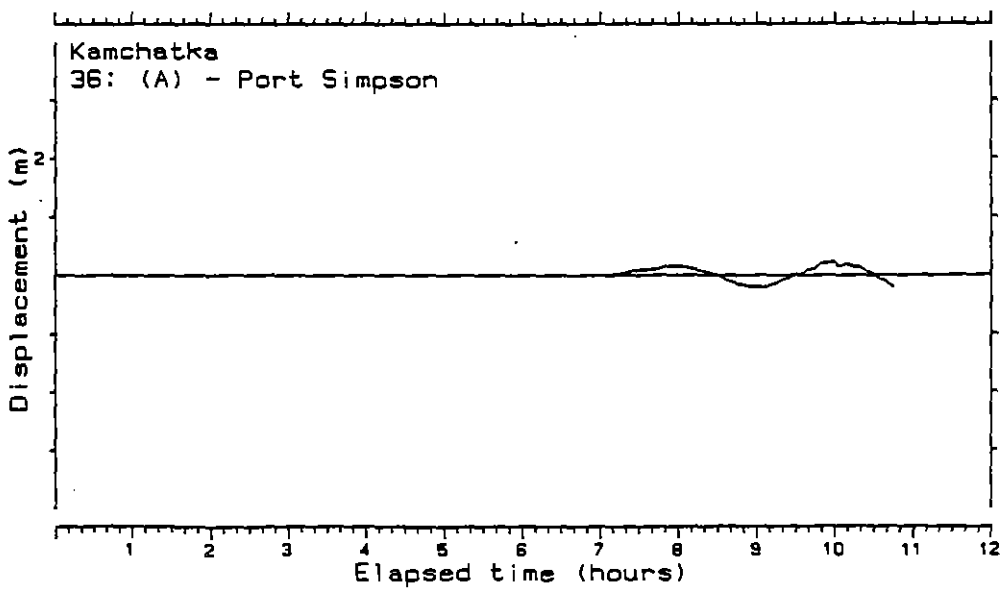
Kamchatka
36: (A) - Port Simpson
Displacement (m)
2
1 2 3 4 5 6 7 8 9 10 11 12
Elapsed time (hours)

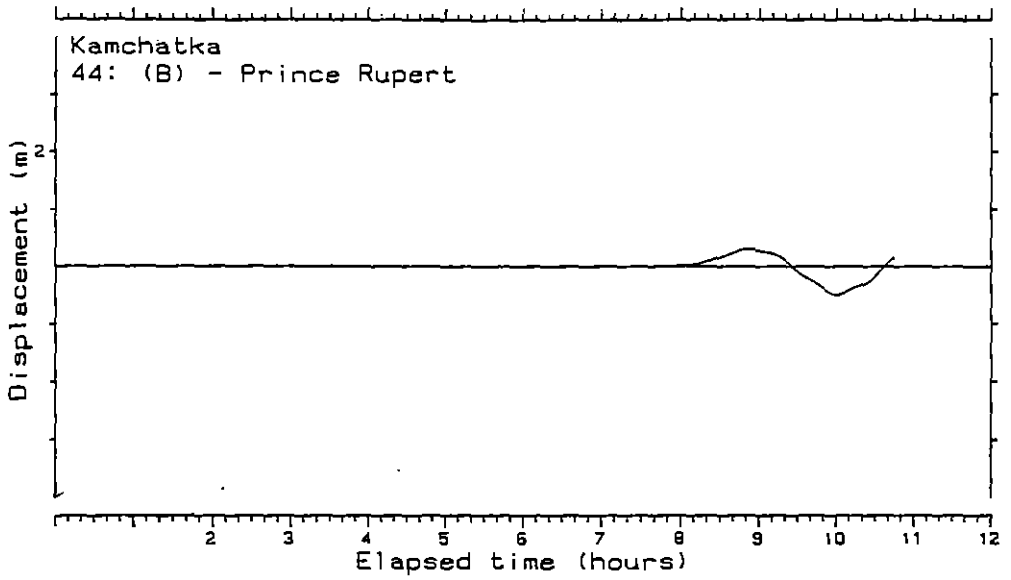
Kamchatka
44: (B) - Prince Rupert
Displacement (m)
2
2 3 4 5 6 7 8 9 10 11 12
Elapsed time (hours)

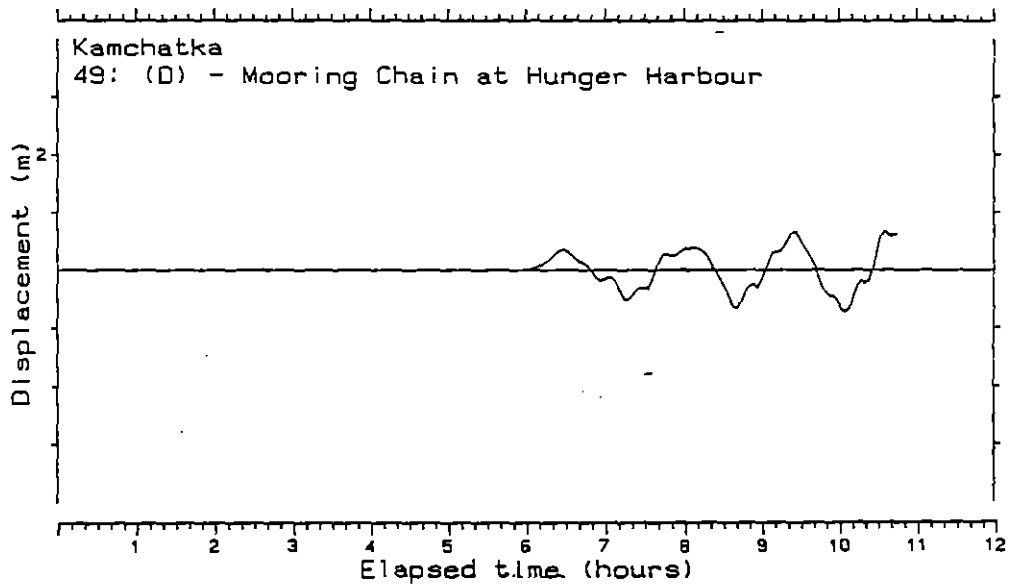
Kamchatka
49: (D) - Mooring Chain at Hunger Harbour
Displacement (m)
2
1 2 3 4 5 6 7 8 9 10 11 12
Elapsed time (hours)

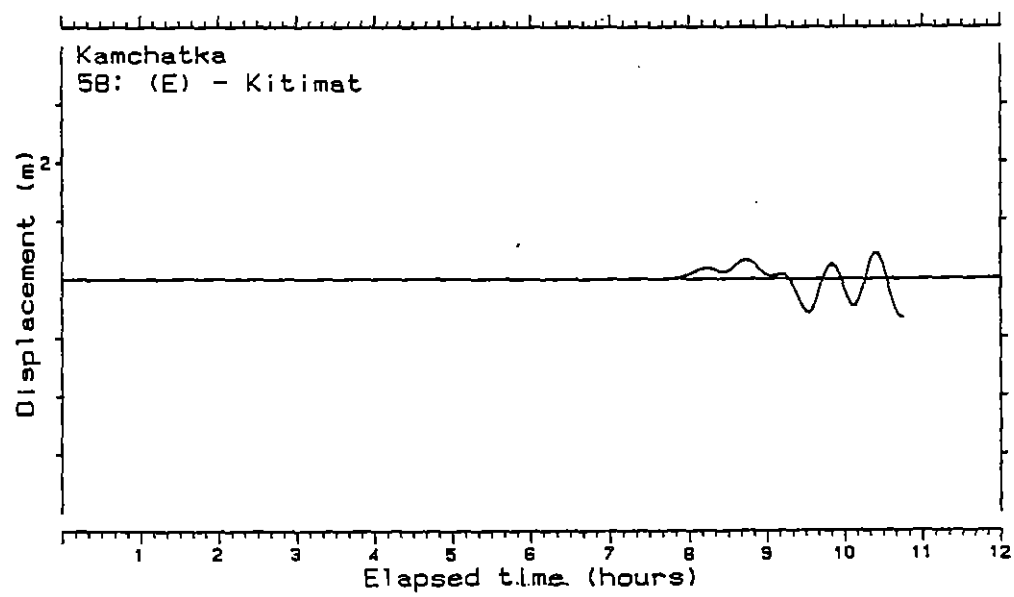
Kamchatka
58: (E) - Kitimat
Displacement (m)
2
1 2 3 4 5 6 7 8 9 10 11 12
Elapsed time (hours)

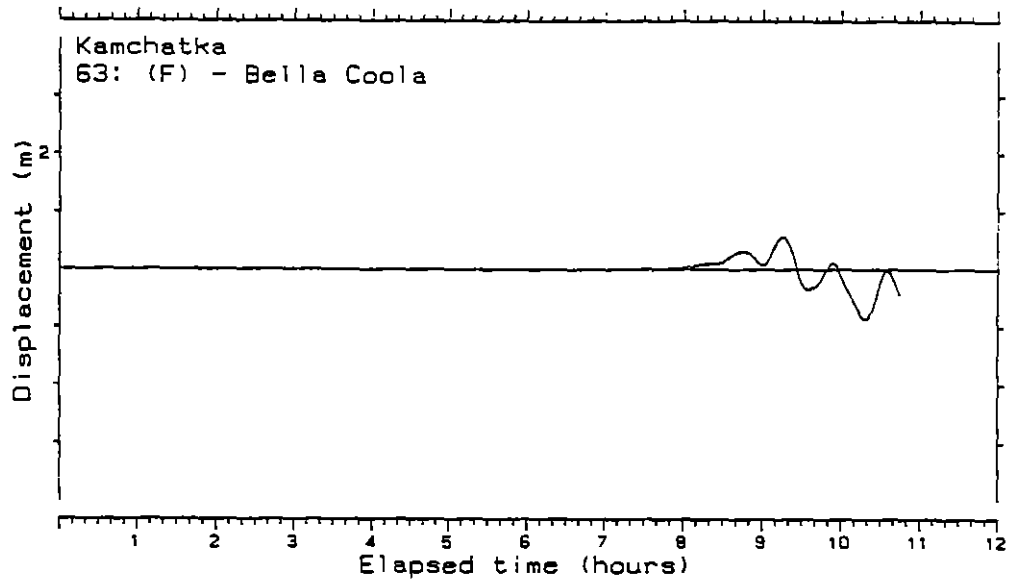
Kamchatka
63: (F) - Bella Coola
Displacement (m)
2
1 2 3 4 5 6 7 8 9 10 11 12
Elapsed time (hours)

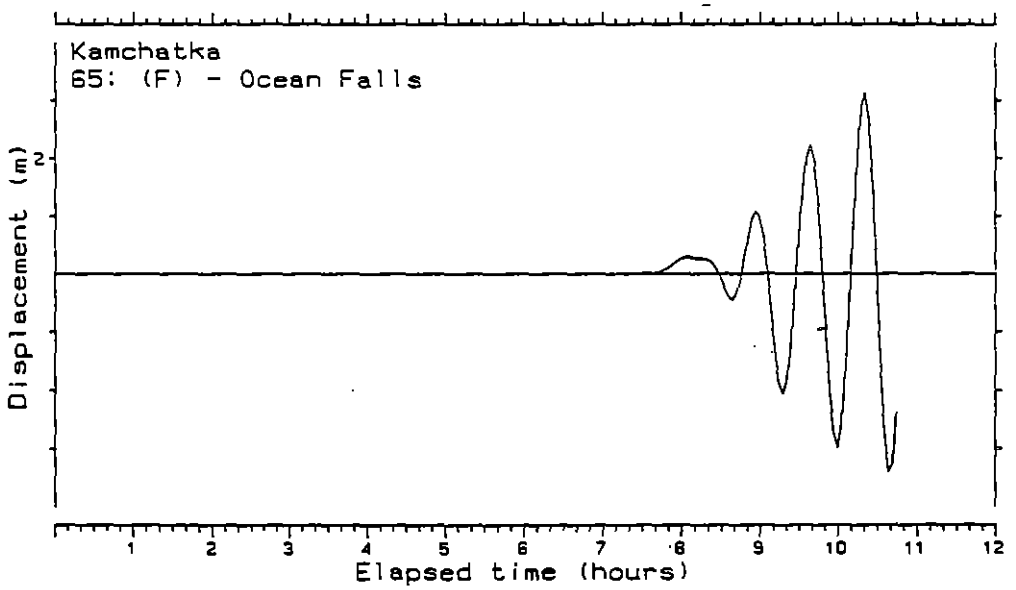
Kamchatka
65: (F) - Ocean Falls
Displacement (m)
2
1 2 3 4 5 6 7 8 9 10 11 12
Elapsed time (hours)

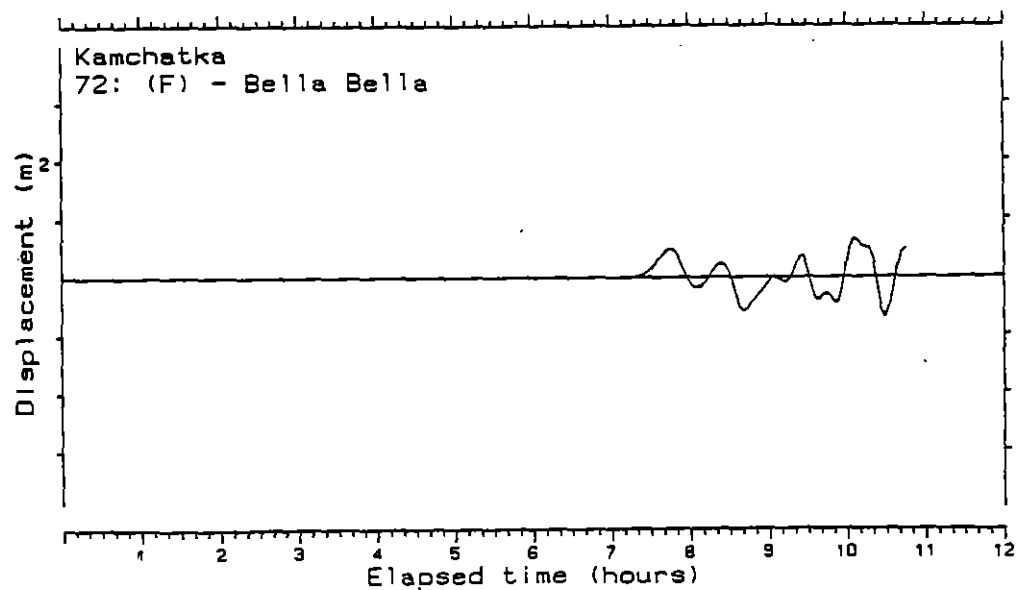
Kamchatka
72: (F) - Bella Bella
Displacement (m)
2
1 2 3 4 5 6 7 8 9 10 11 12
Elapsed time (hours)

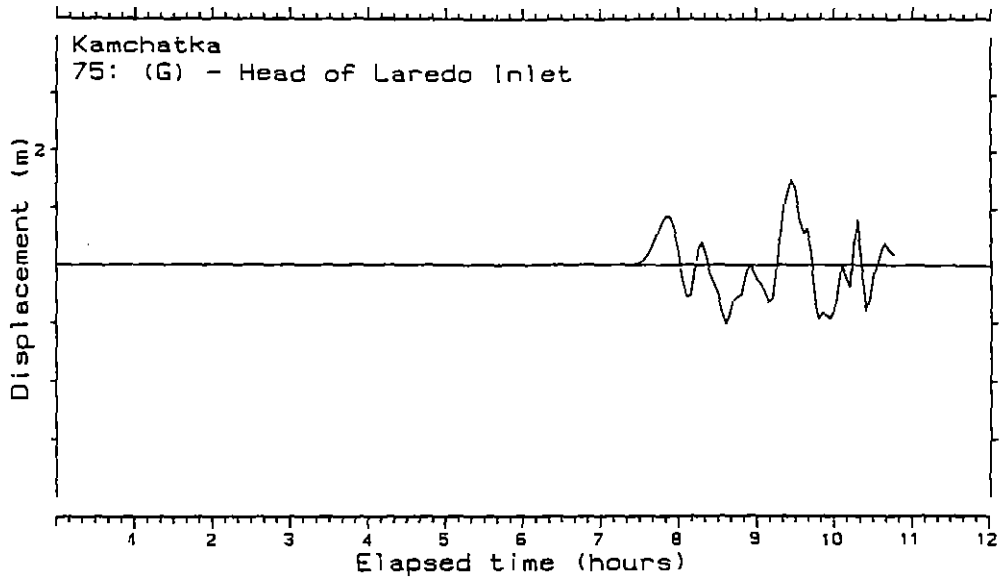
Kamchatka
75: (G) - Head of Laredo Inlet
Displacement (m)
2
1 2 3 4 5 6 7 8 9 10 11 12
Elapsed time (hours)

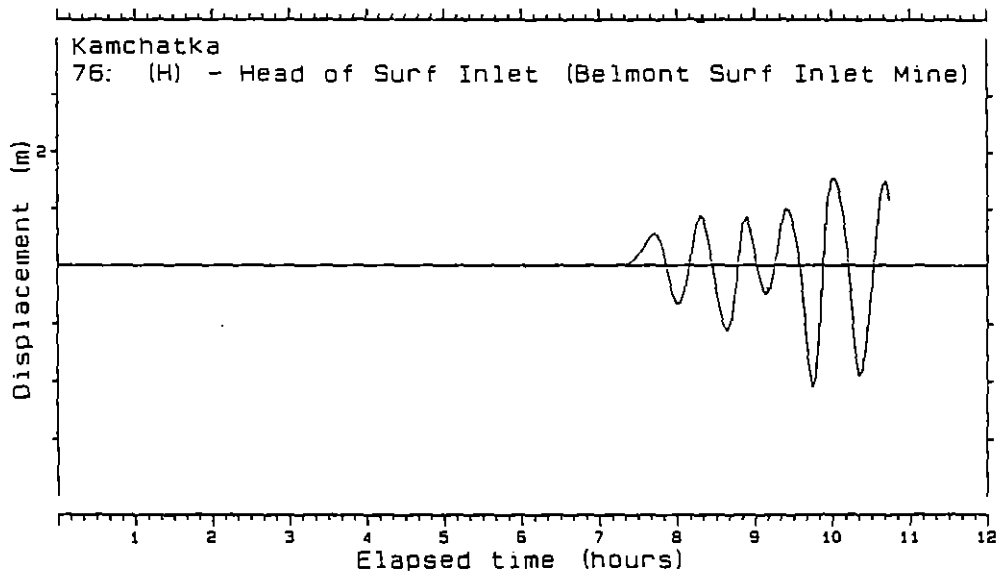
Kamchatka
76: (H) - Head of Surf Inlet (Belmont Surf Inlet Mine)
Displacement (m)
2
1 2 3 4 5 6 7 8 9 10 11 12
Elapsed time (hours)

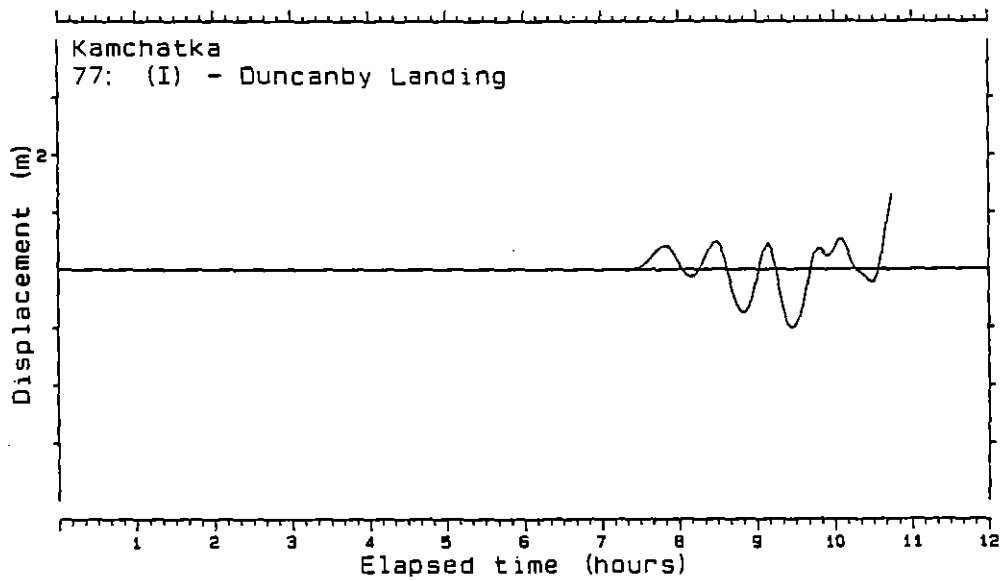
Kamchatka
77: (I) - Duncanby Landing
Displacement (m)
2
1 2 3 4 5 6 7 8 9 10 11 12
Elapsed time (hours)

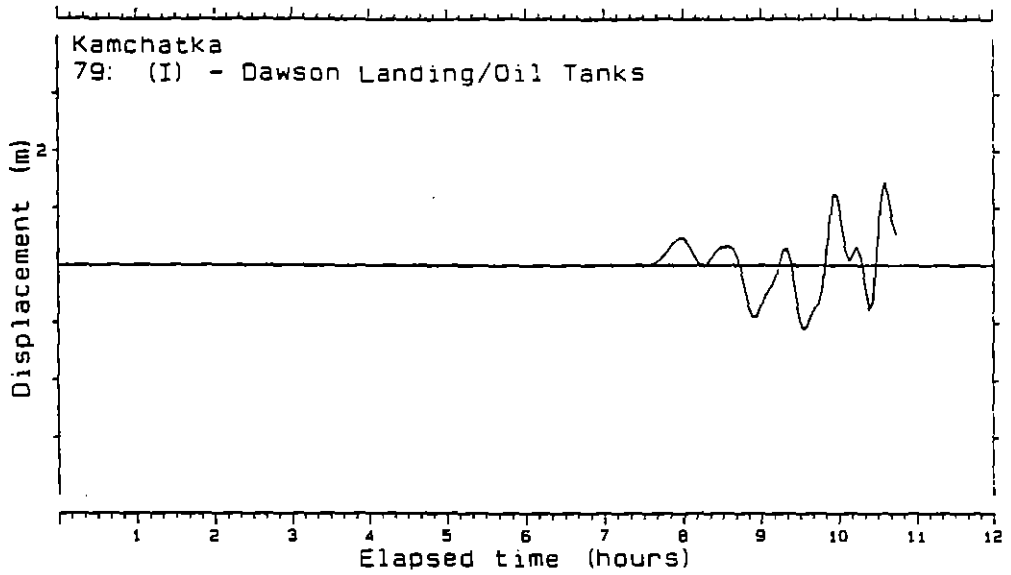
Kamchatka
79: (I) - Dawson Landing/Oil Tanks
Displacement (m)
2
1 2 3 4 5 6 7 8 9 10 11 12
Elapsed time (hours)

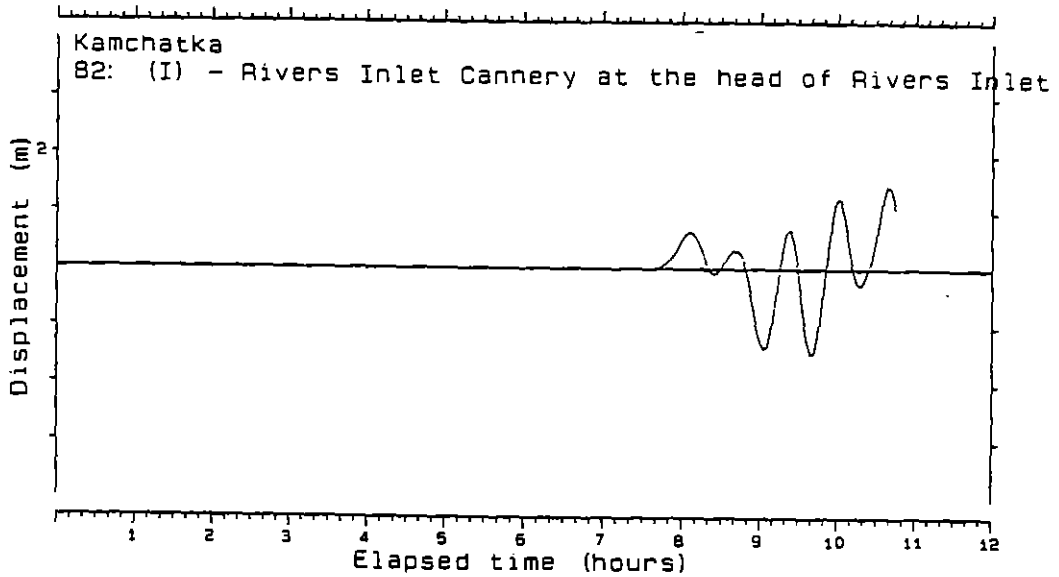
Kamchatka
82: (I) - Rivers Inlet Cannery at the head of Rivers Inlet
Displacement (m)
2
1 2 3 4 5 6 7 8 9 10 11 12
Elapsed time (hours)

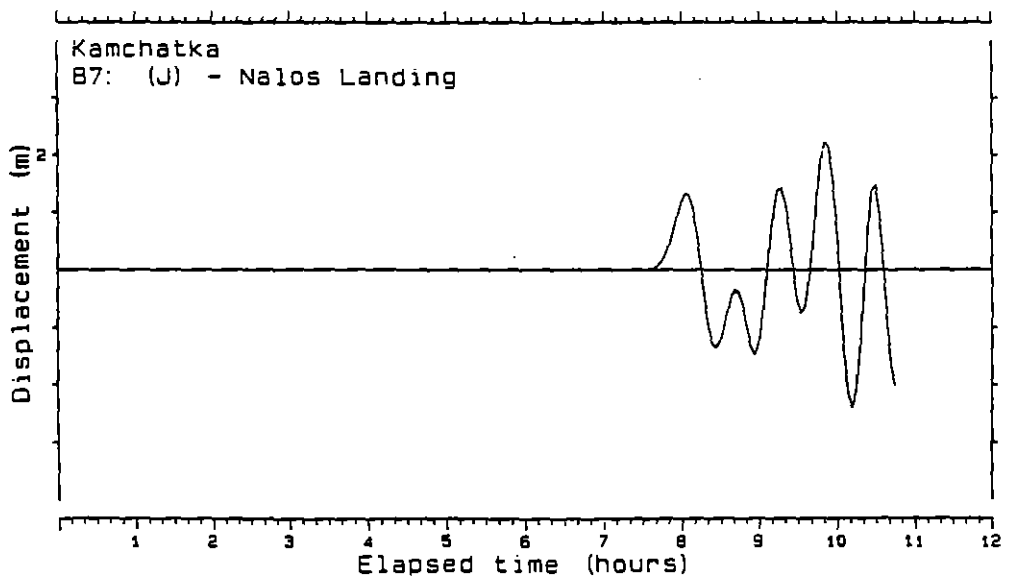
Kamchatka
87: (J) - Nalos Landing
Displacement (m)
2
1 2 3 4 5 6 7 8 9 10 11 12
Elapsed time (hours)

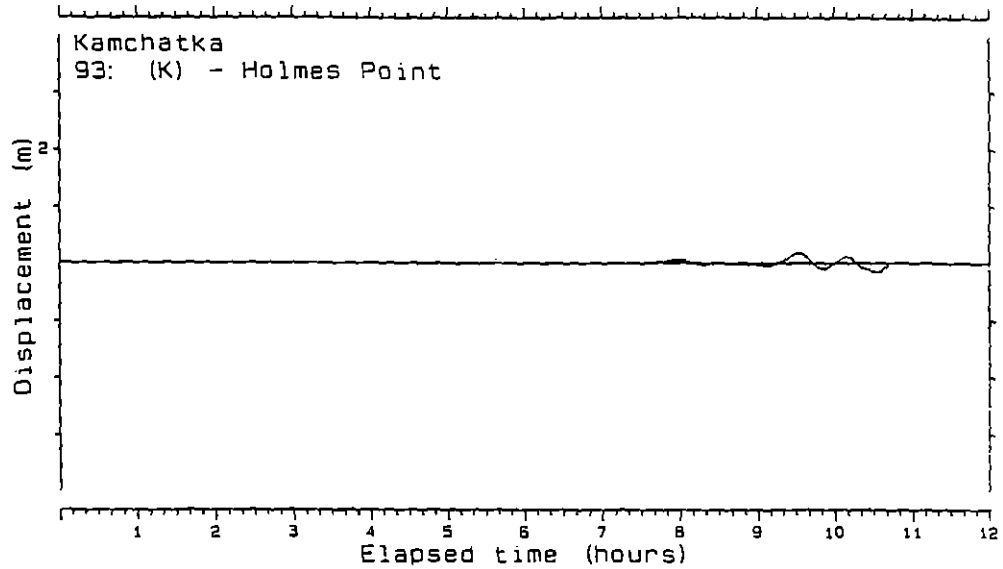
Kamchatka
93: (K) - Holmes Point
Displacement (m)
2
1 2 3 4 5 6 7 8 9 10 11 12
Elapsed time (hours)

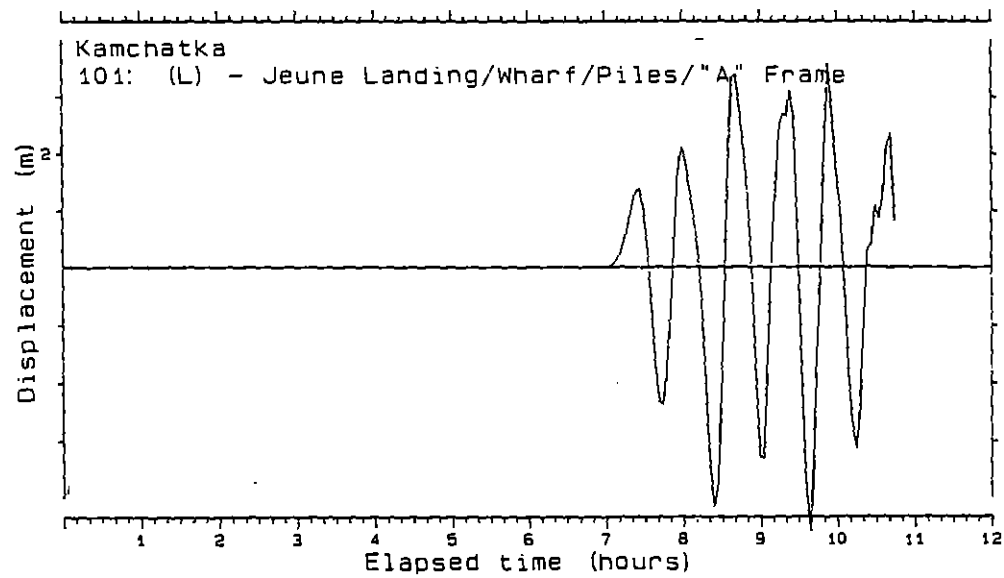
Kamchatka
101: (L) - Jeune Landing/Wharf/Piles/"A" Frame
Displacement (m)
2
1 2 3 4 5 6 7 8 9 10 11 12
Elapsed time (hours)

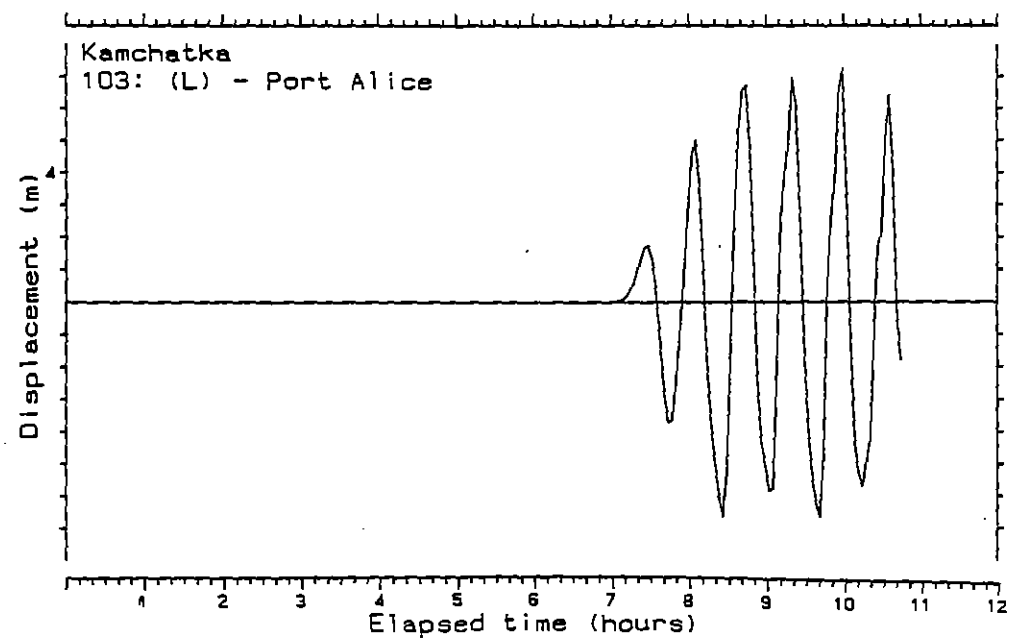
Kamchatka
103: (L) - Port Alice
Displacement (m)
4
1 2 3 4 5 6 7 8 9 10 11 12
Elapsed time (hours)

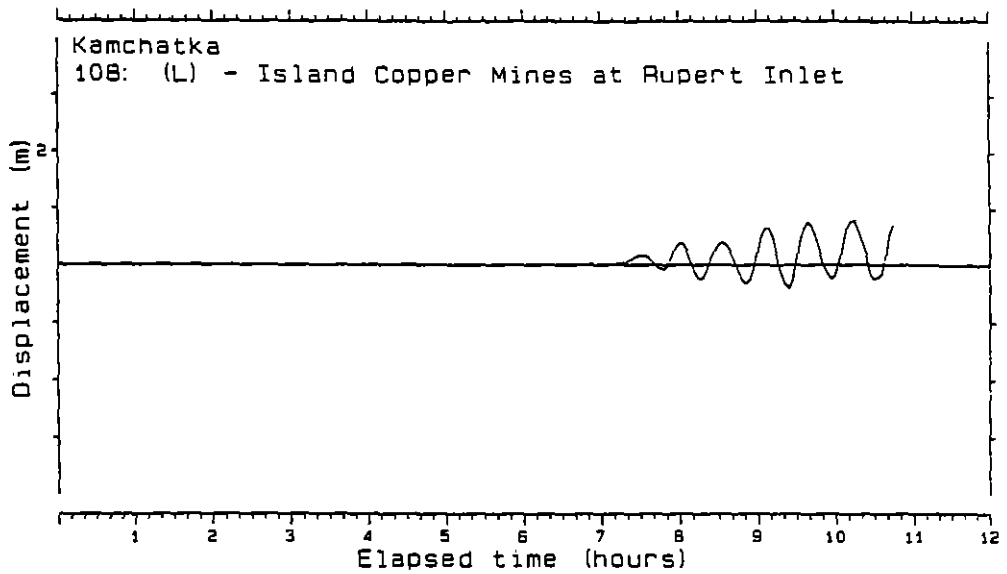
Kamchatka
108: (L) - Island Copper Mines at Rupert Inlet
Displacement (m)
2
1 2 3 4 5 6 7 8 9 10 11 12
Elapsed time (hours)

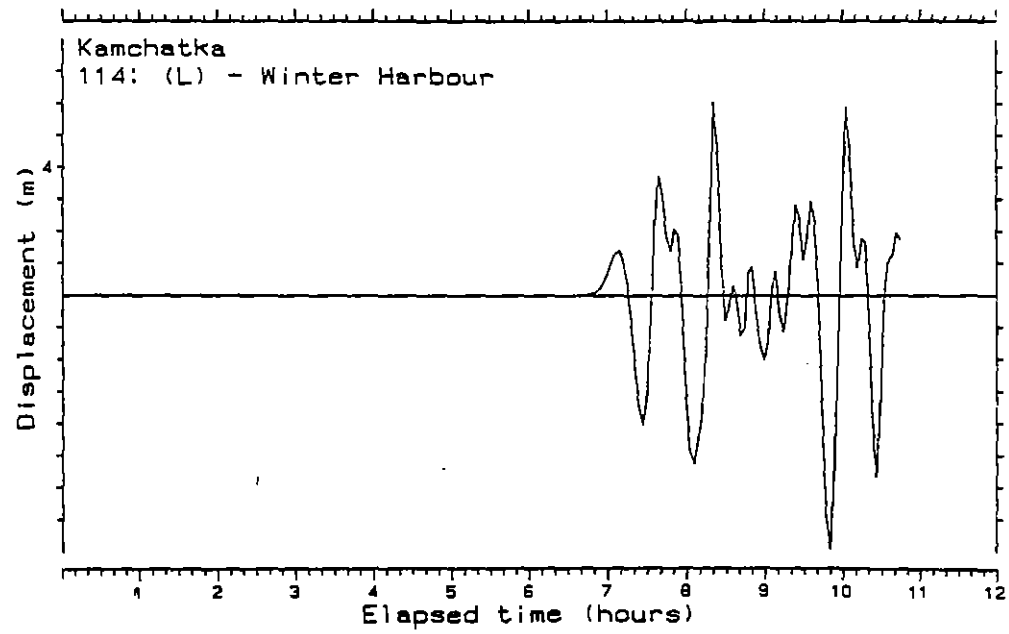
Kamchatka
114: (L) - Winter Harbour
Displacement (m)
4
1 2 3 4 5 6 7 8 9 10 11 12
Elapsed time (hours)

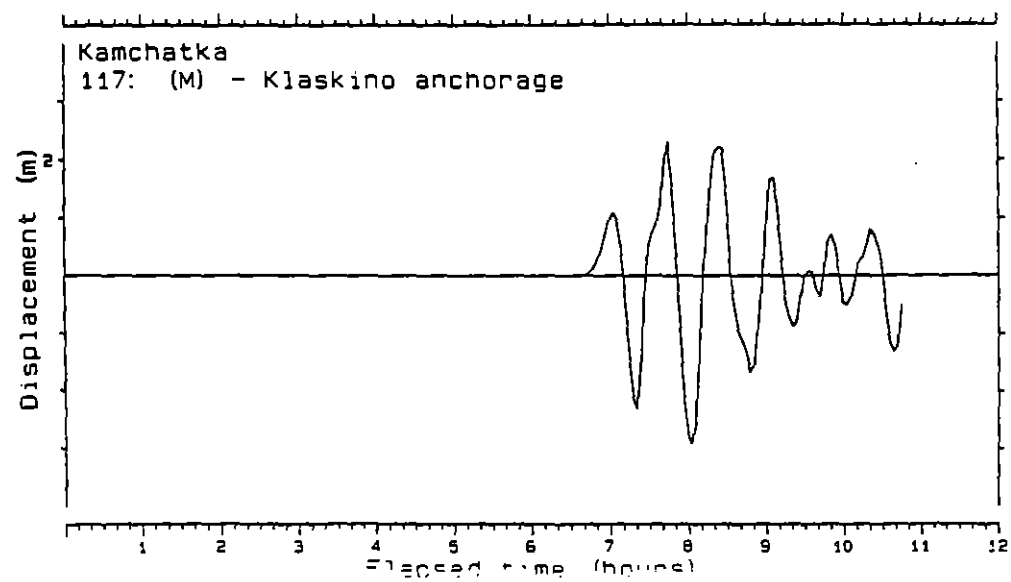
Kamchatka
117: (M) - Klaskino anchorage
Displacement (m)
2
1 2 3 4 5 6 7 8 9 10 11 12
Elapsed time (hours)

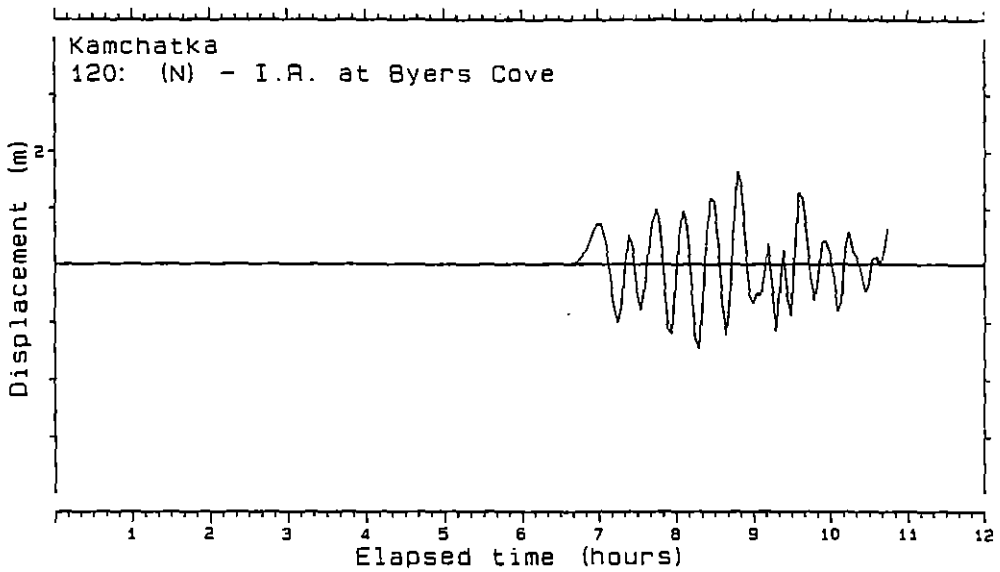
Kamchatka
120: (N) - I.A. at Byers Cove
Displacement (m)
2
1 2 3 4 5 6 7 8 9 10 11 12
Elapsed time (hours)

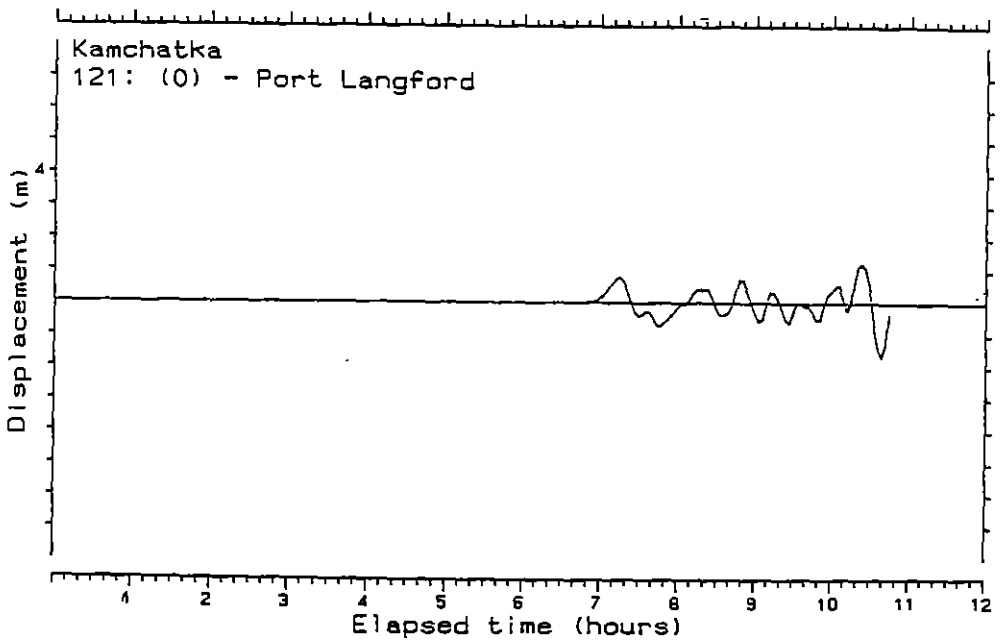
Kamchatka
121: (0) - Port Langford
Displacement (m)
4
1 2 3 4 5 6 7 8 9 10 11 12
Elapsed time (hours)

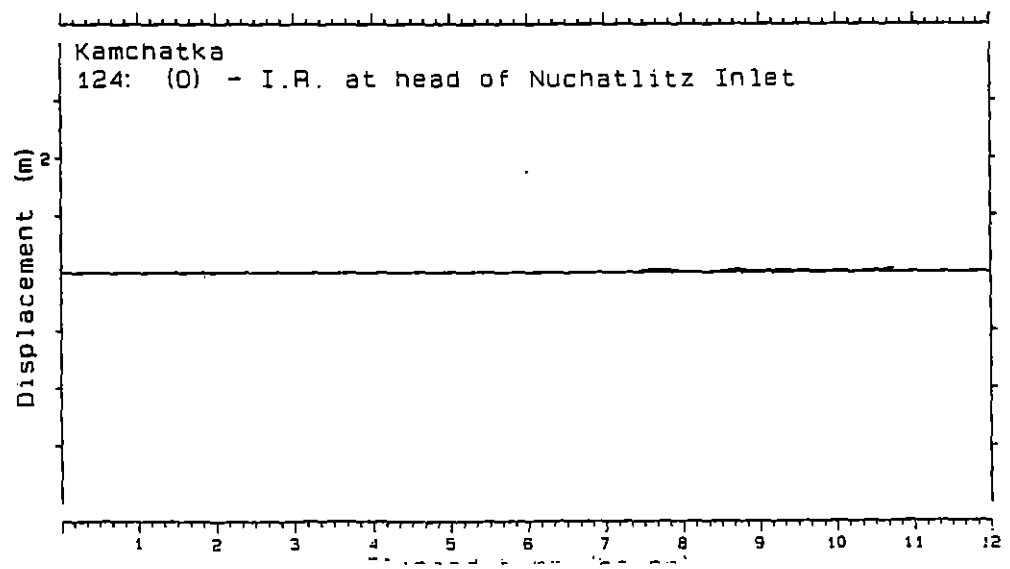
Kamchatka
124: (0) - I.A. at head of Nuchatlitz Inlet
Displacement (m)
2
1 2 3 4 5 6 7 8 9 10 11 12

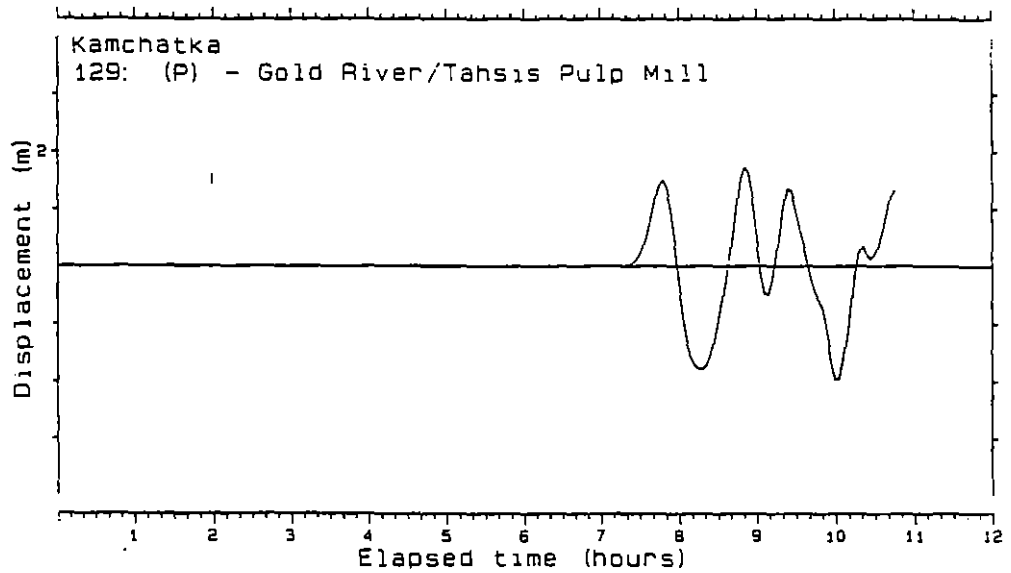
Kamchatka
129: (P) - Gold River/Tahsis Pulp Mill
Displacement (m)
2
1 2 3 4 5 6 7 8 9 10 11 12
Elapsed time (hours)

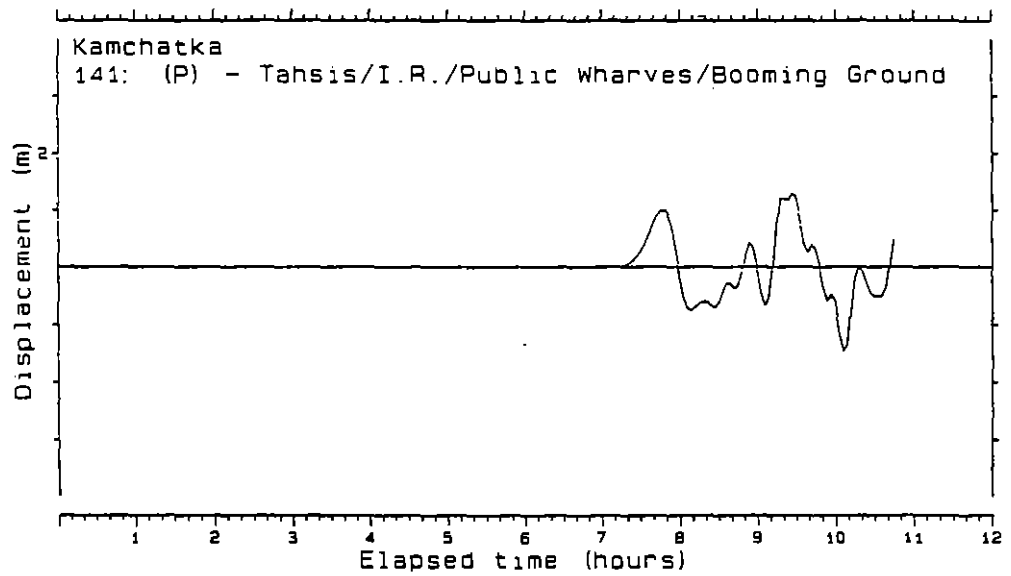
Kamchatka
141: (P) - Tahsis/I.R./Public Wharves/Booming Ground
Displacement (m)
2
1 2 3 4 5 6 7 8 9 10 11 12
Elapsed time (hours)

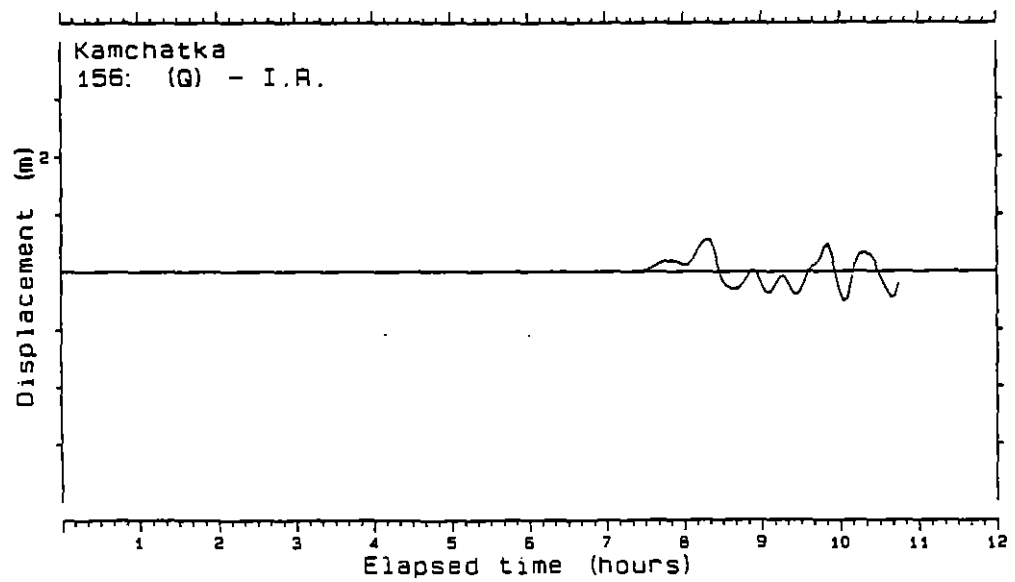
Kamchatka
156: (Q) - I.R.
Displacement (m)
2
1 2 3 4 5 6 7 8 9 10 11 12
Elapsed time (hours)

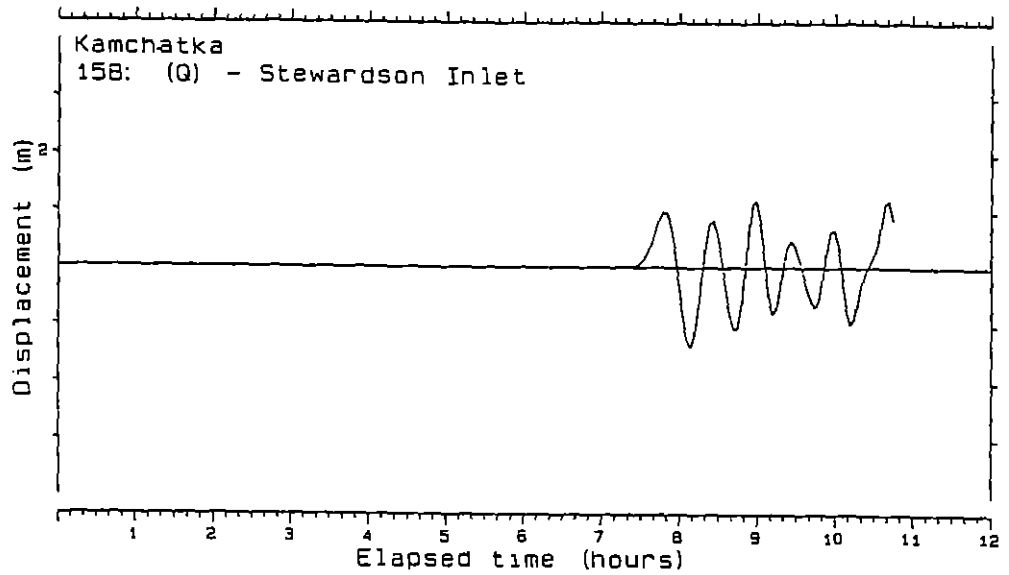
Kamchatka
158: (Q) - Stewardson Inlet
Displacement (m)
2
1 2 3 4 5 6 7 8 9 10 11 12
Elapsed time (hours)

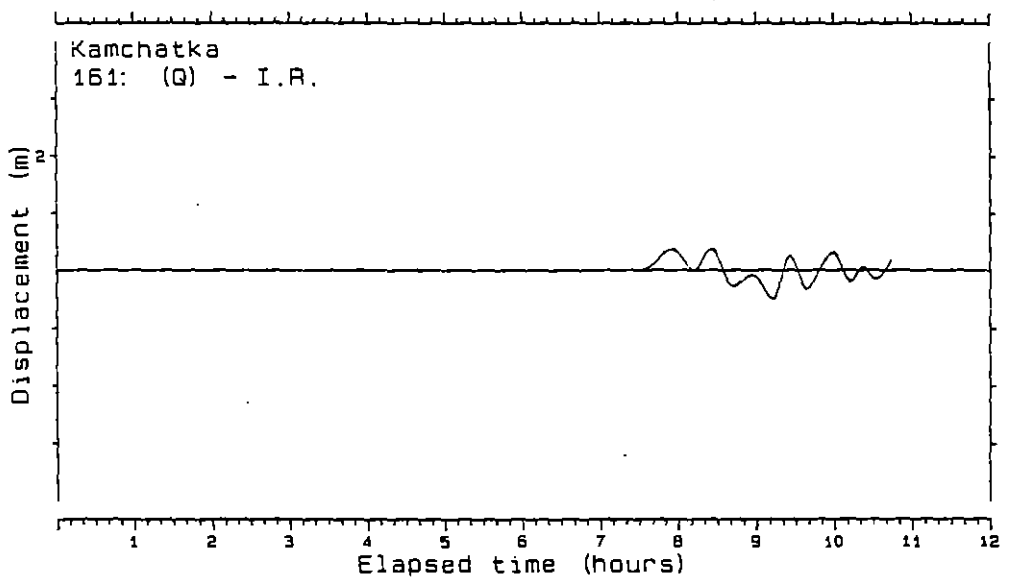
Kamchatka
161: (Q) - I.R.
Displacement (m)
2
1 2 3 4 5 6 7 8 9 10 11 12
Elapsed time (hours)

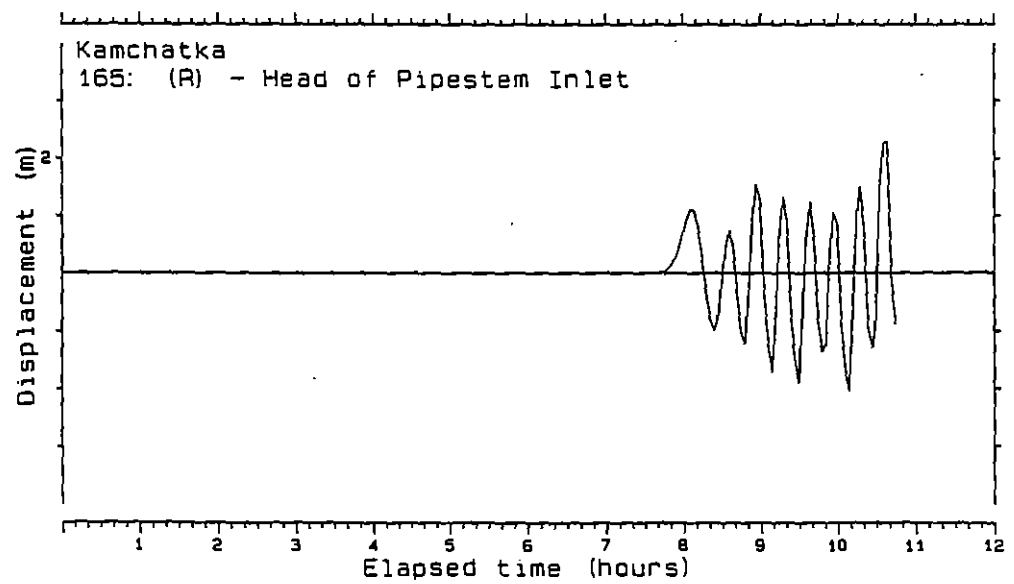
Kamchatka
165: (R) - Head of Pipestem Inlet
Displacement (m)
2
1 2 3 4 5 6 7 8 9 10 11 12
Elapsed time (hours)

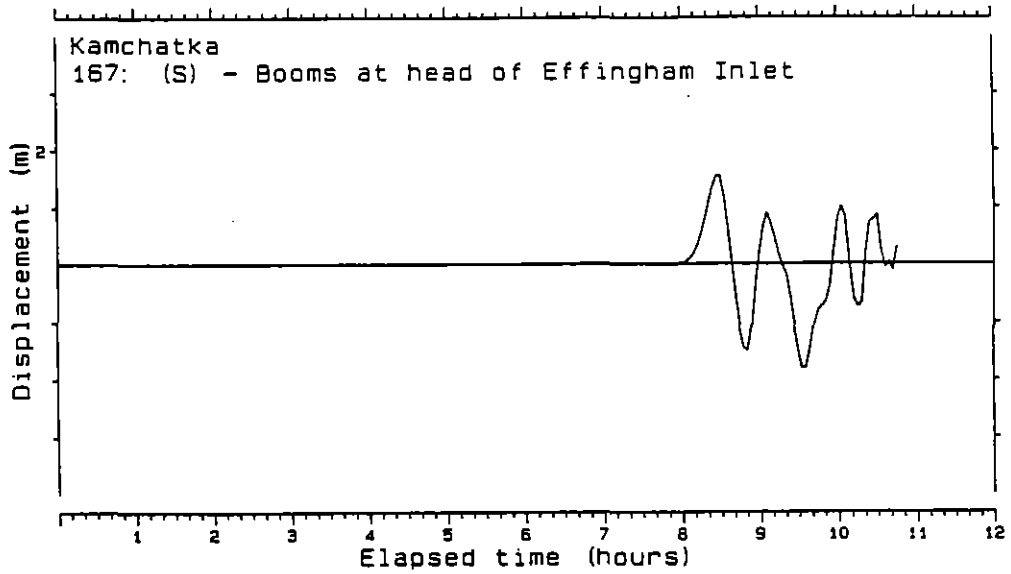
Kamchatka
167: (S) - Booms at head of Effingham Inlet
Displacement (m)
2
1 2 3 4 5 6 7 8 9 10 11 12
Elapsed time (hours)

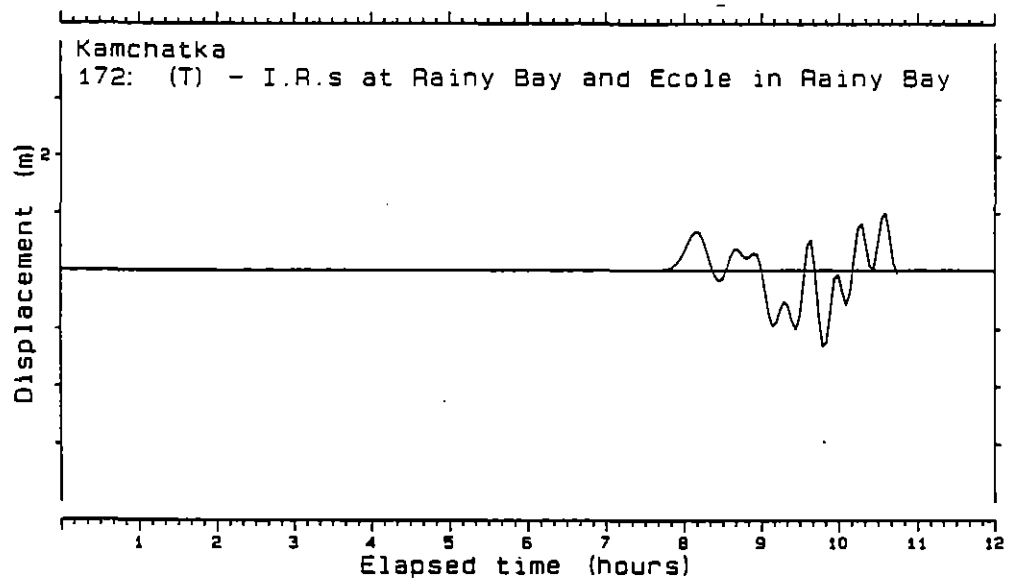
Kamchatka
172: (T) - I.R.s at Rainy Bay and Ecole in Rainy Bay
Displacement (m)
2
1 2 3 4 5 6 7 8 9 10 11 12
Elapsed time (hours)

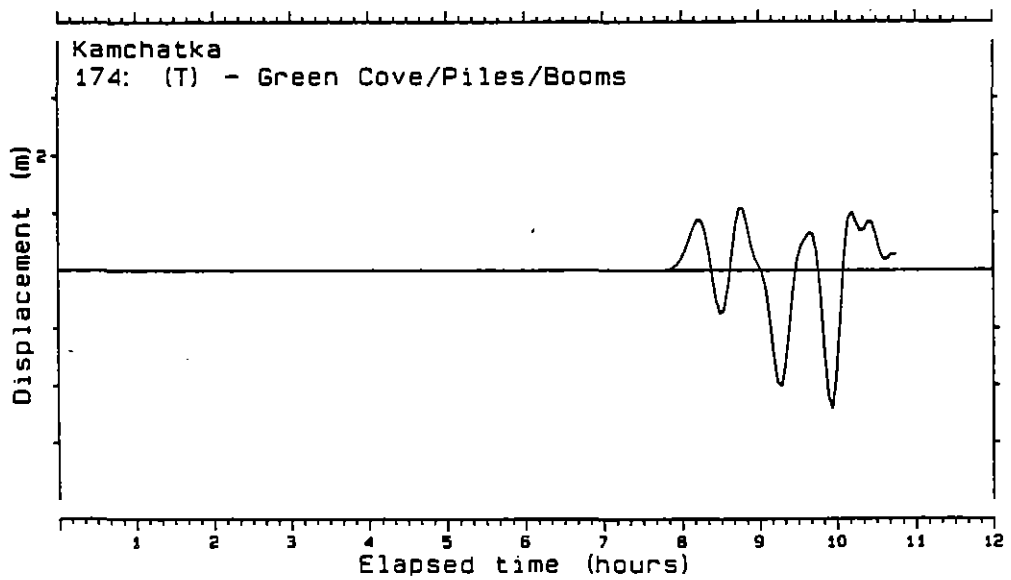
Kamchatka
174: (T) - Green Cove/Piles/Booms
Displacement (m)
2
1 2 3 4 5 6 7 8 9 10 11 12
Elapsed time (hours)

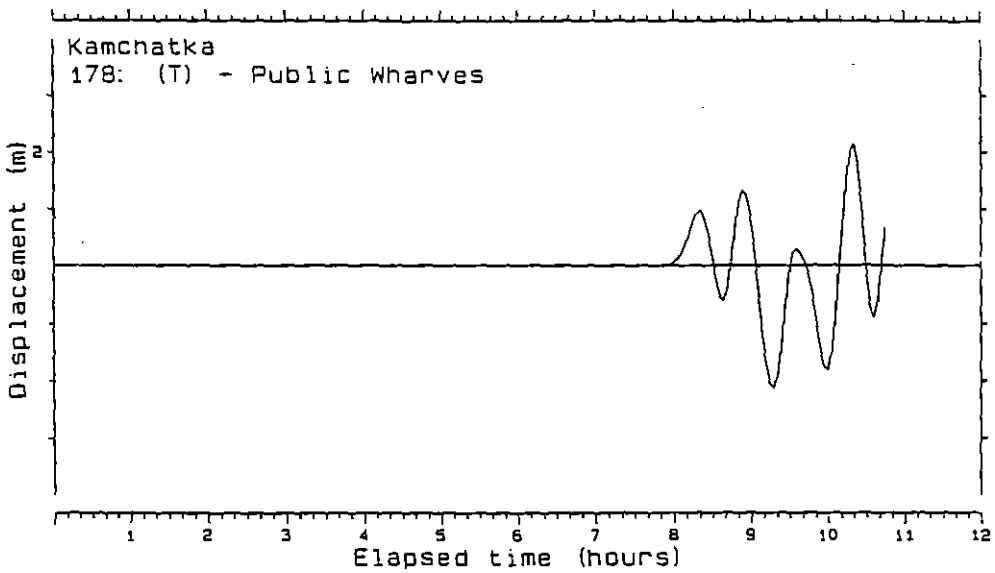
Kamchatka
178: (T) - Public Wharves
Displacement (m)
2
1 2 3 4 5 6 7 8 9 10 11 12
Elapsed time (hours)

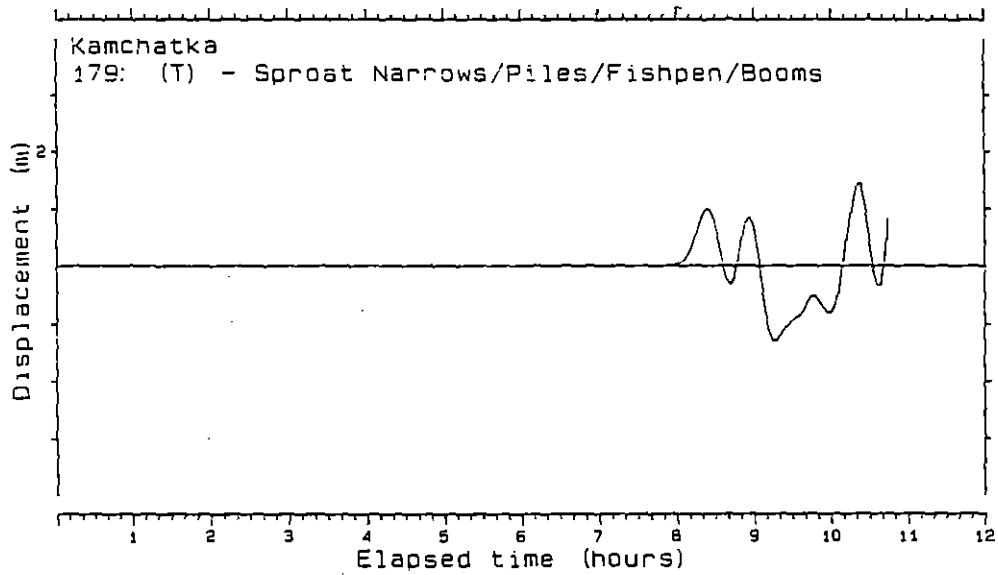
Kamchatka
179: (T) - Sproat Narrows/Piles/Fishpen/Booms
Displacement (m)
2
1 2 3 4 5 6 7 8 9 10 11 12
Elapsed time (hours)

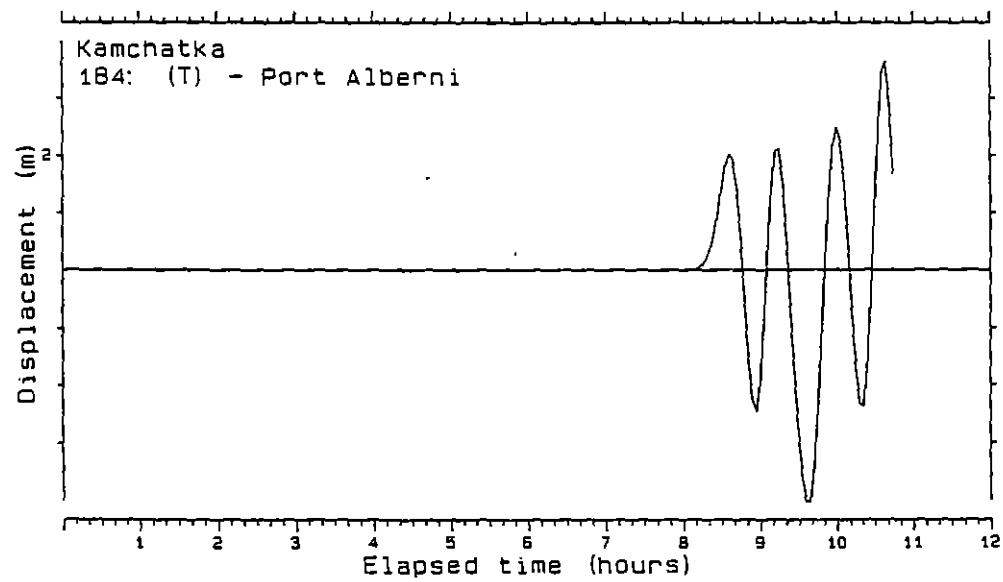
Kamchatka
184: (T) - Port Alberni
Displacement (m)
2
1 2 3 4 5 6 7 8 9 10 11 12
Elapsed time (hours)